JACOBS
UNIVERSITY

Sea-ice thickness and porosity from multi-frequency electromagnetic induction sounding: Application to the sub-ice platelet layer in Atka Bay, Antarctica

by

Priska A. Hunkeler

A thesis submitted in partial fulfillment
of the requirements for the degree of

Doctor of Philosophy

in Geosciences

Approved Dissertation Committee:

Prof. Dr. R. Gerdes[1,2]
Prof. Dr. A. Koschinsky[1]
Dr. S. Hendricks[2]

[1]Jacobs University Bremen
[2]Alfred-Wegener-Institut Helmholtz-Zentrum
für Polar- und Meeresforschung

Date of Defense: August 10, 2015

Abstract

Characterization of the sea-ice cover is of great importance for understanding processes and feedback mechanisms and predicting the evolution of the polar-climate system. One important climate relevant parameter, which can be used for this characterization, is sea-ice thickness. It can be retrieved by a variety of methods, where the majority is based on indirect determination from related parameters such as sea-ice draft or freeboard. A direct method that can be applied on the ground or from airborne platforms is electromagnetic (EM) induction sounding. This geophysical method is sensitive to the subsurface distribution of electrical conductivity. Since the conductivity of snow and sea ice have a low contrast compared to seawater, existing realizations by single-frequency EM sounders do not allow the discrimination between snow and sea ice and therefore only yield the total thickness of snow covered sea ice. In this thesis, I investigated the potential of EM sensors with multiple frequencies for the retrieval of the internal structure of sea ice, not only its thickness.

The first part of this thesis are sensitivity studies of a commercially available small-coil sensor using synthetic and field data at sites with a comprehensive validation dataset. An immediate result of this study was the identification and correction of a nonlinear effect in the signal processing chain that is negligible for geological targets but becomes important in the high conductive sea-ice regime. This so called bucking bias was henceforth used in the analysis of the EM data and further implemented in geophysical inversion algorithms. Two inversion schemes were tested with synthetic data for their potential to retrieve both thickness and bulk sea-ice porosity from multi-frequency EM data. Since the result of the inversion is conductivity and not porosity, an empirical relation between the parameters was established for different sea-ice types based on Archie's Law. This law was verified with actual EM field data with known sea-ice thickness and porosity. The inversion results showed reasonable agreements with either the underlying model of the synthetic data or the actual independently verified sea-ice properties.

After the method was verified in selected case studies, it was used for the first time on a large scale for a multi-frequency EM dataset from the landfast sea-ice in Atka Bay, Antarctica. The dataset consists of a variable sub-ice platelet layer below the solid sea-ice matrix, a layering structure with a large conductivity contrast that cannot be resolved with single-frequency EM. More than 100 km EM data over fast ice were analyzed with a laterally-constrained Marquardt-Levenberg inversion. All free parameters of the inversion, the thicknesses of sea ice and the platelet layer as well as their conductivities are in good agreement with independent measurements obtained from drilling experiments and other sensors. The modal platelet layer in Atka Bay was found between 4 and 6 m thick and increasing toward the resolution limit of the inversion close to ice shelf edges. From

conductivity results an ice-volume fraction distribution was calculated with a peak at 0.29 which is also in good agreement with other studies. If the spatial variability of the platelet-layer thickness and the ice-volume fraction from the EM surveys are taken into account, the estimation of the total platelet-layer volume is higher compared to other estimations that are based on the mass and energy balance considerations at a few selected points.

A second case study over deformed sea ice was based on the hypothesis that multi-frequency EM data allows to retrieve the macro-scale porosity of sea-ice pressure ridges. The voids in the ridge keel could be reproduced with varying success, but the addition of several layers improved the thickness information compared to single-frequency EM. Since the 1D forward model is an insufficient approximation of the complex geometry, the results could be improved in future with 2D forward and inversion schemes. With the adaption of the frequency spectrum to airborne devices, improved sea-ice characterizations could even be obtained on a larger scale than has previously been feasible.

Contents

Acknowledgements

I thank my advisor Stefan Hendricks for his outstanding support during my PhD time. You introduced me to the fascinating topic of sea ice, the usage of the EM-bird, the details about electromagnetics on sea ice and my nowadays favorite programming language Python. You always had good suggestions and ideas for changes to presentations, written documents, and figures; your comments were of very high quality which improved notably the papers and this thesis. I was enjoying working with you, at AWI or on field campaigns. During the three years you were always very optimistic, what was motivating and guided me through the PhD time. You were not only a great supervisor, but you have become a close friend.

I thank Rüdiger Gerdes for being my PhD supervisor, the support during my PhD project and for making it possible to write this thesis in the Sea Ice Physics group at AWI.

I thank Andrea Koschinsky for having agreed to be my second PhD supervisor and for the support during my PhD project.

I am grateful to my Dissertation Committee from Jacobs University (Rüdiger Gerdes, Andrea Koschinsky, Stefan Hendricks), the PhD Committee at AWI (Rüdiger Gerdes, Andrea Koschinsky, Stefan Hendricks and Klaus Grosfeld), Marcel Nicolaus and Hendrik Müller for the attendances during committee meetings, support, feedbacks and suggestions.

Thanks to POLMAR for the stipend and to Claudia Hanfland and Claudia Sprengel for the outstanding help and support during the PhD time. Your doors were always open; you took all concerns and questions seriously and supported me with the three-month prolongation.

Thanks to Colin Farquharson and Thomas Kalscheuer for the support and immediate answers concerning the inversion algorithms EM1DFM and EMILIA.

I thank Mario for his support throughout my PhD time. Thanks for discussing the papers, your careful proofreading, and the great expedition times on Polarstern and at Neumayer III. I really enjoyed working with you; the three years would not have been the same without you.

Thanks to Lera for the supporting words, for coffee and lunch breaks, for being a stipend

together with me, and just for being around.

Thanks to Steffi for the memorable expedition time on Polarstern and our adventures with Mario in Tasmania.

Thanks to Stefan, Andy and Hajo for the support and the unforgettable time during Barrow SIZONet 2012 and 2013 campaigns; to Mario, Stephan, Uwe, Maike and Thomas for the unbelievable experiences and the help on Neumayer III in 2012; to Stefan, Mario, Julie, Steffi, Stephan, Caro, Sandra, Seth, Nander and Kathy for the support and the incredible memories of the Polarstern winter expedition in 2013 (ANT-XXIX/6).

Thanks to the Sea Ice Physics group and fellow PhD students (Robert, Christian, Lera, Mario, Steffi, Ingrid, Giulia and Polona) for discussions, support and coffee breaks.

I thank my office mates (Vera, Polona, and Özgur) for the pleasant time.

Thanks to Lasse for making it possible to start the PhD at AWI.

Thanks for the support and encouragements of my grandiose family (Marie Theres, Erwin, Silvia, Markus), friends (Stephus, Tanja, Tobi, Christiane, Claudi, Selina, Sabina, Sabrina, Nadine, Mechi, Seidi, Yasser, Pascal, Inigo) and my prime team Union 60.

List of publications

P. A. Hunkeler, S. Hendricks, M. Hoppmann, S. Paul, R. Gerdes. Towards an estimation of sub sea-ice platelet-layer volume with multi-frequency electromagnetic induction sounding. Annals of Glaciology, 56(69):137-146, 2015.

P. A. Hunkeler, S. Hendricks, M. Hoppmann, C. Farquharson, T. Kalscheuer, M. Grab, M. S. Kaufmann, L. Rabenstein, R. Gerdes. Improved 1D inversions for sea ice thickness and conductivity from electromagnetic induction data: Inclusion of nonlinearities caused by passive bucking. Geophysics, 81(1):45-58, 2016.

P. A. Hunkeler, M. Hoppmann, S. Hendricks, T. Kalscheuer, R. Gerdes. A glimpse beneath Antarctic sea ice: platelet-layer volume from multi-frequency electromagnetic induction sounding. Geophysical Research Letters, 43(1), 222-231, 2016.

M. Hoppmann, M. Nicolaus, S. Paul, **P. A. Hunkeler**, G. Heinemann, S. Willmes, R. Timmermann, O. Boebel, T. Schmidt, M. Kühnel, G. König-Langlo, R. Gerdes. Ice platelets below Weddell Sea landfast sea ice, Annals of Glaciology, 56(69): 175-190, 2015.

S. Paul, S. Willmes, M. Hoppmann, **P. A. Hunkeler**, C. Wesche, M. Nicolaus, G. Heinemann, R. Timmermann. The impact of early summer snow properties on Antarctic landfast sea-ice X-band backscatter, Annals of Glaciology, 56(69): 263-273, 2015.

M. Hoppmann, M. Nicolaus, **P. A. Hunkeler**, P. Heil, L.-K. Behrens, G. König-Langlo, R. Gerdes. Seasonal evolution of an ice-shelf influenced fast-ice regime, derived from an autonomous thermistor chain, Journal of Geophysical Research, Oceans, 120(3):1703-1724, 2015.

R. Lindsay, C. Haas, S. Hendricks, **P. Hunkeler**, N. Kurtz, J. Paden, B. Panzer, J. Sonntag, J. Yungel, J. Zhang. Seasonal forecasts of Arctic sea ice initialized with observations of ice thickness, Geophysical Research Letters, 39(21), 2012.

1 Introduction

1.1. Sea ice

1.1.1. Role in the climate system

On a global perspective, the sea-ice cover is a very thin insulating layer, located between the ocean and the atmosphere. Chemical and physical processes in atmosphere and ocean directly influence the sea ice, but reversely the sea ice also affects atmosphere and ocean. For example, the sea-ice layer mediates heat and matter fluxes as well as the transfer of momentum between atmosphere and ocean. The effect on these processes is significant, despite the relative thinness of the sea-ice cover, where changes in the sea-ice cover would lead to a notable change in the polar climate system (Dieckmann and Hellmer, 2010). Therefore, sea ice has been named as an essential climate variable.

During the sea-ice freezing process, salt ions from growing sea ice are released into the ocean and contribute to the densification of surface seawater. This leads to convection in the ocean, driving the global thermohaline circulation. Melting of sea ice releases fresh water into the ocean, creating a stable stratification of the upper ocean layers (Brandon et al., 2010). Ocean circulation might further be influenced by sea-ice strength (Itkin et al., 2014) and topographic sea-ice features (Castellani et al., 2014), while ocean currents themselves may affect long-term sea-ice drift (Kwok et al., 2013). The main driver of sea-ice drift, however, is atmospheric forcing (Köberle and Gerdes, 2003; Rigor and Wallace, 2004). Surface winds are an important factor causing divergence or convergence of sea-ice floes and therefore contributing to changes in sea-ice extent. Divergence will create leads with thin sea-ice formation in freezing conditions, while convergence can lead to dynamic thickening of sea ice through deformation of sea ice. As a feedback mechanism, sea-ice extent may influence large-scale atmospheric circulation (Jaiser et al., 2012). Due

to its brighter surface compared to the ocean, sea ice reflects substantially more sunlight back into the atmosphere and consequently plays an important role in the global radiation balance. When sea ice retreats, the high-albedo sea-ice surface is replaced by low-albedo ocean surface, thus enhancing absorption of solar radiation and subsequent warming of the surface water. This in turn will increase the melting of sea ice and forms a positive feedback of sea-ice retreat (Perovich et al., 2008). Snow on sea ice is also an important factor to consider, since it further increases the amount of reflected sunlight (Sturm and Massom, 2010). Snow insulates sea ice from cold air temperatures, consequently slowing down sea-ice growth in winter and delaying melt in summer (Meier et al., 2014). Furthermore, snow is besides sea ice an additional fresh water source (Sturm and Massom, 2010). The availability of light below sea ice depends on the optical transmissivity of sea ice (Nicolaus et al., 2012), which plays an important role for primary productivity (Popova et al., 2012). Finally, sea ice is a platform for human activities and it provides a habitat for marine mammals. Commercial operations, e.g. shipping, offshore structures or port facilities are limited by sea-ice conditions.

1.1.2. Thermodynamics and dynamics

Sea ice starts to form when the seawater temperature is cooled by atmospheric forcing below its freezing point, which depends on its salinity. At a typical seawater salinity of 34, the freezing point of seawater is at -1.86 "°"C (Petrich and Eicken, 2010). Heat from the ocean is then conducted upwards to the atmosphere, where individual sea-ice crystals grow in a preferred orientation of horizontal crystallographic c-axis, forming so called columnar sea ice. Salt ions are either trapped in brine pockets or expelled from the sea-ice matrix downwards within brine channels (Petrich and Eicken, 2010). Therefore, sea-ice salinity is in general much lower than the seawater salinity. The result of above described thermodynamic growth is young, mostly first-year sea ice with flat surfaces, so called level sea ice (Figure 1.1a). In one freezing season, level sea ice can grow in maximum 2.5 m (Haas, 2010), where the grow rate depends on temperature differences between ocean and atmosphere and the thickness of the sea ice and snow cover. With time, sea ice undergoes mechanical deformation and the roughness of sea-ice surface is affected by alternation of melt and freeze processes.

Sea ice drifts mainly as a consequence of pressure exerted by atmospheric systems (Köberle and Gerdes, 2003). In convergent regimes, sea-ice floes may raft on top of each other, crush and form deformed sea ice, i.e. sea-ice pressure ridges (Figure 1.1b) or rubble fields of sea-ice blocks (Figure 1.1c). Pressure ridges are usually characterized by a sail, the part above seawater level, and a triangular-shaped keel, the part below seawater level.

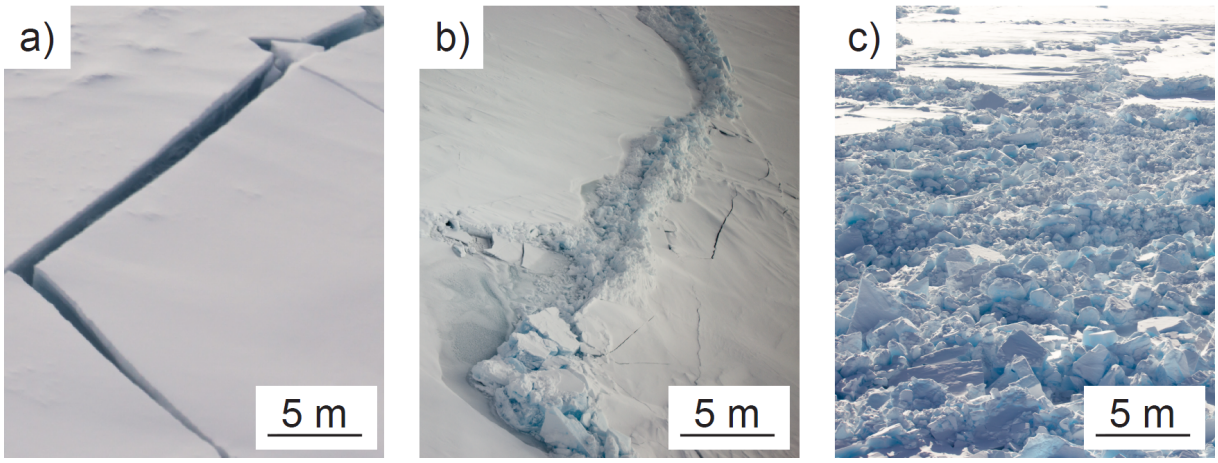

Figure 1.1.: Photographs of a) thermodynamically grown level sea ice, and a dynamically formed b) pressure ridge, and c) rubble field of sea-ice blocks. Photographs were taken in the Western Beaufort Sea, 2012.

From remote distances, pressure ridges are observed as two-dimensional features.

Dynamically deformed sea ice can become much thicker than thermodynamically grown, level sea ice. In the Arctic, ridges can be tens of meters thick, and account for one-third (Multala et al., 1996) to four-fifth (Haas, 2010) of the total sea-ice volume. In the Antarctic, ridging is in general less common compared to the Arctic (Dieckmann and Hellmer, 2010).

1.1.3. Sub-ice platelet layer in Antarctica

The sub-ice platelet layer (Figure 1.2), hereinafter referred to as platelet layer is a sea-ice type commonly found underneath the solid sea-ice layer close to Antarctic ice shelves, which are floating extensions of the continent's ice sheet. Individual disc-shaped ice platelets are some millimeters thick and have a diameter of up to 0.2 m (Eicken and Lange, 1989). They form a semi-consolidated layer of few centimeters to several meters in thickness. It is the most porous of all sea-ice types and composed of approximately 20-30 % ice platelets and 70-80 % seawater by volume (Gough et al., 2012; Hoppmann et al., 2015b). Platelet layers form a unique ice habitat, providing extensive surface area for bacteria and phytoplankton to grow on. Some of the highest concentrations of sea-ice algae can be found in the upper part of the platelet layer (Arrigo et al., 1996, 2010).

Ice platelets form deep in the water column and are the direct result of ocean-ice shelf interaction. Relatively warm water masses enter the ice-shelf cavity (Figure 1.3). Because the ice shelf consists of meteoric ice, basal melt leads to the formation of fresher and less dense water than the surrounding ocean. The water mass moves upwards, cools

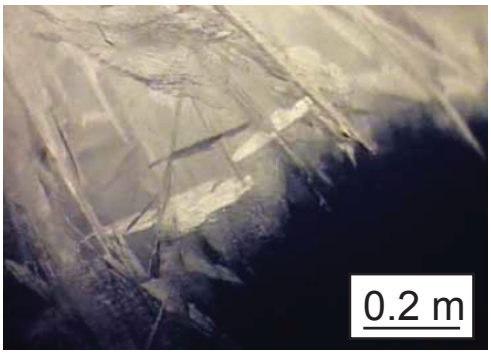

Figure 1.2.: Photograph of the platelet-layer underside, taken with an underwater camera, in Atka Bay, Antarctica, 2012.

adiabatically and, because the seawater freezing point is pressure dependent, the water becomes supercooled. Individual ice platelets start to form, rise upwards following the slope of the ice shelf bottom and accumulate below the solid sea ice (e.g. Mahoney et al., 2011).

Platelet-layer formation can be expected around the Antarctic continent, where ice shelves occur and supercooled-water conditions are found. This is for example supported by studies from Atka Bay (Kipfstuhl, 1991), Weddell Sea (Eicken and Lange, 1989) and McMurdo Sound (Jeffries et al., 1993). But so far no method exists to measure over basin scale the extent and the thickness of this layer.

1.1.4. Trends of Arctic and Antarctic sea-ice cover

The freezing of seawater and melting of sea ice are periodic responses to the seasonal variation of shortwave radiation and air temperature. The seasonal evolution of the sea-ice cover in the Arctic and Antarctic are one of the biggest annual cycles on Earth, covering an area of 3 % (Antarctic summer) to 6 % (Antarctic winter) of the Earth‘s surface (Comiso, 2010). The recent maximum and minimum extents of the Arctic and Antarctic sea-ice cover, obtained by satellite measurements, are shown in Figure 1.4. In the northern hemisphere the maximum sea-ice extent is usually reached in February/March and in the southern hemisphere in September. The minimum sea-ice extent in the Arctic is reached in September and in the Antarctic in February (Comiso, 2010; Meier et al., 2014).

Arctic sea ice forms in a mediterranean ocean, and is largely restricted by the Eurasian and American continents. The relative and absolute seasonal variation of sea-ice extent is therefore much greater in the Antarctic compared to Arctic, where sea-ice formation and drift is not limited by surrounding landmasses. The Arctic sea ice at high latitude generally receives less insolation and is usually more deformed due to the surrounding

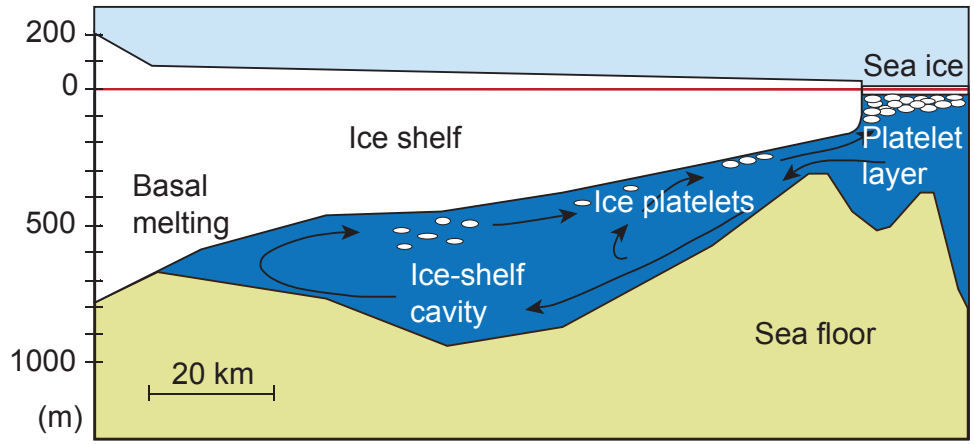

Figure 1.3.: Simplified process of sub-ice platelet layer formation, where black arrows indicate ocean currents. Ice platelets form in ice-shelf cavities in supercooled water masses and rise due to density contrast of ice and seawater. The resulting several meter thick platelet layer consists of loose ice platelets; modified after Kipfstuhl (1991).

land masses compared to Antarctic sea ice. Therefore, the summer survival rate of Arctic sea ice is generally greater than the Antarctic (Dieckmann and Hellmer, 2010).

Sea-ice extent and partially thickness show a significant seasonal variability in both hemispheres that are superimposed by long-term trends. Results from satellite data (passive microwave imagery, e.g. Parkinson and Cavalieri, 2012) imply that sea ice in the Arctic and Antarctic has been changing differently over the last decades (Stammerjohn et al., 2012). Arctic summer minimum sea-ice extent is declining at an average rate of 12.7 % per decade since 1979 (Meier et al., 2014). Moreover, sea-ice in the Arctic is becoming thinner (Kwok et al., 2009; Lindsay and Schweiger, 2015), younger (Maslanik et al., 2011) and more mobile (Rampal et al., 2009; Spreen et al., 2011; Kwok et al., 2013). In the Antarctic, long-term changes of sea-ice extent are regionally very variable. Studies based on satellite observations showed, in contrast to the Arctic, a small, statistically-significant positive trend of 0.9 ± 0.2 % per decade (Massom and Stammerjohn, 2010). However, this trend has to be taken cautiously, since a possible data processing bias was recently identified (Eisenman et al., 2014).

Interaction between ocean and ice shelves can be also affected by a changing climate. For example, warming water masses in cavities below ice shelves will lead to an increase in ice loss due to basal melt (Hellmer et al., 2012). This would immediately influence the platelet layer (section 1.1.3), but trends of this sea-ice type could so far not be determined, since only sporadic measurements were performed.

In general, for monitoring the sea-ice state and understanding seasonal and long-term

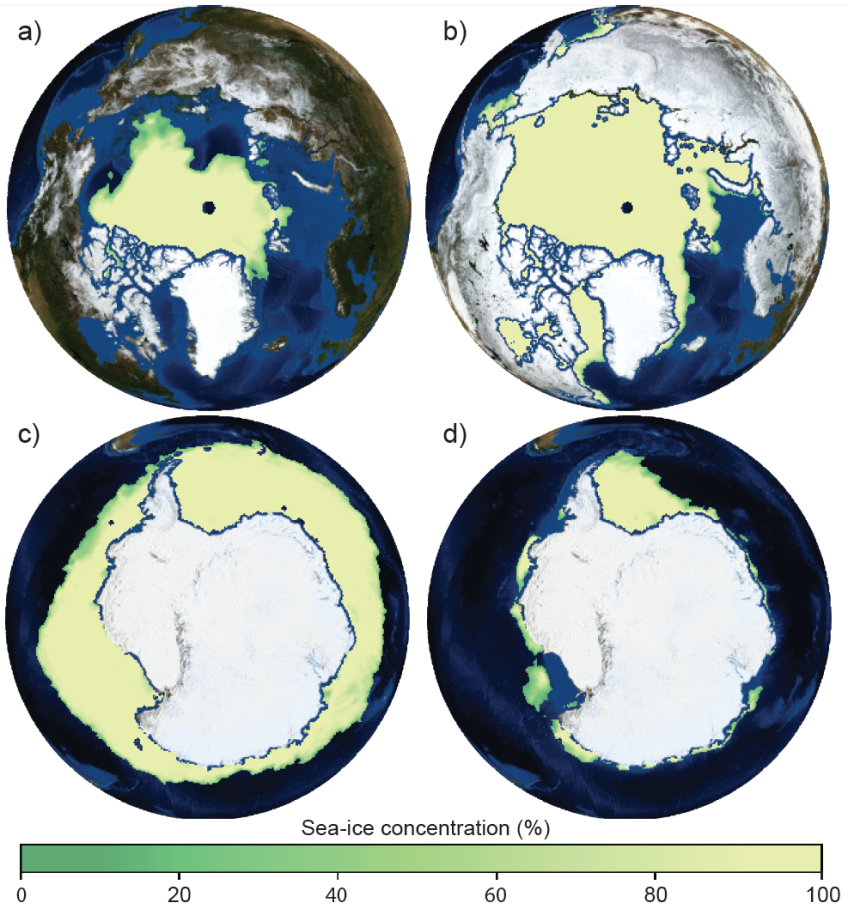

Figure 1.4.: Recent northern and southern hemisphere sea-ice extents in 2014/2015 based on satellite observations (OSI SAF, Ocean and Sea Ice Satellite Application Facility, http://osisaf.met.no/p/) of a) Arctic minimum (17 September 2014), b) Arctic maximum (25 February 2015), c) Antarctic maximum (20 September 2014), and d) Antarctic minimum (20 February 2015), base map credits belong to NASA (http://visibleearth.nasa.gov/).

changes, temporal measurements should be combined with volume quantifications. Besides extent also the thickness of the sea ice or the platelet layer is therefore needed. But often, thicknesses are either obtained in situ on a very local scale or are determined on basin scale with indirect measurements.

1.1.5. Sea-ice thickness retrieval

A variety of methods exist to measure the thickness of sea ice, each with advantages and limitations:

- ▷ The most accurate is by drill-hole surveys, where snow and sea-ice thickness are determined with thickness gauges and measuring tapes.

- ▷ Drifting buoys equipped with acoustic distance sounders above and below sea ice (Ice Mass Balance Buoy, IMB) or thermistor chains frozen into the sea ice (Hoppmann et al. (2015a), Appendix C) provide sea-ice thickness measurements over the lifetime of the buoy, but are limited to a specific location on a drifting floe.

- ▷ The sea-ice draft, the fraction of ice below the seawater surface, is measured with upward-looking sonar systems from moorings (Melling et al., 2005) and submarines (Rothrock and Wensnahan, 2007). The total sea-ice thickness is then calculated assuming isostatic equilibrium. Moorings are stationary installations measuring the draft of passing floes, while data from submarines are acquired over basin-wide scales.

- ▷ The thickness of sea ice can also be derived from airborne (Hvidegaard and Forsberg, 2002) or satellite altimetry, e.g. ICESat and CryoSat-2 (Wingham et al., 2006; Kwok and Cunningham, 2008; Zwally et al., 2008; Ricker et al., 2014), where the freeboard (height of the ice surface above sea level) is measured with radar or laser altimeters and converted into sea-ice thickness.

- ▷ While measurements of the draft or freeboard of sea ice are indirect ways to determine the sea-ice thickness, electromagnetic (EM) induction sounding is the only geophysical method capable of directly measuring sea-ice thickness (Pfaffhuber et al., 2012b). The method is applied by airborne (Kovacs and Holladay, 1990; Peterson et al., 2008; Haas et al., 2009) or ground-based instruments (Eicken et al., 2001; Haas, 2004).

1.2. Electromagnetic (EM) induction sounding

1.2.1. Basic principles

The basic principles of ground-based EM devices (Figure 1.5a, b) and airborne devices (Figure 1.5c) are the same. EM fields are acquired by small coil systems, which consist of transmitter and receiver coils, both in a horizontal plane (horizontal co-planar). "Small-coil" refers to a system with small receiver and transmitter coils compared to their distance, hence the magnetic field generated is assumed to be a dipole field and recordings can be considered as point measurements (Farquharson, 2000). Sinusoidal, time-varying currents in the transmitter generate an alternating magnetic field. This primary field induces eddy currents in the conductive subsurface that are the source of a secondary magnetic field (red, Figure 1.6). The primary plus secondary magnetic field is measured

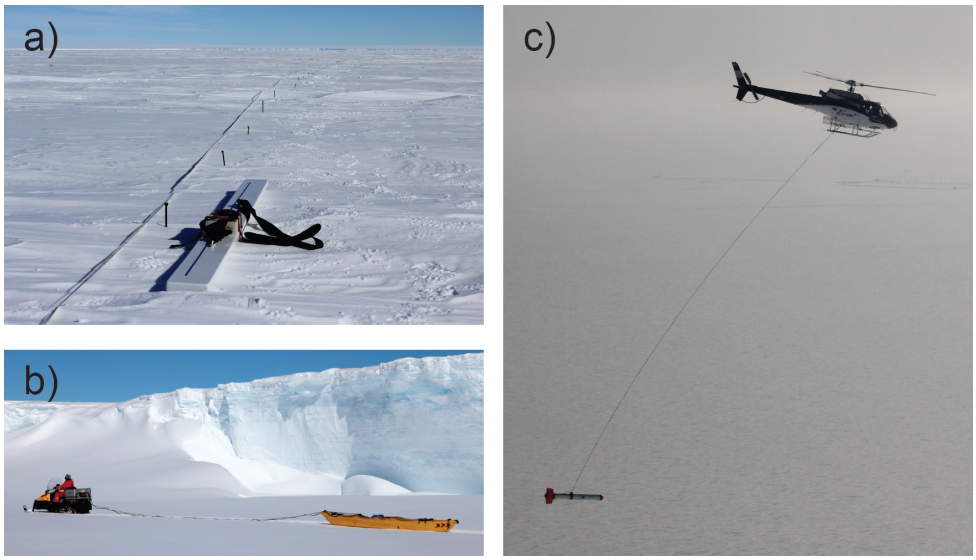

Figure 1.5.: Ground-based and airborne data acquisition, a) GEM-2 on sea ice in Atka Bay, Antarctica, 2012, b) GEM-2 mounted in a kayak and pulled by a snow machine across Atka Bay, Antarctica, 2012, c) airborne EM device operated in the Western Beaufort Sea, 2012, photograph credits belong to David Ball, NRL.

in the receiver coil. Most systems suppress the primary field (bucking) at the receiver coil to enhance the sensitivity with respect to the significantly smaller secondary field.

It is common practice in geophysical prospecting to evaluate the relative secondary magnetic field (secondary/primary field). Besides the subsurface conductivity distribution it is only dependent on the frequency of the harmonic primary field, the coil spacing between transmitter and receiver and the coil orientation with respect to the subsurface. Other instrument specific parameters like the actual current or the number of windings in the transmitter coil, that will influence the total magnetic field strength, can be neglected in this relative approach. The relative secondary field is a complex number that is described by its real (in-phase) and an imaginary (out-of-phase, or quadrature) component, which are typically given in ppm (parts per million). Alternatively, it can be described by an amplitude in ppm and a phase angle. The signal measured at the receiver location typically originates not from a point but from an area underneath the measurement device. The so-called EM footprint is defined as the area where 90 % of the induction process takes place (Liu and Becker, 1990). The extent of the induction process and thus the relative secondary field depends on the electromagnetic properties of the subsurface, i.e. the electrical conductivity σ (S/m), the magnetic permeability μ (H/m) and the dielectric permittivity ϵ (F/m). Hence, an analysis of the relative secondary field reveals information about the subsurface, when a sufficient contrast of the EM properties be-

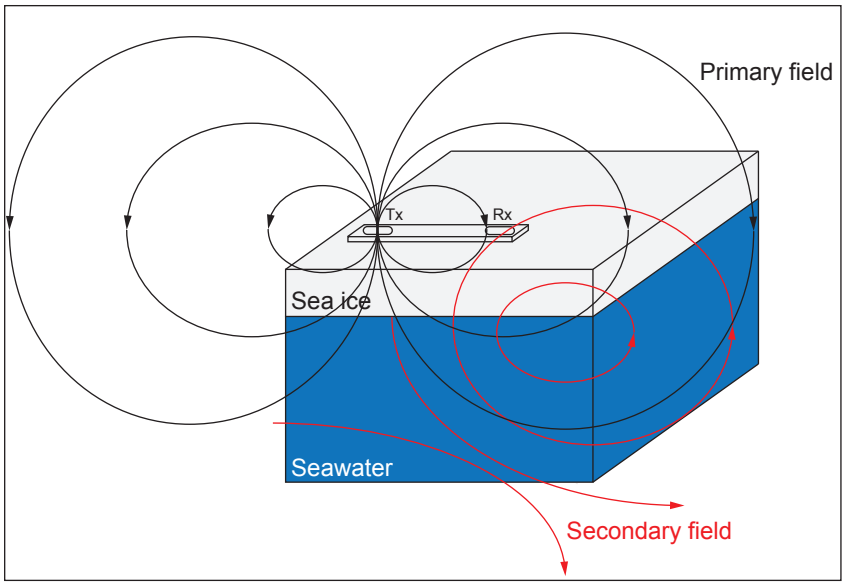

Figure 1.6.: Basic principles of electromagnetic induction sounding on level sea ice. A primary magnetic field is generated by the transmitter coil (Tx) and a secondary magnetic field (red) is induced in the conductive subsurface. The superimposed fields are measured at the receiver coil (Rx). The sounding depth varies with different frequencies.

tween individual mappable targets is given. For sea ice-seawater applications the contrast of electrical conductivity is most important and the other two properties are insignificant for my purpose.

The basis of this method are the Maxwell Equations (Maxwell, 1873). Maxwell introduced four uncoupled differential equations in time-domain based on empirical relations of Faraday and Ampere (Ward and Hohmann, 1988):

$$\nabla \times \mathbf{e} + \frac{\partial \mathbf{b}}{\partial t} = 0, \tag{1.1}$$

$$\nabla \times \mathbf{h} - \frac{\partial \mathbf{d}}{\partial t} = \mathbf{j}, \tag{1.2}$$

$$\nabla \cdot \mathbf{b} = 0, \tag{1.3}$$

$$\nabla \cdot \mathbf{d} = \rho, \tag{1.4}$$

where $\mathbf{e}$ is the electric field intensity (V/m), $\mathbf{b}$ is the magnetic induction (T), $\mathbf{d}$ is the dielectric displacement (C/m^2), $\mathbf{h}$ is the magnetic field intensity (A/m), $\mathbf{j}$ is the electric current density (A/m^2), ρ is the electric charge density (C) and $\partial/\partial t$ is the time rate of change. The subsurface electromagnetic properties σ, μ and ϵ are introduced by the

constitutive relations, which couple equations 1.1-1.4:

$$\mathbf{d} = \epsilon \mathbf{e}, \tag{1.5}$$

$$\mathbf{b} = \mu \mathbf{h}, \tag{1.6}$$

$$\mathbf{j} = \sigma \mathbf{e}. \tag{1.7}$$

In order to calculate the EM field at the receiver with specified electromagnetic subsurface properties, the Maxwell Equations and constitutive relations have to be reformulated using assumptions that properties are scalar, isotropic, and non-dispersive (Ward and Hohmann, 1988). After reformulation, the frequency-domain wave equations for electric (**E**) and magnetic (**H**) fields are obtained, called Helmholtz Equations:

$$\nabla^2 \mathbf{E} + (\mu\epsilon\omega^2 - i\mu\sigma\omega)\mathbf{E} = 0, \tag{1.8}$$

$$\nabla^2 \mathbf{H} + (\mu\epsilon\omega^2 - i\mu\sigma\omega)\mathbf{H} = 0, \tag{1.9}$$

where ω is the angular frequency. These equations determine the propagation of electromagnetic energy with the propagation constant $k = \sqrt{\mu\epsilon\omega^2 - i\mu\sigma\omega}$. For low frequencies ($< 10^5$ Hz) $\mu\epsilon\omega^2$ is generally much smaller than $\mu\sigma\omega$. This so called quasi-static assumption describes that displacement currents are negligibly smaller than conduction currents and equations are simplified to diffusion equations (Ward and Hohmann, 1988).

The wave equations (Equations 1.8 and 1.9) are satisfied by the formulation of the so-called Hankel Transformation of the relative secondary magnetic field (H_s/H_p) for the horizontal-coplanar geometry of the coils, e.g. given by (Mundry, 1984)

$$\frac{H_s}{H_p} = r^3 \int_0^\infty R\lambda^2 e^{-2\lambda h} J_0(\lambda r) d\lambda, \tag{1.10}$$

where R is a function which depend amongst others on frequency and electrical properties of the subsurface, r is the coil spacing, h is the height of transmitter and receiver above homogeneous half-space, λ is the integration constant, and J_0 is a Bessel functions of the first kind (Fitterman and Yin, 2004). There is no analytical solution for the Hankel Transformation, therefore linear digital filters are used for calculations of the relative secondary magnetic field (e.g. Anderson, 1979). The assumptions in the calculation of the relative secondary field are only valid under the quasi-static assumption in the very-low frequency range, were phase shifts due to wave propagation are much smaller than phase shifts by induction processes. The skin-depth, which is a measure for the penetration of an electromagnetic signal into a conductive medium, is significantly variable in the frequency

range between 1-100 kHz and for the case of sea ice or seawater more information is gained with several frequencies.

1.2.2. Single-frequency sea-ice thickness retrieval

Electromagnetic induction sounding has been used for sea-ice thickness retrieval for decades (e.g. Kovacs and Holladay, 1990). Traditional EM sensors often use a single-frequency transmitter-receiver coil pairs that uses a resonant circuit tuned for this specific frequency for signal amplification. Data from single-frequency devices are processed under the assumption of 1D subsurface geometries (Figure 1.6) and negligible sea-ice conductivities (0 S/m, same as air). This case is essentially a homogeneous half-space with a conductive (ocean) and perfectly resistive (air, snow, sea ice) part. The boundary between the two half-spaces is then situated at the sea ice-ocean interface.

For ground-based devices that are situated directly on the sea ice (Figure 1.5a), the distance to the half-space interface is the sum of snow depth and sea-ice thickness. The EM response as a function of this distance can be derived by the Hankel transformation (Equation 1.10). It has become common practice to calculate the EM response for a defined seawater conductivity and approximate the result for easier inversion by an exponential function or a series of exponential functions. In this case the inverted approximation can then be used to convert the measured EM response (either in-phase or quadrature) to the total, snow + sea-ice thickness. This method is called according to Pfaffling et al. (2007) EMPEX (empirical exponential) approach.

Sea-ice thickness retrieval from airborne instruments works similarly (Figure 1.5c) with the addition that the height of the EM sensor is an additional variable. From the measured EM response the distance to the sea-ice/seawater interface is calculated by comparison of the measured signal to the modeled response over the seawater half-space. At the same time, a laser altimeter is used to determine the distance to sea-ice (+ snow) surface. The difference of the two distances corresponds to the total sea-ice + snow thickness.

Level sea ice that fulfills the 1D geometry assumption can be determined from airborne devices with an accuracy of 0.1 m for a single measurement (Holladay et al., 1990; Haas et al., 2009). However, large parts of the sea-ice cover shows thickness variation well below the EM footprint of typical ground or airborne sensors. In addition, these sea-ice regimes are typically formed by dynamic deformation processes and may include water-filled voids with a non-negligible electrical conductivity. For example, the underestimation of triangle-shaped sea-ice pressure ridge thickness from EM data can be as much as 40-80% of the true maximum ridge thickness (Haas and Jochmann, 2003; Reid et al., 2003; Hendricks, 2009; Pfaffhuber et al., 2012b). These underestimations associated with deformed sea

ice leads to uncertainties of ice-volume determination in Polar seas. Analysis of EM sea-ice thickness data are therefore mostly based on (i) the mode of the sea-ice thickness probability density function (Thorndike et al., 1975) in a given region that represents the thickness of level ice, for which the 1D assumption is valid (Rabenstein et al., 2010), or (ii) mean thickness over a larger area under the assumption that footprint smoothing is mass-conserving.

1.2.3. EM properties of sea ice

The assumption of negligible conductivity in cases of cold and undeformed sea ice is mostly valid for EM sensors that employ frequencies in the lower frequency range of about 1-10 kHz (Pfaffling and Reid, 2009). The use of multiple frequencies over a large frequency range, however, should enable insights not only in the thickness but also in the internal properties of sea ice that change its internal conductivity (Spies and Frischknecht, 1991).

Level sea ice

Sea-ice and seawater conductivities differ usually by two orders of magnitude. Seawater conductivity is routinely determined in field and a function of salinity and water temperature. The upper layer of sea-ice covered oceans is usually mixed to a depth below the skin depth of common EM induction frequencies. Therefore vertical seawater conductivity changes are not relevant of EM sea-ice thickness surveys and also lateral variations are negligible for the scope of EM field work. For the northern and southern polar ocean's surface, the seawater conductivity ranges between 2.2 and 2.7 S/m (Figure 1.7a).

The conductivity of sea ice varies and depends on freeze and melt processes and therefore also on the age of sea ice. In general, older sea ice has released more brine and may have already been flushed by surface melting, leading to an almost resistive target (< 0.05 S/m). However, due to melting processes in summer, internal melting may lead to the formation of large pores. Conductive seawater enters the sea-ice matrix, resulting in higher sea-ice conductivities (> 0 S/m). Furthermore, level sea ice is not completely uniform on micro-structure scale, since it contains due to the columnar grow vertical brine cells and drainage tubes. This leads to a vertical-to-horizontal electrical conductivity anisotropy with approximately 10 times higher vertical than horizontal sea-ice conductivities (Reid et al., 2006). However, for a first approximation, level sea ice is treated as an isotropic target also due to the fact that the eddy currents are mostly horizontally orientated.

Dry and cold snow is assumed to be resistive, but because of high snow load, especially in Antarctica, sea ice might be flooded by conductive seawater, adding an additional

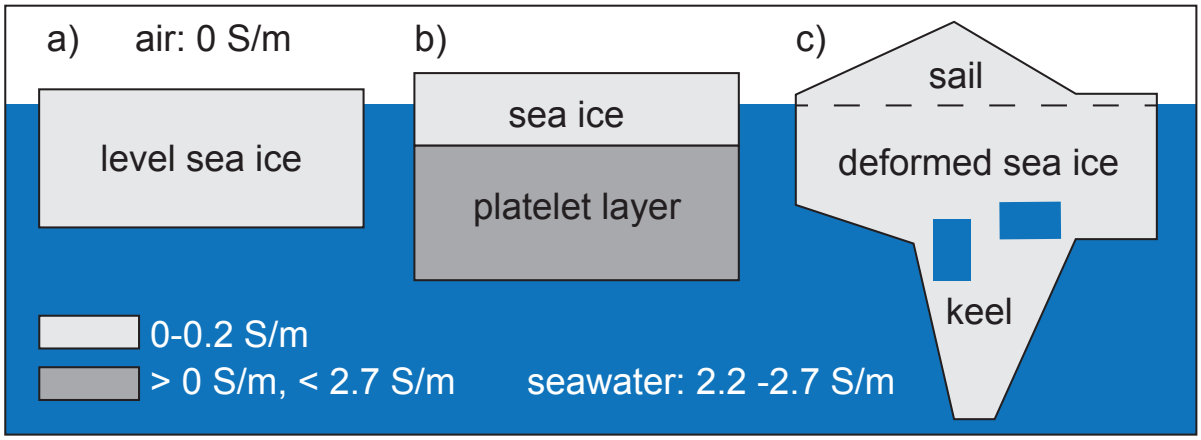

Figure 1.7.: Electromagnetic properties of sea ice. a) Homogeneous level sea ice with conductivities between 0 and 0.2 S/m, b) sea ice with underlying platelet layer with a conductivity between sea ice and seawater, and c) deformed sea ice with conductive macro-scale voids in the keel part.

conductive layer on top of sea ice.

Sub-ice platelet layer

One form of sea ice that appears near ice shelves (section 1.1.3) consists of a layer of loose fresh platelets, surrounded by conductive seawater. These platelets aggregate in a layer that can be described by a 1D geometry, however, with significantly higher seawater content and thus much higher conductivity compared to level sea ice (Figure 1.7b). The platelet layer is often formed under a regular layer of level ice, essentially leading to a multi-layered case that cannot be approximated by half-space considerations any longer. The orientation of the ice platelets (Gough et al., 2012; Hoppmann et al., 2015b) and therefore the bulk conductivity is assumed to be isotropic with conductivities between seawater and sea ice. It is however not possible to measure the bulk conductivity with conductivity meters in the field. The electrical properties of the platelet layer are therefore a free parameter in the evaluation of the EM response.

Deformed sea ice

Deformed sea ice (section 1.1.2) can contain a very complex geometry (Figure 1.1b, c, Figure 1.7c). It is formed by dynamic processes during events of sea-ice convergence. Structural failures of level ice lead to an aggregation of individual sea-ice blocks, which in an idealized case form a triangular shaped pressure ridge. The main part of the blocky structure is constituted below the water line. This ridge keel initially contains large sea-

water filled voids, which may widen through melting or consolidate in freezing conditions. The pores or gaps above seawater level are filled with snow or air. In summer, melting leads to erosion and consolidated structures, so called hummocks. Voids are assumed to be resistive, in cases sea ice is not flooded by conductive seawater. The pores of the keel (e.g. 30%, Multala et al., 1996; 30-40%, Nuber et al., 2013) are filled with conductive seawater. They may vary in amount, shape and size and individual gaps can be several meters thick. If the pressure field that has caused the formation of the ridge persists, sea ice may be suppressed below seawater. This would lead to flooding of the sea ice, leading to conductive wet snow.

1.2.4. Multi-frequency EM and geophysical inversions

Development of EM sensor technology has led to broadband EM sensors that are not limited to one frequency per transmitter-receiver coil pair, but use signal generators that provide a magnetic field with multiple frequency components. The evaluation of the additional parameters compared to the single-frequency approach enables to resolve conductivity structures that are more complex than the homogeneous half-space. The potential ambiguities of the empirical solutions for several layers, however, also need a corresponding more complex methodology. The superimposed EM responses can be processed not only for the retrieval of sea-ice thickness as described in chapter 1.2.2, but also for the conductivity of the individual layers, given that there is a frequency component that is sensitive to conductivity changes in the respective depth.

For sea-ice thickness and conductivity retrieval from EM responses, I tested three different geophysical inversion algorithms, (I) a 1D smoothness-constrained inversion, (II) a 1D Marquardt-Levenberg inversion, and (III) a slightly modified version of (II), a laterally-constrained Marquardt-Levenberg inversion (Figure 1.8). All algorithms use a starting model, which is a plausible subsurface model of thicknesses and conductivities. The algorithm calculates the theoretical EM response of this model, which is then compared to the measured response. The model is adapted iteratively, until the algorithm finds a subsurface model which theoretical response fits the measured response within the data uncertainty (Farquharson et al., 2003). This strategy does not require an exact solution and can be preconditioned with a priori information to minimize the convergence into false solutions in the case of ambiguous signal response.

For the 1D smoothness constrained inversion (I, EM1DFM, Figure 1.8a, Farquharson, 2000; Farquharson et al., 2003), individual layers are fixed, and only their conductivity is allowed to vary from one iteration to the next. A vertical conductivity smoothing is applied (blue arrows in Figure 1.8a), which means that the algorithm is based on a

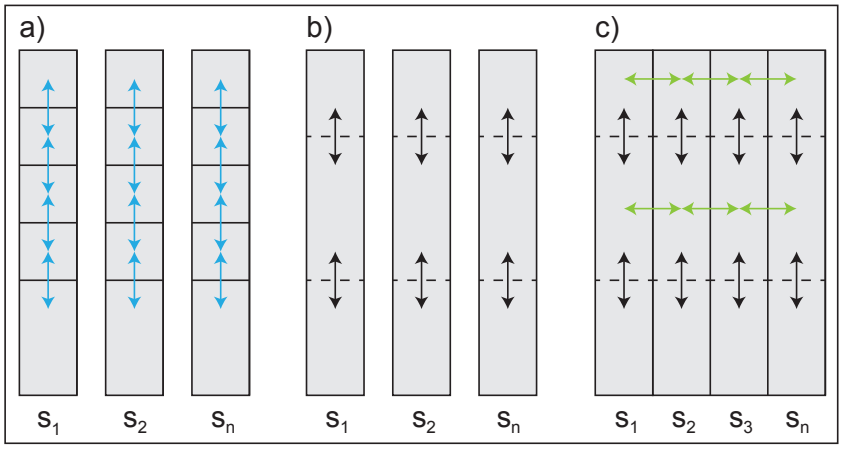

Figure 1.8.: Basic principles of the used inversion algorithms, a) 1D smoothness-constrained inversion, b) 1D Marquardt-Levenberg inversion, and c) laterally-constrained Marquardt-Levenberg inversion. Solid black lines indicate that layers are fixed, whereas dashed lines that layers adapt their thickness during inversion. Blue arrows indicate vertical smoothing of conductivity, whereas green arrows the lateral constraints of thickness and conductivity. s refers to individual stations.

subsurface model with small conductivity changes between multiple layers of high vertical resolution.

The 1D Marquardt-Levenberg inversion (II, Lines and Treitel, 1984) was used from EMILIA, ElectroMagnetic Inversion with Least Intricate Algorithms (Kalscheuer et al., 2010, 2012; Grab, 2012; Kalscheuer, 2014). A certain number of layers is defined, depending on the subsurface structure. In addition to the conductivity, the layer thickness is allowed to vary during inversion (black arrows in Figure 1.8b). Between vertical adjacent layers, no conductivity smoothing is applied, which results in models with vertical conductivity discontinuities.

Lateral constraints were implemented into the Marquardt-Levenberg inversion algorithm (III, Kaufmann, 2014) in order to minimize thickness and conductivity changes of horizontally adjacent stations (Auken et al., 2005) and therefore to suppress convergence into false solutions of individual stations. The lateral constraints (green arrows, Figure 1.8c) are similar to the horizontal smoothing in the 1D smoothness-constrained inversion.

Inversion algorithms (I) and (II) calculate the new models for individual stations in 1D which means that the conductivity varies for each station only with depth and adjacent stations do not have an influence on the conductivity retrieval (Figure 1.8a,b). Algorithm (III) calculates the model in 1D, but the retrieved conductivities are smoothed in lateral direction, which results in a pseudo 2D model (Figure 1.8c).

1.3. Scope and content of this work

The use of multi-frequency EM sensors has the prospect of yielding either additional information by resolving complex layered cases or the internal properties of sea ice. Layering is found for flooded sea ice or the sea ice with an underlying platelet layer. These are cases where the use of a single-frequency would lead to a highly under-determined and probably false solution. It is therefore the first goal of this work to evaluate the use of multi-frequency EM sensors in sea-ice research in order to improve the understanding of the physics of different sea-ice regimes. While a successful EM inversion strategy results in additional information of electrical conductivity, this is not the physical parameter relevant for processes inside the sea-ice layer.

The second goal of this work is therefore to investigate to which uncertainty the electrical conductivity of sea ice can be used as a proxy measurement for porosity and to verify this relationship with independent data in dedicated case studies. This main case study is a field experiment in Atka Bay, Antarctica over a three-layer case (level ice, platelet layer and seawater) with distinct conductivity ranges and verifiable porosities. Other field trials include the macro-scale porosity inside sea-ice deformation structures and high-conductive surface flooding layers. The required steps for these overarching goals were subdivided in the following points:

- ▷ **The utilization of commercial broadband multi-frequency EM sensors for sea-ice research**
  Other applications in geophysical conductivity prospecting often do not require an absolute calibration of EM sensors, but are rather based on the analysis of conductivity anomalies. In addition, sensors are optimized for far more resistive subsurface structures. One finding of this work was that common sensor-internal processing design will lead to wrong results in highly conductive environments such as sea ice. While this bias is usually removed in single-frequency EM by manual calibration, the multi-frequency EM approach needed an analytical correction of the nonlinear frequency specific bias.

- ▷ **The development of suitable 1D inversion schemes for sea ice**
  Sea ice can be characterized by a large conductivity discontinuity at the ice-ocean interface or by a low internal gradient. Therefore multiple inversion schemes were tested for different sea-ice cases. In addition, the sensor specific bias for high conductive environments had to be included in all inversion schemes.

- ▷ **The collection of field and validation data**
  The aim of this work is to test the capability of multi-frequency EM to resolve internal conductivity structures and how these relate to changes in porosity. To verify the findings for the different case studies, field validation data were obtained by independent methods. From temperature and salinity measurements of sea-ice cores bulk conductivities were calculated. For the main case study in Atka Bay this meant the independent estimation of platelet-layer thickness and its ice-volume fraction. For a case study of deformed sea ice an independent estimation of extent and location of voids was required.

- ▷ **The joint interpretation of multi-frequency EM and validation data**
  This major part of this work step is focused on the data in Atka Bay. So far, it was not possible to measure platelet-layer thickness and its ice-volume fraction on a larger scale, beside dedicated drill-hole measurements. Little is known of the temporal evolution and spatial variability of the platelet layer that could place the results of the EM study into context. It was therefore necessary to validate the results of the EM surveys at selected sites and then assess the physical properties and spatial distribution of the platelet layer based on the results of the multi-frequency EM inversions.

1.4. Structure of the thesis

The main work of this thesis is represented by three manuscripts, which are included here as individual chapters (chapters 2 - 4). Together with chapter 5 and the appendices, they follow the main points of section 1.3.

The goal of my first manuscript (chapter 2)

> P. A. Hunkeler, S. Hendricks, M. Hoppmann, S. Paul, R. Gerdes. **Towards an estimation of sub sea-ice platelet-layer volume with multi-frequency electromagnetic induction sounding**. Annals of Glaciology, 56(69):137-146, 2015.

was to provide a proof-of-concept of multi-frequency EM measurements and the potential to resolve internal properties of sea-ice and the platelet-layer in the Atka Bay. First step for this goal was to determine noise of the instrument, to calibrate it for all frequencies at dedicated locations with variable sea-ice thicknesses and conductivities, and to calculate instrument-specific calibration coefficients. Second step was then to compare EM

measurements to validation data from sea-ice cores and forward models.
In the first manuscript, a conductivity depended instrument-specific bias was identified and included in forward models, but the effect on sea-ice thickness and conductivity retrieval was not identified. The goal of the second manuscript (chapter 3)

> P. A. Hunkeler, S. Hendricks, M. Hoppmann, C. Farquharson, T. Kalscheuer, M. Grab, M. Kaufmann, L. Rabenstein, R. Gerdes. **Improved 1D inversions for sea ice thickness and conductivity from electromagnetic induction data: Inclusion of nonlinearities caused by passive bucking**. Geophysics, 81(1):45-58, 2016.

was therefore to modify two geophysical inversion algorithms for this bias and to assess sensitivities of the algorithm by using synthetic data calculated for the used instrument (GEM-2) and a variety of sea-ice conductivities and thicknesses values. Uncertainties of resulting sea-ice conductivity and the related porosity were evaluated and discussed. In the second manuscript synthetic level sea-ice data were used, whereas the goal of my third manuscript (chapter 4)

> P. A. Hunkeler, M. Hoppmann, S. Hendricks, T. Kalscheuer, R. Gerdes. **A glimpse beneath Antarctic sea ice: platelet-layer volume from multi-frequency electromagnetic induction sounding**. Geophysical Research Letters, 43(1), 222-231, 2016.

was to apply the algorithm to a more complex 1D case with an additional layer. First step was to test and validate the inversion performance of the three-layer problem with synthetic data. Next step was then to process the transect data across Atka Bay in Antarctic with a slightly modified inversion algorithm, and finally to calculate from platelet-layer conductivity distributions ice-volume fractions. Interpretation of these results were facilitated by comparing them to studies shown in Appendix B (Hoppmann et al., 2015b) and Appendix C (Hoppmann et al., 2015a), which provide platelet-layer thickness and ice-volume fraction validation data, and study in Appendix D (Paul et al., 2015), which describes snow properties in Atka Bay.

So far, the algorithms were applied to simplified 1D features, either level sea ice or landfast sea ice with underlying platelet layer. The goal of chapter 5 was to evaluate the sensitivity of the method by applying it to deformed sea ice with internal macro-scale pores. With extensive datasets from drill-hole measurements, the results across deformed

sea ice were validated.

As an example for the use of airborne single-frequency EM data, which were collected during this PhD project, the paper by Lindsay et al. (2012) is shown in Appendix A.

In chapter 6, all key findings are summarized and their relevance and implication are discussed.

2 Towards an estimation of sub sea-ice platelet-layer volume with multi-frequency electromagnetic induction sounding

2.1. Abstract

Ice-platelet clusters modify the heat and mass balance of sea ice near Antarctic ice shelves and provide a unique habitat for ice-associated organisms. The amount and distribution of these ice crystals below the solid sea ice provide insight on melt rates and circulation regimes in the ice-shelf cavities, which are difficult to observe directly. However, little is known about the circum-Antarctic volume of the sub sea-ice platelet layer, because observations have mostly been limited to point measurements. In this study, we present a new application of multi-frequency electromagnetic (EM) induction sounding to quantify platelet-layer properties. The combination of in-situ data with the theoretical response yields a bulk platelet-layer conductivity of 1154 mSm^{-1} $\pm$ 271 mSm^{-1} and ice-volume fractions of 0.29-0.43. Calibration routines and uncertainties are discussed in detail to facilitate future studies. Our results suggest that multi-frequency EM induction sounding is a promising method to efficiently map platelet-layer volume on a larger scale than has previously been feasible.

2.2. Introduction

The Antarctic coastline is fringed by ice shelves, floating extensions of continental ice sheets (Le Brocq et al., 2010). Basal melt of ice shelves leads to the formation of water masses that are fresher and less dense than the surrounding ocean body (Mahoney et al., 2011). As the seawater freezing point depends on pressure (Foldvik and Kvinge, 1974), the water becomes supercooled when the less dense plume rises. Ice platelets nucleate in the supercooled water, but the process of ice formation varies (Smith et al., 2001). Near the Ekström Ice Shelf in the eastern Weddell Sea, large amounts of ice platelets rise from

the cavity below the ice shelf and accumulate underneath the sea ice (Eicken and Lange, 1989; Hoppmann et al., 2015b). In McMurdo Sound near the Ross Ice Shelf, platelet growth is often associated with an in-situ formation of ice platelets directly underneath the sea ice (Smith et al., 2001) or is interpreted as a combination of the two processes (Jeffries et al., 1993; Dempsey et al., 2010).

The resulting sub sea-ice platelet layer, hereafter referred to as platelet layer, may contribute significantly to the heat- and mass-balance of adjacent sea ice (Eicken and Lange, 1989) and represents a unique ice habitat (Arrigo et al., 1993). The additional buoyancy modifies the sea-ice freeboard, influencing satellite remote sensing near coastal areas in Antarctica (Rack et al., 2013; Price et al., 2014). Furthermore, the platelet layer is a direct indicator of ocean-ice shelf interaction and the amount of basal ice-shelf melt might be reflected in the volume of ice platelets found below landfast sea ice (Hoppmann et al., 2015b), a region much more accessible than the cavities below ice shelves.

The total volume of ice platelets below the sea ice is a product of the layer thickness, the area and the ice-volume fraction. The up to several meter thick platelet layer is commonly determined with a thickness gauge and the horizontal extend is given by point measurements. Previous investigations of ice-volume fractions in McMurdo Sound used estimates from core holes, ice-temperature profiles and horizontal thin sections. Results ranged from 0.2 to > 0.5, while a recent study found an ice-volume fraction of 0.25 ± 0.06 using heat-flux calculations (Gough et al., 2012). At Atka Bay, Günther and Dieckmann (1999) calculated a value of 0.46 based on consideration of sea-ice isostasy. Kipfstuhl (1991) and Hoppmann et al. (2015b) compared their sea-ice thickness observations to a localized growth model and estimated ice-volume fractions of 0.2 and 0.25 ± 0.1 respectively.

One physical parameter, which depends on the ice-volume fraction of the platelet layer, is the electrical conductivity. Differences in conductivity are fundamental for sea-ice thickness retrieval with electromagnetic (EM) induction sounding, a common method typically applied with airborne (Haas et al., 2009) or ground-based devices (Kovacs and Morey, 1991; Haas et al., 1997; Haas, 1998; Reid et al., 2003). In general, a single frequency in the range of 3000 to 10000 Hz is used to estimate the distance of the sensor to the ice-water interface. The method is based on the assumption that sea ice can be described as a single level layer with negligible electrical conductivity ($<$100 mSm^{-1}, e.g. Reid et al., 2006) compared to seawater (e.g. 2690 mSm^{-1} in the winter Weddell Sea). This is a reasonable assumption for most offshore sea ice, but in the presence of a porous platelet layer it becomes invalid. In this case, a single-layer assumption will lead to either an overestimation of the solid sea-ice thickness (Rack et al., 2013), or an underestimation of total (solid ice + platelet layer) thickness with no possibility to resolve both layers. Single-frequency

systems are sensitive to the thickness and the electrical bulk conductivity of the platelet layer, but do not provide enough observational constraints for an unambiguous resolution of layer thicknesses and conductivities. Therefore, those systems are not able to resolve multiple sea-ice layers with different electrical parameters. In exploration geophysics, it is therefore common to resolve a multi-layered subsurface structure using either multiple frequencies, several transmitter/receiver configurations, or a combination of the two.

The aim of this study is to lay the foundation for a rapid and large-scale platelet-layer volume estimation, without the need for time consuming sea-ice drilling experiments. We focus here on the analysis of multi-frequency electromagnetic induction sounding data at platelet-free calibration sites with known sea-ice thickness to assess calibration coefficients and data uncertainties for the individual instrumental frequencies. We apply calibration coefficients and uncertainties to a more complex situation with a platelet layer, to derive limitations for the parameterization of the platelet-layer conductivity and to investigate its relationship to ice-volume fraction.

2.3. Method

We used a commercial EM induction sensor (GEM-2, Geophex Ltd) for multi-frequency soundings on sea ice with an underlying platelet layer at several survey sites in Atka Bay. An estimation of instrumental uncertainties requires knowledge of the subsurface structure. At Atka Bay, these requirements were not given, since the electrical bulk conductivity of the platelet layer is unknown and its estimation is a major goal of this study. Therefore, two additional datasets over simpler geophysical calibration targets were acquired to calculate calibration coefficient and the uncertainties of the measurements. These calibrations were conducted over level sea ice in the central Weddell Sea (no platelet layer) and over the North Sea in Germany, where no sea ice was present (seawater only). Figure 2.1 shows the sea-ice survey and calibration sites.

2.3.1. Multi-frequency EM sounding

The GEM-2 instrument (Fig. 2.2) is a ground-based induction sensor with promising specifications for multi-layer sea-ice thickness retrieval. It can be used either in horizontal or vertical coplanar mode with a transmitter-receiver coil spacing of 1.66 m. The coil spacing is a critical parameter, since it limits the sounding depth together with the chosen frequency. Although the coil spacing of the GEM-2 is small compared to the often used single-frequency Geonics EM-31 (3.67 m), it was considered to be sufficient for our

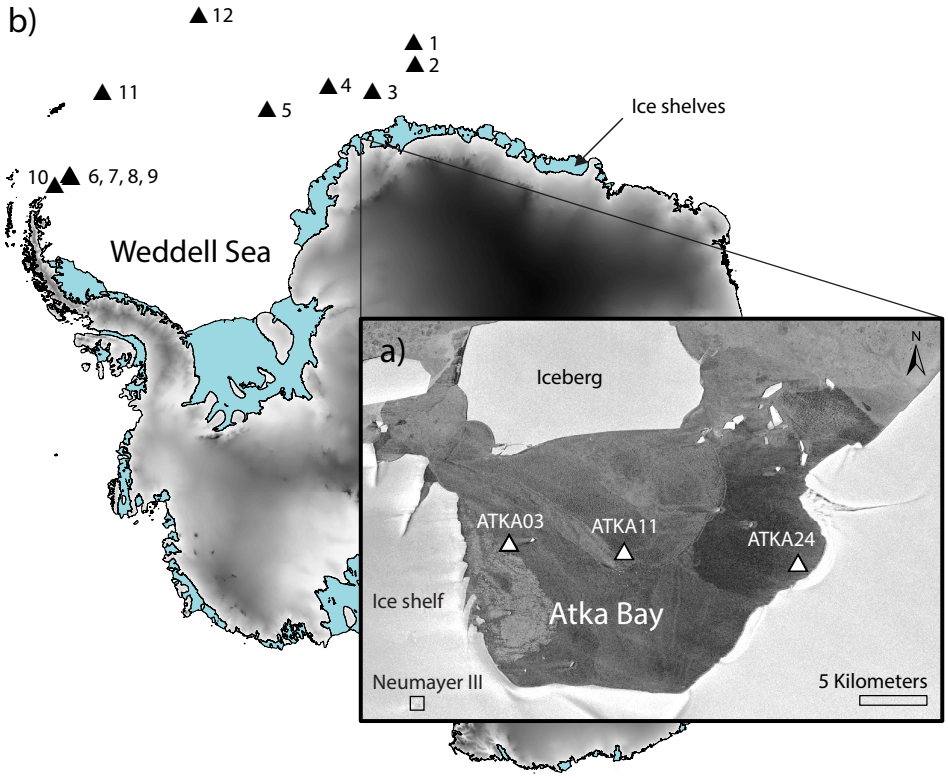

Figure 2.1.: Map of sea-ice study sites. a) Enlarged map of the Atka Bay, where the survey sites with an underlying platelet layer are shown (white triangles). Background: TerraSAR-X image from 15th November 2012, provided by the German Aerospace Center (DLR). b) Calibration sites in the Weddell Sea without a platelet layer (black triangles). Blue areas indicate the locations of ice shelves (Fretwell et al., 2013, Bedmap2).

purposes. The GEM-2 instrument can be operated simultaneously with up to five frequencies in a range from 330 to 96000 Hz. For calibration measurements in the Weddell and North seas we used frequencies of 1530, 5310, 18330, 63030 and 93090 Hz. At Atka Bay we used slightly different frequencies (450-93030 Hz) at a sampling rate of 10 Hz.

During operation, a primary electromagnetic field is generated by the transmitter coil of the EM instrument. The primary field induces a secondary magnetic field in all nearby conductive layers. The receiver coil measures the superimposed signal of all resulting magnetic fields. The EM response is defined as the relative secondary field, which is the secondary field divided by the primary field. It can be expressed as a complex number with the in-phase I (real part) and the quadrature Q (imaginary part). In-phase and quadrature are dimensionless and are recorded in parts per million (ppm). An alternative representation is given by the amplitude Amp and the phase φ, where $\varphi = \arctan(Q/I)$ and $Amp = \sqrt{I^2 + Q^2}$.

Figure 2.2.: Multi-frequency EM induction sounding data are recorded with the GEM-2 at different heights above sea ice. The signal directly depends on the distances to the conductive layers. Photograph by Sandra Schwegmann, 24th June 2013.

In practice, the primary field is often suppressed at the receiver coil to measure the minor secondary field with a sufficient resolution. This is realized in the GEM-2 with a bucking coil, which is connected in series to the receiver coil, but has an opposite polarity (Won et al., 2003). The bucking coil has a defined area, number of turns and distance to the transmitter (1.035 m) to cancel the primary field at the receiver location with an equal current.

According to Frischknecht et al. (1991), three types of systematic errors exist in in-phase and quadrature recordings due to improper adjustment and calibration of the sensor: (1) Zero-level offsets I_c and Q_c, (2) scaling coefficients A and (3) phase-mixing coefficients P_c have to be applied to the measured in-phase and quadrature components (I_m and Q_m). The corrected in-phase I and quadrature Q are calculated by

$$I = A[(I_m + I_c)\cos(P_c) - (Q_m + Q_c)\sin(P_c)] \tag{2.1}$$

and

$$Q = A[(Q_m + Q_c)\cos(P_c) + (I_m + I_c)\sin(P_c)]. \tag{2.2}$$

A similar approach was presented by Deszcz-Pan et al. (1998); Reid and Bishop (2004);

Brodie and Sambridge (2006) and Minsley et al. (2012). Because of systematic errors in our instrument, we corrected our data according to Equations 2.1 and 2.2 to get reliable results.

2.3.2. Bucking coil bias

We compared field data to numerical 1D forward models (Anderson, 1979) to obtain the calibration coefficients at specific calibration sites. Model parameters were the EM frequency, the coil spacing and orientation, as well as the thickness and conductivity of multiple layers.

We found a significant bias between the actual GEM-2 response and the forward models at all sites and all frequencies. This deviation could neither be explained with realistic calibration coefficients, nor with the layer conductivities at the calibration sites. We finally found that the bucking coil picked up in addition to the primary field a signal from the subsurface (secondary field), which could not be described with a constant factor as described in literature and done in the internal instrumental processing. To account for the secondary field measured by the bucking coil, we implemented the bucking coil in our forward models as a second receiver and subtracted the result from the receiver response. By doing so, we achieved a good agreement between data and forward models with realistic calibration coefficients.

2.3.3. Relation of electrical conductivity and porosity

Archie's law relates the bulk electrical conductivity σ of a porous layer to the porosity Φ, the brine conductivity σ_b and the cementation factor m (Archie, 1942):

$$\sigma = \sigma_b(\Phi)^m. \tag{2.3}$$

We used this law to convert (1) brine conductivity and brine volume of sea ice to bulk conductivity of the solid sea-ice layer and (2) bulk conductivity of the platelet layer to the actual ice-volume fraction. The empirical factor m depends to a large extent on the material grain shape and pore geometry (Salem and Chilingarian, 1999). Previous studies often used a value of 1.75 for solid sea ice, while a range of 1.55 to 2.2 is reported in literature (Reid et al., 2006). Because of the different structure of the unconsolidated platelet layer with its higher connectivity and brine volume compared to solid sea ice, the cementation factor of solid sea ice might not be applicable to the platelet layer. We

therefore tested a broad range of cementation factors from 1.5 to 2.5, values which are usually used for saturated sandstones (Glover et al., 1997). These structures are more likely to describe the connected pores of the platelet layer.

2.3.4. Field data

Atka Bay

We investigated properties of the platelet layer at Atka Bay at three sites between November 2012 and January 2013, operating from the German research station Neumayer III. The sites ATKA03, ATKA11 and ATKA24 (Fig. 2.1 and Tab. 2.1) represent different fast-ice regimes. At ATKA11, where we repeated EM data acquisition five times, sea ice was approximately 4 months old, formed after a breakout in August 2012. Consequently, ATKA11 showed the thinnest sea ice of all sites. We found older first-year sea ice at ATKA24 and thicker rafted sea ice at ATKA03. The detailed description of sea-ice conditions can be found in Hoppmann et al. (2015b). At each site, we removed the snow and acquired multi-frequency EM data in 0.1 m steps in sensor altitude from the sea-ice surface to a maximum height of 2 m above the sea ice (Fig. 2.2).

After the EM sounding, we measured the freeboard (F), the sea-ice thickness (IT) and the platelet-layer thickness (PLT) with a modified thickness gauge trough 0.05 m drill-holes (Tab. 2.1). Individual ice platelets of up to 0.1 m in diameter were observed. Manual sea-ice thickness measurements yielded an uncertainty of less than 0.1 m for solid sea ice. But we could only determine the platelet-layer thickness with an accuracy of about 0.3 m as verified by an underwater camera (Hoppmann et al., 2015b). The platelet layer often consisted of internal dense layers, where in the vicinity of the seawater the platelet layer was generally looser than in the middle of the layer. Surprisingly, we found often a less dense layer next to the solid sea ice. For our further calculations, however, we assumed a homogeneous platelet layer.

To determine conductivities of the water column and the interstitial platelet-layer water, we performed with a conductivity-temperature-depth probe (CTD75M, Sea & Sun Technology GmbH) in total 22 down- and upward casts between 21 November 2012 and 7 January 2013. The instrument was operated through core-holes 0.1 m in diameter, with a maximum depth range of 250 m. Small ice crystals regularly blocked the conductivity cell while the instrument was operated in the platelet layer, resulting in spuriously low conductivity values. We tried to minimize this risk by repeated up- and downward movements of the instrument. As the downward casts still contained spurious data, we determined from the undisturbed upward casts an average seawater conductivity of 2690

Table 2.1.: Summary of GEM-2 datasets at Atka Bay. Date format is day/month. IT: Measured sea-ice thickness (snow was removed), PLT: measured platelet-layer thickness, F: measured freeboard, T: air temperature measured at Neumayer III station, σ_i: estimated sea-ice conductivity, σ_{pl}: estimated platelet-layer conductivity, used frequencies.

Site	Date (2012)	IT m	PLT m	F m	T °C	σ_i mSm^{-1}	σ_{pl} mSm^{-1}	Frequencies Hz
ATKA11	21/11	0.67	1.17	-0.03	-1.0	200	1225	475, 1525, 5325, 18325, 63025
ATKA11	26/11(1)	0.68	1.23	-0.01	-4.2	200	1125	5310, 18330, 63030, 93090
ATKA24	26/11(2)	1.89	2.24	0.15	-4.6	40	1340	5310, 18330, 63030, 93090
ATKA11	01/12(1)	0.70	1.43	0.01	-1.5	200	1017	450, 1530, 5310, 18330, 63030
ATKA11	01/12(2)	0.70	1.43	0.01	-1.5	200	1075	5310, 18330, 63030, 93090
ATKA03	27/12(1)	2.69	4.21	0.33	-0.9	40	-	1530, 5310, 18330, 63030, 93090
ATKA11	27/12(2)	0.79	1.11	0.07	-1.2	200	1143	1530, 5310, 18330, 63030, 93090

mSm^{-1} below the platelet layer.

To compare the electrical conductivity of the solid sea-ice layer with results from the GEM-2, we retrieved several sea-ice cores and measured temperature and salinity profiles in 0.1 m intervals. Brine volume (porosity) was calculated according to Cox and Weeks (1983) and Leppäranta and Manninen (1988). Brine conductivity σ_b was determined after Stogryn and Desargant (1985) and Reid et al. (2006). The bulk conductivity of the solid sea-ice layer σ was then calculated using Equation 2.3 and a cementation factor m of 1.75 (Reid et al., 2006).

Weddell Sea and North Sea

EM calibration data without the presence of a platelet layer were acquired in the central Weddell Sea at 12 calibration sites during two winter expeditions with the German ice-breaker RV Polarstern between June and September 2013 (Tab. 2.2). Sea-ice thickness was measured with a thickness gauge and the conductivity of the seawater was obtained by the keel salinometer of RV Polarstern (IT and σ_w in Tab. 2.2).

On first-year sea ice the snow was removed, which made surface flooding visible at site 3 (Tab. 2.2). On multi-year sea ice, where it was not possible to remove the snow in the

Table 2.2.: Summary of Weddell Sea and North Sea calibrations operated with frequencies 1530, 5310, 18330, 63030 and 93090 Hz. Date format is day/month. IT: measured sea-ice thickness (snow was removed), F: measured freeboard, T: air temperature measured by Polarstern, σ_i: estimated sea-ice conductivity, σ_w: sea-water conductivity measured by Polarstern (daily average, Weddell Sea data) and by a handheld instrument (North Sea data) * flooded calibration site, $^\bullet$ 0.69 m snow included, $^\nabla$ > 1m snow included. Note the low seawater conductivity in the North Sea due to the inflow of fresh water (site 13).

Site	Date(2013)	IT	F	T	σ_i	σ_w
		m	m	°C	mSm^{-1}	mSm^{-1}
1	20/6	0.53	0.05	-21	80	2708
2	21/6	0.54	0.04	-19	80	2707
3	3/7	0.60	-0.20*	-28	80	2698
4	8/7	0.58	0.01	-13	50	2708
5	15/7	0.58	-	-3	10	2706
6	26/7	3.44	-	-20	5	2712
7	1/8(1)	2.75$^\bullet$	-0.01	-28	15	2715
8	1/8(2)	2.06	-0.01	-28	15	2715
9	1/8(3)	0.74	0.00	-28	100	2715
10	5/8	4.26$^\nabla$	-	-6	2	2718
11	31/8	0.41	0.00	-14	0	2712
12	25/9	0.72	0.00	-11	300	2686
13	2/12	-	-	5	-	1200

footprint area, we placed the GEM-2 on top of the snow and consequently included a second layer of 0 mSm^{-1} in the forward models (site 7). At site 10, we were not able to estimate the thick snow depth because of internal icy layers and consequently used the same conductivity for the sea ice and the snow layer. The bulk conductivity σ of the solid sea ice was obtained in the same way as at Atka Bay.

An additional calibration dataset was acquired on the North Sea over mixed ocean and river inflow water at the mouth of the river Weser near Bremerhaven, Germany (last calibration in Tab. 2.2). The conductivity of the seawater was measured with a hand-held conductivity meter (1200 mSm^{-1}). Without the presence of a sea-ice layer the EM response could be modeled as an ideal homogeneous half-space.

2.4. Results

Calibration coefficients and uncertainties were calculated by using the calibration data from the Weddell Sea and the North Sea. Coefficients were then applied to the Atka Bay data to estimate sea-ice and platelet-layer conductivities and the ice-volume fraction of

the platelet layer.

2.4.1. GEM-2 uncertainties

Calibration coefficients and uncertainties were obtained by manually minimizing the difference between the GEM-2 data and theoretical forward models. Figures 2.3a and b show typical 63030 Hz EM responses for different heights above seawater for the Weddell Sea calibrations. For the forward model (blue dashed line) the sea-ice layer was initially assumed to be non-conductive (0 mSm^{-1}) and a conductivity of 2700 mSm^{-1} was assigned to the seawater. The uncorrected datasets for in-phase and quadrature (Fig. 2.3a and b) differ significantly from each other and from the forward models. Reasons for this variability may originate from the incorrect calibration of the GEM-2 in general, the dependence of the EM response on environmental temperatures, the influence of sea-ice conductivity and variabilities of the drill-hole sea-ice thickness estimations within the footprint of the instrument.

We therefore categorize the deviation from the forward models into two main parts: First, imprecise calibration of the individual frequencies as a mean offset to the forward models (systematic error); second, the influence of environmental temperature, sea-ice conductivity and uncertainties of thickness estimations as the inter-variability between different calibrations. The first factor can be corrected by averaging the calibration coefficients for each frequency over all calibrations. The second factor describes the uncertainty of these mean calibration coefficients.

Zero-level offset coefficients (I_{c0} and Q_{c0}, Tab. 2.3) were measured by lifting the GEM-2 with RV Polarstern's crane and acquiring data from several meters above ground. This free-air response was obtained for around 30 minutes after the instrument was in temperature equilibrium. To investigate the long-term drift and the temperature dependency, these measurements were carried out multiple times. Although the crane measurements were conducted at temperatures from -24°C up to -10°C, we did not observe a strong temperature dependency of the zero-level offsets for all frequencies. After the instrument was in temperature equilibrium, the instrumental noise (I_n and Q_n) was determined as the standard deviation of the time series. Mean scaling A and phase-mixing coefficients P_c were obtained at each site (Tab. 2.2) by manually minimizing the root mean square error (RMSE) between in-phase and quadrature data and the forward models. It was necessary to use different zero-level offset coefficients (I_c and Q_c) than those obtained from the free-air experiment to reach a satisfactory agreement with the forward models. These changes significantly increased the standard deviation and thus, the uncertainty of zero-level offset coefficients of the individual frequencies. The average of all calibration

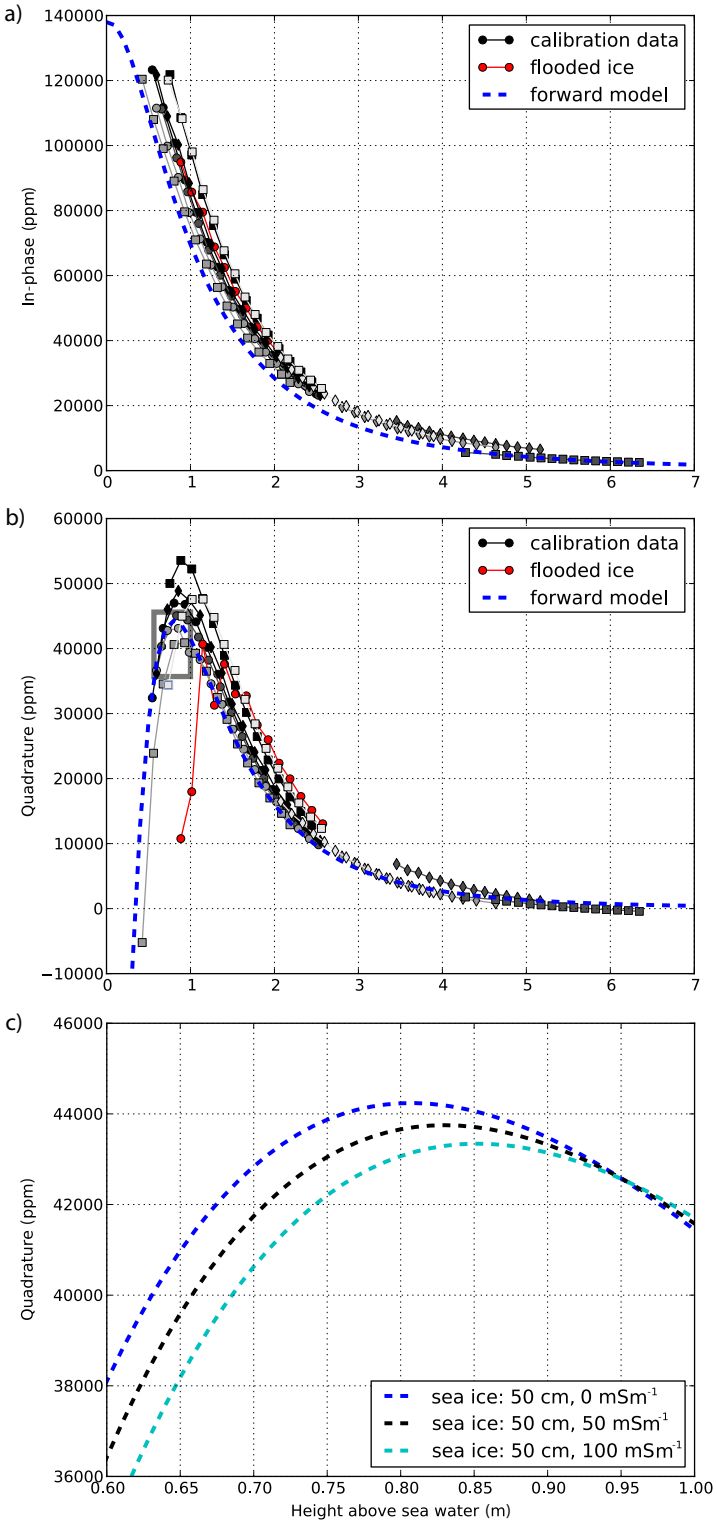

Figure 2.3.: Raw electromagnetic data (63030 Hz) for all Weddell Sea datasets. a) In-phase, b) quadrature and c) enlargement of box in b). The forward models (blue dashed line) in a), b) and c) were calculated by assuming a homogeneous half-space of 2700 mSm^{-1} and resistive sea ice (0 mSm^{-1}). Two additional forward models with increasing sea-ice conductivities (50 mSm^{-1} and 100 mSm^{-1}) are shown in c).

coefficients, the standard deviations from individual calibration sites and the instrumental noise are summarized in Table 2.3. We did not use the data from thick sea ice (site 10, Tab. 2.2) to calculate these coefficients, because the signal values were low and calibration coefficients depended mostly on the estimated sea-ice conductivity.

The sea-ice conductivities σ_i for the forward models were determined with the local maximum of quadrature components of frequencies 63030 and 93090 Hz, which are assumed to be most sensitive to sea-ice conductivity due to low penetration depth. This method was applied because it is almost independent from any zero-level offset, scaling and phase-mixing corrections. In Figure 2.3c this is shown for theoretical forward model curves. One particular example is the calibration at flooded site 3 (Tab. 2.2), which exhibits a conductivity of 1700 mSm^{-1} for the top 20 cm and the local maximum is shifted significantly to higher values (Fig. 2.3b, red). Also for non-flooded calibration sites, small conductivity changes were necessary to fit the local maximum. Estimated sea-ice conductivities σ_i are summarized in Table 2.2.

Using Equations 2.1 and 2.2, all calibration data were corrected with the mean coefficients I_c, Q_c, A, P_c (Tab. 2.3). The total uncertainty for the in-phase component ΔI was calculated with the Gaussian law of error propagation according to

$$\Delta I^2 = \left(\frac{\delta I}{\delta I_c}\sigma_{I_c}\right)^2 + \left(\frac{\delta I}{\delta Q_c}\sigma_{Q_c}\right)^2 + \left(\frac{\delta I}{\delta A}\sigma_A\right)^2 + \left(\frac{\delta I}{\delta P_c}\sigma_{P_c}\right)^2 + \left(\frac{\delta I}{\delta I_m}\sigma_{I_n}\right)^2 + \left(\frac{\delta I}{\delta Q_m}\sigma_{Q_n}\right)^2 \tag{2.4}$$

under the assumption that the uncertainty of the measured in-phase and quadrature signal (I_m, Q_m) is described by the noise (I_n, Q_n) and the uncertainty of the remaining contributions is given by the standard deviations of calibration coefficients. The calculation for ΔQ was performed accordingly. The corrected data (dots), the respective forward models (solid lines) and the estimated uncertainties (ellipses) for in-phase and quadrature are shown for one example dataset (site 1, Tab. 2) in Figure 2.4. Using forward models as in Figure 2.4 and increasing the sea-ice thickness in 0.1 m steps (sea ice with 100 mSm^{-1}), over a depth of 10 m, the calculated uncertainties exceed in 3 m depth the difference of two consecutive responses. This means that it is possible to resolve solid sea ice up to 3 m thick at an accuracy of 0.1 m with GEM-2 specifications and given uncertainties.

2.4.2. Sea-ice conductivity

The conductivity of the solid sea ice was estimated for all calibration and survey sites by aligning the measured quadrature components of the two highest frequencies (63030 and 93090 Hz) to the modeled data. This procedure yielded sea-ice conductivities of

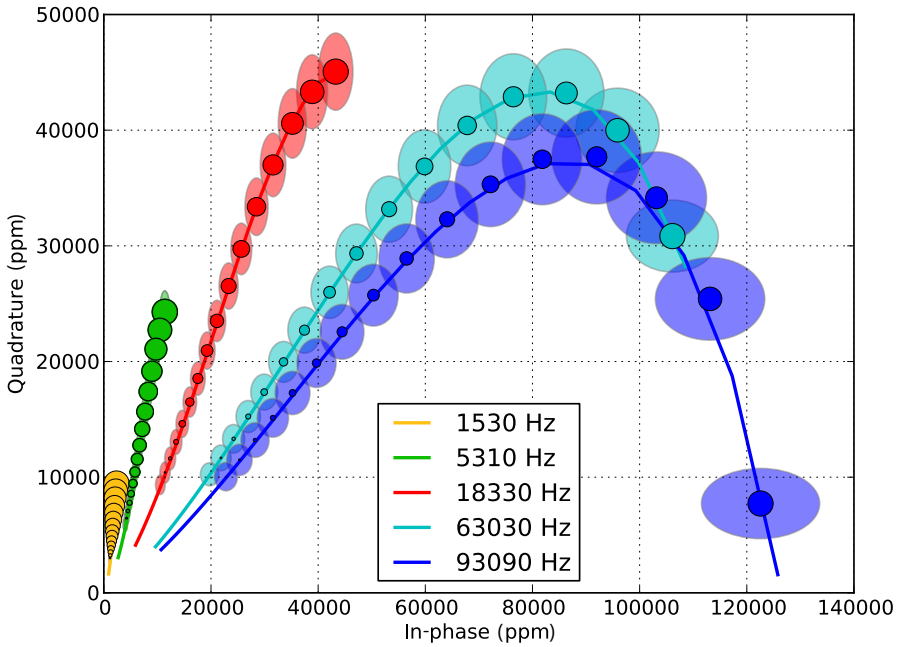

Figure 2.4.: Data from calibration site 1 (Tab. 2.2) with applied calibration coefficients. The instrument was lifted from zero (large dots) to two meters (smaller dots) over 0.53 m thick sea ice with a conductivity of 80 mSm^{-1}. The semi-axes of the ellipses indicate the in-phase and quadrature uncertainties. The forward models (solid lines) from zero to three meters are shown for the different frequencies.

200 mSm^{-1} for thin sea ice ($<$ 1 m) at ATKA11 and conductivities of 40 mSm^{-1} for thicker sea ice at ATKA03 and ATKA24 (Tab. 2.1).

Brine porosity and conductivity were used to calculate the reference bulk conductivity values (Equation 2.3). The conductivities of the three ATKA11 sea-ice cores were 139 $\pm$ 113, 141 $\pm$ 102, and 149 $\pm$ 77 mSm^{-1}. These high standard deviations were mostly due to high conductivities at the ice/water interface. If these were omitted, overall conductivities reduced to 100 $\pm$ 18, 114 $\pm$ 73, and 127 $\pm$ 47 mSm^{-1}. Sea-ice cores at ATKA03 and ATKA24 yielded a sea-ice conductivity of 56 $\pm$ 23 and 101 $\pm$ 35 mSm^{-1}, respectively.

In the Weddell Sea, nine sea-ice cores ($<$ 1 m) revealed sea-ice conductivities between 35 and 72 mSm^{-1}, with an average of 56 $\pm$ 14 mSm^{-1}. The highest standard deviation in a single core was 55 mSm^{-1}. A thicker sea-ice core of 1.77 m yielded a bulk sea-ice conductivity of 17 mSm^{-1} $\pm$ 8 mSm^{-1}.

In contrast, sea-ice conductivities based on forward model fitting at 63030 and 93090 Hz ranged from 0 to 100 mSm^{-1} with one outlier of 300 mSm^{-1} for thin sea ice ($<$ 1 m) and from 2 to 15 mSm^{-1} for thicker sea ice ($>$ 1 m; Tab. 2.2). A value of 300 mSm^{-1} is a

Table 2.3.: Calibration coefficients for all frequencies (Freq). Noise of in-phase I_n and quadrature Q_n components estimated by long time series, zero-level offset coefficients I_{c0} and Q_{c0} measured with a crane away from any conductive material. Zero-level offset coefficients I_c and Q_c, scaling coefficients A and phase-mixing coefficients P_c obtained by minimizing the difference between field data and forward models. P_{c2} are the phase-mixing coefficients adjusted for the Atka Bay datasets. $\overline{x}$ is the arithmetic average and σ the 1σ-standard deviation of the individual calibration coefficients.

Freq Hz	$\overline{x}/\sigma$	I_n ppm	Q_n ppm	I_{c0} ppm	I_c ppm	Q_{c0} ppm	Q_c ppm	A	P_c ∘	P_{c2} ∘
1530	$\overline{x}$			-200	-45	-190	118	0.82	-0.07	-1.17
	σ	138	137	256	138	25	137	0.05	1.51	3.58
5310	$\overline{x}$			-799	-405	77	328	0.82	0.65	-1.10
	σ	128	127	249	269	12	365	0.06	0.66	0.61
18330	$\overline{x}$			-183	417	487	671	0.83	0.87	-0.14
	σ	125	125	242	547	6	576	0.06	0.73	1.28
63030	$\overline{x}$			-932	-757	1331	1081	0.87	0.92	1.79
	σ	146	135	284	695	133	498	0.07	0.98	2.98
93090	$\overline{x}$			-3474	-3420	240	39	0.89	0.27	4.72
	σ	204	193	352	683	460	685	0.08	1.35	4.24

rather high conductivity for first-year sea ice, and may be explained by the presence of surface flooding or internal layers. Excluding the outlier (300 mSm^{-1}), the conductivities from the sea-ice cores are in the same range as the conductivities from our results obtained by the GEM-2.

2.4.3. Bulk platelet-layer conductivity

The sea-ice conductivity at each site at Atka Bay fast ice was used as an input parameter for a series of forward models, together with the known thicknesses of solid sea ice and the platelet layer. We varied the electrical conductivity of the platelet layer using the full range of physically plausible conductivities, from a fully resistive layer (0 mSm^{-1}) to conductive seawater (2700 mSm^{-1}) in steps of 50 mSm^{-1}. From the series of forward models (example of ATKA11 at 18330 Hz, Fig. 2.5) we calculated the best fit between the corrected GEM-2 data (applied calibration coefficients) and the forward models, based on the local minimum of the RMSE. This procedure was repeated at all sites at Atka Bay for both in-phase and quadrature components and for each frequency. We found that the best fit of in-phase and quadrature components did not always result in the same bulk platelet-layer conductivity. Assuming that both components should yield the same conductivity, we applied at each site for every frequency an additional phase correction. The new

phase-mixing coefficients were averaged and included into the uncertainty estimation (P_{c2}, $\sigma_{P_{c2}}$; Tab. 2.3). The averaged coefficients were again applied to both components for all frequencies at all sites, except at ATKA03 (Tab. 2.1), where the signal was too insensitive towards the bulk platelet-layer conductivity due to generally low signal values on the thick sea ice. We repeated the estimation of bulk platelet-layer conductivity by finding the local minimum of the RMSE and also considered the upper and lower limit of the in-phase (Fig. 2.6) and quadrature uncertainties.

We excluded the 450 Hz frequency and the in-phase component of the 1530 Hz channel from the analysis, due to a poor signal-to-noise ratio. We found that the quadrature component of the two highest frequencies only weakly depended on the bulk-conductivity variations of the platelet layer at most sites and were subsequently excluded from further analysis. Based on the small penetration depth of these frequencies and the typical thickness of the fast ice, this was not fully unexpected.

The local minimum of the RMSE of all processed frequencies and components were averaged by survey site (Fig. 2.7) and by individual frequencies (Fig. 2.8). For individual sites we found mean bulk platelet-layer conductivities from 1017 mSm^{-1} to 1340 mSm^{-1} (Fig. 2.7, best fit). The mean of these values resulted in a bulk platelet-layer conductivity of 1154 mSm^{-1} (Fig. 2.7, solid black line). The mean value of the lower uncertainty limit was 883 mSm^{-1} and of the upper uncertainty limit 1425 mSm^{-1}, which resulted in an overall uncertainty of $\pm$ 271 mSm^{-1}. We observed highest bulk platelet-layer conductivity at ATKA24, the site with thicker sea ice and platelet layer (1.89 m + 2.24 m) than at ATKA11. Here we assume that an internal conductive layer was located in the platelet layer.

We observed a frequency dependence of the bulk platelet-layer conductivity (Fig. 2.8), where higher frequencies tended to result in higher conductivities, even though upper layers may be, in general, more consolidated. Whether the reason for this relationship is a calibration error or insufficient description of the layering by the forward models is not known.

2.4.4. Ice-volume fraction of platelet layer

The next step was to convert the layer conductivity to porosity. We used Archie's law (Equation 2.3), where the brine conductivity σ_b is the conductivity of the liquid phase in the platelet layer. In a first-order approximation, σ_b can be described by the conductivity of the seawater column below.

In 8 down- and 2 upward CTD casts the water in the platelet layer appeared to be much fresher than the seawater (1800 mSm^{-1} compared to 2690 mSm^{-1}), but we interpret these

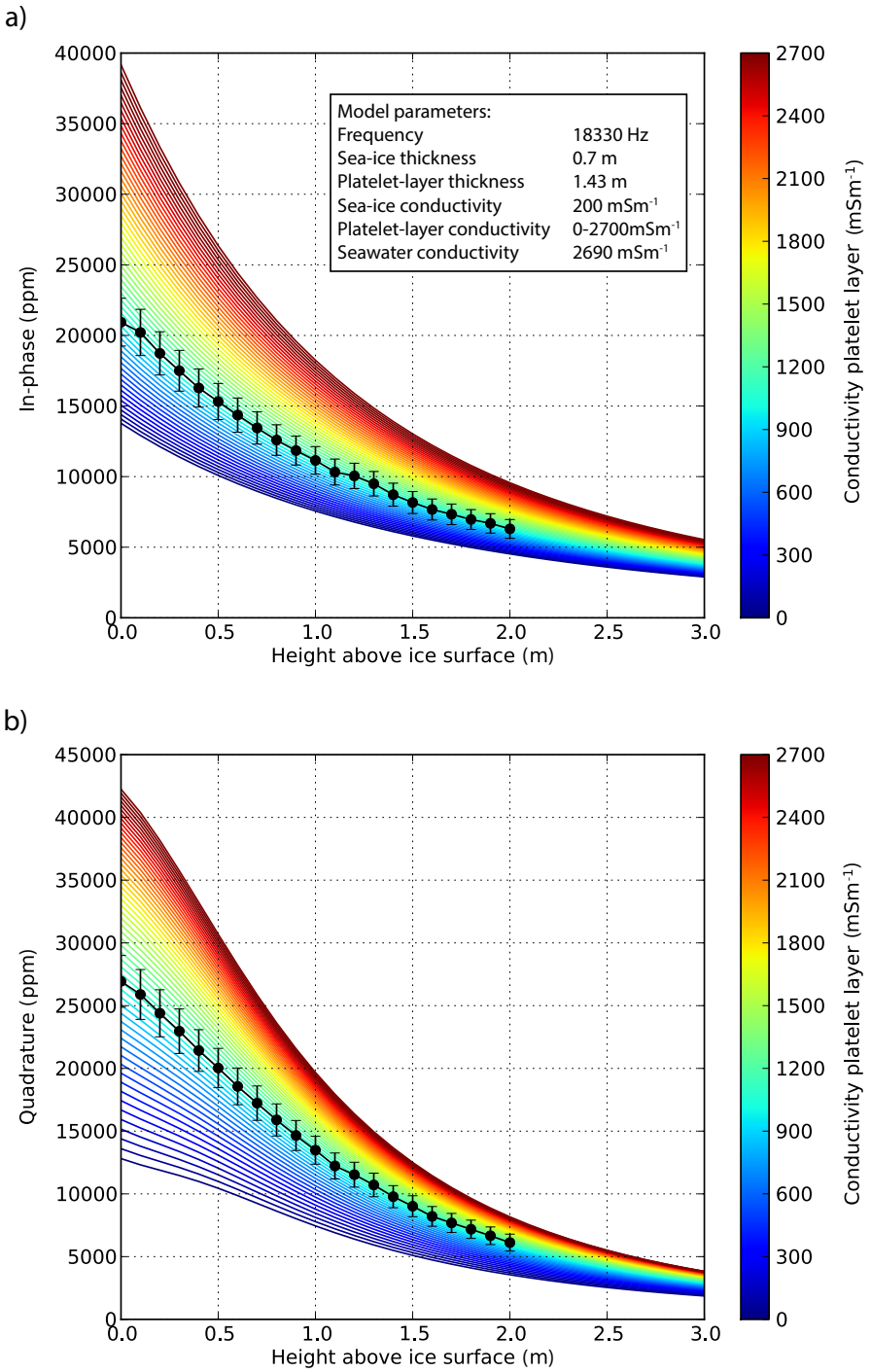

Figure 2.5.: Corrected dataset and corresponding uncertainties for the a) in-phase and b) quadrature 18330 Hz component at ATKA11 (1 December 2012). The forward models were calculated by assuming various platelet-layer conductivities (color bar).

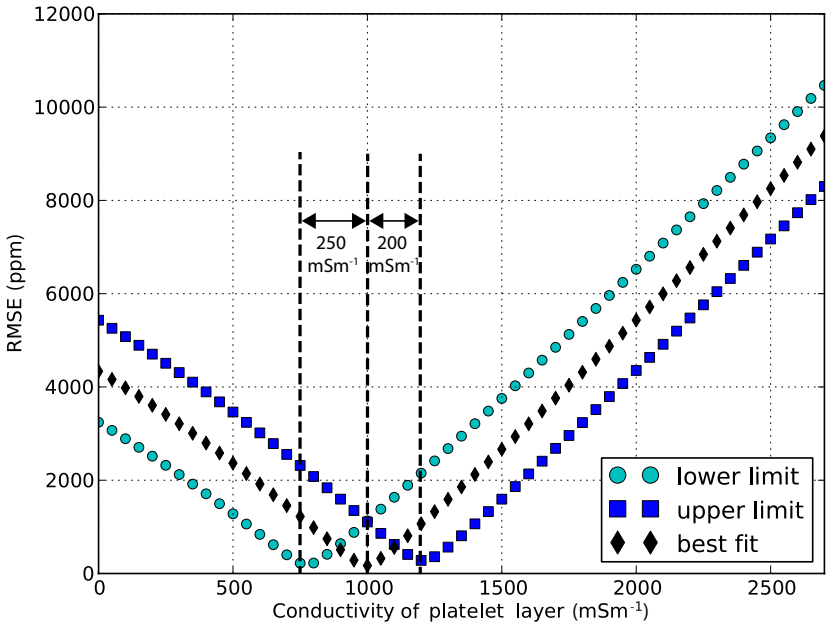

Figure 2.6.: Root-mean square errors (RMSE) were calculated for the in-phase component (Fig. 2.5a) to find the smallest difference between dataset and individual forward models. This is shown for the best fit, for the lower limit of uncertainties and for the upper limit. The bulk platelet-layer conductivity is in this example 1000 mSm^{-1} with a difference of 250 mSm^{-1} to the lower and 200 mSm^{-1} to the upper limit.

Table 2.4.: Ice-volume fractions of the platelet layer assuming different values for cementation factor m, conductivities of interstitial water in the platelet layer σ_b and bulk platelet-layer conductivities σ of the lower uncertainty limit (883 mSm^{-1}), the best fit (1154 mSm^{-1}) and the upper uncertainty limit (1425 mSm^{-1}).

σ_b (mSm^{-1})	1800			2690		
σ (mSm^{-1})	883	1154	1425	883	1154	1425
$m = 1.5$	0.38	0.26	0.14	0.52	0.43	0.35
$m = 2.0$	0.30	0.20	0.11	0.43	0.35	0.27
$m = 2.5$	0.25	0.16	0.09	0.36	0.29	0.22

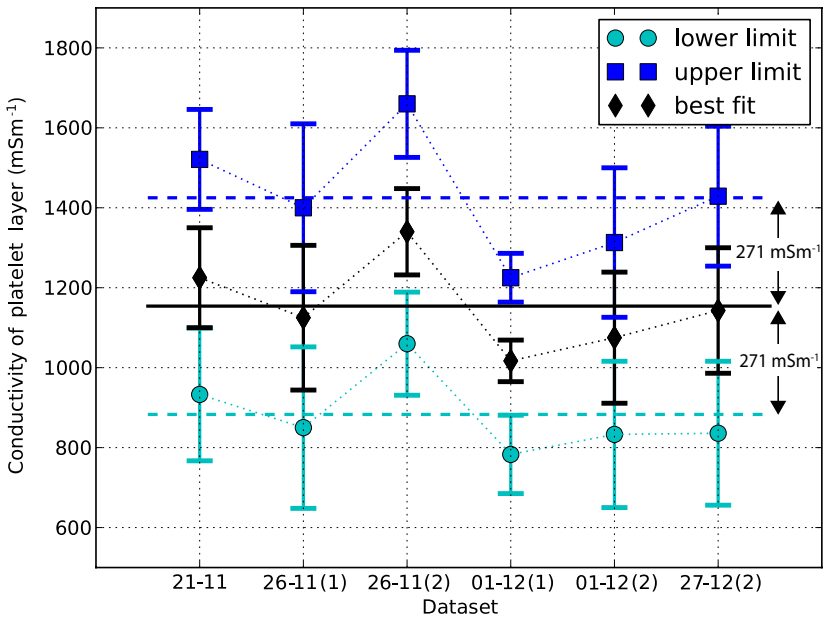

Figure 2.7.: Bulk platelet-layer conductivities. The results obtained by different frequencies are averaged and shown for the individual sites. The conductivities and the corresponding standard deviations are shown for the best fit, the lower and upper limit of uncertainties. Dataset format is day-month of 2012.

low values as an interaction between ice platelets and the conductivity sensor. We assumed cementation factors m between 1.5 and 2.5. Applying these parameters to different brine conductivities σ_b and bulk platelet-layer conductivities σ with lower and upper limits of uncertainties, we found a range of ice-volume fractions (1 - Φ, where Φ is porosity; Tab. 2.4).

The resulting ice-volume fractions ranged from 0.16 to 0.26 for seawater conductivities $\sigma_b = 1800$ mSm^{-1}, which we considered to be spuriously low. For regular seawater of $\sigma_b = 2690$ mSm^{-1} the ice-volume fractions were in the range from 0.29 to 0.43. Accounting for the lower and upper uncertainty limits, ice-volume fractions for spuriously low brine conductivity σ_b ranged between 0.09 and 0.38 and for seawater brine conductivity between 0.22 and 0.52. The ice-volume fraction was equally influenced by the choice of cementation factor m and brine conductivity σ_b.

2.5. Discussion

We have shown that for given thicknesses of solid sea ice and the platelet layer, it is possible to use multi-frequency EM induction soundings to resolve the bulk platelet-layer

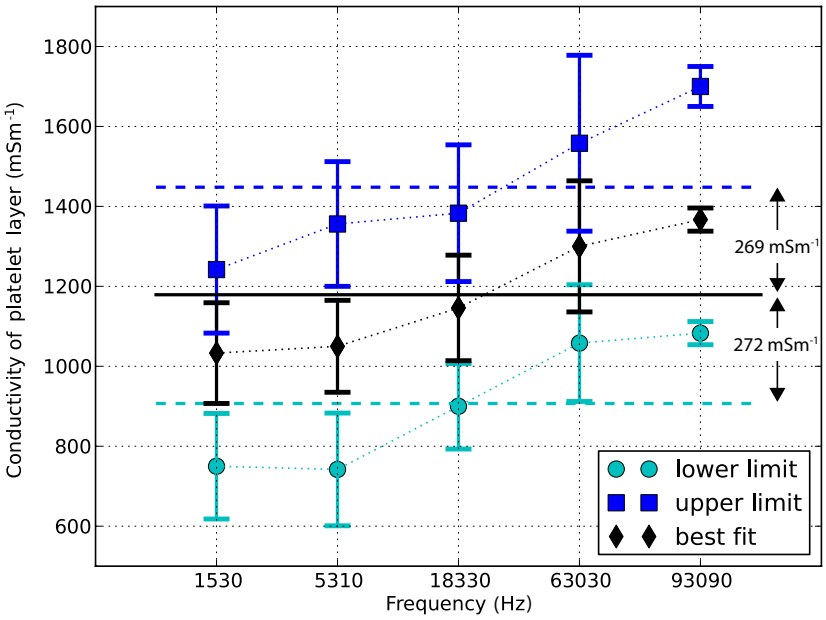

Figure 2.8.: Bulk platelet-layer conductivities. The results obtained by the different sites are averaged and shown for the individual frequencies. The conductivities and the corresponding standard deviations are shown for the best fit, the lower and upper limit of uncertainties.

conductivity within an uncertainty range of 271 mSm^{-1}. The uncertainty is mainly governed by the inter-variability between calibrations rather than by the actual instrumental noise of the GEM-2. Consequently, the uncertainties of the calibration coefficients can be reduced significantly with proper calibrations. As stated earlier, we are able to resolve with GEM-2 data a solid sea-ice layer of three meter with an accuracy of 0.1 m based on calculated uncertainties. Reducing the uncertainty by 50 percent will allow us to resolve solid sea ice of up to 4.20 m at an accuracy of 0.1 m. ATKA03 with its 2.69 m solid sea ice and 4.21 m platelet layer could not be resolved by the used setup. Theoretical calculations, however, showed that it would be possible to resolve these layers with frequencies up to 18330 Hz by reducing the uncertainties even more.

During our first operations of the GEM-2 at Atka Bay fast ice, we tested different frequency configurations in order to evaluate its potential (Tab. 2.1). The frequencies of 1530, 5310, 18330, 63030 and 93090 Hz showed promising results, as the various frequencies are sensitive to different depths, while a frequency as low as 450 Hz was too noisy. In general, lower frequencies are more sensitive to deeper structures and higher frequencies to the shallower sea ice. With the two highest frequencies, we obtained sea-ice conductivities similar to those from independent results of sea-ice cores. This can be very useful

for other studies, especially for a non-destructive determination of sea-ice properties (e.g. Haas et al., 2008a). Although first-year sea ice is generally more electrically conductive than thick sea ice, the sea-ice conductivities from forward-model fitting at ATKA11 were with 200 mSm^{-1} unexpectedly high. At this site, the freeboards were close to zero and a slushy snow-ice interface was observed after the snow was removed, which probably influenced the GEM-2 recordings.

For further GEM-2 studies, where an absolute calibration is desired, we strongly suggest calculating calibration coefficients and uncertainties for all the individual frequencies. Nevertheless, the instrument can still be used in a traditional way for single-frequency sea-ice thickness retrievals, similar to an EM-31, where an exponential fit to calibration data at a single frequency is used to directly determine the sea-ice thickness (e.g. Haas et al., 1997). The advantages of the GEM-2 over the EM-31 are the different sounding depths due to several frequencies and the recording of in-phase and quadrature. The two components provide independent measurements at one single frequency and thereby reduce the ambiguity of the recorded signal, which is important for the determination of the calibration coefficients. The in-phase component of the EM-31 is often in saturation and the apparent conductivity is calculated with the quadrature component. In general, the in-phase component is more sensitive to deeper structures compared to the quadrature component.

Correcting the Atka Bay data with the calibration coefficients revealed that an additional phase shift had to be applied. This is possibly linked to the fundamentally different temperature regimes at calibration sites, where the mean calibration coefficients were obtained. Slightly different frequency configurations only had a minor influence. This also implies the importance of careful calibration measurements for future field campaigns. We measured environmental temperatures during all our surveys, but we could not see a strong temperature dependency of individual measurements, although the instrument was in temperature equilibrium with its surrounding.

While the uncertainty associated with the GEM-2 data mainly affects the estimation of the platelet-layer conductivity, the subsequent conversion to ice-volume fraction strongly depends on physical assumptions of pore and ice-platelet shapes. For example, we assume that the pore water is connected, which would generally indicate a low value for the cementation factor m in Archie's law (Glover, 2009). A lower value indicates spherical pores and grains (Salem and Chilingarian, 1999), but this is not the case for individual disc-shaped ice platelets within the platelet layer. Using thin sections for sea-ice cores from Atka Bay, Hoppmann et al. (2015b) found randomly oriented ice platelets (which agrees with recent findings of Gough et al., 2012). This factor might results again in a lower value

of m due to less angularity. But up to now, no studies exist that describe the cementation factor m for the platelet layer by independent measurements. Instead, we calculated a brine platelet-layer conductivity with a range of values from 1.5 to 2.5, normally observed in sandstones (Glover et al., 1997). In general, we get a better agreement with results from recent studies (Hoppmann et al., 2015b; Gough et al., 2012) with higher cementation factors or lower brine conductivities.

The brine conductivity σ_b measured by CTD casts is an additional uncertainty factor. Hoppmann et al. (2015b) showed that the platelet layer was already thinning when the GEM-2 surveys were conducted (between November 2012 and January 2013) due to the inflow of warm water masses. Hence, the brine conductivity may have been decreased due to ice melt in late December. Nevertheless, these melt rates and the associated freshening do not explain the low conductivities (in the range of 1800 mSm^{-1}) recorded. Also, the bulk platelet-layer conductivity at ATKA11 on 27th December (Fig. 2.7) did not decrease compared with earlier calibrations.

Apart from the physical assumptions of the platelet layer and the conversion of conductivities to ice-volume fraction, we assumed the ideal case of two layers, which are level within the footprint of the sensor. We tried to compensate for this effect by measuring sea-ice thickness in the footprint range of the instrument through several drill-holes. This assumption most likely does not hold for thicker sea ice and platelet layers, where sub-ice topographies or internal layers may more often be present.

With frequencies more sensitive to the solid sea-ice layer and the significant extension of the frequency range to lower values, we are confident to resolve both platelet-layer thickness and conductivity using a geophysical inversion scheme. The result of the inversion might be that a two-layer case is not sufficient; instead it may be necessary to have several platelet-layers to explain the apparent relationship (Fig. 2.8) between bulk platelet-layer conductivity and frequency. However, data inversion is only possible when the bias of the bucking coil is included into inversion algorithms first.

2.6. Conclusion

This study is a step towards sub-sea-ice platelet-layer volume estimation of Antarctic fast ice with electromagnetic induction sounding. We used the multi-frequency ground-based instrument GEM-2 operated at frequencies between 450 and 93090 Hz. We compared measurements at sites of known sea ice and platelet-layer thicknesses at Atka Bay to two-layered forward models, deriving a mean bulk platelet-layer conductivity of 1154 mSm^{-1} $\pm$ 271 mSm^{-1}. Assuming a range of cementation factors for the platelet layer, we obtained

ice-volume fractions of 0.29 to 0.43, while values of 0.25 ± 0.06 and 0.25 ± 0.1 have been found recently by other methods (Gough et al., 2012; Hoppmann et al., 2015b). Using the quadrature component of higher frequencies, 63030 and 93090 Hz, we were able to estimate conductivities of the solid sea-ice layer. Accurate calibrations are required to reduce the uncertainties of multi-frequency electromagnetic measurements to make them useful for the determination of the platelet-layer volume. Comparisons of calibration data and forward models revealed that it is crucial to include the signal response of the bucking coil in the theoretical calculations. In general, multi-frequency soundings are superior to single-frequency soundings and may also improve sea-ice thickness retrieval over deformed and porous sea ice that has similar macro-scale properties to the platelet layer in Antarctica. Our results provide elemental physical constraints for the layer conductivities and ice-volume fractions. As we continue this work, we intent to conduct a joint analysis of all frequencies using a geophysical inversion to retrieve platelet-layer thickness and conductivity simultaneously. Multi-frequency electromagnetic induction sounding will enable to survey ice-platelet volume below the Antarctic near-coastal sea ice on a much larger scale than by direct measurements trough drill-holes. Our method can also be applied to data from multi-frequency airborne sensors, which have been recently developed (Pfaffhuber et al., 2012a).

2.7. Acknowledgments

The authors are most grateful to Thomas Schmidt, Meike Kühnel and Uwe Baltes for their field work at Atka Bay. We thank the German Space Agency (DLR) for the TerraSAR-X image and Christine Wesche for post-processing and calibrating the data. We highly acknowledge Robert Ricker, Thomas Krumpen and Martin Schiller for their field work on-board RV Polarstern (ANT-XXIX/6 and 7) and Xenia II. We thank Jean-Louis Tison for providing the sea-ice core data from the Weddell Sea campaign and the AWI logistics for their support. This work was partly supported by the German Research Council (DFG) in the framework of the priority program Antarctic Research with comparative investigations in Arctic ice areas by grants SPP1158, NI1092/2 and HE2740/12, the graduate school POLMAR and the Alfred-Wegener-Institut Helmholtz-Zentrum für Polar- und Meeresforschung. The authors are grateful to the reviewers whose comments and suggestions improved the clarity of the manuscript.

This paper was reprinted from the Annals of Glaciology with permission of the International Glaciological Society.

3 Improved 1D inversions for sea ice thickness and conductivity from EM induction data: Including nonlinearities caused by passive bucking

3.1. Abstract

The porosity of sea ice is a fundamental physical parameter that governs the mechanical strength of sea ice and the mobility of gases and nutrients for biological processes and biogeochemical cycles in the sea ice layer. Except from few coring sites little is known on the spatial distribution of the sea ice porosity and the variability of different sea ice types. But an efficient and non-destructive method to measure this property is currently missing. Sea ice porosity is however linked to the bulk electrical conductivity of sea ice, a parameter routinely used to discriminate between sea ice and seawater below by electromagnetic (EM) induction sensors. Here we evaluate the prospect of porosity retrieval of sea ice by means of bulk conductivity estimates using 1D multi-frequency EM inversion schemes. We focused on two inversion algorithms, a smoothness-constrained inversion and a Marquardt-Levenberg inversion, which we modified for the nonlinear signal bias caused by a passive bucking coil operated in such a highly conductive environment. Using synthetic modeling studies, 1D inversion algorithms and multiple frequencies, we show that we can resolve the sea ice conductivity within $\pm$ 0.01 S/m. Using standard assumptions for the conductivity-porosity relation of sea ice, we are able to estimate porosity with an uncertainty of $\pm$ 1.2 % which enables fast and non-destructive surveys of the internal state of the sea ice cover.

3.2. Introduction

Along with the shrinking of the sea ice extent (Stroeve et al., 2012; Comiso and Hall, 2014) Arctic sea ice is thinning (Lindsay and Zhang, 2005; Haas et al., 2008b; Kwok et al., 2009) and becoming younger (Maslanik et al., 2011). The change towards a younger sea ice cover leads to changes in the average internal structure. For example, first-year sea

ice shows higher absorption rates of shortwave radiation than does older sea ice, leading to a stronger internal warming and melting (Perovich et al., 2011; Nicolaus et al., 2012). This in turn, results in an increase of the connectivity of pores and brine channels, which governs the exchange of gases (Gosink et al., 1976) and nutrients (Krembs et al., 2011), as well as the mechanical strength (Kovacs, 1996). Here we develop and present a methodology to improve the use of electromagnetic (EM) induction sounding instruments to retrieve information related to the internal structure of different sea ice types, based on measurements of bulk electrical sea ice conductivity, hereinafter referred to as conductivity.

A physical parameter linked to the conductivity of the sea ice layer is its porosity (Archie, 1942). Pores of young sea ice are usually filled with highly saline brine left from the formation process, while in older, multi-year sea ice, this brine is usually replaced by fresher water due to meltwater flushing (Eicken et al., 2002; Vancoppenolle et al., 2007) or gravity drainage (Niedrauer and Martin, 1979; Notz and Worster, 2008). This also means that older, multi-year sea ice is electrically more resistive, while young, porous sea ice still has a high conductivity due to brine inclusions. Summer sea ice often shows macro-scale pores, as brine channels are widened and connected by melt processes. These pores then contain a mix of melt water and brine, which change the geochemistry of sea ice and the availability of nutrients for biological processes (Thomas and Dieckmann, 2009; Vancoppenolle et al., 2010). Mapping sea ice layer porosity by proxy measurements of sea ice conductivity would therefore enable improved process studies of sea ice mass balance and especially complex biogeochemical cycles at the atmosphere - sea ice - ocean interface. Information on the spatial variability, large-scale gradients and the annual cycle of internal sea ice properties is only sparsely available (e.g. Golden et al., 2007; Pringle et al., 2009). Current methods to obtain information on sea ice porosity are based on manual coring, whereas the high spatial variability in the sea ice cover calls for a rapid and non-destructive method.

The conductivity of sea ice, and in particular its large contrast with that of the ocean, is routinely utilized for sea ice thickness retrieval by frequency-domain electromagnetic induction sounders, which usually employ a single frequency in the range from 4 to 10 kHz. This method is deployed from helicopters (Kovacs and Holladay, 1990; Haas et al., 2009), aircraft (Haas et al., 2010), ship-mounted booms (Haas, 1998; Reid et al., 2003) or directly on the sea ice surface for high-resolution case studies (Eicken et al., 2001; Haas, 2004; Druckenmiller et al., 2009; Weissling et al., 2011). The retrieval algorithm assumes that sea ice and snow can be described by a single, flat 1D layer, which is usually the case for level sea ice, and that the effect of sea ice and snow conductivity on the EM response is

negligible compared to the contribution from the underlying seawater. The EM response can be approximated with an exponential relation to the distance of the sea ice-water interface of either the in-phase or quadrature (out-of-phase) component, parameterized from calibration measurements or 1D forward models. The inverse of the exponential function then directly relates the EM response to the total thickness (snow and sea ice) for the given height of the sensor above the surface layer (Kovacs and Morey, 1991). We refer this method as EMPEX (empirical exponential), according to Pfaffling et al. (2007). This approach has proven to be a robust methodology for empirical sea ice thickness retrieval, but it inherently has to neglect any changes of the sea ice conductivity.

The assumption of a perfectly resistive, single layer of sea ice and snow is is justified in most cases, since the influence of the sea ice conductivity of dry cold level sea ice with typical thicknesses of 1-2 meters is small at the traditionally used frequency range (Pfaffling and Reid, 2009). However, there are cases, where the sea ice conductivity is a desired information for sea ice type classification and even becomes a dominant factor, e.g. for summer melt or the so-called sub-ice platelet layer. The latter is a layer of loose ice crystals (ice platelets) with a bulk conductivity between those of sea ice and ocean water (Rack et al., 2013; Hunkeler et al., 2015), may be located underneath coastal sea ice in Antarctica. Ice platelets originate from supercooled water in cavities below ice shelves and are a main contributor to the local sea ice mass balance. This special sea ice type is currently unmapped, except for sporadic manual measurements (e.g. Hoppmann et al., 2015b).

The sea ice thickness can vary on instrument sub-footprint scales, and not all sea ice structures can be sufficiently described by a 1D geometry approximation within the footprint. The traditional 1D assumption leads to thickness biases for deformed sea ice, partly due to the geometric effect of sub-footprint scale thickness variability (Kovacs et al., 1995; Reid et al., 2003; Pfaffhuber et al., 2012b) and partly due to the intrusion of saline seawater into the sea ice layer (Reid et al., 2006).

Operational needs for in-situ high-resolution sea-ice surveys require a small sensor package that can be towed by foot or snow machine. It is a particular characteristic of such surveys that measurements are taken in a highly conductive environment given that the sensor is usually meters above seawater. The conductivities of sea ice layers we aim to resolve (0.01-0.2 S/m) can be 1 to 2 orders of magnitude smaller than the conductivity of the ocean (e.g. 2.7 S/m). Distances between the sensor and the saline ocean water can easily become smaller than the dimensions of the sensor itself. Previous EM sea ice studies have accounted for sea ice conductivities, such as Pfaffling and Reid (2009), who revealed that the lower frequency (3.68 kHz) of an airborne device is mostly sensitive to

sea ice thickness, while higher frequencies (112 kHz) are needed to resolve sea ice conductivity. However, the difference in conductivity between first-year sea ice (0.05 S/m) and multi-year sea ice (< 0.01 S/m) could not be resolved for sea ice thinner than 2 m. In contrast, Holladay et al. (1998) used airborne EM induction sounding to distinguish between first and multi-year sea ice by using 30 kHz and 90 kHz. Reid et al. (2003) concluded that it is necessary for sea ice thickness retrieval to account for conductive sea ice.

Since empirical analytic approaches for processing single-frequency EM data are insufficient to resolve thickness and conductivity of even a single layer, we assess the prospect of using 1D inversion algorithms on multi-frequency EM data, where (i) conductivity within fixed layers and (ii) conductivity and thickness of sea ice layers are adapted to minimize the difference between the signal response and forward models. In a previous study, Hunkeler et al. (2015) performed case studies with a ground-based device (GEM-2, Geophex Ltd.) at frequencies of 63.03 and 93.09 kHz and a coil spacing of 1.66 m, being able to resolve sea ice conductivities in agreement with estimates from sea ice cores. The assessment of sea ice conductivity in the present study is based on the same small-coil instrument, where 'small coil' refers to transmitter and receiver coils that have small diameters compared to the distance between them. Hence, the magnetic field generated by the transmitter is represented by a magnetic dipole and the measurements at the receiver coil are considered to be point measurements of the magnetic field (Farquharson, 2000). Processing routines of data from such small-coil instruments in highly conductive environments cannot be based on existing algorithms because of a nonlinear signal bias introduced by the passive bucking coil of the instrument. This coil is used to null the primary field at the receiver location and effectively acts as a second receiver. In low conductivity environments, the contribution of this second receiver can safely be approximated by a linear factor and the correction is often integrated in the sensor calibration. However, the contribution of the bucking coils significantly depends on the subsurface conductivity itself (Fitterman, 1998) and needs to be taken into account in the forward model and inversion scheme.

In this study, we use two modified geophysical inversion algorithms that specifically include the bucking coil. We use synthetic data and specific instrumental noise characteristics to run inversions for different thickness and conductivity scenarios as a proof-of-concept for the application to actual field data. We analyze the sensitivity of the inversion results and their success in resolving sea ice thickness and conductivity simultaneously. Finally, the porosity and its uncertainty is estimated from conductivity retrievals.

3.3. Methods

We first describe principles behind multiple frequencies and passive EM bucking, and then review two inversion algorithms with integrated contribution of the bucking coil correction for a small-coil EM instrument.

3.3.1. Multi-frequency measurements with small-coil systems

The quasi-static near-field zone (Spies and Frischknecht, 1991) is defined by the transmitter-receiver distance x_{Rx} being much smaller than the quasi-static plane-wave skin depth δ which is defined as

$$\delta = \sqrt{\frac{2}{\omega\mu\sigma}}, \tag{3.1}$$

where ω is the angular frequency ($\omega = 2\pi f$), μ is the magnetic permeability of free space ($\mu = 4\pi 10^{-7}$H/m) and σ is the conductivity. In the near-field zone using the same transmitter-receiver geometry, measurements at multiple frequencies do not add information over a single-frequency measurement, unless the conductivity shows frequency dependence. To increase the sounding depth, the transmitter-receiver distance has to be increased or the coil orientation has to be changed. The quasi-static transition zone corresponds to measurements with $x_{Rx} \sim \delta$. Compared to measurements in the near-field zone, the sounding depth increases additionally with decreasing frequency (Spies and Frischknecht, 1991). This results in additional information being retrieved using different frequencies.

The lower frequencies considered in our study, i.e. f_1=1.53 and f_2=5.31 kHz, represent measurements in the near-field zone. For instance, for measurements at frequency f_1, the skin depths in seawater (conductivity of 2.7 S/m) and sea ice of 0.2 S/m are $\delta = 7.8$ m and $\delta = 28.8$ m, respectively. Both skin depths are significantly larger than the transmitter-receiver separation of 1.66 m. However, measurements at higher frequencies, i.e. f_3=18.33, f_4=63.03 and f_5=93.09 kHz are effectively in the transition zone. For frequency f_5, $\delta = 1.0$ m and $\delta = 3.6$ m for seawater and sea ice with a conductivity of 0.2 S/m, respectively. This suggests that in highly conductive sea ice environments, soundings can be carried out by varying frequency even at transmitter-receiver separations as small as 1.66 m. Moreover, in our case of a moderately conductive layer being underlain by a highly conductive layer, resolution of layer parameters is generally much better than in the opposite case of a highly conductive layer being underlain by a moderately conductive layer (Spies and Frischknecht, 1991).

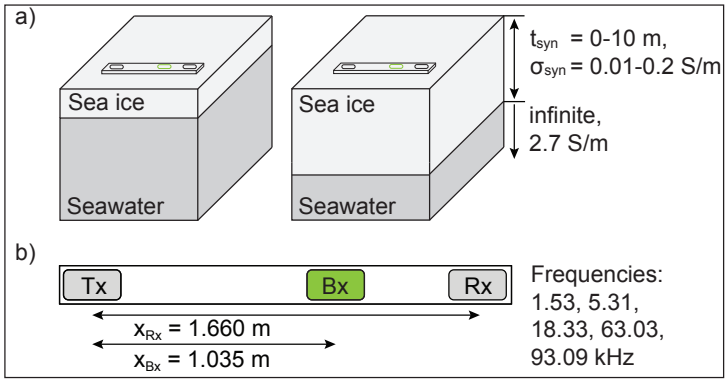

Figure 3.1.: Diagrammatic sketch of multi-frequency EM device on level sea ice. In a) two exemplary stations with different sea ice thicknesses are shown. Synthetic data were calculated by assuming level sea ice thicknesses t_{syn} from 0-10 m in increments of 0.1 m and conductivities σ_{syn} of 0.01, 0.05, 0.10, 0.15 and 0.20 S/m. In b) the internal coil configuration and frequencies used for calculation of synthetic data are shown, x_{Rx} and x_{Bx} are the distances from the transmitter (Tx) to the receiver (Rx) and bucking coil (Bx), respectively. The bucking coil is used to null the primary field at the receiver location. Algorithms needed to be modified for a nonlinear bucking bias arising from measurements in highly conductive regimes.

3.3.2. Passive EM bucking

Current EM induction instruments operate at single to multiple discrete frequencies. A typical EM instrument consists of three coils (Figure 3.1): transmitter coil (Tx), bucking coil (Bx) and receiver coil (Rx). The transmitter coil generates a primary magnetic field, inducing a secondary magnetic field in a conductive subsurface. The signal strength of this secondary field depends, amongst other things, on the distance from the instrument to a body and its conductivity. During a survey, the receiver coil records the superposition of the primary and secondary magnetic fields minus the bucking field.

The purpose of a bucking coil is to null the primary field at the receiver, which also avoids receiver saturation, and increases the dynamic range of the instrument (Won et al., 2003). It is connected in series and in opposite polarity to the receiver coil and technically acts as a second receiver. In free space the bucking coil measures the same absolute primary field signal as does the receiver coil when the following relation according to Won et al. (2003) is valid:

$$\frac{A_{Rx} n_{Rx}}{x_{Rx}^3} = \frac{A_{Bx} n_{Bx}}{x_{Bx}^3}, \tag{3.2}$$

where x_{Bx} is the distance between Tx and Bx, x_{Rx} is the distance between Tx and Rx and A and n are the area and number of turns of the respective coil. Typically x_{Bx} and x_{Rx}

are in the order of 1-4 m, e.g., one particular commercial realization has $x_{Bx} = 1.035$ m and $x_{Rx} = 1.66$ m, and accommodates simultaneous operation of 0.3-96 kHz. The bucking coil, which is assumed to be linearly sensitive to the conductive subsurface, compensates internally for the primary field at the receiver location. However, in the seawater environment, the response of the bucking coil to the secondary field is nonlinear, leading to an overcorrection of the receiver signal depending on the conductivity structure of the subsurface (Fitterman, 1998). Hunkeler et al. (2015) accounted for this so-called bucking bias by modifying forward modeled data according to

$$\mathbf{d} = \mathbf{d}_{Rx} - \mathbf{d}_{Bx} = (\mathbf{I}_{Rx} + i\mathbf{Q}_{Rx}) - (\mathbf{I}_{Bx} + i\mathbf{Q}_{Bx}), \tag{3.3}$$

where $\mathbf{d}$ is the signal response at the receiver ($\mathbf{d}_{Rx}$) and bucking coil ($\mathbf{d}_{Bx}$) location. These signals can also be expressed as a complex number with real (in-phase I) and imaginary parts (quadrature Q), where I and Q are dimensionless and are measured in ppm (parts per million). An alternative representation of the signal is by its amplitude $A = \sqrt{I^2 + Q^2}$ and phase $\varphi = \arctan(Q/I)$. Hunkeler et al. (2015) achieved a satisfying agreement between field data and corrected forward modeled data by applying coefficients obtained from calibration experiments. In this study, we build upon these findings to implement the bucking coil directly into two different inversion algorithms.

3.3.3. Inverse modeling

The aim of an inversion algorithm is to find a plausible model (usually the simplest) which adequately fits the observed data within the data uncertainty (Farquharson et al., 2003). The process consists of two components: forward modeling and inversion. Forward modeling generates the data of a specific model; inversion automatically changes the model to reduce the misfit between measured and forward modeled data (Menke, 1989). We tested two inversion algorithms to resolve synthetic data of homogeneous sea ice for different thicknesses and conductivities. Forward modeling and inversion calculations were performed in 1D. We stitched the 1D inversion results of individual stations together, which results in a 2D impression. With the first algorithm (EM1DFM, Farquharson, 2000; Farquharson et al., 2003), we only inverted for the conductivity within fixed layers of 0.1 m thickness, using vertical smoothing between layers. We call this inversion algorithm throughout the manuscript smoothness-constrained inversion. Since a vertical conductivity smoothing is not ideal in the case of a sharp sea ice-seawater interface, we applied a second algorithm, the Marquardt-Levenberg inversion (Jupp and Vozoff, 1975; Lines and Treitel, 1984). With only two distinct instead of many individual

layers and with sea ice thickness as an additional free parameter, this scheme may better reflect reality. In our study we used the Marquardt-Levenberg inversion algorithm from EMILIA (Electro Magnetic Inversion with Least Intricate Algorithms, Kalscheuer et al., 2010, 2012; Grab, 2012).

Smoothness-constrained inversion (EM1DFM)

The inversion problem is ill-posed and nonlinear. Therefore we derived at each iteration n a linearized approximation by searching for a change in the conductivity model which minimize the cost function

$$\Phi^n = \phi_d^n + \beta^n \phi_m^n, \tag{3.4}$$

where ϕ_d is the data misfit, β is the trade-off parameter and ϕ_m is the model-structure component (Farquharson et al., 2003). The data misfit ϕ_d is calculated according to Farquharson et al. (2003) by the l_2-norm

$$\phi_d^n = \|\mathbf{W}_d(\mathbf{d}^n - \mathbf{d}_{syn})\|^2, \tag{3.5}$$

where $\mathbf{d}_{syn}$ are the synthetic EM data. $\mathbf{d}^n$ are the forward-modeled data for the model $\mathbf{m}^n$ of the n^{th} iteration, where $\mathbf{d}^n$ is defined as the nonlinear forward operator $\mathbf{F}[\mathbf{m}^n]$. By accounting for the bucking bias, $\mathbf{d}_{syn}$ and $\mathbf{d}^n$ need to be modified according to Equation 3.3. $\mathbf{W}_d$ is a diagonal weighting matrix. For the bucking coil quantification (experiment 1, see below), $\mathbf{W}_d$ includes the reciprocal value of one percent of the synthetic data. For the synthetic modeling studies (experiments 2-4, see below), $\mathbf{W}_d$ includes the reciprocal standard deviations of the data, which were calculated from 30 minutes of free-air recordings of noise at each frequency for both in-phase and quadrature components (Hunkeler et al., 2015).

The model-structure component in Equation 3.4 is defined by

$$\phi_m^n = \alpha_s \|\mathbf{W}_s \mathbf{m}^n\|^2 + \alpha_z \|\mathbf{W}_z \mathbf{m}^n\|^2, \tag{3.6}$$

where $\mathbf{m}$ is the model vector of the logarithms of the layer conductivities and α_s (= 0.05) and α_z (= 1) are scaling coefficients. The diagonal matrix $\mathbf{W}_s$ contains elements which are equal to the square roots of the individual layer thicknesses (= 0.1 m). The matrix $\mathbf{W}_z$ is a first-order finite-difference operator. The rows are scaled by the reciprocals of the square roots of half the distance between the centers of two layers (Farquharson et al., 2003). The left term in Equation 3.6 quantifies the deviation from a reference model of 1 S/m and the right term the roughness of the model. Since α_s is significantly smaller

than α_z, the right term dominates the model-structure component.

The trade-off parameter β (Equation 3.4) is a parameter which determines the balance between the data misfit and the model-structure component and is responsible to fit the observed data closely, whereas the constructed model should be as simple as possible (Farquharson et al., 2003). The noise is well known and therefore we adjusted β with a univariate search until the misfit ϕ_d matches a pre-defined target misfit in every iteration n. This is the maximum of the number of calculated responses N_d=10 (in-phase and quadrature for the five frequencies), or equal to $0.5\phi_d^{n-1}$, in order to allow only small changes in model structure at each iteration (discrepancy principle, Farquharson, 2000). In case the target misfit cannot be reached, the inversion algorithm searches for the smallest misfit.

The new model $\mathbf{m}^n$ is calculated from the previous model $\mathbf{m}^{n-1}$ by

$$\mathbf{m}^n = \mathbf{m}^{n-1} + \upsilon\delta\mathbf{m}^n, \tag{3.7}$$

where $\delta\mathbf{m}$ is the model update step and υ is the step length, which is halved when the cost function (Equation 3.4) does not immediately decrease. To find the model update step $\delta\mathbf{m}$, Equation 3.4 is differentiated with respect to $\delta\mathbf{m}$, set equal to zero and solved by a least-square approach for $\delta\mathbf{m}$ (Paige and Saunders, 1982; Farquharson et al., 2003). By doing so, the forward modeled data $\mathbf{d}^n$ in Equation 3.5 are approximated in the derivation of the inversion algorithm by

$$\mathbf{d}^n \approx \mathbf{d}^{n-1} + \mathbf{J}^{n-1}\delta\mathbf{m}^n, \tag{3.8}$$

where $\mathbf{J}$ is the Jacobian matrix of sensitivities (Farquharson and Oldenburg, 1996). $\mathbf{J}$ consists of the partial derivatives of the data with respect to the model parameters (logarithms of conductivities, σ) for the j^{th} layer and i^{th} station:

$$J_{ij}^n = \frac{\partial d_{Rx,i}}{\partial \log\sigma_j^n} - \frac{\partial d_{Bx,i}}{\partial \log\sigma_j^n}, \tag{3.9}$$

where d is the signal response at the receiver coil (d_{Rx}) and bucking coil (d_{Bx}) locations. These sensitivities quantify how the forward modeled data are affected by changing the conductivity of each layer (Farquharson and Oldenburg, 1993). The second term in Equation 3.9 is not required if the bucking coil modification is to be ignored.

To evaluate the compatibility of the new model $\mathbf{m}^n$ with the field data, the full forward response $\mathbf{d}^n = \mathbf{F}[\mathbf{m}^n]$ is then used to calculate ϕ_d (not approximation in Equation 3.8). The convergence of the inversion algorithm is determined using two convergence criteria

according to Gill et al. (1981) and Farquharson (2000).

To assess how well synthetic data for a constructed model fit the measured data, we calculated the root-mean square error (RMSE)

$$\mathrm{RMSE} = \sqrt{\frac{1}{N_d}\phi_d}. \tag{3.10}$$

An inversion with RMSE close to 1 is considered reliable without fitting too much to noise (Kalscheuer et al., 2013).

Marquardt-Levenberg inversion (EMILIA)

The Marquardt-Levenberg algorithm of EMILIA was recently modified to account for the bucking-coil bias by implementation of Equations 3.3 and 3.9 (Kaufmann, 2014). The cost function Φ is similar to Equation 3.4. The quantity ϕ_d is defined in a similar manner to Equation 3.5 (more below). The quantity β governs the magnitude of the damping and specifies the confidence in the previous model (damping factor). The quantity ϕ_m is now defined as

$$\phi_m^n = \|(\mathbf{m}^n - \mathbf{m}^{n-1})\|^2 \tag{3.11}$$

for the nth iteration. Since the difference between the new model $\mathbf{m}^n$ and the previous model $\mathbf{m}^{n-1}$ is limited, the inversion result is influenced by the starting model. The starting model is the first assumed subsurface model with defined thicknesses and conductivities of sea ice and underlying seawater, which is adapted during the inversion process. The RMSE is calculated according to Equation 3.10, where for RMSE > 1 a line search is performed for β and the model is adapted accordingly (Kalscheuer et al., 2013). In order to improve sea ice thickness results from the Marquardt-Levenberg inversion, we weighted the data misfit ϕ_{dw} according to Kalscheuer et al. (2013):

$$\phi_{dw}^n = \|\frac{\mathbf{W}_d(\mathbf{d}^n - \mathbf{d}_{syn})}{w}\|^2, \tag{3.12}$$

where the weight factor w, obtained from normalized synthetic data of one frequency and one component, decreases exponentially for different stations, but is kept constant as the iterations proceed. Small values of w were assigned to stations of thick sea ice to increase their weights. The misfit ϕ_{dw} is normalized by the sum of the squared weight factor w^2 to achieve the intended weighted RMSE (RMSE$_w$) of 1

$$\mathrm{RMSE}_w = \sqrt{\frac{w^2}{N_d}\phi_{dw}}, \tag{3.13}$$

where ϕ_{dw} is the weighted data misfit and N_d the number of calculated responses.

3.3.4. Most-squares inversion

For sensitivity calculations, we applied to some of our 2-layer Marquardt-Levenberg inversions a model error and resolution analysis. This method is based on the truncated singular value decomposition (TSVD) of the sensitivity matrix (Kalscheuer and Pedersen, 2007). Since the effective number of model parameters is two (conductivity σ and thickness t of sea ice), the truncation level of the TSVD was set to two in the analyses of these models. Due to the very limited number of model parameters, both layer parameters are perfectly resolved. Hence, in assessing how well the layer parameters are constrained, only the model parameter uncertainties need to be further considered.

To partly account for the nonlinearity of the inversion problem, we computed error estimates for the final inversion models using most-squares inversion (Jackson, 1976; Meju and Hutton, 1992; Meju, 1994). A most-squares inversion is an iterative method that determines, starting from the least-squares inversion results, bounding model values which represent the variability of the model parameters. Hence, most-squares inversion assess the stability of model parameters (Meju and Hutton, 1992). Owing to the logarithmic transformation of model parameters during inversion, the most-squares errors $1/f^{-}_{MSQ}$ and f^{+}_{MSQ} correspond to parameter ranges $\sigma/f^{-}_{MSQ}, \ldots, f^{+}_{MSQ} \cdot \sigma$ and $t/f^{-}_{MSQ}, \ldots, f^{+}_{MSQ} \cdot t$ of layer conductivities and thicknesses, respectively. Hence, a model parameter is well constrained with most-squares errors close to 1.

3.3.5. Synthetic data

To test the inversion algorithms, we used synthetic datasets for the in-phase and quadrature components, calculated by a 1D forward model using the implementation of Anderson (1979). We calculated two different types of synthetic datasets: (i) neglecting ($\mathbf{d}_{syn}$=$\mathbf{d}_{Rx}$); and (ii) accounting ($\mathbf{d}_{syn}$=$\mathbf{d}_{Rx}$-$\mathbf{d}_{Bx}$) for the bucking coil correction according to Equation 3.3. One dataset includes 101 stations, where the sea ice was increased from 0 to 10 m from one station to the next in increments of 0.1 m. These true thicknesses are hereinafter referred to as t_{syn}. Two exemplary stations are illustrated in Figure 3.1a, where a snow layer was neglected. We used typical conductivities σ_{syn} of different sea ice types between 0.01 and 0.2 S/m (Hunkeler et al., 2015) and a homogeneous half-space conductivity of 2.7 S/m, representing seawater. In-phase and quadrature responses were calculated at frequencies of 1.53, 5.31, 18.33, 63.03 and 93.09 kHz, a setup also used during surveys on sea ice (Hunkeler et al., 2015). For this proof-of-concept of the bucking coil implemen-

tation we did not account for any noise of the instrument (experiment 1). To simulate realistic data, we added Gaussian noise (corresponding to one standard deviation) to the in-phase and quadrature components, based on the free-air response for the respective frequencies (experiments 2-4). The assumed standard deviations between 125 and 204 ppm were calculated in an earlier study by Hunkeler et al. (2015), where higher frequencies showed higher instrumental noise. The synthetic data from the implementation of Anderson (1979) were compared to data forward modeled by the inversion algorithms considered here. The datasets computed by all three programs differed only by a few ppm, which is well within the noise level of the instrument.

3.4. Results

We applied the two inversion algorithms to synthetic data. We first identify the impact of the bucking coil on the performance of the EM1DFM inversion (experiment 1). We then investigate whether multi-layered, Marquardt-Levenberg inversions are able to reliably reproduce t_{syn} and σ_{syn} (experiments 2-4).

3.4.1. Experiment 1: Influence of bucking coil

We used two synthetic datasets, with and without bucking bias, and two versions of EM1DFM, ignoring and considering the bucking bias. We tested the following three scenarios: (i) bucking bias neither in the data nor considered in EM1DFM, (ii) bucking bias in the data but not considered in EM1DFM, and (iii) bucking bias in the data and considered in EM1DFM. For all calculations we used $\sigma_{syn} = 0.1$ S/m, a seawater conductivity of 2.7 S/m, and t_{syn} of 0-10 m. For the starting model, we assigned to all stations 1 m thick sea ice with conductivities of 0.05 S/m and 2.7 S/m to the underlying sea water. We allowed a maximum of 40 iterations and set the uncertainties in $\mathbf{W}_d$ to one percent of the synthetic data.

For the first scenario, the RMSE (Equation 3.10) was, for most inversions, close to one and RMSE > 2 was found for only three stations (Figure 3.2a). Although the level of agreement between inversion results and the synthetic data was generally good, an accurate determination of sea ice thickness from these stations was difficult, because conductivities varied little between vertically adjacent layers, resulting in a smooth conductivity transition between sea ice and seawater. This transition zone from sea ice to seawater conductivities was small for thinner sea ice ($t_{syn} < 4$ m, white steps in Figures 3.2a-c), but widened towards thicker sea ice (3 m for $t_{syn} = 10$ m). Apart from this variable transition

zone, σ_{syn} of 0.1 S/m (yellow in Figure 3.2a) and seawater conductivity of 2.7 S/m (blue in Figure 3.2a) were reasonably reproduced.

We used for the second scenario the same setup as for the first scenario, and included the bucking bias in the synthetic data (Equation 3.3, Figure 3.2b), but not in the inversion algorithm. The algorithm completely failed to reproduce the data for $t_{syn} < 0.5$ m, where high RMSE values indicated that the target misfit was often not achieved. For t_{syn} between 0.5 and 1 m, the algorithm added an additional conductive layer close to the surface. Between 0.5 and 10 m, the transition zone was approximately 1 m too deep compared to t_{syn}. σ_{syn} of 0.1 S/m was only rarely reproduced, with sea ice conductivity in individual fixed layers being either too high (approximately 0.3 S/m, red in Figure 3.2b) or too low (close to 0 S/m, white in Figure 3.2b). For $t_{syn} > 5$ m, the algorithm added a conductive layer in the middle of the too resistive sea ice.

For the third scenario, we used the modified synthetic data from the second scenario together with the modified EM1DFM inversion algorithm (Equations 3.3 and 3.9). The results (Figure 3.2c) showed a substantial improvement over the second scenario (Figure 3.2b), where the RMSE and the resolved sea ice thickness and conductivity were comparable to those from the first scenario. For $t_{syn} < 0.5$ m, conductivities similar to the underlying seawater indicate that σ_{syn} could not be resolved.

For all further experiments, we included the bucking coil in the synthetic data and inversions.

3.4.2. Experiment 2: Smoothness-constrained inversion

In a second experiment, we used synthetic data with added Gaussian noise and with σ_{syn} of 0.01, 0.05, 0.1 and 0.2 S/m. For each sea-ice conductivity σ_{syn}, we calculated the EM response for thicknesses t_{syn} from 0 to 10 m. The starting model contained for each station 3 m of 0.05 S/m (sea ice) and an underlying homogeneous half-space of 2.7 S/m (seawater). The data uncertainty was set to the standard deviation of the noise and a maximum of 40 iterations were allowed. At all stations, the algorithm stopped before 40 iterations, because convergence to the target misfit was reached, convergence to a minimum was reached, or no suitable model update step was found.

The results of the four scenarios generally showed a good agreement with the synthetic data (Figure 3.3). The number of stations for which the target misfit could not be achieved were 3, 19, 31 and 29 for σ_{syn} of 0.01, 0.05, 0.1 and 0.2 S/m, respectively. For all inversions, the first two stations with t_{syn} of 0 and 0.1 m showed high RMSE values (> 2). Nevertheless, for stations with RMSE < 2, sea ice thickness was reasonably resolved for all four scenarios, but the transition zone between sea ice and seawater conductivity became

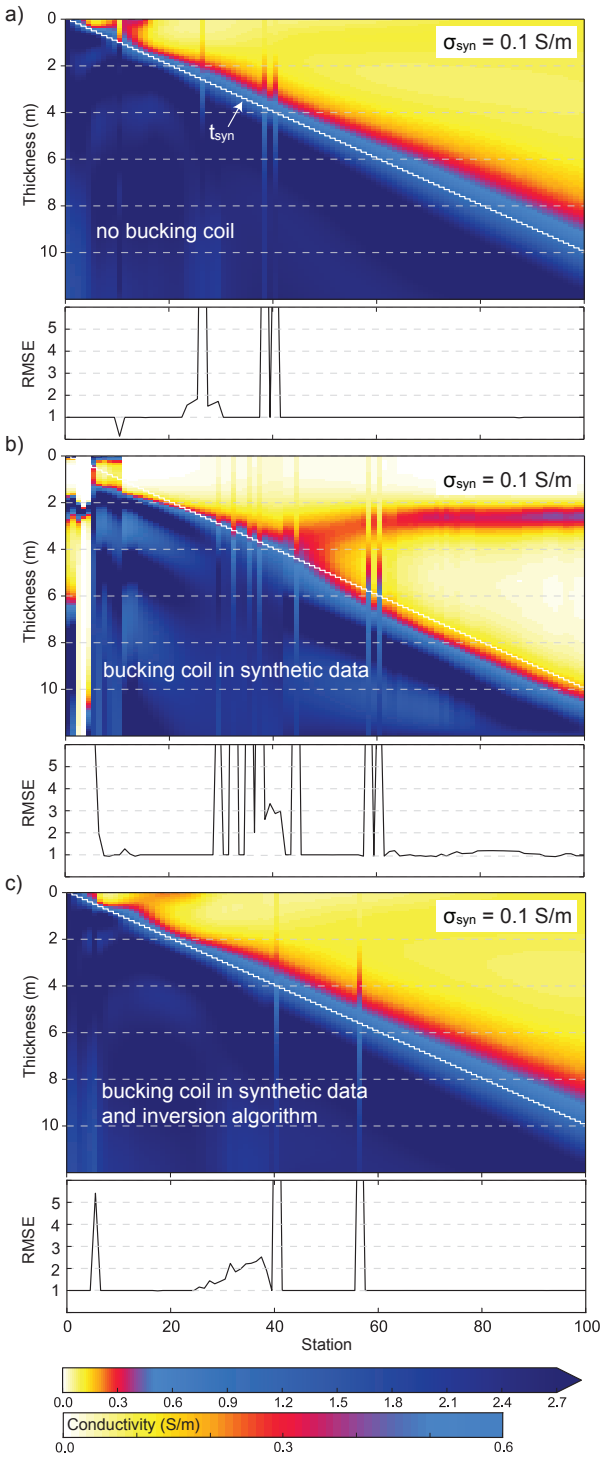

Figure 3.2.: Influence of the bucking bias on sea ice thickness and conductivity retrieval (experiment 1). Each station represents a smoothness-constrained 1D inversion result (EM1DFM). The bucking-coil modification was applied to a) neither synthetic data nor inversion (scenario s1); b) only synthetic data (scenario s2); c) synthetic data and inversion (scenario s3). The colored regions show the resulting conductivities, from which we infer the sea ice thickness. σ_{syn} of 0.1 S/m, seawater conductivity of 2.7 S/m and t_{syn} (white steps) were reproduced best for scenarios s1 and s3. Below each scenario the RMSE is shown for all stations. The target misfit was reached when RMSE = 1.

broader for higher σ_{syn}. At station 30 with 3 m thick sea ice for example, the zone was for $\sigma_{syn} = 0.01$ S/m only 0.5 m (Figure 3.3a), whereas for $\sigma_{syn} = 0.2$ S/m it was 1 m wide (Figure 3.3d). The resulting sea ice conductivity was also more uniform for low σ_{syn} (Figure 3.3a), compared to the patchy conductivity results from higher σ_{syn} (Figure 3.3d). However, the sea ice conductivities were clearly distinguishable for the individual scenarios and can be resolved well within 0.05 S/m using EM1DFM.

For each of the four scenarios we obtained after the last iteration ten Jacobian matrices of sensitivities (Equation 3.9) from the five frequencies and both components (in-phase and quadrature). Each Jacobian matrix includes entries at every station in each layer for the respective scenario. In order to provide a quantified reliability estimate, we normalized all entries of the Jacobian matrices by the respective forward modeled data $\mathbf{d}$, which were obtained after the last iteration. From the calculated normalized Jacobian matrices we selected for each layer the maximum of the ten entries. Here we show for each scenario the resulting 0.5%, 1% and 2% contour lines, along with the four resulting reliability areas (shaded areas in Figure 3.3). Small values of normalized Jacobian matrices indicate that a change in the conductivity barely affects the forward modeled data (Farquharson and Oldenburg, 1993), hence we trust regions with high sensitivities most.

3.4.3. Experiment 3: Marquardt-Levenberg inversion and most-squares inversion

We inverted the same synthetic data used in the second experiment (including Gaussian noise) by the Marquardt-Levenberg algorithm. The data uncertainty was again set to the standard deviation of the noise, and we used a starting model for each station of 0.05 S/m for the upper 3 m (sea ice) and 2.7 S/m for the homogeneous half-space below (seawater). The latter was fixed during this inversion since seawater conductivity is usually known and can be determined with tight bounds by sampling through boreholes. In the Eastern Weddell Sea, for example, the seawater conductivity ranged from 2.686 to 2.718 S/m over a time period of roughly three months (Hunkeler et al., 2015) and is usually assumed to be constant during a survey period. Tests showed that the Marquardt-Levenberg inversion performed considerably worse when allowing for a free seawater conductivity. Therefore only sea-ice thickness t and sea-ice conductivity σ were allowed to vary during a maximum of 300 iterations.

After the maximum of iterations was reached, t was for $t_{syn} < 5$ m well resolved for all four scenarios (Figure 3.4). The RMSE was generally higher for thicker sea ice compared to thinner sea ice in all scenarios. Most stations with a high RMSE were found for sea ice

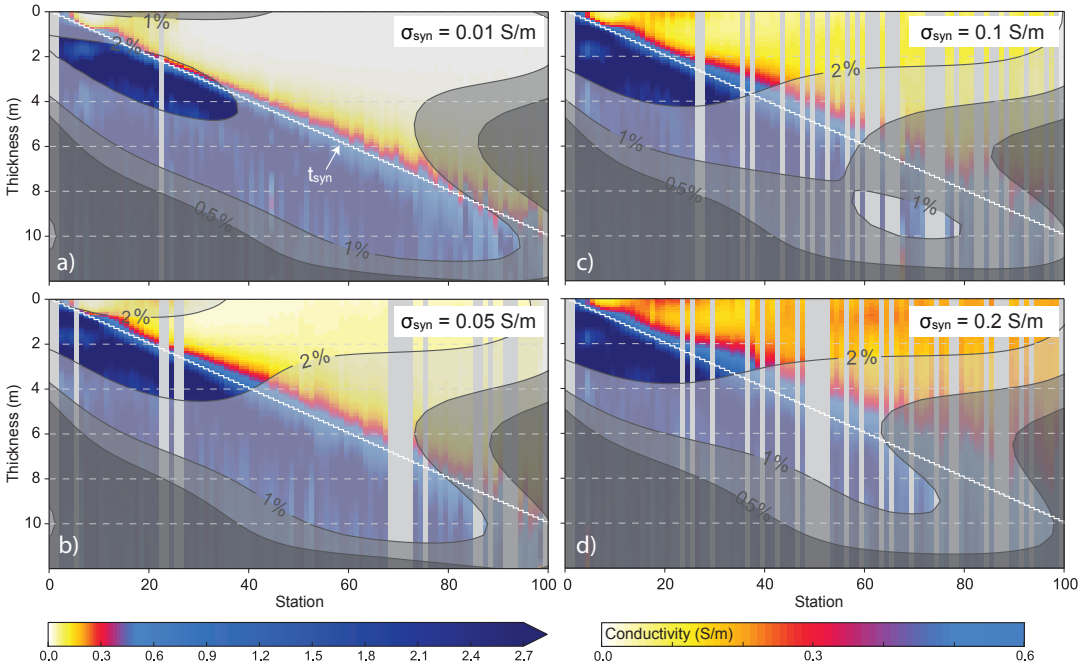

Figure 3.3.: Results of smoothness-constrained inversions (EM1DFM, experiment 2). Each station represents a 1D inversion result. The colored regions show the resulting conductivities, from which we infer the sea ice thickness. σ_{syn} of a) 0.01, b) 0.05, c) 0.1, and d) 0.2 S/m, and seawater conductivity of 2.7 S/m were reproduced for all scenarios. Because of vertical smoothing, sea ice thickness can be approximated within a transition zone, which becomes broader for higher t_{syn} (white steps) and σ_{syn}. Four reliability areas from normalized Jacobian matrices are indicated with contour areas, below 0.5%, between 0.5 and 1%, between 1 and 2%, and above 2% which is considered to be a high sensitivity. Stations with high RMSE (> 2) were covered by a gray bar to highlight the reliable inversion results. Highest RMSE values were obtained for $\sigma_{syn} = 0.2$ S/m.

conductivity σ_{syn} of 0.2 S/m, where approximately half of the stations contained a RMSE > 1 (Figure 3.4d). The lowest values of RMSE and accurately recovered t (for $t_{syn} < 7$ m) were found for the inversions with $\sigma_{syn} = 0.05$ S/m, which is also the conductivity defined in the starting model (Figure 3.4b).

To quantify these findings, we compared the inversion results (plus results with $\sigma_{syn} = 0.15$ S/m) to t_{syn} (Figure 3.5a, scenarios s1-s5). The best resolved sea ice thickness t was found, as stated before, for $\sigma_{syn} = 0.05$ S/m (s2). However, t was generally reasonable reproduced for all scenarios $t_{syn} < 5$ m.

For comparison to resulting sea ice thickness t, we calculated thicknesses with the EMPEX approach. For the latter, we used the 5310 Hz in-phase forward responses, added Gaussian noise and fitted a single-exponential curve through the data (in-phase response

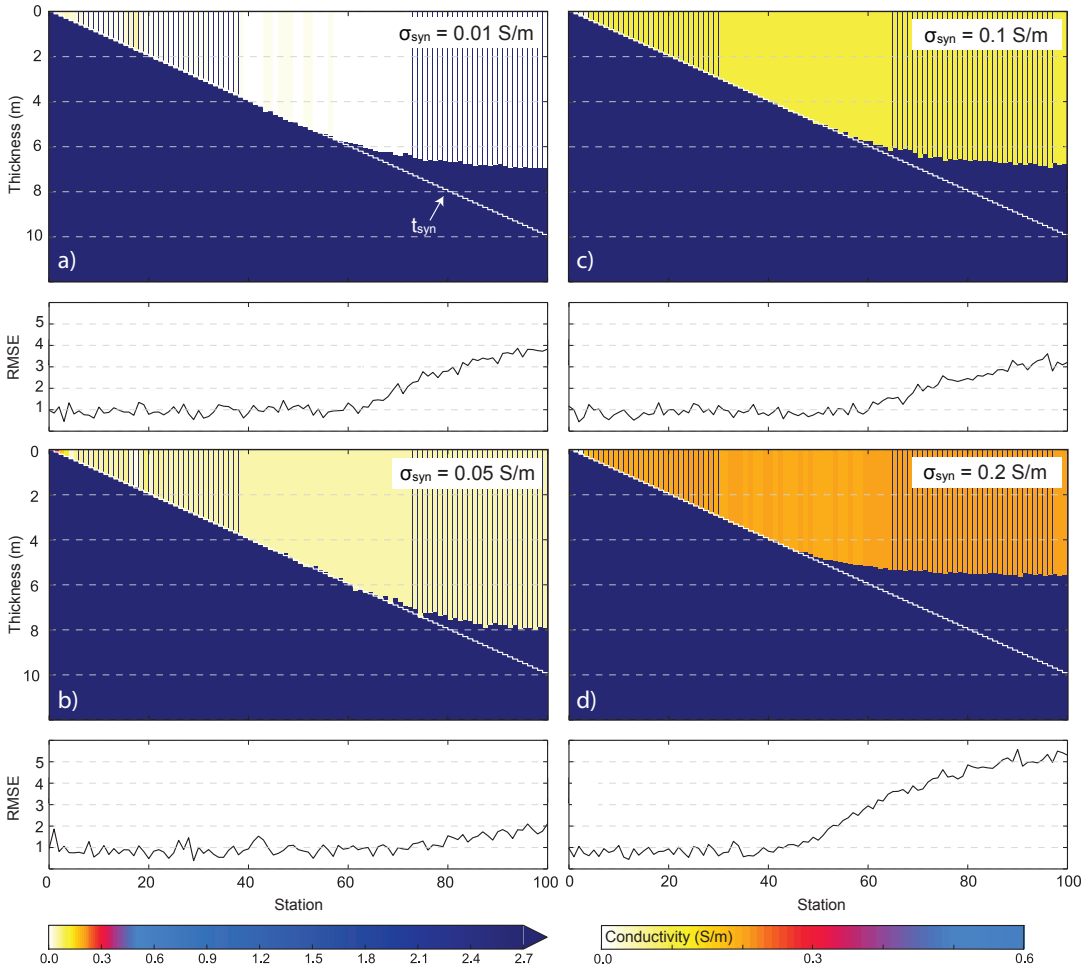

Figure 3.4.: Results of sea ice thickness t and conductivity σ from Marquardt-Levenberg inversions (experiment 3). Each station represents a 1D inversion result. The colored regions show the resulting conductivities σ, from which we directly obtain the sea ice thickness t. σ_{syn} of a) 0.01, b) 0.05, c) 0.1, and d) 0.2 S/m were reproduced for all four scenarios. t_{syn} (white steps) were better reproduced for a), b) and c) compared to d). Below each scenario the RMSE is shown for individual stations, where the RMSE increases in all scenarios with higher t_{syn}, which causes smaller signal responses.

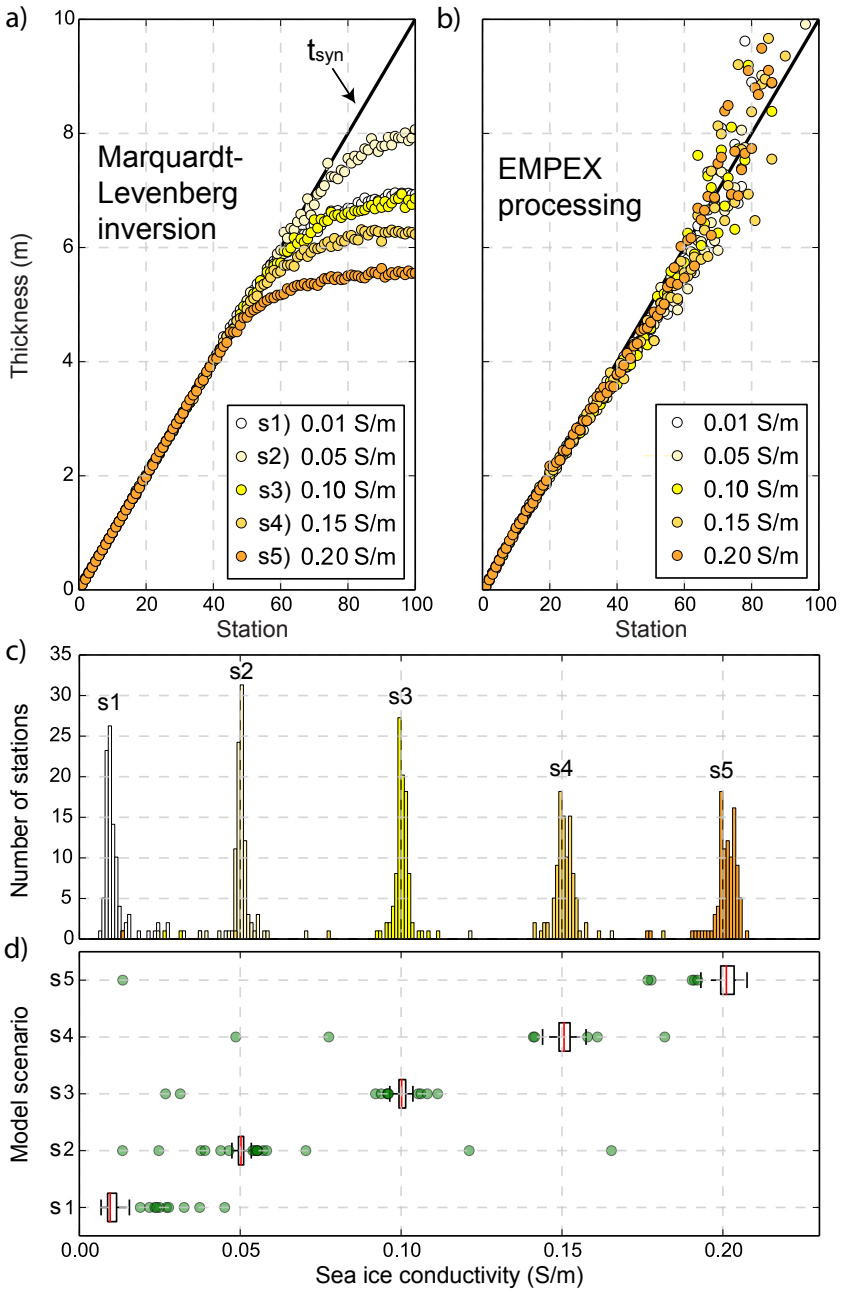

Figure 3.5.: Validation of sea ice thickness t and conductivity σ from a) Marquardt-Levenberg inversions (experiment 3), and b) classical single-frequency processing (EMPEX) using the in-phase 5310 Hz component. In a) and b) t is compared to t_{syn} of 0-10 m. The Marquardt-Levenberg inversions underestimated t at stations of thick sea ice ($t_{syn} > 5$ m) for all scenarios with σ_{syn} of 0.01 (s1), 0.05 (s2), 0.10 (s3), 0.15 (s4), and 0.20 (s5) S/m. σ_{syn} is compared to σ obtained from the scenarios s1-s5, illustrated with histograms in c) and box plots in d). Excluding the outliers, σ can be resolved within $\pm$ 0.01 S/m, independent from t.

vs. sea ice thickness). This curve fit represents the exponential function which is normally calculated from calibration measurements in the field. We used the in-phase component because it is more sensitive to deeper structures, and is monotonically decreasing with thickness in contrast to the quadrature component. The noise of the data was larger than the changes of the exponential function for thick sea ice with low signal responses. Hence, large sea ice thicknesses were poorly constrained. Because the exponential function was not approaching zero, a corresponding sea ice thickness could not always be found for low signal responses and sea ice > 8 m (Figure 3.5b).

In general, sea ice thickness t was underestimated with the Marquardt-Levenberg inversion, but overestimated with the calculated exponential function. With both methods reliable results were found for sea ice < 5 m. For thicker sea ice, the Marquardt-Levenberg inversion depends on σ_{syn}, on the starting model and the weighting of the data (more below). The sea ice thickness determination by the exponential approach did not depend on sea ice conductivity, because we calculated the exponential fit from the respective in-phase components.

The sea ice conductivity σ, however, could be resolved for scenarios s1-s5 (Figure 3.5a). Figure 3.5c shows distributions of σ, where individual histograms are clearly separated. For the scenario with the best resolved sea ice thickness t (s2), the narrowest conductivity distribution was found (0.05 S/m in Figure 3.5c). For scenarios s1-s5, the interquartile ranges of σ were within 0.01 S/m (Figure 3.5d).

In Table 3.1, we present the estimated model errors from most-squares inversion of the Marquardt-Levenberg inversion models for stations 11 and 31 (t_{syn} of 1 m and 3 m) for σ_{syn} of 0.05, 0.1 and 0.2 S/m (cf. Figures 3.4 and 3.5a). While the sea ice thicknesses t for station 11 were tightly constrained with $1/f^{-}_{MSQ} = 0.99$ and $f^{+}_{MSQ} = 1.01$ for all three cases, the sea ice conductivities σ showed more variability with $1/f^{-}_{MSQ}$ and f^{+}_{MSQ} varying from 0.92 to 0.99 and from 1.02 to 1.20, respectively. Similar results were found for thicker sea ice (station 31) with $1/f^{-}_{MSQ}$ between 0.97 and 0.99 and f^{+}_{MSQ} between 1.01 and 1.02 for t. σ showed again more variability with $1/f^{-}_{MSQ}$ between 0.95 and 0.97 and f^{+}_{MSQ} between 1.01 and 1.09. These results were not unexpected, because the thickness of a resistive layer is typically better constrained than its conductivity from inductive EM methods (e.g. Pfaffling and Reid, 2009). Similarly, the increase in error with increasing thickness is consistent. σ is better constrained for higher σ_{syn}, whereas the most-squares errors of σ are larger for thinner sea ice. Generally, all errors are very low and all parameters are well constrained, because only two model parameters are considered.

Table 3.1.: Error estimates for sea ice conductivities σ and thicknesses t of the 2-layer Marquardt-Levenberg models for stations 11 and 31 in Figures 3.4 and 3.5a. Error estimates $1/f^{-}_{MSQ}$ and f^{+}_{MSQ} were computed using most-squares inversions involving truncated singular value decomposition with a truncation level $p = 2$, the effective number of model parameters. A model parameter is well constrained with most-squares errors close to 1.

Parameter	$\sigma_{syn} = 0.05$ S/m		$\sigma_{syn} = 0.1$ S/m		$\sigma_{syn} = 0.2$ S/m	
	$1/f^{-}_{MSQ}$	f^{+}_{MSQ}	$1/f^{-}_{MSQ}$	f^{+}_{MSQ}	$1/f^{-}_{MSQ}$	f^{+}_{MSQ}
station 11						
σ	0.95	1.20	0.92	1.03	0.99	1.02
t	0.99	1.01	0.99	1.01	0.99	1.01
station 31						
σ	0.97	1.09	0.95	1.02	0.96	1.01
t	0.99	1.02	0.98	1.01	0.97	1.01

Table 3.2.: Number of iterations and total RMSE of scenarios from Figure 3.6. The starting model contained sea ice conductivities σ_{start} of 0.05, 0.1 or 0.2 S/m. Scenarios s1-s3: starting model with 3 m thick sea ice and underlying homogeneous half-space of 2.7 S/m for all stations. Scenarios s4-s6: same starting model as for scenarios s1-s3, but weighted synthetic data. Scenarios s7-s9: starting model with sea ice thicknesses from single-frequency EMPEX processing.

	Scenarios s1-s3		Scenarios s4-s6		Scenarios s7-s9	
σ_{start}	RMSE	iterations	RMSE	iterations	RMSE	iterations
0.05 S/m	1.74	300	0.99	104	1.04	300
0.1 S/m	1.87	300	0.99	58	1.04	300
0.2 S/m	1.80	300	1.16	300	1.10	300

3.4.4. Experiment 4: Marquardt-Levenberg inversion

In order to quantify the effect of a priori information, we inverted synthetic data (σ_{syn} of 0.1 S/m and t_{syn} = 0-10 m) with different starting models and data weighting.

In a first step, the dataset was inverted in a similar manner to experiments 2 and 3. We varied the starting model (Figure 3.6a), by using for each station 3 m thick sea ice, σ_{syn} of 0.05 (s1), 0.1 (s2) and 0.2 S/m (s3) and a homogeneous half-space of 2.7 S/m. The starting model did not have a strong influence on sea ice thickness t, where $t_{syn} < 6$ m was reliably reproduced from all conductivities in the starting model (Figure 3.6a). But even after 300 iterations, the RMSE did not reach 1 (scenarios s1-s3 in Table 3.2 with RMSE values of 1.74-1.87).

In a second step, we used the same starting model as in scenarios s1-s3, but weighted the data misfit according to Equation 3.12. We calculated the weight factors w by using the

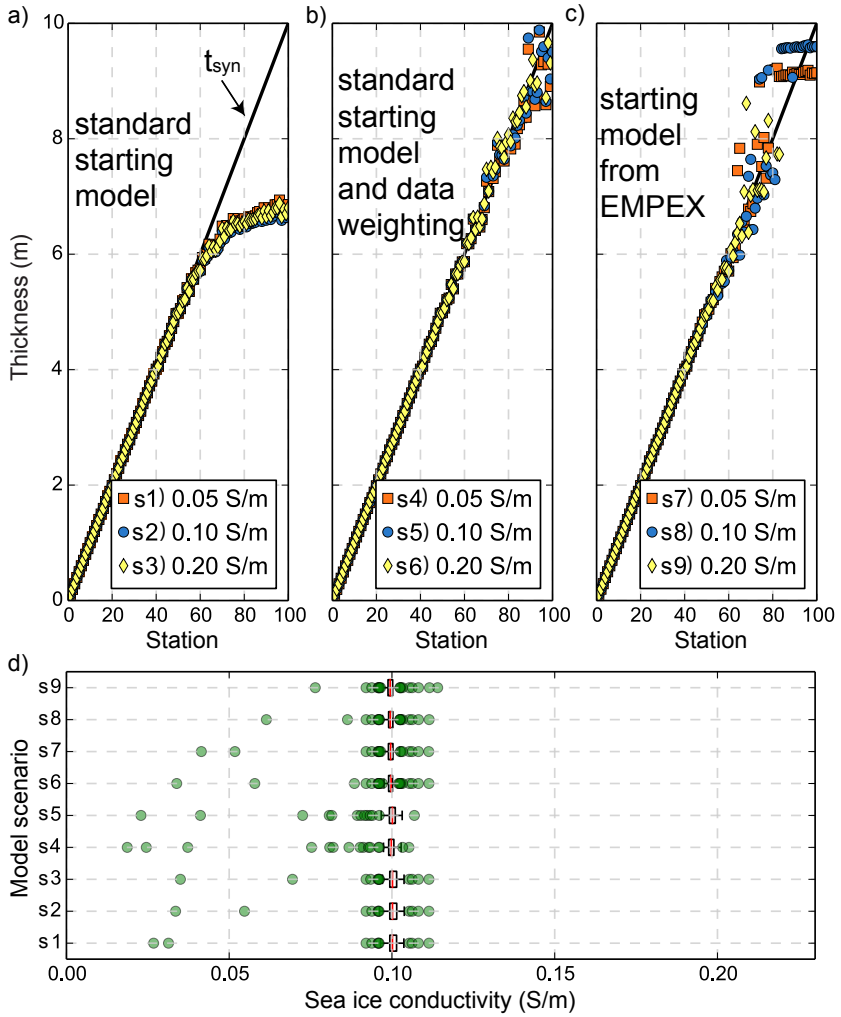

Figure 3.6.: Influence of starting model and data weighting on sea ice thickness t and conductivity σ from Marquardt-Levenberg inversions (experiment 4). In comparison to the experiments before, we used here one σ_{syn} of 0.1 S/m, but several starting models which refer to scenarios s1-s9. In a), b) and c) t is compared to t_{syn} of 0-10 m. In a) the standard starting model was used with 3 m thick sea ice, but variable conductivities of 0.05 (s1), 0.1 (s2), 0.2 (s3) S/m, and an underlying fixed homogeneous half-space of 2.7 S/m. In b) the same starting model was used as in a), but the data were weighted (s4, s5, s6). In c) sea ice thickness results from EMPEX processing (0.1 S/m in Figure 3.5b) and sea ice conductivities of 0.05 (s7), 0.1 (s8), 0.2 (s9) S/m were used for the starting model. t improved with data weighting and a modified starting model obtained from EMPEX thicknesses. In d) σ_{syn} of 0.1 S/m is compared to the resulting sea ice conductivities σ from the individual scenarios, where σ was recovered for each scenario within $\pm$ 0.01 S/m.

normalized synthetic data of the 5310 Hz in-phase component with added Gaussian noise. Sea ice thickness t (for $t_{syn} > 6$ m) was better resolved compared to the results without weighting (Figure 3.6b), which was also supported by the reduced RMSE values of 0.99-1.16 (scenarios s4-s6 in Table 3.2). For the starting models with sea ice conductivities of 0.05 S/m and 0.1 S/m, convergence was reached after 104 and 58 iterations, respectively, which was faster than for the other scenarios.

In a third step, we did not weight the data, but used the sea ice thickness results from the 0.1 S/m exponential fit from Figure 3.5b in the starting model. In the cases for which it was not possible during EMPEX processing to find for low in-phase values a corresponding sea ice thickness, we used the thickness from the previous station. This is still apparent in the results, where layered structures are recognizable for sea ice > 9 m (Figure 3.6c). But sea ice thickness t again improved for $t_{syn} > 6$ m compared to the case in Figure 3.6a. RMSE values of 1.04-1.10 for scenarios s7-s9 were smaller than for scenarios s1-s3 (Table 3.2). Sea ice thicknesses t from scenarios s7-s9 were similar and therefore did not depend much on sea ice conductivities of the starting model (Figure 3.6c).

In general, sea ice thickness t was reasonably resolved by the Marquardt-Levenberg algorithm for $t_{syn} < 6$ m, regardless of weights and starting model. With weight factors and results from single-frequency thickness estimates, t improved for $t_{syn} > 6$ m. Although it was not always possible to resolve t up to 10 m, the sea ice conductivities σ were resolved within $\pm$ 0.01 S/m for all scenarios (Figure 3.6d). Outliers of σ rather contained a too low than a too high conductivity value.

3.4.5. Porosity estimation

We reformulated Archie's Law (Archie, 1942) to calculate the sea ice porosity Φ

$$\Phi = \left(\frac{\sigma}{\sigma_b}\right)^{\frac{1}{m}}, \tag{3.14}$$

where σ is the bulk electrical conductivity, σ_b is the brine conductivity, and m is an empirical cementation factor. Our previous results showed that the uncertainty of σ is 0.01 S/m.

The cementation factor m depends on the connectivity of the pores and the pore shapes which is related to the structure of sea ice and the c-axis orientation of individual crystals (Reid et al., 2006). The mobility of ions and the permeability are therefore closely linked to this parameter. With respect to sea ice, the literature suggests m between 1.55 and 2.2 (Thyssen et al., 1974; Morey et al., 1984). Haas et al. (1997) and Worby et al. (1999)

used a cementation factor of 1.75 for their calculations. Reid et al. (2006) used values of 1.75 and 2.2, stating that the horizontal conductivity of the sea ice is overestimated with a value of 1.75. Since this parameter is not better constrained for sea ice and also depends on sea ice types and seasonality we used a value of 1.75.

With temperature measurements of nine first-year sea ice cores from the winter Weddell Sea (Hunkeler et al., 2015), we calculated the mean brine conductivity of 4.69 $\pm$ 0.91 S/m according to Stogryn and Desargant (1985). At the same locations, Hunkeler et al. (2015) obtained from EM measurements at 63.03 and 93.09 kHz an average bulk conductivity of 0.06 S/m from seven experiments above thin sea ice ($<$ 1 m). Assuming now $\sigma_b = 4.69 \pm 0.91$ S/m, $m = 1.75$, and $\sigma = 0.06 \pm 0.01$ S/m, we obtain by applying Gaussian law of error propagation a porosity of $\Phi = 8.3 \pm 1.2\%$. From the nine sea-ice cores, we calculated according to Cox and Weeks (1983) and Leppäranta and Manninen (1988) average brine volumes (porosities) of $\Phi = 9.5 \pm 5.0\%$. The good agreement between porosities calculated from conductivities and direct measurements in sea-ice cores implies, that with the obtained uncertainty to determine the bulk conductivity from EM, a reasonable sea-ice porosity can be estimated.

3.5. Discussion

We have shown that 1D inversions of EM data from passively bucked small coil systems must include the nonlinear contribution of the bucking coil when working close to a highly conductive environment. In our case of obtaining sea ice thickness and conductivity, the negligence of this contribution would lead to grossly wrong results for sea ice thinner than 2 m (Figure 3.2b), which is the typical level sea ice thickness in the Arctic and Antarctic. We calculated synthetic data based on a typical commercial instrument for sea ice research (Figure 3.1). The algorithm of including the bucking coil, however, will need to be made for all frequency-domain EM sensors that utilize passive-bucking in high conductive environments (Fitterman, 1998). With the effect included, we were able to resolve conductivity and ultimately porosity with uncertainty values that motivate further studies and usage of the 1D inversions for field data. This and earlier case studies have shown that especially a high frequency range is required for the retrieval of sea ice conductivity.

Our aim was to jointly resolve sea ice thickness t and conductivity σ for a single layer with a thickness range of t_{syn} of 0-10 m and conductivities σ_{syn} of 0.01-0.2 S/m. We have tested two inversion methods, a smoothness-constrained (EM1DFM) and a Marquardt-Levenberg (EMILIA) inversion. In each scenario, we inverted synthetic data with constant

conductivity σ_{syn} and the full range of physically feasible sea ice thicknesses t_{syn}, where the upper range includes extreme cases like decadal sea ice. During each iteration one β (trade-off parameter in EM1DFM or damping factor in EMILIA) is used for all stations simultaneously. The alternative would be separate inversions of all stations with individual β. This approach may lead to a faster convergence with less iterations. We however chose the single β approach, since we assume that stations are not independent and we want to reduce the potential for a wrong minimum of individual inversions.

EM1DFM inverts for the conductivity of multiple fixed layers; therefore the resolution of thickness depends on how the vertical conductivity gradient is evaluated (Figure 3.3). The conductivity transition zone between sea ice and seawater gets broader for thicker sea ice and also depends on σ_{syn}, thus, subsequently increasing the uncertainty of the thickness estimate. The Marquardt-Levenberg algorithm instead uses layer thickness as well as layer conductivity as free parameters, therefore removing the need for retrieving layer interfaces from conductivity gradients (Figure 3.4). While the description of sea ice as a layer of defined thickness with a conductivity discontinuity at the ice-water interface is a more realistic description of undeformed sea ice, internal structures such as from sea ice deformation or complex layering potentially can be better described by EM1DFM. However, the uncertainty of the interface location will be elevated by the process of vertical conductivity smoothing by EM1DFM. The choice of inversion scheme will therefore fall to the user and the specific application.

The best sea ice thickness results from the Marquardt-Levenberg inversions were found using data weights or tuning the starting model using single-frequency processing results (Figure 3.6). Higher weights for the weaker signals of thicker sea ice do increase the convergence rate and precision (Table 3.2). For real field data, we need to be careful when weighting low signal responses, since signal noise and instrument attitude errors may have an increased effect. In any case, with both inversion methods $t_{syn} < 5$ m were reasonably resolved. The conductivities of the starting model seemed to have little effect on the inversion results ($t_{syn} < 5$ m). The constant 3 m thick starting model probably favored the better retrieval of thin sea ice.

Although the sea ice thickness is better constrained than the sea ice conductivity based on the most-square inversion (Table 3.1), it is determined by the Marquardt-Levenberg inversion with the five used frequencies within $\pm$ 0.01 S/m no matter how well the thickness was resolved, independent from the starting model, the weight factors and σ_{syn} (Figures 3.5d and 3.6d). Likewise sea ice conductivities can be reasonably well resolved for most of the fixed layers of EM1DFM inversions, provided that RMSE < 2 (Figure 3.3).

We have simplified sea ice as one homogeneous layer of prescribed thicknesses and

conductivities, not accounting for any anisotropy due to higher conductivities in vertical brine channels (Reid et al., 2006). In nature, the simplification of level sea ice most likely applies to thermodynamically grown sea ice, which grows to a maximum of 2.5 meters (Thomas and Dieckmann, 2009) or to the Antarctic sub-ice platelet layer with multiple layers of different conductivities (Hunkeler et al., 2015). The sea ice-ocean interface or the interface between sea ice and the platelet layer are characterized by discontinuities in the vertical conductivity structure and by far smaller variability in the horizontal direction. To resolve such structures, lateral constraints between the models of adjacent stations (Auken et al., 2005) are assumed to be an appropriate modification of the Marquardt-Levenberg inversion resulting in a pseudo 2D inversion. But even pseudo 2D inversion cannot account for sea ice deformation features, where conductivities and sub-ice topographies vary additionally on sub-footprint scale. To account for complex topographies of deformed sea ice, we need to include the bucking bias in a full 2D inversion, where forward modeling responses and sensitivities are calculated in 2D.

The conversion of conductivity into porosity requires the knowledge of two parameters in Archie's Law (i) the cementation factor and (ii) the brine conductivity. First, we assume a cementation factor that is based on results from previous sea ice field experiments. Second, we used brine conductivities found in Antarctic winter sea ice cores. For sea ice throughout the freezing season this parameter is of second-order significance, since it is not assumed to vary much. In summer, the brine contains a mixture of saline brine and fresh water due to surface and internal melting, yielding a higher porosity than winter or spring sea ice (Vancoppenolle et al., 2007; Tison et al., 2008). In such cases, we can still make assumptions about the brine conductivity, but since we deal with higher uncertainties, the effect of porosity and brine conductivity on the bulk sea ice conductivity might not be fully separated in summer cases.

However, the uncertainty range of the sea ice conductivity in this idealized case is promising for retrieving porosity from actual field data. The improvement of 1D sea ice inversions presented in this study has therefore the potential to improve biogeochemical sea ice studies (e.g Arrigo et al., 1997) and estimations of sea ice density for satellite altimetry retrieval of sea ice thickness (Ricker et al., 2014) by large scale mapping of sea ice porosity.

3.6. Conclusion

Sea ice conductivity is a proxy parameter which can be used to derive porosity, albeit systematic measurements on scales larger than point measurements have been rare mostly due

to a lack of suitable methodology. With the non-destructive method of multi-frequency EM sounding, this study aims to lay the foundation for a fast joint retrieval of sea ice thickness and porosity. We varied parameters of a synthetic dataset (thickness and conductivity) to assess the sensitivity of different parameter combinations in two geophysical inversion algorithms. Furthermore, we tested the influence of the starting model and data weighting. We calculated the synthetic data for a a small-coil system with frequencies relevant for sea ice research in the range of 1 to 100 kHz. The existing inversion algorithms were modified for a nonlinear correction of signal bias that is caused by passive bucking of the primary EM field close to highly conductive environments. Only with the integration of this sensor specific correction, were we able to resolve sea ice conductivity with a resolution of 0.01 S/m with 1D inversion methods. This resolution is sufficient to initiate field trials, to estimate sea ice porosity of different sea ice types, or the thickness and porosity in multi-year cases, such as flooded snow layers or sub-ice platelet layers near Antarctic ice shelves. Furthermore, detailed knowledge of porosity facilitates biogeochemical studies of sea ice, and sea ice densities estimated from porosities yield freeboard validations of satellites measurements. Though our approach improves sea ice surveying with EM induction sounding methods, it suffers the same limitations caused by the use of 1D forward models for essentially 3D targets with a significant sub-footprint scale variability. Since real world sea ice surveys are mostly conducted along transects, we suggest to modify 2D inversions methods to resolve thickness and internal conductivity changes at sub-footprint scales. Such a method would enable further studies of sea ice deformation, relevant for the improved estimation of sea ice volume.

3.7. Acknowledgment

Computing resources were provided by SNIC through the Uppsala Multidisciplinary Center for Advanced Computational Science (UPPMAX, Uppsala, Sweden) under project snic2014-1-243 and by Eidgenössische Technische Hochschule (ETH) in Zurich, Switzerland. Johan Hermansson at UPPMAX and Heinrich Horstmayer at ETH are acknowledged for assistance concerning technical and implementational aspects in making the code run. This work was partly funded by the POLMAR graduate school and the Alfred-Wegener-Institut Helmholtz-Zentrum für Polar- und Meeresforschung.

This paper was reprinted from Geophysics with permission of the Society of Exploration Geophysicists.

4 A glimpse beneath Antarctic sea ice: platelet-layer volume from multi-frequency electromagnetic induction sounding

4.1. Abstract

In Antarctica, ice crystals emerge from ice-shelf cavities and accumulate in unconsolidated layers beneath nearby sea ice. Such sub-ice platelet layers form a unique habitat, and serve as an indicator for the state of an ice shelf. However, the lack of a suitable methodology impedes an efficient quantification of this phenomenon on scales beyond point measurements. In this study, we inverted multi-frequency electromagnetic (EM) induction soundings of > 100 km length, obtained on fast ice with an underlying platelet layer in the eastern Weddell Sea. EM-derived platelet-layer thickness and conductivity are consistent with other field observations. Our results suggest that platelet-layer volume is higher than previously thought in this region, and that platelet-layer ice-volume fraction is proportional to its thickness. We conclude that multi-frequency EM is a suitable tool to determine platelet-layer volume, with the potential to obtain crucial knowledge of associated processes in otherwise inaccessible ice-shelf cavities.

4.2. Introduction

Around Antarctica, unconsolidated accumulations of randomly-oriented, individual ice crystals (platelets) are frequently observed below sea ice adjacent or attached to ice shelves. This phenomenon, hereinafter referred to as (sub-ice) platelet layer, is a consequence of basal melt processes in nearby ice-shelf cavities (Robinson et al., 2014; Jordan et al., 2015) and part of a process referred to as "ice pump" (Lewis and Perkin, 1986). This special sea-ice type not only modifies the properties, mass- and energy balance of an overlying solid sea-ice cover (Eicken and Lange, 1989; Gough et al., 2012; Hoppmann et al., 2015b), it also acts as a habitat for a substantial seasonal bloom of micro algae

(e.g. Günther and Dieckmann, 1999) and provides a protective environment for coastal fish species (Vacchi et al., 2000). Ice platelets are subsequently incorporated into the solid sea-ice matrix through the freezing of the interstitial water. The resulting (solid) ice type is usually referred to as incorporated platelet ice (Langhorne et al., 2015), and contributes to the stabilization of breeding sites for penguins and seals. The additional buoyancy provided by the underlying platelets modifies the sea-ice freeboard, influencing sea-ice thickness retrieval by altimetry methods (Price et al., 2014). The seasonality and amount of ice platelets accumulated beneath sea ice potentially allows conclusions about processes in the ice-shelf cavities (Langhorne et al., 2015), which are otherwise difficult to investigate albeit their potential impact on sea-ice thickness (Hellmer, 2004) and -extent (Bintanja et al., 2013) in the Southern Hemisphere.

The total volume of loose ice platelets below a sea-ice cover is the product of the platelet-layer thickness, area and ice-volume fraction. The platelet-layer thickness is usually determined with a weighted measuring tape (Crocker, 1988), an approach which is time-consuming and only allows for a very limited spatial coverage. The temporal evolution of platelet-layer thickness is obtained by repeated drill-hole measurements, or by autonomous instrumentation at a fixed site (Hoppmann et al., 2015a). Ice-volume fractions have been determined using a variety of methods (Hoppmann et al., 2015b, and references therein), most of which are based on point measurements. Rack et al. (2013) used a traditional airborne EM system to measure the thickness of the McMurdo Ice Shelf, and found that the presence of sub-ice platelet layers lead to an overestimation of the ice thickness. However, they were not able to resolve the thickness of the platelet layer itself. We conclude that a determination of platelet-layer volume over geophysically relevant length scales still remains a challenge due to the lack of a suitable methodology.

A promising approach to efficiently determine platelet-layer volume by a non-destructive method has recently been identified. Hunkeler et al. (2015) used the response of a ground-based, multi-frequency electromagnetic (EM) induction sounding instrument to measure the electrical conductivity (hereinafter referred to as conductivity) of the platelet layer. They found an average conductivity of 1.154 Sm^{-1}, and calculated ice-volume fractions of 0.29 - 0.43 using Archie's Law (Archie, 1942) with varying cementation factors.

In the present study, we build upon these investigations and present the first consistent, high resolution platelet-layer thickness and -conductivity dataset recorded on Antarctic sea ice. We applied a laterally-constrained Marquardt-Levenberg inversion to a unique multi-frequency EM induction sounding dataset obtained on immobile sea ice (fast ice) which was attached to an ice shelf in the eastern Weddell Sea. We tested the performance of the inversion using synthetic EM data and validated the final inversion results with

drill-hole measurements.

4.3. Methods

4.3.1. Field conditions and measurements

The area under investigation was the seasonal fast ice of Atka Bay, a sheltered embayment in the front of the Ekström Ice Shelf in the eastern Weddell Sea, Antarctica (Figures 4.1a,b). The fast ice at Atka Bay exhibits a several meter thick platelet layer and a large fraction of incorporated platelet ice, both of which have been the subject of several studies (Kipfstuhl, 1991; Günther and Dieckmann, 1999; Hunkeler et al., 2015; Hoppmann et al., 2015b,a). This region is also one of the rare locations around coastal Antarctica where year-round studies of sea ice are possible, due to the presence of the German wintering station Neumayer III. Sea ice at Atka Bay is characterized by a distinct seasonal cycle: a continuous sea-ice cover typically establishes between March and May, destabilizing and breaking up between December and February. Between breakup and new formation, the entire bay is usually free of sea ice. The sea-ice conditions in 2012, the year the present study was performed, were slightly different: during August, approximately one third of the 440 km^2 fast ice area broke up during a storm. A continuous sea-ice cover was re-established in the breakup area after a large iceberg grounded in front of Atka Bay in October. Otherwise, the sea-ice conditions were comparable to other years: sea ice in the western part was deformed due to moderate ridging and rafting caused by predominantly easterly winds, while the eastern part exhibited mainly thermodynamically grown sea ice. As a result, sea ice in the east was generally thinner than the deformed sea ice of the western part. The thickest and oldest sea ice was observed in the southwestern part of Atka Bay. Drill-hole measurements at several sites between June 2012 and February 2013 indicated that the platelet layer reached its spatial average maximum of around 4 m in December. Additional information is available in Hoppmann et al. (2015b).

We operated a commercially available multi-frequency EM induction instrument (GEM-2, Geophex Ltd.) on the fast ice on four occasions between 26 November and 21 December 2012. We configured the instrument to simultaneously record GPS position and EM soundings at frequencies of 1530, 5310, 18330, 63030 and 93090 Hz with a sampling rate of 10 Hz. The instrument was mounted in a kayak and pulled over the sea ice a few meters behind a snowmobile. In total, we acquired 118 km of multi-frequency EM data across Atka Bay over a period of 25 days (Figure 4.1a, Table S1). Transect 1 recorded on 26 November was excluded from all further calculations, since the frequency setup was

different (no 1530 Hz data), and the same track was repeated later in December. Based on our knowledge from other studies (Hoppmann et al., 2015b), we assume no significant change in platelet-layer physical properties between 16 and 21 December (Table S1), and consequently regard them as one synoptic measurement.

Sea-ice thickness, snow depth and freeboard were measured with regular thickness tapes. Platelet-layer thickness was determined using the metal-bar method (Crocker, 1988), with a potential underestimation of up to 0.3 m as apparent from simultaneous real-time video. The data were already presented in Hoppmann et al. (2015b), and are used here for validation. The solid sea-ice cover consisted of a substantial fraction of incorporated platelet ice, which was handled as solid sea ice in this study.

4.3.2. Geophysical inversion of EM data

A geophysical inversion algorithm calculates and iteratively adjusts a model of the subsurface, until the modeled signal response fits the measured response within its uncertainty. Sea ice with an underlying platelet layer, such as found in Atka Bay, represents a simple, almost 1D target for geophysical inversions. In our study, we defined three separate layers: 1) sea ice plus snow (including incorporated platelet ice), 2) the sub-ice platelet layer, and 3) seawater (Hunkeler et al., 2015). These layers are mainly characterized by their different conductivities, with distinct conductivity interfaces in the vertical and smooth horizontal conductivity gradients within each layer. Because of the pronounced increase in conductivity with depth, the three-layer case of sea ice, platelet layer and seawater is an ideal application for the inversion of electromagnetic induction sounding data (Spies and Frischknecht, 1991). Although the snow cover usually exhibits a much lower electrical conductivity than sea ice (or much higher in case of surface flooding), we regard sea ice and snow as one layer.

To account for the sharp conductivity interfaces between the layers, we used a 1D Marquardt-Levenberg (ML) inversion (Lines and Treitel, 1984) implemented in the software package EMILIA (Electro-Magnetic Inversion with Least Intricate Algorithms, Grab, 2012; Kalscheuer, 2014; Kaufmann, 2014; Kalscheuer et al., 2015). In contrast to an inversion in which the only free parameters are the conductivities in multiple fixed layers (e.g. EM1DFM, Farquharson et al., 2003), the ML inversion can directly invert for thicknesses without the need for evaluating a broad conductivity transition zone. In contrast to an inversion in which the only free parameters are the conductivities in multiple fixed layers (e.g. EM1DFM, Farquharson et al., 2003), the ML inversion can directly invert for thicknesses without the need for evaluating a broad conductivity transition zone. In order to test the general performance and reliability of the ML inversion, we first created

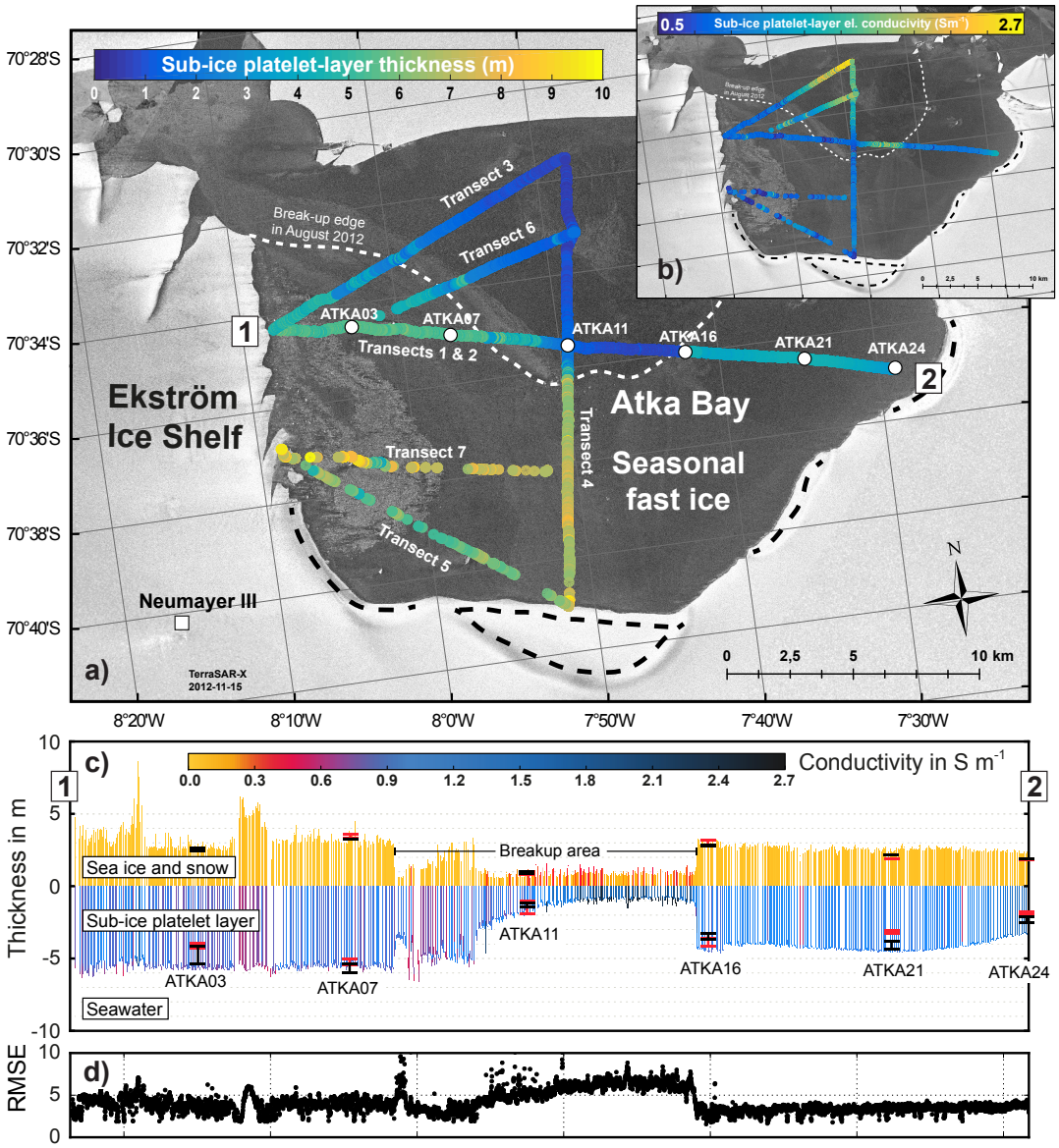

Figure 4.1.: Platelet-layer thickness (a) and electrical conductivity (b) below Atka Bay landfast sea ice, obtained from a laterally-constrained Marquardt-Levenberg inversion of multi-frequency EM data. Background: TerraSAR-X image from 15 November 2012, provided by the German Aerospace Agency (DLR). The ice sheet is grounded at several locations, forming ice rises and rumples (dashed black lines). The August 2012 sea-ice breakup edge (dashed white line) and sites of regular drillings (circles) are also indicated. c) Sea-ice and platelet-layer thickness and -conductivity from inversion of Transect 2 (between "1" and "2" indicated in Figure 4.1a), along with the range of simultaneous drill-hole measurements obtained in November (red bars) and December 2012 (black bars). d) Corresponding root-mean-square errors (RMSE) of field data inversions.

and inverted a synthetic dataset with different starting models (see supporting information: Text S2 and Figure S3), following the method of Hunkeler et al. (2016a). To determine which model parameters are constrained well by our data, we performed a non-linear most-squares inversion (Meju and Hutton, 1992; Kalscheuer and Pedersen, 2007; Kalscheuer et al., 2015, see supporting information: Text S2 and Table S4). Finally, we used a laterally-constrained ML inversion (Auken et al., 2005; Kaufmann, 2014) for field data processing, resulting in a pseudo-2D model.

All inversions were performed using the above-mentioned three layers, allowing for four free parameters: 1) sea-ice plus snow thickness and 2) -conductivity, as well as 3) platelet-layer thickness and 4) -conductivity. The seawater layer was considered as a homogeneous halfspace with a constant conductivity of 2.7 Sm^{-1}.

For each inversion model, we calculated the root-mean-square error (RMSE):

$$\mathrm{RMSE} = \sqrt{\frac{1}{N}\sum_{i=1}^{N}\left(\frac{d_{meas,i} - d_{cal,i}}{\sigma_{d,i}}\right)^2}, \tag{4.1}$$

where N is the number of measurements, i is a data index, $d_{meas,i}$ is the i-th measured signal, $d_{cal,i}$ is the i-th calculated signal of the subsurface model, and $\sigma_{d,i}$ is the estimated uncertainty of $d_{meas,i}$. An inversion model with a RMSE close to 1 is considered optimal, because the model response explains the measured data without fitting too much to the noise which is contained in the data (Kalscheuer et al., 2013).

Transects and laterally-constrained ML inversion

The transect data were filtered to obtain a spacing of 4 m between measurements, in order to reduce the computing time. All data were corrected using instrument-specific calibration coefficients, and the uncertainties for in-phase and quadrature recordings at all frequencies were determined from noise measurements in free air (Hunkeler et al., 2015).

In Hunkeler et al. (2016a), individual 1D models were stitched together to get a 2D impression of the inversion results along a transect. To build a laterally smooth 2D model, the ML inversion was augmented with horizontal smoothness constraints that were implemented as first-order differences of the layer parameters between adjacent stations (Kaufmann, 2014). The resulting pseudo 2D model contains distinct layers, but smooth lateral variations of conductivity and thickness within each layer. Since we expect the layer thicknesses of adjacent stations to vary more than their conductivities, we weighted the penalty on conductivity variation four times that of thickness variation. We allowed for a maximum of 100 iterations.

In all inversions of field data, we used a starting model of 1 m with a conductivity of 0.05 Sm^{-1} (sea ice plus snow), 2 m with 1.15 Sm^{-1} (platelet layer), and a homogeneous half space with 2.7 Sm^{-1} (seawater).

After the inversion, we excluded stations with a $RMSE > 10$ from all further calculations. This threshold was determined by visual inspection of the results, omitting outliers and implausible values. We additionally defined upper and lower conductivity thresholds for the platelet-layer at 2.7 and 0.5 Sm^{-1}, between which the data was considered plausible.

4.4. Results

4.4.1. Sea ice and platelet-layer spatial variability

Figures 4.1a and b show the filtered platelet-layer thicknesses (t_p) and conductivities (σ_p), calculated from the inversion of the multi-frequency EM field data. The background shows a TerraSAR-X image from 15 November 2012, obtained shortly before the GEM-2 transects. t_p ranged between 0.3 and 9.15 m, with the lowest values (< 2 m) within the August breakup area and the highest (7-9.15 m) in the southern half. t_p generally increased towards the ice-shelf edges bordering the bay in the west and south, but decreased towards the eastern margin. σ_p covered the entire allowed range from 0.5 to 2.7 Sm^{-1}, with the highest values in the August breakup area.

Figure 4.1c gives a more detailed view of the inversion results of Transect 2, which followed a regular route between the northern sea-ice ramp (labeled "1") and the westernmost point, ATKA24 (labeled "2"). In total, 291 of 6442 stations from Transect 2 exceeded the quality threshold of RMSE > 10 (Figure 4.1d) or exhibited a platelet-layer conductivity < 1 and > 2.7 Sm^{-1}. These data are not shown here.

The combined sea-ice plus snow thickness t_s in Transect 2 (plotted on the positive y-axis) ranged between 0.56 and 9.15 m. A thin sea-ice plus snow layer was found in the breakup area, whereas the largest t_s was found in the dynamically deformed area in the west. Thick sea ice plus snow between ATKA03 and ATKA07 is the result of snow accumulation behind an iceberg. t_s in the eastern part of the bay was mainly thermodynamically grown, and was therefore generally more homogeneous compared to the deformed ice regime in the west (also indicated by a region of higher backscatter in the TerraSAR-X image). The present results are generally consistent with an earlier study (Hoppmann et al., 2015b), in which the overall snow and sea-ice conditions at Atka Bay in 2012 were discussed in more detail. The combined conductivity of sea-ice plus snow, σ_s,

varied between 0.013 and 0.538 Sm^{-1}. Highest conductivities were found in the breakup area, most likely corresponding to extended surface flooding which were also observed in the field.

The platelet-layer thickness t_p (plotted on the negative y-axis) ranged between 0.63 and 6.63 m. In the western part of the bay, t_p was generally homogeneous, and on average about 1 m thicker than in the eastern part. In the breakup area, t_p was characterized by a high variability at the western breakup edge, a continuous decrease near ATKA11, and a sharp transition at the eastern break-up edge near ATKA16. The platelet-layer conductivity σ_p covered the entire allowed range. The highest σ_p was found in the breakup area, whereas the lowest values were observed in strongly deformed areas and at the locations of the thickest sea ice plus snow. The latter data have to be interpreted with care, since they are likely an indication of the method's limits.

The EM-derived thickness results for both, sea-ice and platelet-layer thickness, are within uncertainty in a very good agreement to drill-hole measurements obtained at regular measurements sites on 17 November 2012 (red bars in Figure 4.1c) and 14 December 2012 (black bars). The bars show the total range of up to 5 measurements taken at each site. The level of agreement between t_p and the manual measurements is remarkable, especially when taking into account that the manual measurements by the metal-bar method likely underestimated the true thickness by up to 0.3 m (Hoppmann et al., 2015b).

4.4.2. Thickness and conductivity distributions

The probability density distributions (pdd) of t_s (Figure 4.2b) shows peaks at 0.8 and 2.6 m, representing the thermodynamically grown fast ice 1) formed in the breakup area in October, and 2) the older fast ice formed in May. The pdd of t_p (Figure 4.2a) reveals a distribution with four peaks at 0.8, 4.3, 5.4 and 6,6 m. These represent the conditions 1) in the breakup area, 2) in the eastern part of the bay, 3) in the western part, and 4) in the south. The corresponding 2D histogram (Figure 4.2d) underlines the correlation between the two pdds, where a higher platelet-layer thickness corresponds to a higher sea-ice thickness.

The pdd of σ_p shows a broad distribution, with a peak at around 0.9 Sm^{-1} (Figure 4.2c). The 2D histogram of σ_p and t_p reveals an inversely proportional dependency (Figure 4.2e), where a thicker platelet-layer is accompanied by a low conductivity.

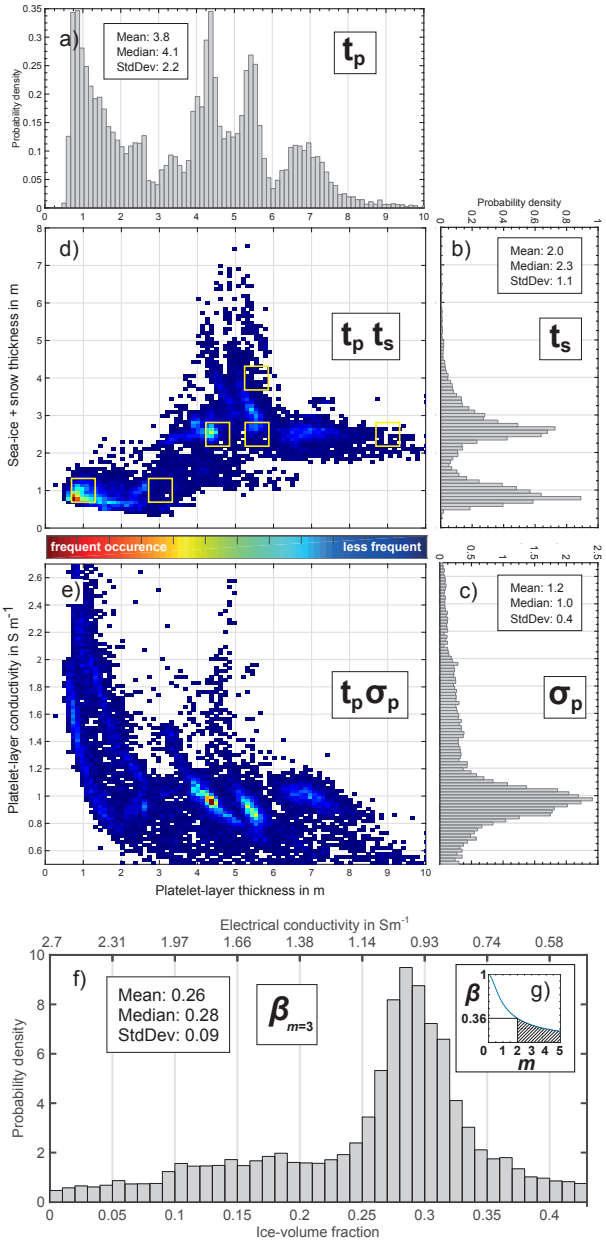

Figure 4.2.: Probability density distribution of Transects 2-7 of a) platelet-layer thickness t_p, b) sea-ice plus snow thickness t_s, and c) platelet-layer conductivity σ_p. 2D histograms of d) platelet-layer vs. sea-ice plus snow thickness and e) platelet-layer thickness vs. platelet-layer conductivity. Yellow squares in d) indicate the thicknesses used for most-squares inversions of synthetic data (Table S4). f) Distribution of platelet-layer ice-volume fractions (β) calculated from Archie's Law, assuming a cementation factor m = 3. g) Relationship between m and β (Archie, 1942) for our conductivity dataset. Plausible values for β are achieved for $m > 2$ (dashed area).

4.4.3. Platelet-layer ice-volume fraction

As demonstrated in Hunkeler et al. (2015), we converted σ_p to an ice-volume fraction β using Archie's law (Archie, 1942):

$$\beta = 1 - \sqrt[m]{\frac{\sigma_p}{\sigma_b}}, \tag{4.2}$$

where σ_b is the brine conductivity, which is assumed to correspond to the seawater conductivity (2.7 Sm^{-1}), m is the cementation factor, and β is 1 minus the porosity Φ. The cementation factor is an empirical factor, which depends on the pore geometry, its connectivity and the shape of the ice platelets. However, their influence on m is not well known for the platelet layer (Hunkeler et al., 2015).

The distribution of ice-volume fractions β is shown in Figure 4.2f for $m = 3$. The mean, median and standard deviation are 0.26, 0.28 and 0.09, respectively. Depending on the choice of m, the distribution of β shifts to smaller ($m > 3$) or higher ($m < 3$) values. For $m = 2$ for example, the mean, median and standard deviation are 0.36, 0.39 and 0.12, respectively. For $m = 4$, the mean, median and standard deviation are 0.2, 0.22 and 0.07 (not shown), respectively (Figure 4.2g with mean ice volume fractions on y-axis).

4.5. Discussion

4.5.1. Reliability and limits of the presented method

The great complexity of multi-frequency EM sensor calibration and data inversion presents many potential error sources, and care has to be taken when interpreting the results. In the present study we tried to ensure the reliability of the method by 1) performing sensitivity studies and most-squares inversion, 2) checking the consistency by comparison to earlier studies and 3) validating the final results using drillhole measurements. Combining all the results, we were able to demonstrate the potential to simultaneously determine sea-ice and sub-ice platelet-layer -thickness and conductivity using a carefully calibrated, multi-frequency EM instrument in combination with a suitable inversion algorithm. However, in order to achieve reliable results, an absolute calibration of the instrument (as described in detail in Hunkeler et al. (2015)), and a carefully prepared inversion algorithm (accounting for passive bucking as described in Hunkeler et al. (2016a)) are crucial prerequisites.

The proposed method also has its limits and caveats, some of which warrant further discussions. First, the lowest RMSE for each transect was found after iteration 100, the defined maximum value. Higher RMSE values in field data inversion compared to

synthetic data inversion may originate from 2D or 3D structure of the sea-ice and platelet layer and the higher number of stations. Systematic errors, like an incorrect calibration or the drift of the instrument, as well as vibrations of the EM instrument in the kayak, provide an additional error source, high RMSE, thus slow convergence. Furthermore, for the inversion to converge at adequate speed, the applied ML damping requires the start model to be relatively close to the true model. Hence, with an increasing number of stations, a start model which is the same for all stations (as used by us) may pose increasing difficulty to obtain convergence. Highest RMSE of individual 1D inversions were found (and excluded from further processing for RMSE > 10) for the transects in which the sea ice plus snow layer was especially thick (Transect 5 and 7, Figure 4.1a).

Second, the calculations were performed under the assumption of three distinct, locally homogeneous layers. However, field measurements of sea-ice or platelet layer thickness often revealed inhomogeneities in either layer, especially in the more deformed sea ice. Inverting for only three layers is therefore an oversimplification, but is needed to study the main parameter of interest, the platelet-layer thickness. The results of the synthetic study indicated that a retrieval of platelet-layer thickness is poorly constrained for relatively thick sea ice and platelet layers (Figures S3 b and h, Table S4, see supporting information). However, most of the field data were in a range which yielded reliable results (1 m $< t_p <$ 7 m), a finding which was confirmed by the generally plausible geographical distribution pattern (Figure 4.1a) and the good agreement with simultaneous drill-hole measurements (Figure 4.1c).

Third, interior melt of fast ice in summer (Hoppmann et al., 2015a) leads to an increased permeability. Once a certain permeability is reached, it may lead to surface flooding, given that the snow load on top is high enough to suppress the sea-ice surface below the water level. By this process, a highly conductive layer of slush is formed on top of the sea ice. This process was directly observed in the break-up area around ATKA11, but also evident in the inversion results (Figure 4.1c, red tones within yellow area). Since it is in principle possible to determine the presence of surface flooding from EM data (Hunkeler et al., 2015), we performed additional experiments trying to invert for a conductive layer on top of the sea ice. However, our results (not shown here) were not able to accurately resolve this additional layer. It is likely that the sea-ice layer itself was highly porous, resulting in high conductivities.

4.5.2. Geophysical implications of the data

Under the assumption that the results produced by our method are reliable, the EM-derived data enhance the understanding of the complex processes and interactions between

ocean, ice shelf and sea ice in several ways. Discussion of the dataset in exhaustive detail is beyond the scope of this paper, but in the following we highlight three important aspects.

First, it is now possible to more accurately determine the contribution of ocean/ice-shelf interaction to sea-ice mass balance in the study area, and to relate the overall volume to ice-shelf basal melt volume of the Ekström Ice Shelf. In their study, Hoppmann et al. (2015b) assumed an average platelet-layer thickness of 4 m based on the drillhole measurements indicated in Figure 4.1 to show that ice platelets contribute 43 % to total sea-ice mass at Atka Bay, corresponding to 22 % of the Ekström Ice Shelf annual basal melt volume. The sub-ice platelet layer thickness distribution from our study reveals that the point measurements from Transect 2 do not account for the thicker platelet layer in the southern half of the bay, leading to an overall underestimation of the average platelet-layer thickness of up to 1.3 m (neglecting the area of young ice in the breakup area). Using the corrected average thickness of 5.3 m, the contribution of ocean/ice-shelf interaction to annual (first-year) sea-ice mass in this region is 49 %, representing about 27 % of the annual basal melt volume. Since Transect 2 is also the basis of ongoing sea-ice monitoring activities, it needs to be considered to relocate or add measurement sites in the southern Atka Bay (i.e. including Transect 4) to more accurately determine the average annual ice-platelet accumulation.

Second, the thickness and conductivity maps in Figure 4.1 are useful to identify outflow regions of ice crystals in a supercooled plume (Robinson et al., 2014; Hughes et al., 2014). The observed north-south and east-west gradients of platelet-layer thickness (with thicker platelet layers in the south and in the west) either indicate an enhanced accumulation in that region, or a redistribution towards the southwest. There are however several indications that the main outflow area is in the central western part of Atka Bay, and that currents redistribute suspended and loosely attached ice platelets towards the eastern part of the bay:

1. The thickness pattern from Transect 2 (Figure 4.1c), especially the generally decreasing thickness towards the east and the gradual decrease near ATKA11 suggest that platelets are advected towards the east. Eastward currents are in general not expected close to the Antarctic continent since the Antarctic Coastal Current (ACoC) flows mainly westwards. However, Fahrbach et al. reported a weak current in our study area which is influenced by sea floor topography and tides. Also Hoppmann et al. (2015b) concluded that the platelet release might be related to episodic events connected to tides.

2. The rather small part of the Ekström Ice Shelf, which lies east of Atka Bay, is likely not a source of supercooled water due to the limited depth. The more likely source

is the deep part of the western Ekström Ice Shelf several hundred kilometers to the south.

3. Due to the presence of several ice rises and ice rumples (where the ice sheet is grounded) in the southwest, south and east of the bay (dashed black lines in Figure 4.1), there are only a few locations where the plume could emerge from below the ice shelf.

4. Episodic events of platelet-layer riseup from below were recorded by cameras in the western part of the bay (Hoppmann et al., 2015b).

In order to draw more conclusions about the main ice-shelf outflow areas, the entire ice shelf edge, and especially the passages between the areas of grounded ice, need to be covered by EM transects.

Third, the conductivity retrieved from the inversion (Figure 4.1b) gives an impression of the relative compaction of the ice platelets. Higher conductivities found in the sea-ice breakup area, where a relatively new platelet layer formed form October on, are related to a higher seawater content in the pore space between the platelets. Lower platelet-layer conductivities in the more typical first-year sea ice in other parts of the bay are an indication of more ice and less seawater in the interstices. These findings are generally consistent with drillhole measurements, where the mechanical resistance during platelet-layer thickness measurements was significantly lower in the area of newer platelet layers. In general, conductivity is higher for a thinner and younger platelet layer, which implies that an older thick platelet layer is more compacted and denser than a young thin platelet layer (Figure 4.2e). A thicker platelet layer is potentially more compressed because of increased buoyancy of underlying platelets and compaction due to ocean currents, leading to lower conductivity.

The conversion of electrical conductivity to ice-volume fraction was performed using Archie's Law (Equation 4.2), a procedure which very much depends on a yet not well known cementation factor. Hunkeler et al. (2015) used calibration measurements over thin sea ice and platelet layer at site ATKA11 to calculate a mean platelet-layer conductivity of 1154 $\pm$ 271 Sm^{-1}. The conversion to ice-volume fraction yielded values of 0.29 (m = 2.5) to 0.43 (m = 1.5). These results were too high compared to other recent studies, which found ice-volume fractions of 0.25 $\pm$ 0.06 (Gough et al., 2012), 0.16 $\pm$ 0.07 (Price et al., 2014), 0.22 (Wongpan et al., 2015) and 0.18 $\pm$ 0.09 (Hoppmann et al., 2015a). In Figure 4.2g, the relation between the average ice-volume fraction and cementation factor m is shown using our electrical conductivity dataset. By using a higher m, the ice-volume fraction is shifted towards higher values. To obtain the best agreement with the ice-

volume fractions suggested by the studies mentioned above, a cementation factor of $m = 3$ or even higher may need to be considered. Only a limited number of studies is available which empirically determined a cementation factor for disc-shaped geometries: Jackson et al. (1978) for example used platy shell fragments with a sphericity of 0.5 and found a cementation factor of 1.9. But loose platelets may even be less spherical, which would lead to a higher cementation factor. However, for further studies it might be necessary to model cementation factors for different platelet-layer arrangements.

4.6. Conclusions

In this study, we obtained a substantial multi-frequency EM induction sounding dataset on an Antarctic fast-ice regime with an underlying platelet layer. We calculated fast-ice and platelet-layer thicknesses and conductivities, using this unique dataset as an input for a laterally-constrained Marquardt-Levenberg inversion scheme. Our results provide evidence that platelet-layer thickness retrieval is possible from the surface using a non-destructive method, a finding which we expect to significantly facilitate its volume estimation in the future. Given that the sub-ice platelet layer is one of the most productive marine habitats, biological studies would also benefit from such kind of data. The high resolution achieved with this method is suitable to reveal accumulation patterns and identify ice-shelf outflow regions, albeit complementary oceanographic measurements are still needed. The presented methodology is a crucial step in determining the relative contribution of sub-ice shelf processes to sea-ice mass balance in the Southern Ocean, and hence a valuable tool to better understand ocean/ice-shelf interaction without the need for extensive logistics. However, this study is only a starting point, and it is necessary to repeat measurements for time series and to collect more multi-frequency data on other sea-ice sites in coastal Antarctica. The current limitation to spatial scales of up to 100 km due to operation by snowmobiles could be overcome by an adaptation of this methodology to airborne multi-frequency EM measurements.

4.7. Acknowledgments

This work would not have been possible without the Neumayer III infrastructure and the help of the wintering crew 2012. The authors are grateful to Stephan Paul and Uwe Baltes for their assistance in the field, and to the AWI logistics for their support. The computations were performed on resources provided by SNIC through Uppsala Multidisciplinary Center for Advanced Computational Science (UPPMAX) under Project snic2014-1-243.

Johan Hermansson at UPPMAX is acknowledged for assistance concerning technical and implementational aspects in making the code run on the UPPMAX resources. This work was funded by the POLMAR graduate school and the German Research Council (DFG) in the framework of its priority program "Antarctic Research with comparative investigations in Arctic ice areas" by grants to SPP1158, NI 1092/2 and HE2740/12. The data used here are publicly available at http://doi.pangaea.de/10.1594/PANGAEA.845535.

4.8. Supporting Information

4.8.1. Introduction

Table S1 provides detailed information about the transects across which the multi-frequency EM data of this study were acquired.

Text S2, Figure S3 and Table S4 assess the performance of the inversion algorithm by describing the methodology and results of 1) a Marquardt-Levenberg inversion of synthetic data, 2) a model error and resolution analysis and 3) a most-squares inversions in order to assess how well the free model parameters are resolved and constrained by the data.

4.8.2. Table S1: Summary of transect data

Table 4.1.: Summary of multi-frequency EM data collected across Atka Bay. T corresponds to the transects as indicated in Figure 4.1; the date refers to the year 2012; n is the total number of individual stations for the respective transect; sub-T refers to the number of sub-transects used for an inversion; dist is the straight-line distance, and dist true is the true distance between first and last station.

T	Date	n	sub-T	dist (km)	dist true (km)
1	26-Nov	6442	3	24.6	25.8
2	16-Dec	6339	2	24.6	25.4
3	20-Dec	3464	2	13.4	13.9
4	20-Dec	4588	2	17.7	18.4
5	20-Dec	3365	2	12.9	13.5
6	21-Dec	2322	1	9.2	9.3
7	21-Dec	2887	1	10.6	11.5

4.8.3. Text S2: Inversion performance

Synthetic data and ML inversion

To test the performance of the ML algorithm, we inverted a set of synthetic data based on the conditions encountered in the field. We calculated synthetic data for a series of 1D models, assuming our standard frequency setup and instrument-specific parameters, and using Anderson's [1979] forward modeling. The considered three-layer models have the following parameters: sea-ice with a conductivity of 0.05 Sm^{-1} and thicknesses of 0.5 - 4 m (increments of 0.5 m), platelet-layer with a conductivity of 0.05 Sm^{-1} and thicknesses of 0.5 - 10 m (increments of 0.5 m) and seawater with a conductivity of 2.7 Sm^{-1}. In order to better represent real data, we added Gaussian noise corresponding to one standard deviation from a series of EM recordings in free air to the synthetic data (Hunkeler et al., 2015).

We then inverted different synthetic data subsets, each comprising of one defined sea-ice thickness (e.g. 0.5 m) and of increasing platelet-layers thicknesses (0.5 to 10 m, in increments of 0.5 m). Each of those scenarios represents one 1D ML inversion. This procedure was repeated for the range of sea-ice thicknesses indicated earlier, resulting in a total of eight scenarios. The starting model used in these scenarios was 1) a layer with a thickness (conductivity) of 1 m (0.05 Sm^{-1}), representing sea ice plus snow; 2) a layer with a thickness (conductivity) of 2 m (1.15 Sm^{-1}), representing the platelet layer; and 3) a homogeneous half space with a conductivity of 2.7 Sm^{-1} (Hunkeler et al., 2015), representing the seawater beneath. To determine the influence of the starting model, the eight scenarios were repeated four times with slightly modified starting models, with sea-ice and platelet-layer conductivities (in Sm^{-1}) of 1) 0.03 and 1.15, 2) 0.07 and 1.15, 3) 0.05 and 0.90, and 4) 0.05 and 1.40, respectively.

The differences between the inversion results and the synthetic (true) data for the four free parameters and five different starting models are shown in Figure 4.3, normalized to the true values. The eight columns of each box correspond to the eight scenarios outlined above. For most of the inversions, the RMSE was close to 1 (Figures 4.3e and k, green colors). In general, the RMSE was < 1 for thinner platelet layers, indicating that noise was fitted. For thicker platelet layers, the RMSE was > 1, indicating that the desired misfit was not reached.

The calculated sea-ice thicknesses and conductivities (Figures 4.3a, c, g and i) generally agreed well with the true values, with thin sea ice (0.5 m) and thin platelet layers (0.5 and 1 m) being the exceptions. In these cases, the conductivity and thickness of the sea ice were overestimated. The platelet-layer conductivity (Figures 4.3d and j) was also well

reproduced (± 10 %), except for thin platelet-layer thickness (0.5 and 1 m), where the conductivity was overestimated. The platelet-layer thickness (Figures 4.3b and h) was overestimated for a thin platelet layer (0.5 m), and underestimated for a thick platelet layer (> 7 m). But in-between, the platelet-layer thickness was resolved within ± 10 %. Since we seldom observed sea-ice thicknesses < 0.5 m and platelet-layer thicknesses > 7 m in the field, we consider the performance of the inversion algorithm to be reliable. The general dependence of the results on the starting model was low. Only the the sea-ice conductivity depended on the initial sea-ice conductivity of the starting model, most pronounced for sea-ice thickness < 2.5 m (upper two panels in Figure 4.3i). Between 3 (3, 3.5, 4 m sea ice) and 54 (0.5 m sea ice) iterations were necessary to match the target RMSE of 1 for Figures 4.3a-e. For several inversions with a different starting model (Figures 4.3g-k), the maximum number of iterations was needed.

Most-squares inversion

For the assessment of how well our free model parameters are resolved and constrained by the data, we performed 1) a model error and resolution analysis and 2) most-squares inversions, similarly to Hunkeler et al. (2016a).

We have applied first the model error and resolution analysis to ML models from synthetic data (Figure 4.3a-e) for frequent occurring sea-ice and platelet-layer thicknesses as indicated in Figure 4.2d. This calculation is based on the truncated singular value decomposition (TSVD) of the sensitivity matrix (Kalscheuer and Pedersen, 2007; Kalscheuer et al., 2015). Since the effective number of model parameters is four (conductivities and thicknesses of the upper two layers, i.e. of the sea ice and platelet layer), a truncation level of four was used in the analyses of these models.

To validate the linearized error estimates obtained from TSVD analyses, we computed error estimates for the final inversion models using most-squares inversion (e.g. Meju and Hutton, 1992; Meju, 1994; Kalscheuer and Pedersen, 2007; Kalscheuer et al., 2015), partly accounting for the non-linearity of the inversion problem. Owing to the logarithmic transformation of model parameters during inversion, the most-squares uncertainties $1/f^{-}_{MSQ}$ and f^{+}_{MSQ} correspond to parameter ranges $\sigma/f^{-}_{MSQ}, \ldots, f^{+}_{MSQ} \cdot \sigma$ and $t/f^{-}_{MSQ}, \ldots, f^{+}_{MSQ} \cdot t$ of layer conductivities and thicknesses, respectively.

The results of our TSVD error and resolution analyses suggest that due to the limited number of model parameters, all four layer parameters are perfectly resolved. Hence, in assessing how well the layer parameters are constrained, only the model parameter uncertainties obtained from the most-squares inversions need to be further considered.

In Table S4, we present the model uncertainties of six of the 3-layer ML inversion

models (cf. Figure 4.2d, yellow squares). In accordance with our expectation that the thickness of a resistive layer is typically better constrained by inductive EM methods than its conductivity (e.g. Pfaffling and Reid, 2009), the thicknesses t_s of the sea-ice layer are more tightly constrained than the sea-ice conductivities σ_s ($1/f^-_{MSQ} \geq 0.97$ and $f^+_{MSQ} \leq 1.04$ for t_s compared to $1/f^-_{MSQ} \geq 0.86$ and $f^+_{MSQ} \leq 1.21$ for σ_s). For the sea-ice thicknesses considered here, the uncertainty of the thickness t_p of the platelet layer increases systematically with increasing combined thickness of the sea ice and platelet layers ($1/f^-_{MSQ} = 0.94$ and $f^+_{MSQ} = 1.19$ for $t_s + t_p = 2\,\mathrm{m}$ compared to $1/f^-_{MSQ} = 0.83$ and $f^+_{MSQ} = 1.58$ for $t_s + t_p = 11.5\,\mathrm{m}$). This suggests that, for the larger combined thicknesses, the EM data provide only limited constraints for the deeper part of the platelet layer. The uncertainty of the conductivity σ_p of the platelet layer varies with the thickness of the overlying sea-ice ($1/f^-_{MSQ} \geq 0.91$ and $f^+_{MSQ} \leq 1.06$, $1/f^-_{MSQ} \geq 0.95$ and $f^+_{MSQ} \leq 1.06$ and $1/f^-_{MSQ} = 0.90$ and $f^+_{MSQ} = 1.12$ for $t_s = 1\mathrm{m}$, $2.5\,\mathrm{m}$ and $4\,\mathrm{m}$, respectively). That σ_p appears to be more tightly constrained for $t_s = 2.5\mathrm{m}$ may mean that $t_s = 2.5\mathrm{m}$ matches more favorably to the depth of investigation range of the instrument than the other values of t_s analyzed.

4.8.4. Figure S3: Inversion of synthetic data

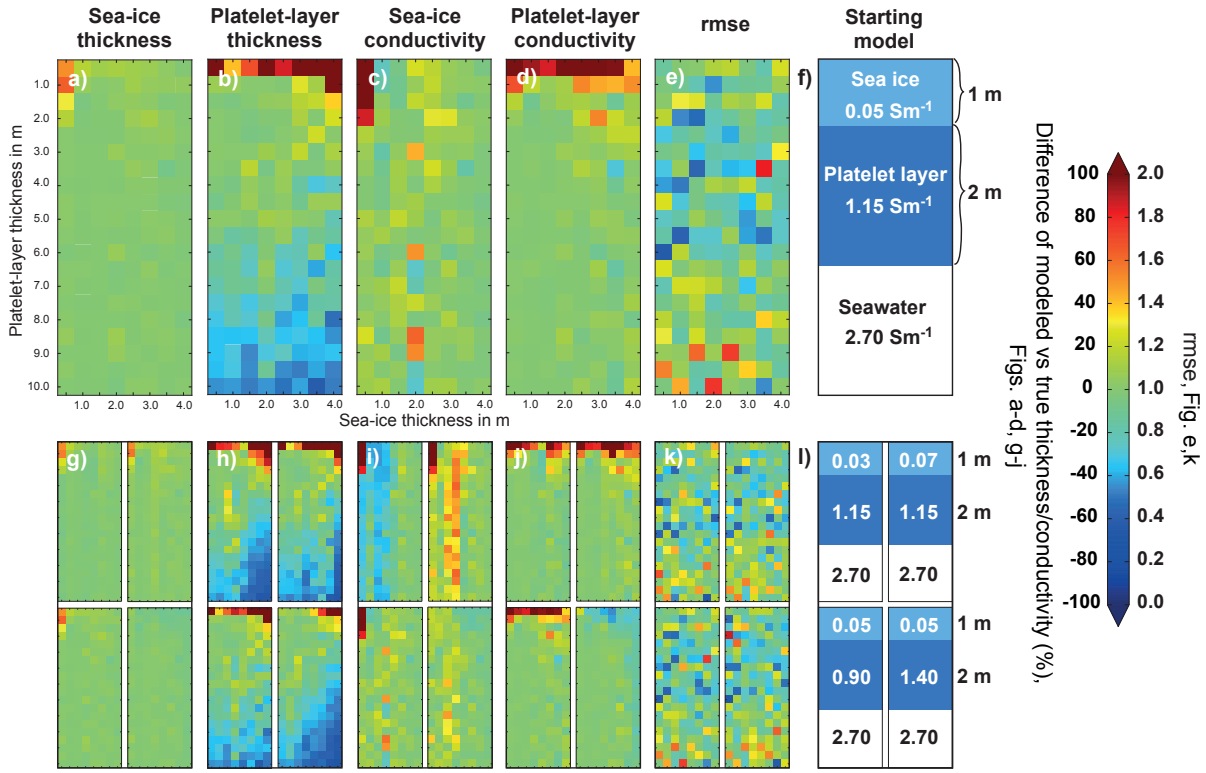

Figure 4.3.: Normalized differences between synthetic (true) model and ML inversion results for various combinations of sea-ice (0.5-4 m) and platelet-layer (0.5-10 m) thicknesses, and with different starting models. True sea-ice, platelet-layer and seawater conductivities were 0.05 Sm^{-1}, 1.15 Sm^{-1} and 2.7 Sm^{-1}, respectively. Normalized differences of a) sea-ice thickness, b) platelet-layer thickness, c) sea-ice conductivity, d) platelet-layer conductivity, and e) RMSE. Inversions were performed with a starting model according to f). Green colors indicate a very good agreement between modeled and true thickness/conductivity, while red and blue colors represent over- and underestimations of the inversion results compared to the true model, respectively. g-k) Corresponding results for four other starting models, which are indicated in l).

4.8.5. Table S4: Error estimates

Table 4.2.: Error estimates for conductivities σ and thicknesses t of the sea ice (subscript s) and platelet (subscript p) layers of some of the 3-layer Marquardt-Levenberg models in Figure 4.3. Error estimates $1/f^{-}_{MSQ}$ and f^{+}_{MSQ} were computed using most-squares inversions involving truncated singular value decomposition with a truncation level $p = 4$, the effective number of model parameters. Error estimates were calculated for most frequent sea-ice and platelet-layer thicknesses, marked in Figure 4.2d.

Parameter	$1/f^{-}_{MSQ}$	f^{+}_{MSQ}	$1/f^{-}_{MSQ}$	f^{+}_{MSQ}
	1 m sea ice + 1 m platelet layer		1 m sea ice + 3 m platelet layer	
σ_s	0.92	1.04	0.91	1.02
σ_p	0.91	1.06	0.99	1.01
t_s	0.97	1.04	0.99	1.01
t_p	0.94	1.19	0.96	1.09
	2.5 m sea ice + 4.5 m platelet layer		2.5 m sea ice + 5.5 m platelet layer	
σ_s	0.88	1.17	0.86	1.21
σ_p	0.95	1.06	0.95	1.05
t_s	0.97	1.03	0.97	1.03
t_p	0.89	1.16	0.84	1.32
	2.5 m sea ice + 9 m platelet layer		4 m sea ice + 5.5 m platelet layer	
σ_s	0.86	1.21	0.96	1.05
σ_p	0.95	1.05	0.90	1.12
t_s	0.97	1.03	0.97	1.03
t_p	0.83	1.58	0.80	1.31

5 Deformed sea ice - preliminary results

So far, the focus of the multi-frequency retrieval studies was of 1D geometry, i.e. level sea ice and the platelet layer. The next case study for the retrieval of internal sea-ice properties are blocky sea-ice deformation zones, where the assumption of 1D geometry is usually invalid, even for the small footprint of a handheld EM sensor. This chapter investigates and discusses the limitations in the thickness and conductivity retrieval when the geometry dimension of the forward model is an oversimplification of the actual sea-ice geometry. It is well known that the oversimplification leads to a thickness bias known as footprint smoothing, but the prospect of determining macro-scale porosity has not been investigated before.

The study is based on measured EM data from several Antarctic sea-ice pressure ridges (Figure 5.1a). To ensure that the geometry does sufficiently fulfill a 2D approximation, ridges were chosen that showed linear surface features. The case studies then consisted of 40-50 m long transects with EM measurements every 0.5 to 1 m, centered over the ridges main sail and perpendicular to the ridge orientation. A typical survey transect perpendicular to a sea-ice pressure ridge is illustrated in Figure 5.2 on an aerial photography. We acquired the EM data with two persons, one handling the EM device and the other one the hand-held PC (Figure 5.1b). For each recording, we placed the device on the ground and recorded the signal several seconds.

After the EM data were recorded, validation data of snow thickness, sea-ice thickness, the depth and extent of voids between ice blocks, and the freeboard were measured at drill holes with rulers and measuring tapes (Figures 5.1c-f). Since the instrument is sensitive to the footprint area also features from the left and right of the survey profile have an impact on the signal response. Therefore, we repeated the validation measurements of the survey transect on two parallel transects 1 m aside (Figure 5.2). In total, the geometry of each ridge was validated at 120 to 150 drill holes.

The EM data were averaged in post processing, corrected with obtained calibration coefficients (Table 2.1) and processed with a laterally-constrained Marquardt-Levenberg inversion similar to the platelet-layer data (chapter 4.8.3). I used a four-layered model, where I fixed the deepest layer to 2.7 S/m (homogeneous half-space with seawater conductivity). This results in six free parameters, namely three thickness and three conductivity parameters. The resulting three layers can for example explain two sea-ice layers with a porous layer in between, a conductive porous top layer and two underlying sea-ice layers, or three sea-ice layers. However, with the three free layers it is not possible to resolve for a conductive top layer and underlying sea ice with voids in between. Conductivities of 0.05 S/m were assigned to the upper three 0.5 m thick layers of the starting model and I allowed for 300 iterations. The EM data were inverted by assuming that measurements were performed without the influence of sea-ice surface topography. Results were plotted by correcting for the topography measured, i.e. freeboard of zero equals elevation zero. For comparison to inversion results, I calculated sea-ice thicknesses with the in-phase 5310 Hz component according to the single-frequency approach EMPEX (Pfaffling et al., 2007).

Inversion results of four sea-ice pressure ridges are shown in Figures 5.3 - 5.7, referred to ridges R1 - R4. In each figure the top panel shows the measured reference thicknesses and freeboards for mean, maximum and minimum values of the left, center and rights transects. The voids are indicated for each transects with down-pointing triangle for the void upper border and with up-pointing triangles for the void lower border. In the middle panels the RMSE is shown, where a RMSE of 1 is desired and means that subsurface parameters are found which explain the EM data within their uncertainty. The reference thicknesses, the single-frequency processing thicknesses and the voids from the center transect are shown in the lowest panels superimposed the inversion results.

Sea-ice pressure ridge R1

Sea-ice pressure ridge R1 (Figure 5.3) is a typical 2D ridge with level sea ice on both ends of the profile. The inversion results underestimated the pressure-ridge thickness between stations 17 and 25 m. Highest RMSE values were found in the same region between stations 14 and 19 m. Although a 1 m discrepancy between processed and observed thickness was obtained, RMSE values were low for the rest of the transect. This means that the algorithm could explain data with the resulting model equally well. The thick porous layer of nearly one meter appears 0.5 m too shallow in the inversion result. But nevertheless, the conductive layer of 1 meter in thickness was reproduced. The thickness

Figure 5.1.: Impressions of EM and validation measurements in the winter Weddell Sea, 2013. In a) a sea-ice pressure ridge is shown parallel to its sail and perpendicular to the transect, b) EM data were acquired with a GEM-2. c), d), e) and f) show validation measurements of snow thickness, sea-ice thickness, freeboard and voids between sea-ice blocks. Photograph credits belong of a) and b) to Sandra Schwegmann, c) to Stefan Hendricks, d) and f) to Bruno Jourdain and e) to Mario Hoppmann.

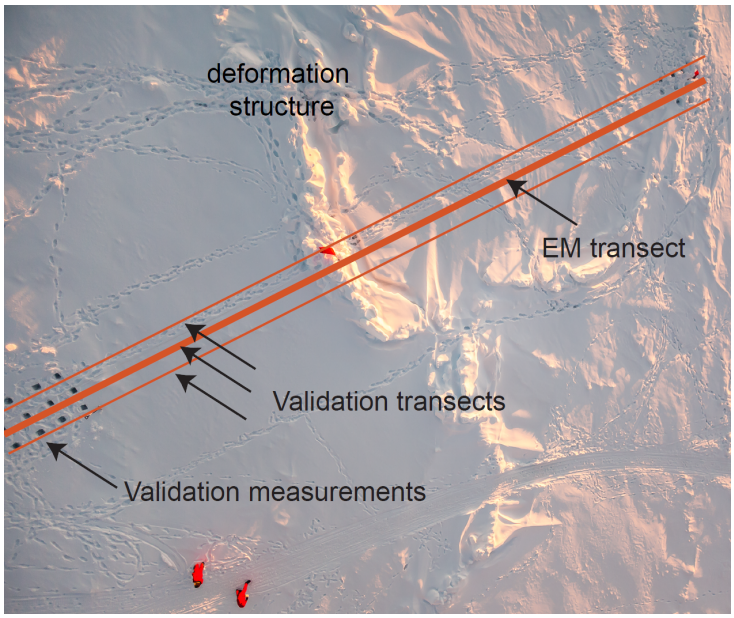

Figure 5.2.: Aerial photography of deformed sea ice with illustrated survey and validation transects. At the beginning and end of the transect, validation data were acquired, indicated by the removed snow. Notice the people in the lower left corner for the scale.

of the level sea ice at the beginning and the end of the transect was reliably resolved. The EMPEX approach performed well for level sea ice, but underestimated the total sea-ice thickness in the ridge zone, even more than the thicknesses obtained by the inversion.

The level sea ice contained often negative freeboards, meaning that the sea-ice surface was below seawater level. This leads to a flooding of the sea ice with seawater, which results in a slushy wet snow layer. Generally, the top layer is resolved with a higher conductivity (stations 0-13 m and 36-45 m) and corresponds to snow thickness. For a detailed illustration of the conductive top layer, the black box of ridge R1 (Figure 5.3) is enlarged in Figure 5.4a. The snow thickness from validation measurements was from stations 0-13 m thinner than the top layer resolved by the algorithm. In addition, the total thickness from the inversion was approximately 0.3 m too thick. These results indicate that the inversion resolved the top layer too thick or its conductivity too low.

Sea-ice pressure ridge R2

Sea-ice pressure ridge R2 (Figure 5.5) contains complex rafted sea-ice blocks on one side of the transect and thinner level sea ice on the opposite transect side. The thicknesses of ridge R2 were reliably resolved by the inversion algorithm, especially the level sea ice

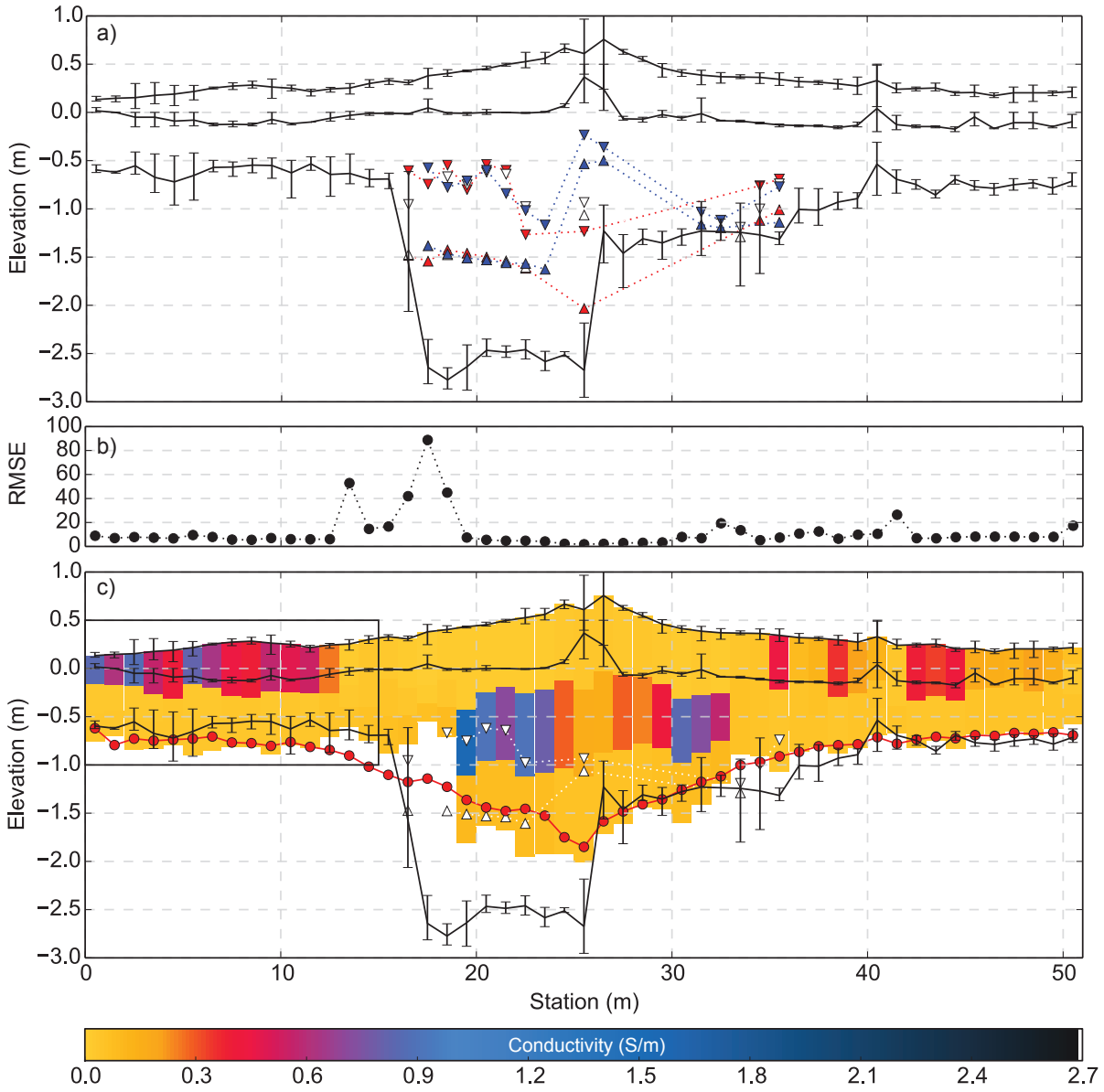

Figure 5.3.: Sea-ice pressure ridge R1 (data from 03 July 2013), comparison between data from drill-hole measurements and EM inversions. In a) snow, freeboards and sea ice of three parallel transects are shown with mean, minimum and maximum values. The internal voids are indicated for each of the three transects (blue, white, red) with down-pointing triangle for the upper border and with up-pointing triangles for the lower border. In b) the RMSE is shown for individual Marquardt-Levenberg inversions. In c) the reference data from a), the voids from the middle transect, and the sea-ice thickness from EMPEX processing (red) are superimposed the inversion results. The colors represent the retrieved conductivities. The enlargement of the box is shown in Figure 5.4a.

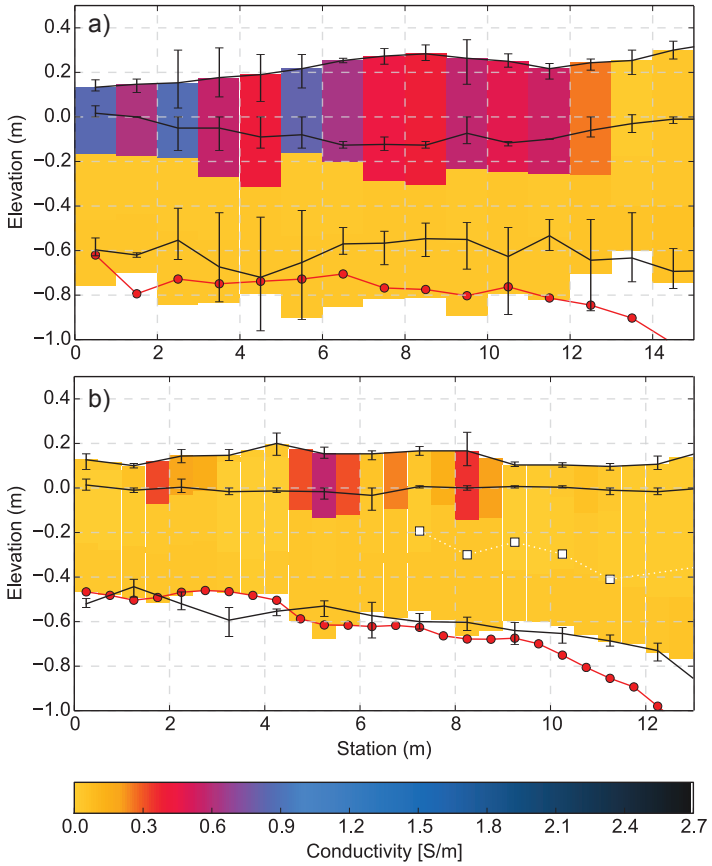

Figure 5.4.: Inversion results of sea-ice flooding. Transects are enlargements of boxes in a) Figure 5.3 and b) Figure 5.7. Reference measurements (black), porous sea ice (white squares), and sea-ice thicknesses from single-frequency processing (red) are superimposed the conductivities from the inversion results (colored cells). High conductivities were resolved at locations with a negative freeboard, indicating a flooded sea-ice layer.

between stations 30-50 m. The freeboard was always close to zero, but rarely negative. Nevertheless, a conductive topmost zone was resolved at several stations, which might indicate flooded sea ice. Drill-hole measurements show conductive voids at a few stations, which are not seen the same in the inversion results, although the inversion resolves for some voids in the keel area of the ridge. The thinner sea-ice thickness between stations 7 and 10 m could not be resolved by the inversion algorithm. But it might be possible that the measured sea-ice thickness was actually the void upper surface and we missed with the measuring tapes the underlying sea ice. Sea-ice thicknesses from the EMPEX processing agree generally well with inversion and drill hole data.

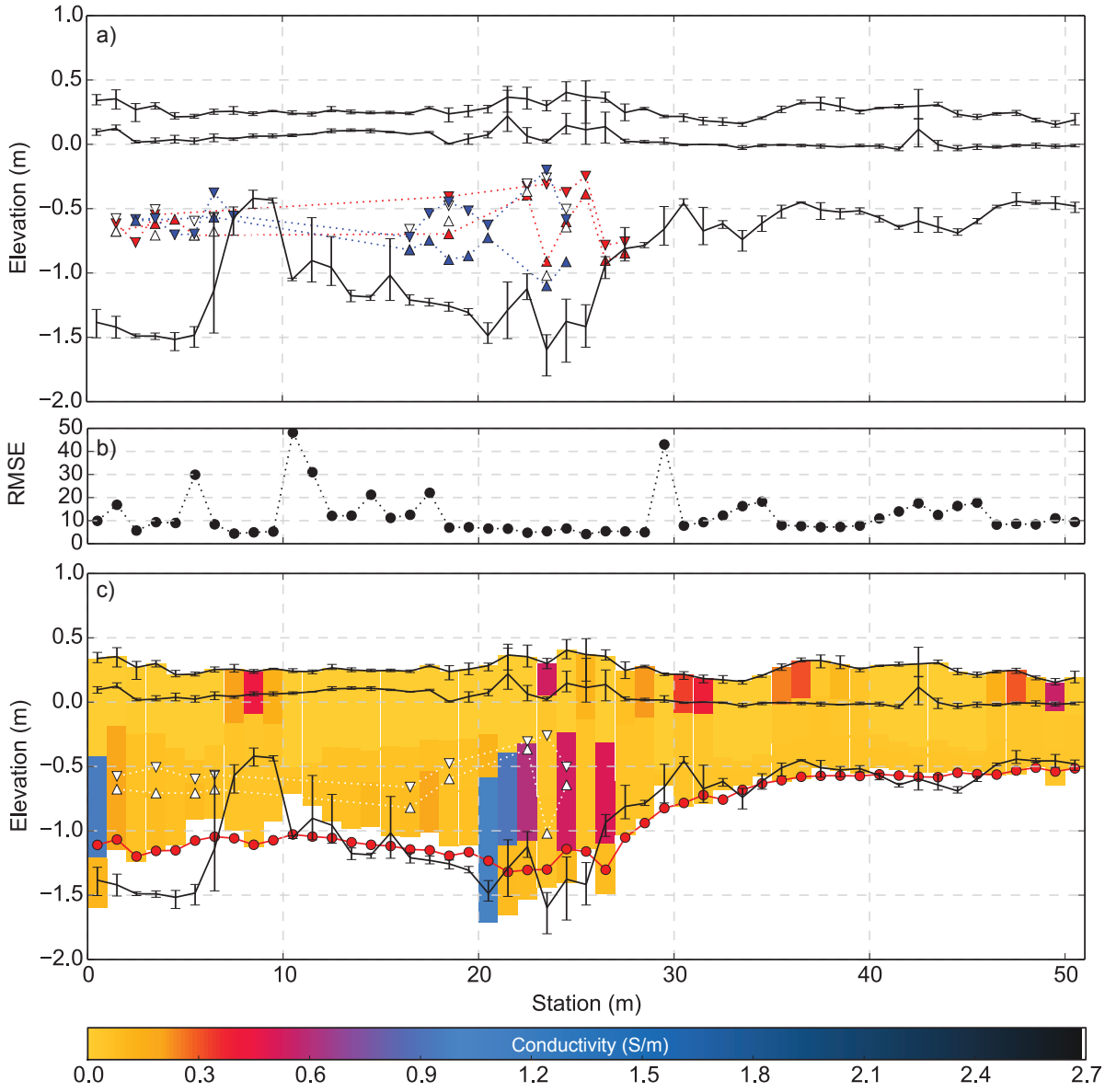

Figure 5.5.: Sea-ice pressure ridge R2 (data from 11 July 2013), comparison between data from drill-hole measurements and EM inversions. In a) snow, freeboards and sea ice of three parallel transects are shown with mean, minimum and maximum values. The internal voids are indicated for each of the three transects (blue, white, red) with down-pointing triangle for the upper border and with up-pointing triangles for the lower border. In b) the RMSE is shown for individual Marquardt-Levenberg inversions. In c) the reference data from a), the voids from the middle transect, and the sea-ice thickness from EMPEX processing (red) are superimposed the inversion results. The colors represent the retrieved conductivities.

Sea-ice pressure ridge R3

Sea-ice pressure ridge R3 (Figure 5.6) contains rafted sea ice with porous structures in the keel part and level sea ice on both transect sides. The sea-ice thickness of ridge R3 were accurately resolved for level sea ice at the beginning and the end of the transect. At location freeboards were observed close to zero, conductive layers were resolved by the algorithm throughout the transect. The small scale thin-ice feature between stations 28 and 30 was resolved reasonably well (blue cell). The voids of around 0.1 m in extend between stations 33 and 35 m could not be resolved; in contrast, the resulting sea-ice thickness was underestimated with 0.5 m. Compared to the total thicknesses from the inversion results, sea-ice thicknesses from the EMPEX approach performed equally well.

Sea-ice pressure ridge R4

Sea-ice pressure ridge R4 (Figure 5.7) contains 1 m thick level sea ice on one side of the transect and 5 m thick sea ice on the other side. A typical ridge sail and keel were because of the relative thinness of the thin sea ice not developed. Sea ice of ridge R4 was well resolved in thickness. Since there were no thick internal voids present, the algorithm probably performed better to find correct thicknesses. At 15 m, two floes were rafted and the sea-ice thickness became immediately thicker. At the transition from thin to thick sea ice a conductive layer was resolved by the inversion, collocated to confirmed gaps in the sea-ice layer. The box in Figure 5.7 (ridge R4) is enlarged in Figure 5.4b. Between stations 0-10 m, the freeboard was negative or close to zero, indicating wet snow. A conductive layer was resolved, which corresponds roughly to measured snow thickness. For thick sea ice, the EMPEX approach underestimated the true thickness. This might probably be an effect of the exponential fitting of the forward model, which leads due to an improper approximation to an underestimation of thick sea ice.

In general, the laterally-constrained Marquardt-Levenberg inversion algorithm performed well and additional information was gained compared to a simple 1D sea-ice thickness processing (EMPEX). The total sea-ice and snow thickness was well reproduced for level sea ice at the beginning and end of the transects. The topmost layer often contained high conductivities when the freeboard was close to zero or negative and snow potentially was conductive due to flooding. Internal porous structures in the ridge keel could be resolved as well, but the location and thickness of the structures were not always reproduced.

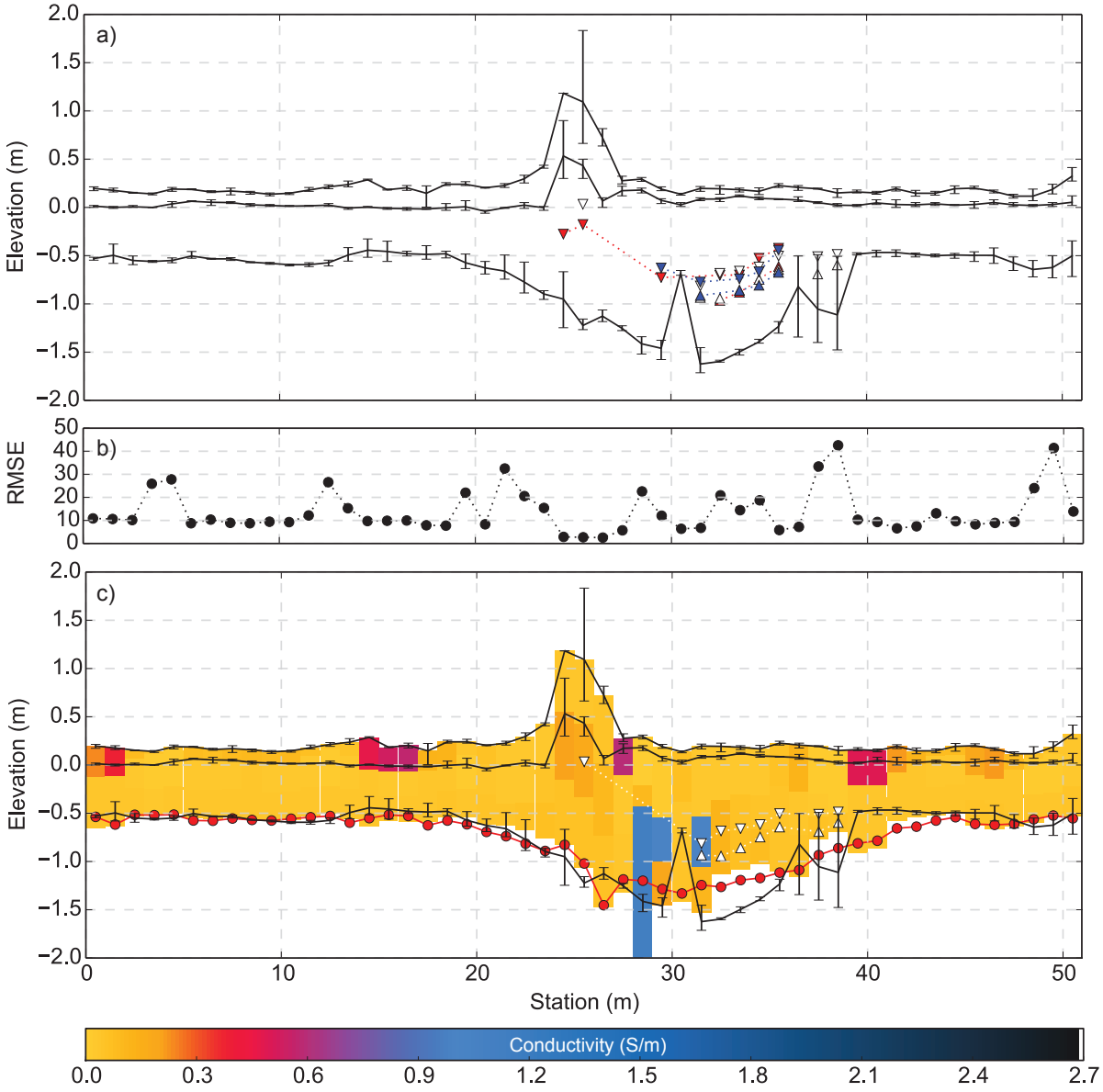

Figure 5.6.: Sea-ice pressure ridge R3 (data from 13 July 2013), comparison between data from drill-hole measurements and EM inversions. In a) snow, freeboards and sea ice of three parallel transects are shown with mean, minimum and maximum values. The internal voids are indicated for each of the three transects (blue, white, red) with down-pointing triangle for the upper border and with up-pointing triangles for the lower border. In b) the RMSE is shown for individual Marquardt-Levenberg inversions. In c) the reference data from a), the voids from the middle transect, and the sea-ice thickness from EMPEX processing (red) are superimposed the inversion results. The colors represent the retrieved conductivities.

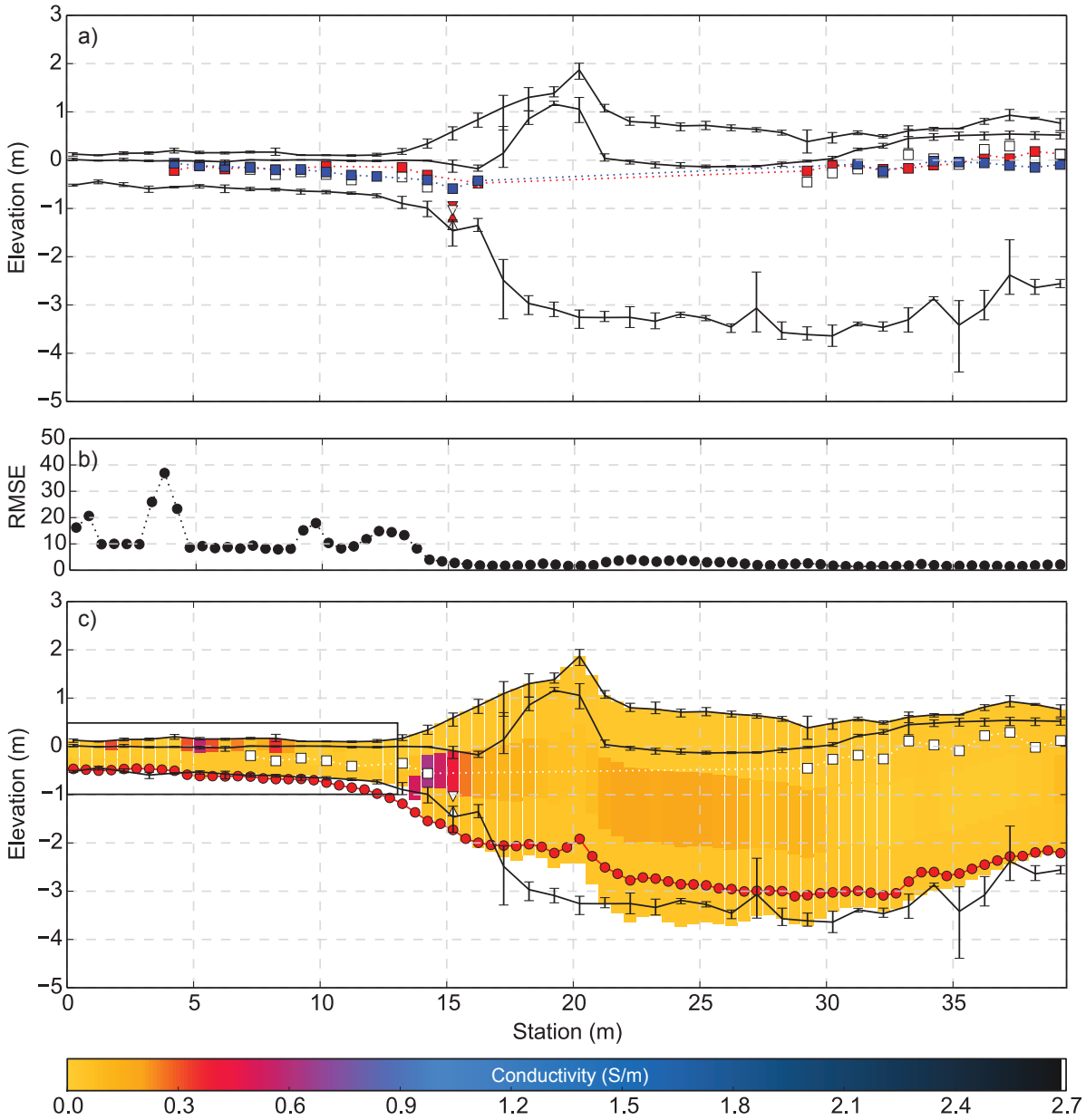

Figure 5.7.: Sea-ice pressure ridge R4 (data from 25 September 2013), comparison between data from drill-hole measurements and EM inversions. In a) snow, freeboards and sea ice of three parallel transects are shown with mean, minimum and maximum values. Porous sea ice is indicated with squares for each of the three transects (blue, white, red) and internal voids with down-pointing triangle for the upper border and with up-pointing triangles for the lower border (white, red). In b) the RMSE is shown for individual Marquardt-Levenberg inversions. In c) the reference data from a), the voids from the middle transect, and the sea-ice thickness from EMPEX processing (red) are superimposed the inversion results. The colors represent the retrieved conductivities. The enlargement of the box is shown in Figure 5.4b.

6 Conclusion and outlook

6.1. Key findings

Scientific background

Single-frequency EM sensors in the range from 4 to 10 kHz are and have been routinely employed for sea-ice thickness retrievals by various agencies (Kovacs and Holladay, 1990; Peterson et al., 2008; Haas et al., 2009). The assumption of a homogeneous half-space, and therefore resistive level sea ice, is justified for cold, dry and undeformed sea ice in this frequency range (Pfaffling and Reid, 2009). For measurements of all sea-ice types, including deformed sea ice with sub-footprint thickness variability, it has been shown that regional scale mean thickness estimates from EM sources generally agree well with data from other methods (Lindsay and Schweiger, 2015), though the probability density functions of sea-ice thicknesses might differ (Mahoney et al., 2015). Single-frequency EM data can be used to get insights of long-term thickness changes over decades (Haas et al., 2008b) or can be assimilated into numerical models. The benefit of using airborne EM data for seasonal sea-ice forecasting is shown in the paper by Lindsay et al. (2012) (Appendix A) at the example of sea-ice thickness data collected during this PhD project. This paper shows the usefulness of large-scale EM surveys even with a simplified interpretation of the EM response. However, my fist goal of the thesis was to evaluate the use of multi-frequency EM in sea-ice research to improve the understanding of the physics of different sea-ice regimes. The second goal was to provide from conductivity results additional information on internal sea-ice properties, such as the sea-ice porosity and the ice-volume fraction of the platelet layer. These are parameters, which add to the understanding of the physical state of sea ice and its changes, but which are beyond the capabilities of single-frequency EM to resolve.

Multi-frequency EM for sea-ice studies

The application of commercial multi-frequency EM handheld sensors for sea-ice surveying requires a thorough investigation of sensor characteristics in a cold and conductive environment. For data analysis the relative secondary magnetic field is used, for which the primary field needs to be decoupled from the measured magnetic field at the receiver. This is usually done with a bucking coil, which compensate the primary field at the receiver coil location. While this correction is assumed to be linear by instrument internal settings, the sensitivity of the bucking coil to the secondary field requires in highly conductive regimes, such as the seawater environment, a nonlinear correction. This effect was described first by Fitterman (1998), but it was never factored in processing of sea ice related EM data. However, a correction is usually not necessary for anomaly surveys on geological targets or if the relation between sea-ice thickness and the EM response of a given frequency is established by a functional dependence from in-field calibrations. But it is essential for my purpose, since the exponential relation (EMPEX) is often determined from approximations of actual EM forward models and geophysical inversion routines compare absolute measured to theoretical data. In Figure 6.1, the magnitude of the bucking bias is shown at the example of calibration data and the forward model with and without the bucking coil correction, calculated for a homogeneous half-space of 2.7 S/m and resistive sea ice (0 S/m). The maximal signal response of the forward model varies between 45000 and 100000 ppm, depending on whether the bucking bias is included or not. The difference of the two signal responses (with and without bucking coil) is highest for thin sea-ice regimes below a thickness of 2 m to the conductive seawater, which correspond to the most frequently measured sea-ice thicknesses in Arctic and Antarctic (Figure 6.1).

The implementation of the bucking bias in forward models (1st manuscript) and into two inversion algorithms (2nd manuscript) was therefore the logical consequence of using passively bucked EM sensors and a necessity for analyzing field data. The correct mathematical formulation was verified by inversions with and without the bucking coil, implying that sea ice < 2 m and its conductivity cannot be reproduced when the algorithms do not account for the bias (Figure 3.2).

Synthetic data for sensitivity studies

To show how well parameters theoretically can be resolved with a multi-frequency EM sensor, sensitivity studies were performed with two geophysical inversion algorithms, modified for the bucking bias. In the synthetic datasets, I accounted for multiple frequencies, instrumental noise, the specified coil separation, and typical subsurface thicknesses and

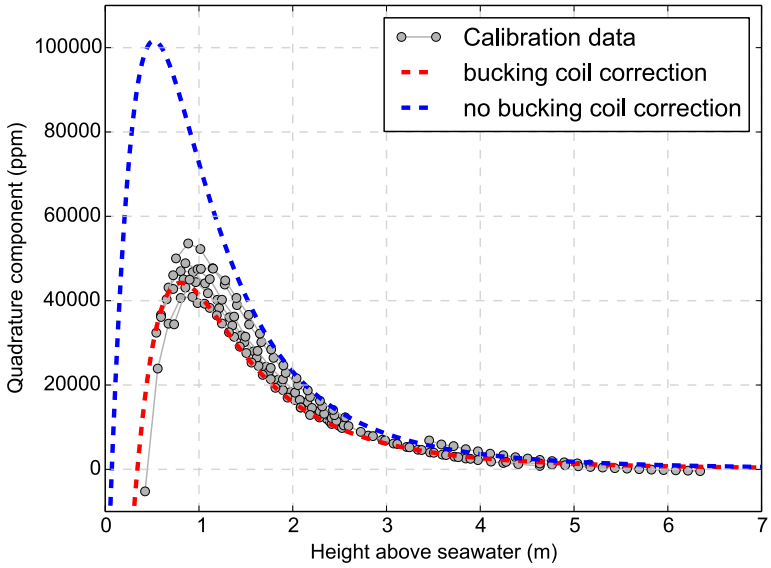

Figure 6.1.: Bucking bias illustrated with raw calibration data. Forward models were calculated with the quadrature 63 kHz component for a homogeneous half-space of 2.7 S/m and resistive sea ice (0 S/m), without (blue) and with (red) bucking coil correction. The corrected forward model shows a better agreement with calibration data over sea ice. Residual offsets between model and data show the effect of sea-ice conductivity at the different sites in 63 kHz data.

conductivities.

The first case describes level sea-ice with variable conductivity, consisting of two layers that represent sea ice and underlying seawater (2nd manuscript). This dataset accounted for plausible thicknesses, including rare cases of thick decadal landfast sea ice (0-10 m). The prescribed seawater conductivity is based on values typical for polar seas (2.7 S/m). Sea-ice conductivities which were used to calculate synthetic data (0-0.2 S/m) were estimated in the 1st manuscript by comparing calibration data of winter (Weddell Sea) and summer (Atka Bay) sea ice to forward modeled data of the 63 and 93 kHz quadrature components. The method is based on the fact that these frequencies are strongly depended on the sea-ice conductivity and already small changes shift the peaks of the respective calibration curves.

The next sensitivity study with synthetic data was tailored to situation with a sub-ice platelet layer (3rd manuscript). Here, the case of three layers of sea ice (0.05 S/m), the underlying platelet layer (1.15 S/m) and seawater (2.7 S/m) was chosen. The range of sea-ice thicknesses 0-4 m and platelet-layer thicknesses 0-10 m are based on independent field measurements. The platelet-layer conductivity of 1.15 S/m was obtained by finding

the smallest RMSE between EM calibration measurements and forward modeled data (1st manuscript). The sea-ice conductivity of 0.05 S/m is based on the high frequency EM data at selected calibration sites.

Two inversion strategies were subsequently employed for these two synthetic datasets: One with variable conductivity as a free parameter of multiple, but fixed layers (smoothness-constrained inversion) and a second approach, with less layers, but with thickness and conductivity as free parameters for each layer (Marquardt-Levenberg inversion).

From the first dataset, a variety of combinations of sea-ice thicknesses and conductivities were inverted with both inversion algorithms. Results imply that sea-ice thicknesses < 5 m and sea-ice conductivities within $\pm$ 0.01 S/m can be reliably reproduced (2nd manuscript). From the results of both algorithms I used, I conclude that for distinct layered cases, such as level sea ice, the Marquardt-Levenberg algorithm is more suitable, because it can reproduce the conductivity discontinuities, where the smoothness-constrained inversion will only yield gradients in conductivity.

Therefore only the Marquardt-Levenberg algorithm was used in the 3rd manuscript for the platelet-layer case with three distinct layers (sea ice, platelet layer and seawater). Conductivity and thickness of the sea ice and the platelet layer were free and unconstrained parameters in the inversion, only the conductivity of the ocean, was fixed at 2.7 S/m. This sensitivity study showed that the platelet-layer thickness limit of the EM sensor used in the field (GEM-2) was approximately 7 meter. Above this limit, the thickness of the platelet layer will very likely be underestimated by the inversion. But for typical sea-ice and platelet-layer thicknesses the inversion algorithm performed within acceptable limits for conditions found in Atka Bay. The platelet layer-thickness can be resolved reliably below 7 m and sea-ice and platelet-layer conductivities within $\pm$ 10 % (3rd manuscript).

EM field data for case studies

The evaluation of sensitivity studies with synthetic datasets and their promising results were subsequently followed by evaluation of actual EM field data. A therefore important part of my work was the validation of these EM results by independent measurements of sea-ice properties, such as thickness and porosity.

Porosity of level sea ice

First step was to compare conductivities from calibration experiments and forward models (63 and 93 kHz) to conductivities obtained from in total 15 sea-ice cores, which were taken in the summer Atka Bay from November-December 2012 and in the winter Weddell Sea

from June-August 2013 (1st manuscript). Sea-ice core temperatures and salinity were measured in 0.1 m intervals shortly after the cores were extracted from the sea ice to preserve the brine in the core. From these samples, brine conductivity was calculated according to Stogryn and Desargant (1985), and the porosity according to Cox and Weeks (1983) and Leppäranta and Manninen (1988).

The obtained parameters of the sea-ice cores (brine conductivity and porosity) are related to their bulk sea-ice conductivity by Archie's Law (Archie, 1942, Equation 2.3). This law was originally determined for saturated sandstones, but is also valid for other media and regularly applied in sea-ice research (e.g. Reid et al., 2006). Archie's Law also requires an empirical calculated cementation factor which depends on pore shapes and their connectivity. This factor may vary within one sea-ice core (Morey et al., 1984), but is usually assumed constant with a value of 1.75 (e.g. Haas et al., 1997; Worby et al., 1999). With the specifications from the above described sea-ice cores, i.e. brine conductivity and porosity, and the additionally assumed cementation factor, the bulk electrical conductivity of a sea-ice core can be calculated (Figure 6.2). Results indicate that summer sea ice (Atka Bay) was expectedly more conductive than winter sea ice (Weddell Sea) and thinner sea ice (< 1 m) in both region was generally more conductive than thicker sea ice (> 1 m). The obtained conductivities from sea-ice cores agree well with the conductivities obtained from comparison of EM data at different heights to forward models of the quadrature 63 and 93 kHz components. This implies that for level sea ice the bulk conductivity can be related to the bulk porosity in a meaningful way and that EM frequencies above 60 kHz can be used to retrieve bulk sea-ice conductivity with a reasonable accuracy (1st manuscript).

In the previous example, the brine volume and the brine conductivity were determined from temperature and salinity measurements of the sea-ice core and then converted to conductivity with Archie's Law, which depends only on the assumed cementation factor. From electromagnetic surveys, bulk conductivities can be retrieved, but the conversion to porosity is more difficult, since besides the cementation factor also the brine conductivity is unknown. This brine conductivity differs from summer to winter sea ice, since temperature and salinity changes and subsequently the bulk conductivity.

For calculations of the porosities from bulk conductivities, I used in the 2nd manuscript the mean brine conductivities of 4.69 ± 0.91 S/m, obtained from the Weddell Sea sea-ice cores. By further assuming a cementation factor of 1.75, a bulk conductivity of 0.06 S/m (average value from sea-ice cores), and uncertainties of bulk sea-ice conductivities obtained from our sensitivity studies ($\pm$ 0.01 S/m, 2nd manuscript), the porosity of level sea ice can be obtained within $\pm$ 1.2 %. Sea-ice cores from winter contain generally high brine

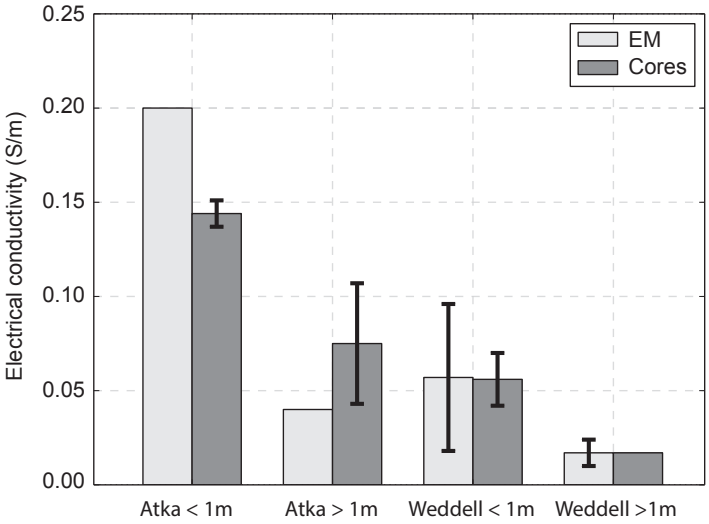

Figure 6.2.: Conductivity obtained from summer sea-ice cores in the Atka Bay 2012 (Atka) and from winter sea-ice cores in winter Weddell Sea 2013 (Weddell) in comparison to conductivities obtained from EM calibrations of the 63 and 93 kHz frequencies. Standard deviations are shown with error bars. Sea ice < 1 m are generally more conductive than those > 1 m.

conductivities due to the release of salt ions during freezing. Average brine conductivities of the summer Atka Bay sea-ice cores were for example lower with 2.7 ± 0.5 S/m. Since the bulk conductivity directly depends on the brine conductivity, it is a critical factor for the conversion from conductivity to porosity. By making situation depended assumptions for typical conditions during surveys, presented at the example for the conductivity-porosity conversion above, the overall uncertainty might decrease. Further, as shown with the good agreement of conductivities between sea-ice core conductivities and conductivities obtained from EM, the relation of Archie's Law is with reasonable assumptions valid for our purpose.

Platelet layer in Atka Bay

So far, I verified my EM derived sea-ice porosities with independent values obtained from sea-ice cores. Next step was to evaluate EM transect data of sea ice and underlying platelet layer, which represents with several layers a more complex 1D case in this thesis.

The EM data at the coring sites (1st manuscript) consisted of stationary measurements at different heights above the sea ice, where at each height the data was stacked to reduce sensor noise. Also, the sensor was always horizontally orientated. The transect data in Atka Bay (3rd manuscript) originates from a moving platform and could not be stacked and potential pitch or roll errors of the sensor add to the uncertainty of EM data. Also

the distance that had to be covered for a survey did not allow regular manual calibrations. The inversion of an actual field dataset with the presence of a sub-ice platelet layer was therefore meant as a full proof-of-concept for multi-frequency EM inversions.

In total 118 km of EM data were inverted with a Marquardt-Levenberg algorithm with additional implemented lateral constraints to smooth changes in horizontal direction (3rd manuscript). I inverted for three layers, where sea-ice and platelet-layer thicknesses and conductivities were allowed to vary during inversion. The ocean, the third layer, was fixed at 2.7 S/m. I used a RMSE and platelet-layer conductivity thresholds to exclude outliers. The calculation of the platelet layer ice-volume fraction (1-porosity) was again based on Archie's Law and was calculated from the measured platelet-layer conductivity. The cementation factor of the platelet layer was never determined before and therefore essentially unknown. This factor is different to the sea-ice case, since pore shapes are larger, different in shape and also the connectivity between pores must be assumed to be much larger than for a solid sea-ice matrix. Therefore, I used different cementation factors, whereas the best results were obtained with a factor of 3 (3rd manuscript). The loose ice platelets are surrounded by seawater and therefore the brine conductivity can safely be assumed to be the same to underlying seawater of 2.7 S/m (1st manuscript).

The resulting sea-ice and platelet-layer thicknesses and conductivities were in physically plausible ranges and in agreement with available validation data. The thickest platelet layer was found in the southwestern area of Atka Bay, where probably most ice platelets are released from the ice-shelf cavity. The thinnest layer was found in a zone, where sea ice broke up some months before our measurements started. From resulting conductivity distributions, I obtained an ice-volume fraction distribution with a peak at 0.29. The ice-volume fraction was generally smaller for thinner and younger platelet layer which is consistent with the assumption that an older thicker platelet layer is more compacted and dense compared to a thin layer.

For further validation of our results, we investigated in Hoppmann et al. (2015b) (Appendix B) the seasonal sea-ice and platelet-layer cycle. The results of platelet layer thickness and ice-volume fraction were generally in good agreement with results from EM data. On the same transect snow physical properties, i.e. snowpack temperature, density gradients and snow stratigraphies were measured with the goal to retrieve such properties from X-band SAR backscatter (Paul et al., 2015, Appendix D). For interpretation of my data, these snow properties were helpful, since for example conductive wet snow can influence the EM signal, as it was the case in the break-up area, where a topmost conductive layer was resolved by the inversion (3rd manuscript). Model studies in Atka Bay during the same time period (Hoppmann et al., 2015b, Appendix B) indicated mean

platelet-layer ice-volume fractions of 0.25 ± 0.1 with variabilities at different locations from 0.18 to 0.35. The lowermost value corresponded to the study site ATKA03, where an autonomous thermistor chain was installed (Hoppmann et al., 2015a, Appendix C), from which an ice-volume fraction of 0.18 ± 0.09 was obtained. The ice-volume fractions from EM conductivities agree well with these results, especially due to the fact that the thermistor chain was installed at the site with a thick platelet layer and lowest ice-volume fraction from the modeling study.

These results imply that we obtained consistent results from three different methods to determine ice-volume fractions of the platelet layer (modeling, thermistor chain, EM). With thermistor chains the platelet-layer thickness and the ice-volume fraction can be determined over lifetime of the buoy or floe at one location. But only with EM, the spatial variability of ice-volume fractions can be resolved.

The total volume of ice platelets is given by the product of ice-volume fraction, thickness and area. By accounting for incorporated ice platelets in the solid sea-ice layer and using from sporadic measurements the mean platelet-layer thickness of 4 m in December 2012, a total annual platelet volume of 0.57 km^3 was found in the study of Hoppmann et al. (2015b) (Appendix B). Taking the spatial variability from EM measurements into account, I retrieved besides thin platelet layers in the break-up area modes of platelet-layer thicknesses at 4.3 and 5.5 m (Figure 4.2). This may indicate that the annual platelet volume might have been even higher in winter 2012 than 0.57 km^3.

Deformed sea ice

1D inversions of single or multiple layers showed promising results. In a last case study I inverted EM data from deformed sea ice, where a 1D geometry is usually not valid and the forward model is a simplification of the complex geometry. The goal here was to evaluate macro-scale porosity estimations directly from conductivity results and to investigate the usefulness of approximating a 2D porous sea-ice feature with several 1D layers.

The field data over several sea-ice pressure ridges were inverted with the laterally-constrained Marquardt-Levenberg inversion algorithm, conductivities and thicknesses were free to vary in the three upper layers and the fourth layer was fixed at a conductivity of 2.7 S/m (seawater). RMSE values were for most of the transects small, indicating that a minimum was found within the data uncertainty. The resolved conductivities and thicknesses, though not constrained by a priori information, were in a plausible range.

Comparisons of inversion results with the data from coincident drill-hole surveys showed in general a good agreement of general pressure ridge shapes, and were expectedly best in level sea-ice areas. Often a highly conductive top layer was found in the inversion

result, which might have been caused by submerged and flooded sea ice to the sides of the ridge. Validation data support this result with findings of negative freeboards in the affected areas. Porous structures could be resolved as layers of elevated conductivity to some degree, but often the locations of these structures were not correctly reproduced. Furthermore, the total sea-ice thickness in the keel part was often resolved too thin. This is most likely the effect of the inability of the 1D forward models to represent 2D geometries. For triangular shaped ridge keels, this leads to the long known underestimations in total sea-ice thickness (e.g. Pfaffling and Reid, 2009). However, it was shown that this underestimation is smaller in the multiple-layer case than in the homogeneous half-space approach used for single-frequency EM data. Whether this is a sign that the effects of macro-scale porosity and geometry can be separated in a 2D inversion scheme cannot be answered with these results alone. But with refinements it might be possible to classify ridges as porous or consolidated, without knowing their exact thickness.

6.2. Implications

The results from this thesis will stimulate the use of multi-frequency EM surveys not only for sea-ice applications. The awareness of the bucking bias is essential for all advanced geophysical analysis tools, not only for the 1D inversions or the EMPEX scheme that have been shown here. Only with the inclusion of the nonlinear factor, the EM response of a passively bucked system can be assigned to a physically correct subsurface conductivity structure. Besides the cases of sea-ice thickness and porosity, this finding affects EM studies in other high conductive regimes, for example the mapping of permafrost regions, were EM induction is a useful tool as well (Dafflon et al., 2013). For sea-ice studies, the next step is the broader and regular use of multi-frequency EM to obtain a comprehensive dataset of internal sea-ice properties of different sea-ice regimes.

A promising application is the evaluation of the spatial distribution of Arctic summer sea-ice porosity. In summer, sea ice often contains large pores due to melting, which are filled with a mixture of fresh and saline brine (Vancoppenolle et al., 2007; Tison et al., 2008). The connectivity of the pores have an influence on the biogeochemistry of sea ice, most notably the presence and vertical distribution of gases and nutrients (Arrigo et al., 1997). Providing a method for large scale sea-ice porosity retrieval may solve the problem of unknown internal sea-ice properties, since manual coring is insufficient to map the spatial distribution in the amount of time that is usually available for on-ice field work.

But also mass balance estimations with satellite remote sensing benefit from a better knowledge of sea-ice porosity. The density of sea-ice, which can be retrieved from porosities (Timco and Frederking, 1996), is required for the transformation of freeboard into thickness that is used by satellite altimetry (e.g. Ricker et al., 2014). Currently, the spatial and temporal variability is only sparsely constrained by field observations, but thickness dependent sea-ice density parameterizations are being discussed (Kwok and Cunningham, 2015).

Sea-ice porosity is further related to internal sea-ice compressive strength (Moslet, 2007), which is used for parametrization of numerical models, e.g. for evaluation of the influence on ocean circulation (Itkin et al., 2014). Sea-ice strength is also an important parameter for shipping industry and offshore facilities, since weaker sea ice will reduce the sea-ice load on ships or structures.

Platelet-layer formation is a direct result of ocean-ice shelf interaction. In a changing climate and possible warmer ocean waters, basal melt of ice shelves may increase (Holland et al., 2008) which leads to fresher surface waters (Hellmer et al., 2012). In supercooled conditions below ice shelves, ice platelet grow might enhance and in case temperatures are sufficiently low also accumulate below landfast sea ice. From regular platelet-volume estimations, it might therefore be possible to investigate processes in the inaccessible ice-shelf cavities with respect to basal melting rates and their effect on sea-ice formation in the southern ocean (Hunkeler et al., 2016b).

The influence of platelet-layer formation on solid sea ice is the additional ice growth which is not caused by the conductive flux to the atmosphere. Incorporation of ice platelets in the solid sea ice thus represent a heat loss to the ocean (Hoppmann et al., 2015b, Appendix A). Ice platelets therefore not only change the mass but also the energy balance of sea ice. By mapping sea ice and the platelet layer with electromagnetic induction sounding, the heat fluxes (Hoppmann et al., 2015a, Appendix B) might be better quantified towards a better understanding of this energy balance.

Sea-ice mass-balance studies with satellite altimetry also require the knowledge of platelet-layer thickness and ice-volume fraction to quantify their effect on the isostatic balance of the total sea-ice column (Rack et al., 2013; Price et al., 2014). Knowing locally more about the platelet-layer distribution from multi-frequency EM, might lead to improved large-scale estimations in combination with remote sensing methods.

My thesis showed that with multiple frequencies it is potentially feasible to distinguish between porous and consolidated ridges. Furthermore, flooded sea ice was indicated in

inversion results with a highly conductive top-layer. However, the true thickness and the locations of the voids were not correctly resolved. A significant amount of Arctic sea-ice volume is located in sea-ice pressure ridges and a better characterization would again improve knowledge of the sea-ice volume budget. Topographic feature influence oceanic circulation (Castellani et al., 2014) and an enhanced pressure-ridge characterization might improve the parametrization of numerical climate models. But to map sub-footprint scale sea-ice geometries accurately, the evaluation of the EM response should not be based on layers, but on a more complex geometry and therefore should incorporate several adjacent stations. Only this approach allows to circumvent the limitations of a 1D interpretation that causes the footprint smoothing of deformed sea-ice features for single-frequency and multi-frequency EM data alike.

The work of this thesis is based on measurements with a handheld sensor, since the multi-frequency EM studies needed to be done in high resolution and in controlled environments with corresponding validation data. First steps are already in place to use broad-band sensors in airborne applications (Pfaffhuber and Hendricks, 2014), though not necessary with the large frequency range of the specific handheld sensor. While the frequency range for the airborne sensor MAiSIE (Pfaffhuber et al., 2012a) was designed for deformed sea-ice studies, an extension towards the range of 60 kHz or higher might lead to an increased sensitivity also for the internal properties of level sea ice.

Bibliography

W. L. Anderson. Numerical integration of related Hankel transforms of orders 0 and 1 by adaptive digital filtering. *Geophysics*, 44(7):1287–1305, 1979.

G. E. Archie. The electrical resistivity log as an aid in determining some reservoir characteristics. *Trans. AIMe*, 146(99):54–62, 1942.

K. R. Arrigo, D. H. Robinson, and C. W. Sullivan. A high resolution study of the platelet ice ecosystem in McMurdo Sound, Antarctica: photosynthetic and bio-optical characteristics of a dense microalgal bloom. *Marine ecology progress series. Oldendorf*, 98(1):173–185, 1993.

K. R. Arrigo, G. Dieckmann, M. Gosselin, D. H. Robinson, C. H. Fritsen, and C. W. Sullivan. High resolution study of the platelet ice ecosystem in McMurdo Sound, Antarctica: biomass, nutrient, and production profiles within a dense microalgal bloom. *Oceanographic Literature Review*, 6(43):557, 1996.

K. R. Arrigo, D. L. Worthen, M. P. Lizotte, P. Dixon, and G. Dieckmann. Primary production in Antarctic sea ice. *Science*, 276(5311):394–397, 1997.

K. R. Arrigo, T. Mock, and M. P. Lizotte. Primary producers and sea ice. In *Sea Ice*, pages 283–325. Wiley-Blackwell, 2010.

E. Auken, A. V. Christiansen, B. H. Jacobsen, N. Foged, and K. I. Sørensen. Piecewise 1D laterally constrained inversion of resistivity data. *Geophysical Prospecting*, 53(4): 497–506, 2005.

R. Bintanja, G. J. van Oldenborgh, S. S. Drijfhout, B. Wouters, and C. A. Katsman. Important role for ocean warming and increased ice-shelf melt in Antarctic sea-ice expansion. *Nature Geoscience*, 6(5):376–379, 2013.

M. A. Brandon, F. R. Cottier, and F. Nilsen. Sea ice and oceanography. In *Sea Ice*, pages 79–111. Wiley-Blackwell, 2010.

R. Brodie and M. Sambridge. A holistic approach to inversion of frequency-domain airborne em data. *Geophysics*, 71(6):G301–G312, 2006.

G. Castellani, M. Losch, and R. Gerdes. Sea ice drag as function of deformation and ice cover: Effects on simulated sea ice and ocean circulation in the Arctic. In *Momentum exchange between atmosphere, sea ice and ocean*, pages 58–80. PhD Thesis, Jacobs University Bremen, 2014.

J. C. Comiso. Variability and trends of the global sea ice cover. In *Sea Ice*, pages 205–246. Wiley-Blackwell, 2010.

J. C. Comiso and D. K. Hall. Climate trends in the Arctic as observed from space. *Wiley Interdisciplinary Reviews: Climate Change*, 5(3):389–409, 2014.

G. F. N. Cox and W. F. Weeks. Equations for determining the gas and brine volumes in sea ice samples. *Journal of Glaciology*, 29(102):306–316, 1983.

G. Crocker. Physical processes in Antarctic landfast sea ice. pages 240–247. PhD Thesis, University of Cambridge, 1988.

B. Dafflon, S. S. Hubbard, C. Ulrich, and J. E. Peterson. Electrical conductivity imaging of active layer and permafrost in an Arctic ecosystem, through advanced inversion of electromagnetic induction data. *Vadose Zone Journal*, 12(4), 2013.

D. E. Dempsey, P. J. Langhorne, N. J. Robinson, M. J. M. Williams, T. G. Haskell, and R. D. Frew. Observation and modeling of platelet ice fabric in McMurdo Sound, Antarctica. *Journal of Geophysical Research: Oceans (1978–2012)*, 115(C1), 2010.

M. Deszcz-Pan, D. V. Fitterman, and V. F. Labson. Reduction of inversion errors in helicopter em data using auxiliary information. *Exploration Geophysics*, 29(2):142–146, 1998.

G. S. Dieckmann and H. H. Hellmer. The importance of sea ice: An overview. In *Sea Ice*, pages 1–22. Wiley-Blackwell, 2010.

M. L. Druckenmiller, H. Eicken, M. A. Johnson, D. J. Pringle, and C. C. Williams. Toward an integrated coastal sea-ice observatory: System components and a case study at Barrow, Alaska. *Cold Regions Science and Technology*, 56(2):61–72, 2009.

H. Eicken and M. A. Lange. Development and properties of sea ice in the coastal regime of the southeastern Weddell Sea. *Journal of Geophysical Research: Oceans (1978–2012)*, 94(C6):8193–8206, 1989.

H. Eicken, W. B. Tucker, and D. K. Perovich. Indirect measurements of the mass balance of summer Arctic sea ice with an electromagnetic induction technique. *Annals of Glaciology*, 33(1):194–200, 2001.

H. Eicken, H. R. Krouse, D. Kadko, and D. K. Perovich. Tracer studies of pathways and rates of meltwater transport through Arctic summer sea ice. *Journal of Geophysical Research: Oceans (1978–2012)*, 107(C10):SHE–22, 2002.

I. Eisenman, W. N. Meier, and J. R. Norris. A spurious jump in the satellite record: has Antarctic sea ice expansion been overestimated? *The Cryosphere*, 8(4):1289–1296, 2014.

E. Fahrbach, G. Rohardt, and G. Krause. The Antarctic Coastal Current in the Southeastern Weddell Sea. *Polar Biology*, 12(2):171–182.

C. G. Farquharson. *Background for Program EM1DFM*. University of British Columbia, 2000.

C. G. Farquharson and D. W. Oldenburg. Inversion of time-domain electromagnetic data for a horizontally layered Earth. *Geophysical Journal International*, 114(3):433–442, 1993.

C. G. Farquharson and D. W. Oldenburg. Approximate sensitivities for the electromagnetic inverse problem. *Geophysical Journal International*, 126(1):235–252, 1996.

C. G. Farquharson, D. W. Oldenburg, and P. S. Routh. Simultaneous 1D inversion of loop-loop electromagnetic data for magnetic susceptibility and electrical conductivity. *Geophysics*, 68(6):1857–1869, 2003.

D. V. Fitterman. Sources of calibration errors in helicopter EM data. *Exploration Geophysics*, 29(1/2):65–70, 1998.

D. V. Fitterman and C. Yin. Effect of bird maneuver on frequency-domain helicopter EM response. *Geophysics*, 69(5):1203–1215, 2004.

A. Foldvik and T. Kvinge. Conditional instability of sea water at the freezing point. *Deep Sea Research and Oceanographic Abstracts*, 21(3):169–174, 1974.

P. Fretwell, H. D. Pritchard, D. G. Vaughan, J. L. Bamber, N. E. Barrand, R. Bell, C. Bianchi, R. G. Bingham, D. D. Blankenship, G. Casassa, et al. Bedmap2: improved ice bed, surface and thickness datasets for Antarctica. *The Cryosphere*, 7(1):375–393, 2013.

F. C. Frischknecht, V. F. Labson, B. R. Spies, and W. L. Anderson. Profiling methods using small sources. *Electromagnetic methods in applied geophysics*, 2:105–270, 1991.

P. E. Gill, W. Murray, and M. H. Wright. *Practical optimization*. Academic Press, London, 1981.

P. Glover. What is the cementation exponent? a new interpretation. *The Leading Edge*, 28(1):82–85, 2009.

P. W. J. Glover, J. B. Gómez, P. G. Meredith, K. Hayashi, P. R. Sammonds, and S. A. F. Murrell. Damage of saturated rocks undergoing triaxial deformation using complex electrical conductivity measurements: Experimental results. *Physics and Chemistry of the Earth*, 22(1–2):57 – 61, 1997.

K. M. Golden, H. Eicken, A. L. Heaton, J. Miner, D. J. Pringle, and J. Zhu. Thermal evolution of permeability and microstructure in sea ice. *Geophysical research letters*, 34 (16), 2007.

T. A. Gosink, J. G. Pearson, and J. J. Kelley. Gas movement through sea ice. *Nature*, 263(5572):41–42, 1976.

A. J. Gough, A. R. Mahoney, P. J. Langhorne, M. J. M. Williams, N. J. Robinson, and T. G. Haskell. Signatures of supercooling: McMurdo Sound platelet ice. *Journal of Glaciology*, 58(207):38–50, 2012.

M. S. Grab. Forward and inverse modelling of frequency-domain electromagnetic data from small coils. *Master Thesis, IDEA League, ETH Zurich*, 2012.

S. Günther and G. S. Dieckmann. Seasonal development of algal biomass in snow-covered fast ice and the underlying platelet layer in the Weddell Sea, Antarctica. *Antarctic Science*, 11(3):305–315, 1999.

C. Haas. Evaluation of ship-based electromagnetic-inductive thickness measurements of summer sea-ice in the Bellingshausen and Amundsen Seas, Antarctica. *Cold Regions Science and Technology*, 27(1):1–16, 1998.

C. Haas. Late-summer sea ice thickness variability in the Arctic Transpolar Drift 1991–2001 derived from ground-based electromagnetic sounding. *Geophysical research letters*, 31(9):L09402, 2004.

C. Haas. Dynamics versus thermodynamics: The sea ice thickness distribution. In *Sea Ice*, pages 113–151. Wiley-Blackwell, 2010.

C. Haas and P. Jochmann. Continuous EM and ULS thickness profiling in support of ice force measurements. In *Proceedings of the 17th International Conference on Port and Ocean Engineering under Arctic Conditions, POAC ´03*, 2003.

C. Haas, S. Gerland, H. Eicken, and H. Miller. Comparison of sea-ice thickness measurements under summer and winter conditions in the Arctic using a small electromagnetic induction device. *Geophysics*, 62(3):749–757, 1997.

C. Haas, M. Nicolaus, S. Willmes, A. Worby, and D. Flinspach. Sea ice and snow thickness and physical properties of an ice floe in the western Weddell Sea and their changes during spring warming. *Deep Sea Research Part II: Topical Studies in Oceanography*, 55(8):963–974, 2008a.

C. Haas, A. Pfaffling, S. Hendricks, L. Rabenstein, J. Etienne, and I. Rigor. Reduced ice thickness in Arctic Transpolar Drift favors rapid ice retreat. *Geophysical Research Letters*, 35(17):L17501, 2008b.

C. Haas, J. Lobach, S. Hendricks, L. Rabenstein, and A. Pfaffling. Helicopter-borne measurements of sea ice thickness, using a small and lightweight, digital EM system. *Journal of Applied Geophysics*, 67(3):234–241, 2009.

C. Haas, S. Hendricks, H. Eicken, and A. Herber. Synoptic airborne thickness surveys reveal state of Arctic sea ice cover. *Geophysical Research Letters*, 37(9):L09501, 2010.

H. H. Hellmer. Impact of Antarctic ice shelf basal melting on sea ice and deep ocean properties. *Geophysical Research Letters*, 31(L10307), 2004.

H. H. Hellmer, F. Kauker, R. Timmermann, J. Determann, and J. Rae. Twenty-first-century warming of a large Antarctic ice-shelf cavity by a redirected coastal current. *Nature*, 485(7397):225–228, 2012.

S. Hendricks. Validierung von altimetrischen Meereisdickenmessungen mit einem helikopter-basierten elektromagnetischen Induktionsverfahren. PhD Thesis, University Bremen, 2009.

J. S. Holladay, J. R. Rossiter, and A. Kovacs. Airborne measurement of sea ice thickness using electromagnetic induction sounding. In *Proceedings of the Ninth International Conference of Offshore Mechanics and Arctic Engineering*, pages 309–315, 1990.

J. S. Holladay, R. Z. Moucha, and S. J. Prinsenberg. Airborne Electromagnetic Sea Ice Sounding Measurements During SIMMS'95. *Canadian Contractor Report of Hydrography and Ocean Sciences 50*, 1998.

P. R. Holland, A. Jenkins, and D. M. Holland. The response of ice shelf basal melting to variations in ocean temperature. *Journal of Climate*, 21(11):2558–2572, 2008.

M. Hoppmann, M. Nicolaus, P. A. Hunkeler, P. Heil, L.-K. Behrens, G. König-Langlo, and R. Gerdes. Seasonal evolution of an ice-shelf influenced fast-ice regime, derived from an autonomous thermistor chain. *Journal of Geophysical Research: Oceans*, 120, 2015a.

M. Hoppmann, M. Nicolaus, S. Paul, P. A. Hunkeler, G. Heinemann, S. Willmes, R. Timmermann, O. Boebel, T. Schmidt, M. Kühnel, G. König-Langlo, and R. Gerdes. Ice platelets below Weddell Sea landfast sea ice. *Annals of Glaciology*, 56(69):175–190, 2015b.

KG Hughes, PJ Langhorne, GH Leonard, and CL Stevens. Extension of an ice shelf water plume model beneath sea ice with application in mcmurdo sound, antarctica. *Journal of Geophysical Research: Oceans*, 2014.

P. A. Hunkeler, S. Hendricks, M. Hoppmann, S. Paul, and R. Gerdes. Towards an estimation of sub sea-ice platelet-layer volume with multi-frequency electromagnetic induction sounding. *Annals of Glaciology*, 56(69):137–146, 2015.

P. A. Hunkeler, S. Hendricks, M. Hoppmann, C. G. Farquharson, T. Kalscheuer, M. Grab, M. S. Kaufmann, L. Rabenstein, and R. Gerdes. Improved 1D inversions for sea ice thickness and conductivity from electromagnetic induction data: Inclusion of nonlinearities caused by passive bucking. *Geophysics*, 81(1):45–58, 2016a.

P. A. Hunkeler, M. Hoppmann, S. Hendricks, T. Kalscheuer, and R. Gerdes. A glimpse beneath Antarctic sea ice: Platelet layer volume from multifrequency electromagnetic induction sounding. *Geophysical Research Letters*, 43(1):222–231, 2016b.

S. M. Hvidegaard and R. Forsberg. Sea-ice thickness from airborne laser altimetry over the Arctic Ocean north of Greenland. *Geophysical Research Letters*, 29(20):13–1, 2002.

P. Itkin, M. Karcher, and R. Gerdes. Is weaker Arctic sea ice changing the Atlantic water circulation? *Journal of Geophysical Research: Oceans*, 119(9):5992–6009, 2014.

D. D. Jackson. Most squares inversion. *Journal of Geophysical Research*, 81(5):1027–1030, 1976.

P. D. Jackson, D. T. Smith, and P. N. Stanford. Resistivity-porosity-particle shape relationships for marine sands. *Geophysics*, 43(6):1250–1268, 1978.

R. Jaiser, K. Dethloff, D. Handorf, A. Rinke, and J. Cohen. Impact of sea ice cover changes on the Northern Hemisphere atmospheric winter circulation. *Tellus A*, 64, 2012.

M. O. Jeffries, W. F. Weeks, R. Shaw, and K. Morris. Structural characteristics of congelation and platelet ice and their role in the development of Antarctic land-fast sea ice. *Journal of Glaciology*, 39(132):223–238, 1993.

James R. Jordan, Satoshi Kimura, Paul R. Holland, Adrian Jenkins, and Matthew D. Piggott. On the conditional frazil ice instability in seawater. *Journal of Physical Oceanography*, 45(4):1121–1138, 2015.

D. L. B. Jupp and K. Vozoff. Stable iterative methods for the inversion of geophysical data. *Geophysical Journal International*, 42(3):957–976, 1975.

T. Kalscheuer. EMILIA - ElectroMagnetic Inversion with Least Intricate Algorithms User manual. Technical report, Uppsala University, Department of Earth Sciences, 2014.

T. Kalscheuer and L. B. Pedersen. A non-linear truncated SVD variance and resolution analysis of two-dimensional magnetotelluric models. *Geophysical Journal International*, 169(2):435–447, 2007.

T. Kalscheuer, M. García, N. Meqbel, and L. B. Pedersen. Non-linear model error and resolution properties from two-dimensional single and joint inversions of direct current resistivity and radiomagnetotelluric data. *Geophysical Journal International*, 182(3): 1174–1188, 2010.

T. Kalscheuer, J. Hübert, A. Kuvshinov, T. Lochbühler, and L. B. Pedersen. A hybrid regularization scheme for the inversion of magnetotelluric data from natural and controlled sources to layer and distortion parameters. *Geophysics*, 77(4):E301–E315, 2012.

T. Kalscheuer, M. Bastani, S. Donohue, L. Persson, A. Pfaffhuber, F. Reiser, and Z. Ren. Delineation of a quick clay zone at Smørgrav, Norway, with electromagnetic methods under geotechnical constraints. *Journal of Applied Geophysics*, 92:121–136, 2013.

Thomas Kalscheuer, Sarah Blake, Joel E. Podgorski, Frederic Wagner, Alan G. Green, Mark Muller, Alan G. Jones, Hansruedi Maurer, Ongkopotse Ntibinyane, and Gomotsang Tshoso. Joint inversions of three types of electromagnetic data explicitly constrained by seismic observations: results from the central Okavango Delta, Botswana. *Geophysical Journal International*, 202(3):1429–1452, 2015.

M. S. Kaufmann. Pseudo 2D inversion of multi-frequency coil-coil FDEM data. *Master Thesis, IDEA League, ETH Zurich*, 2014.

C. Köberle and R. Gerdes. Mechanisms determining the variability of Arctic sea Ice conditions and export. *Journal of Climate*, 16:2843–2858, 2003.

J. Kipfstuhl. On the formation of underwater ice and the growth and energy budget of the sea ice in Atka Bay, Antarctica (Zur Entstehung von Unterwassereis und das Wachstum und die Energiebilanz des Meereises in der Atka Bucht, Antarktis. *Reports on Polar and Marine Research (Berichte zur Polarforschung)*, 85:88p, 1991.

A. Kovacs. Sea ice: Part II. Estimating the full-scale tensile, flexural, and compressive strength of first-year ice. Technical report, DTIC Document, 1996.

A. Kovacs and J. S. Holladay. Sea-ice thickness measurement using a small airborne electromagnetic sounding system. *Geophysics*, 55(10):1327–1337, 1990.

A. Kovacs and R. M. Morey. Sounding sea ice thickness using a portable electromagnetic induction instrument. *Geophysics*, 56(12):1992–1998, 1991.

A. Kovacs, J. S. Holladay, and C. J. Bergeron. The footprint/altitude ratio for helicopter electromagnetic sounding of sea-ice thickness: Comparison of theoretical and field estimates. *Geophysics*, 60(2):374–380, 1995.

C. Krembs, H. Eicken, and J. W. Deming. Exopolymer alteration of physical properties of sea ice and implications for ice habitability and biogeochemistry in a warmer Arctic. *Proceedings of the National Academy of Sciences*, 108(9):3653–3658, 2011.

R. Kwok and G. F. Cunningham. ICESat over Arctic sea ice: Estimation of snow depth and ice thickness. *Journal of Geophysical Research: Oceans (1978–2012)*, 113(C8): C08010, 2008.

R. Kwok and G. F. Cunningham. Variability of Arctic sea ice thickness and volume from CryoSat-2. *Philosophical Transactions of the Royal Society of London A: Mathematical, Physical and Engineering Sciences*, 373(2045):20140157, 2015.

R. Kwok, G. F. Cunningham, M. Wensnahan, I. Rigor, H. J. Zwally, and D. Yi. Thinning and volume loss of the Arctic Ocean sea ice cover: 2003-2008. *Journal of Geophysical Research: Oceans (1978–2012)*, 114:C07005, 2009.

R Kwok, G Spreen, and S Pang. Arctic sea ice circulation and drift speed: Decadal trends and ocean currents. *Journal of Geophysical Research: Oceans*, 118(5):2408–2425, 2013.

P. J. Langhorne, K. G. Hughes, A. J. Gough, I. J. Smith, M. J. M. Williams, N. J. Robinson, C. L. Stevens, W. Rack, D. Price, G. H. Leonard, A. R. Mahoney, C. Haas, and T. G. Haskell. Observed platelet ice distributions in antarctic sea ice: An index for ocean-ice shelf heat flux. *Geophysical Research Letters*, 42(13):5442–5451, 2015.

A. M. Le Brocq, A. J. Payne, and A. Vieli. An improved Antarctic dataset for high resolution numerical ice sheet models (ALBMAP v1). *Earth System Science Data Discussions*, 3(1):195–230, 2010.

M. Leppäranta and T. Manninen. The brine and gas content of sea ice with attention to low salinities and high temperatures. *Internal Report 88-2, Helsinki*, 1988.

E. L. Lewis and R. G. Perkin. Ice pumps and their rates. *Journal of Geophysical Research: Oceans (1978–2012)*, 91(C10):11756–11762, 1986.

R. Lindsay and A. Schweiger. Arctic sea ice thickness loss determined using subsurface, aircraft, and satellite observations. *The Cryosphere*, 9(1):269–283, 2015.

R. Lindsay, C. Haas, S. Hendricks, P. Hunkeler, N. Kurtz, J. Paden, B. Panzer, J. Sonntag, J. Yungel, and J. Zhang. Seasonal forecasts of Arctic sea ice initialized with observations of ice thickness. *Geophysical Research Letters*, 39(21), 2012.

R. W. Lindsay and J. Zhang. The thinning of Arctic sea ice, 1988-2003: Have we passed a tipping point? *Journal of Climate*, 18(22):4879–4894, 2005.

L. R. Lines and S. Treitel. Tutorial: A review of least-squares inversion and its application to geophysical problems. *Geophysical prospecting*, 32(2):159–186, 1984.

G. Liu and A. Becker. Two-dimensional mapping of sea-ice keels with airborne electromagnetics. *Geophysics*, 55(2):239–248, 1990.

A. R. Mahoney, A. J. Gough, P. J. Langhorne, N. J. Robinson, C. L. Stevens, M. M. J. Williams, and T. G. Haskell. The seasonal appearance of ice shelf water in coastal Antarctica and its effect on sea ice growth. *Journal of Geophysical Research: Oceans (1978–2012)*, 116(C15):11032, 2011.

A. R. Mahoney, H. Eicken, Y. Fukamachi, K. I. Ohshima, D. Simizu, C. Kambhamettu, M. V. Rohith, S. Hendricks, and J. Jones. Taking a look at both sides of the ice: comparison of ice thickness and drift speed as observed from moored, airborne and shore-based instruments near Barrow, Alaska. *Annals of Glaciology*, 56(69):363, 2015.

J. Maslanik, J. Stroeve, C. Fowler, and W. Emery. Distribution and trends in Arctic sea ice age through spring 2011. *Geophysical Research Letters*, 38:L13502, 2011.

R. A. Massom and S. E. Stammerjohn. Antarctic sea ice change and variability–physical and ecological implications. *Polar Science*, 4(2):149–186, 2010.

J. C. Maxwell. A treatise on electricity and magnetism. 1873.

W. N. Meier, G. K. Hovelsrud, B. E. H. van Oort, J. R. Key, K. M. Kovacs, C. Michel, C. Haas, M. A. Granskog, S. Gerland, D. K. Perovich, A. Makshtas, and J. D. Reist. Arctic sea ice in transformation: A review of recent observed changes and impacts on biology and human activity. *Reviews of Geophysics*, pages 185–217, 2014.

M. A. Meju. Biased estimation: a simple framework for inversion and uncertainty analysis with prior information. *Geophysical Journal International*, 119(2):521–528, 1994.

M. A. Meju and V. R. S. Hutton. Iterative most-squares inversion: application to magnetotelluric data. *Geophysical journal international*, 108(3):758–766, 1992.

H. Melling, D. A. Riedel, and Z. Gedalof. Trends in the draft and extent of seasonal pack ice, Canadian Beaufort Sea. *Geophysical Research Letters*, 32(24), 2005.

W. Menke. Geophysical data analysis: Discrete inverse theory. *International Geophysics Series, Academic Press, London*, 45, 1989.

B. J. Minsley, B. D. Smith, R. Hammack, J. I. Sams, and G. Veloski. Calibration and filtering strategies for frequency domain electromagnetic data. *Journal of Applied Geophysics*, 80:56–66, 2012.

R. M. Morey, A. Kovacs, and G. F. N. Cox. Electromagnetic properties of sea ice. *Cold Regions Science and Technology*, 9(1):53–75, 1984.

P. O. Moslet. Field testing of uniaxial compression strength of columnar sea ice. *Cold Regions Science and Technology*, 48(1):1–14, 2007.

J. Multala, H. Hautaniemi, M. Oksama, M. Leppäranta, J. Haapala, A. Herlevi, K. Riska, and M. Lensu. An airborne electromagnetic system on a fixed wing aircraft for sea ice thickness mapping. *Cold Regions Science and Technology*, 24(4):355–373, 1996.

E. Mundry. On the interpretation of airborne electromagnetic data for the two-layer case. *Geophysical Prospecting*, (32):336–346, 1984.

M. Nicolaus, C. Katlein, J. Maslanik, and S. Hendricks. Changes in Arctic sea ice result in increasing light transmittance and absorption. *Geophysical Research Letters*, 39(24): L24501, 2012.

T. M. Niedrauer and S. Martin. An experimental study of brine drainage and convection in young sea ice. *Journal of Geophysical Research: Oceans (1978–2012)*, 84(C3):1176–1186, 1979.

D. Notz and M. G. Worster. In situ measurements of the evolution of young sea ice. *Journal of Geophysical Research: Oceans (1978–2012)*, 113(C3):C03001, 2008.

A. Nuber, L. Rabenstein, J. A. Lehmann-Horn, M. Hertrich, S. Hendricks, A. Mahoney, and H. Eicken. Water content estimates of a first-year sea-ice pressure ridge keel from surface-nuclear magnetic resonance tomography. *Annals of Glaciology*, 54(64):33–43, 2013.

C. C. Paige and M. A. Saunders. LSQR: An algorithm for sparse linear equations and sparse least squares. *ACM Transactions on Mathematical Software (TOMS)*, 8(1):43–71, 1982.

C. L. Parkinson and D. J. Cavalieri. Antarctic sea ice variability and trends, 1979-2010. *The Cryosphere*, 6(4):871–880, 2012.

S. Paul, S. Willmes, M. Hoppmann, P. A. Hunkeler, C. Wesche, M. Nicolaus, G. Heinemann, and R. Timmermann. The impact of early-summer snow properties on land-fast sea-ice X-band backscatter. *Annals of Glaciology*, 56(69):263–273, 2015.

D. K. Perovich, J. A. Richter-Menge, K. F. Jones, and B. Light. Sunlight, water, and ice: Extreme Arctic sea ice melt during the summer of 2007. *Geophysical Research Letters*, 35(11), 2008.

D. K. Perovich, K. F. Jones, B. Light, H. Eicken, T. Markus, J. Stroeve, and R. Lindsay. Solar partitioning in a changing Arctic sea-ice cover. *Annals of Glaciology*, 52(57): 192–196, 2011.

I. K. Peterson, S. J. Prinsenberg, and J. S. Holladay. Observations of sea ice thickness, surface roughness and ice motion in Amundsen Gulf. *Journal of Geophysical Research: Oceans (1978–2012)*, 113(C6), 2008.

C. Petrich and H. Eicken. Growth, structure and properties of sea ice. In *Sea Ice*, pages 23–77. Wiley-Blackwell, 2010.

A. A. Pfaffhuber and S. Hendricks. Not extinct yet: innovations in frequency domain HEM triggered by sea ice studies. *Exploration Geophysics*, 46(1):64–73, 2014.

A. A. Pfaffhuber, S. Hendricks, P. Hunkeler, and Y. A. Kvistedal. Introducing a new generation multi-sensor airborne system for mapping sea ice cover of polar oceans. *First Break*, 30(8):83–88, 2012a.

A. A. Pfaffhuber, S. Hendricks, and Y. A. Kvistedal. Progressing from 1D to 2D and 3D near-surface airborne electromagnetic mapping with a multisensor, airborne sea-ice explorer. *Geophysics*, 77(4):109–117, 2012b.

A. Pfaffling and J. E. Reid. Sea ice as an evaluation target for HEM modelling and inversion. *Journal of Applied Geophysics*, 67(3):242–249, 2009.

A. Pfaffling, C. Haas, and J. E. Reid. A direct helicopter EM sea ice thickness inversion, assessed with synthetic and field data. *Geophysics*, 72(4):127–137, 2007.

E. E. Popova, A. Yool, A. C. Coward, F. Dupont, C. Deal, S. Elliott, E. Hunke, M. Jin, M. Steele, and J. Zhang. What controls primary production in the Arctic Ocean? Results from an intercomparison of five general circulation models with biogeochemistry. *Journal of Geophysical Research: Oceans (1978–2012)*, 117(C8), 2012.

D. Price, W. Rack, P. J. Langhorne, C. Haas, G. Leonard, and K. Barnsdale. The sub-ice platelet layer and its influence on freeboard to thickness conversion of Antarctic sea ice. *The Cryosphere Discussions*, 8(1):999–1022, 2014.

D. J. Pringle, J. E. Miner, H. Eicken, and K. M. Golden. Pore space percolation in sea ice single crystals. *Journal of Geophysical Research: Oceans (1978–2012)*, 114(C12), 2009.

L. Rabenstein, S. Hendricks, T. Martin, A. Pfaffhuber, and C. Haas. Thickness and surface-properties of different sea-ice regimes within the Arctic Trans Polar Drift: Data from summers 2001, 2004 and 2007. *Journal of Geophysical Research: Oceans (1978–2012)*, 115:C12059, 2010.

W. Rack, C. Haas, and P. J. Langhorne. Airborne thickness and freeboard measurements over the McMurdo Ice Shelf, Antarctica, and implications for ice density. *Journal of Geophysical Research: Oceans*, 118(11):5899–5907, 2013.

P. Rampal, J. Weiss, and D. Marsan. Positive trend in the mean speed and deformation rate of Arctic sea ice, 1979–2007. *Journal of Geophysical Research: Oceans (1978–2012)*, 114(C5), 2009.

J. E. Reid and J. Bishop. Post-processing calibration of frequency-domain electromagnetic data for sea-ice thickness measurements. *Exploration Geophysics*, 35(4):283–287, 2004.

J. E. Reid, A. P. Worby, J. Vrbancich, and A. I. S. Munro. Shipborne electromagnetic measurements of Antarctic sea-ice thickness. *Geophysics*, 68(5):1537–1546, 2003.

J. E. Reid, A. Pfaffling, A. P. Worby, and J. R. Bishop. In situ measurements of the direct-current conductivity of Antarctic sea ice: implications for airborne electromagnetic sounding of sea-ice thickness. *Annals of Glaciology*, 44(1):217–223, 2006.

R. Ricker, S. Hendricks, V. Helm, H. Skourup, and M. Davidson. Sensitivity of CryoSat-2 Arctic sea-ice freeboard and thickness on radar-waveform interpretation. *The Cryosphere*, 8(4):1607–1622, 2014.

I. G. Rigor and J. M. Wallace. Variations in the age of Arctic sea-ice and summer sea-ice extent. *Geophysical Research Letters*, 31(9), 2004.

N. J. Robinson, M. J. M. Williams, C. L. Stevens, P. J. Langhorne, and T. G. Haskell. Evolution of a supercooled Ice Shelf Water plume with an actively growing subice platelet matrix. *Journal of Geophysical Research: Oceans*, 119, 2014.

D. A. Rothrock and M. Wensnahan. The accuracy of sea ice drafts measured from US Navy submarines. *Journal of Atmospheric and Oceanic Technology*, 24(11):1936–1949, 2007.

H. S. Salem and G. V. Chilingarian. The cementation factor of Archie's equation for shaly sandstone reservoirs. *Journal of Petroleum Science and Engineering*, 23(2):83–93, 1999.

I. J. Smith, P. J. Langhorne, T. G. Haskell, H. J. Trodahl, R. Frew, and M. R. Vennell. Platelet ice and the land-fast sea ice of McMurdo Sound, Antarctica. *Annals of Glaciology*, 33(1):21–27, 2001.

B. R. Spies and F. C. Frischknecht. Electromagnetic sounding. volume 2, pages 285–426. Oklahoma City, OK: Society of Exploration Geophysicists, 1991.

G. Spreen, R. Kwok, and D. Menemenlis. Trends in Arctic sea ice drift and role of wind forcing: 1992–2009. *Geophysical Research Letters*, 38(19), 2011.

S. Stammerjohn, R. Massom, D. Rind, and D. Martinson. Regions of rapid sea ice change: An inter-hemispheric seasonal comparison. *Geophysical Research Letters*, 39(6), 2012.

A. Stogryn and G. Desargant. The dielectric properties of brine in sea ice at microwave frequencies. *Antennas and Propagation, IEEE Transactions on*, 33(5):523–532, 1985.

J. C. Stroeve, M. C. Serreze, M. M. Holland, J. E. Kay, J. Malanik, and A. P. Barrett. The Arctics rapidly shrinking sea ice cover: a research synthesis. *Climatic Change*, 110 (3-4):1005–1027, 2012.

M. Sturm and R. A. Massom. Snow and sea ice. In *Sea Ice*, pages 153–204. Wiley-Blackwell, 2010.

D. N. Thomas and G. S. Dieckmann. *Sea ice*. John Wiley & Sons, 2009.

A. S. Thorndike, D. A. Rothrock, G. A. Maykut, and R. Colony. The thickness distribution of sea ice. *Journal of Geophysical Research*, 80(33):4501–4513, 1975.

F. Thyssen, H. Kohnen, M. V. Cowan, and G. W. Timco. DC resistivity measurements on the sea ice near pond inlet, NWT (Baffin Island). *Polarforschung*, 44(2):117–126, 1974.

G. W. Timco and R. M. W. Frederking. A review of sea ice density. *Cold Regions Science and Technology*, 24(1):1–6, 1996.

J.-L. Tison, A. Worby, B. Delille, F. Brabant, S. Papadimitriou, D. Thomas, J. De Jong, D. Lannuzel, and C. Haas. Temporal evolution of decaying summer first-year sea ice in the Western Weddell Sea, Antarctica. *Deep Sea Research Part II: Topical Studies in Oceanography*, 55(8):975–987, 2008.

M. Vacchi, M. Mesa, and S. Greco. The coastal fish fauna of Terra Nova Bay, Ross Sea, Antarctica. In *Ross Sea Ecology*, chapter 32, pages 457–468. Springer Berlin Heidelberg, 2000.

M. Vancoppenolle, C. M. Bitz, and T. Fichefet. Summer landfast sea ice desalination at Point Barrow, Alaska: Modeling and observations. *Journal of Geophysical Research: Oceans (1978–2012)*, 112(C4):C04022, 2007.

M. Vancoppenolle, H. Goosse, A. De Montety, T. Fichefet, B. Tremblay, and J.−L. Tison. Modeling brine and nutrient dynamics in Antarctic sea ice: The case of dissolved silica. *Journal of Geophysical Research: Oceans (1978–2012)*, 115(C2):C02005, 2010.

S. H. Ward and G. W. Hohmann. Electromagnetic theory for geophysical applications. *Electromagnetic methods in applied geophysics*, 1:131–311, 1988.

B. P. Weissling, M. J. Lewis, and S. F. Ackley. Sea-ice thickness and mass at ice station Belgica, Bellingshausen Sea, Antarctica. *Deep Sea Research Part II: Topical Studies in Oceanography*, 58(9):1112–1124, 2011.

D. J. Wingham, C. R. Francis, S. Baker, C. Bouzinac, D. Brockley, R. Cullen, P. de Chateau-Thierry, S. W. Laxon, U. Mallow, C. Mavrocordatos, L. Phalippou, G. Ratier, L. Rey, F. Rostan, P. Viau, and D. W. Wallis. CryoSat: A mission to determine the fluctuations in Earth's land and marine ice fields. *Advances in Space Research*, 37(4):841–871, 2006.

I. J. Won, A. Oren, and F. Funak. GEM-2A: A programmable broadband helicopter-towed electromagnetic sensor. *Geophysics*, 68(6):1888–1895, 2003.

Pat Wongpan, Patricia J Langhorne, David E Dempsey, Lisa Hahn-Woernle, and Zhifa Sun. Simulation of the crystal growth of platelet sea ice with diffusive heat and mass transfer. *Annals of Glaciology*, 56(69):127, 2015.

A. P. Worby, P. W. Griffin, V. I. Lytle, and R. A. Massom. On the use of electromagnetic induction sounding to determine winter and spring sea ice thickness in the Antarctic. *Cold Regions Science and Technology*, 29(1):49–58, 1999.

H. J. Zwally, D. Yi, R. Kwok, and Y. Zhao. ICESat measurements of sea ice freeboard and estimates of sea ice thickness in the Weddell Sea. *Journal of Geophysical Research: Oceans (1978–2012)*, 113(C2), 2008.

List of Figures

List of Tables

A Co-Author Paper 1

This paper was reprinted from Geophysical Research Letters with permission of John Wiley and Sons.

I contributed with field work to this paper. Between 07 and 12 April 2012, we acquired helicopter EM data in the Western Beaufort Sea during three flights of approximately 220 km each. I was involved in preparing the instrument for surveys, which included several tests with the ground power unit. Furthermore, I was operating the EM-bird from within the helicopter. This includes running the instrument, supervising the data flow, performing calibrations to higher altitudes and controlling the bird height in general, which should be around 30-40 feet above sea ice. In cases the bird loses altitude; it is the responsibility of the operator to inform the pilot by radio. During this field campaign, I learned the basics about electromagnetic induction sounding on sea ice and acquired additional knowledge about different sea-ice regimes, such as landfast, first- and multi-year sea ice.

Seasonal forecasts of Arctic sea ice initialized with observations of ice thickness

R. Lindsay,[1] C. Haas,[2] S. Hendricks,[3] P. Hunkeler,[3] N. Kurtz,[4] J. Paden,[5] B. Panzer,[5] J. Sonntag,[6] J. Yungel,[6] and J. Zhang[1]

Received 15 August 2012; revised 5 October 2012; accepted 5 October 2012; published 8 November 2012.

[1] Seasonal forecasts of the September 2012 Arctic sea ice thickness and extent are conducted starting from 1 June 2012. An ensemble of forecasts is made with a coupled ice-ocean model. For the first time, observations of the ice thickness are used to correct the initial ice thickness distribution to improve the initial conditions. Data from two airborne campaigns are used: NASA Operation IceBridge and SIZONet. The model was advanced through April and May using reanalysis data from 2012 and for June–September it was forced with reanalysis data from the previous seven summers. The ice extent in the corrected runs averaged lower in the Pacific sector and higher in the Atlantic sector compared to control runs with no corrections. The predicted total ice extent is 4.4 +/− 0.5 M km^2, 0.2 M km^2 less than that made with the control runs but 0.8 M km^2 higher than the observed September extent. **Citation:** Lindsay, R., C. Haas, S. Hendricks, P. Hunkeler, N. Kurtz, J. Paden, B. Panzer, J. Sonntag, J. Yungel, and J. Zhang (2012), Seasonal forecasts of Arctic sea ice initialized with observations of ice thickness, *Geophys. Res. Lett.*, *39*, L21502, doi:10.1029/2012GL053576.

1. Introduction

[2] As activities increase in the Arctic in response to reduced summer sea ice extent and increased interest in natural resources, seasonal predictions of ice extent or ice concentration become increasingly requested, both for the region as a whole and for specific locations. To date, most interest is in the total ice extent at the time of the annual minimum, in September. This is a focus of the SEARCH Sea Ice Outlook activity (http://www.arcus.org/search/seaiceoutlook) in which individuals can submit forecasts of the total sea ice extent for the Arctic as measured by the National Snow and Ice Data Center (NSIDC) Sea Ice Index [*Fetterer et al.*, 2002] or for specific regions. A wide variety of methods are utilized in this exercise, from coupled atmosphere–ocean–ice numerical models, to ice–ocean-only models, to a range of statistical methods, and even to heuristic arguments or popular polls. The outlook activity begins with forecasts made in the first week of June. A major limitation of these efforts has been the lack of near-real time estimates of the ice thickness over broad areas of the Arctic that would aid in the forecast procedures.

[3] Here we use newly available quick look estimates of ice thickness made by two different field campaigns in late March and early April 2012 to improve the estimate of the initial conditions for forecasting ice conditions in September. A coupled ice–ocean model is used to project the ice evolution from the springtime measurements to September. The following four steps are performed to make the forecasts.

[4] 1. The model is first initialized using historical reanalysis forcing data starting in 1948 and continuing through the end of March 2012. Ice concentration and sea surface temperatures are assimilated from January 1979 through March 2012. This provides the first guess ice thickness fields for 1 April 2012.

[5] 2. The observations from the two field campaigns (IceBridge and SIZONet, described in section 3) are clustered in 50-km samples. While the observations span the period 14 March–9 April 2012, we consider all of the observations to have been made on 1 April. The PIOMAS first guess thickness distribution for 1 April is then corrected to match the observations with an optimal interpolation procedure.

[6] 3. As the first forecasts are made in the first week of June, the atmospheric reanalysis data for April and May 2012 are used to advance the model to the end of May, including the assimilation of ice concentration and SST data.

[7] 4. For the months of June–September the model is forced with the summer weather as represented in the reanalysis data from the previous seven summers. This creates an ensemble of seven members. The mean ice extent and the standard deviation provide an estimate of the September ice extent and the uncertainty. In addition the ice edge and its variability in specific regions can be examined.

[8] The forecast exercise is made both with the first guess ice thickness fields (control) and the fields corrected to match the ice thickness observations (corrected). Perhaps more interesting than the result of this single exercise are the numerous questions that this type of study raises about the role and utility of observations in improving forecasts. Some of these questions are addressed in section 6.

2. Model and Forcing Data

[9] The numerical ensemble seasonal forecasting system consists of the Pan-Arctic Ice–Ocean Modeling and

[1]Polar Science Center, Applied Physics Laboratory, University of Washington, Seattle, Washington, USA.
[2]Department of Earth and Space Science and Engineering, York University, Toronto, Ontario, Canada.
[3]Alfred Wegener Institute, Bremerhaven, Germany.
[4]Cryospheric Sciences Program, NASA Goddard Space Flight Center, Greenbelt, Maryland, USA.
[5]Center for Remote Sensing of Ice Sheets, University of Kansas, Lawrence, Kansas, USA.
[6]Wallops Flight Facility, NASA Goddard Space Flight Center, Wallops Island, Virginia, USA.

Corresponding author: R. Lindsay, Polar Science Center, Applied Physics Laboratory, University of Washington, 1013 NE 40th St., Seattle, WA 98105-6698, USA. (lindsay@apl.washington.edu)

0094-8276/12/2012GL053576

Assimilation System (PIOMAS) [*Zhang and Rothrock*, 2003], the NCEP/NCAR atmospheric reanalysis forcing data, and satellite observations of ice concentration and sea surface temperature. PIOMAS is a coupled ice–ocean model that assimilates satellite sea ice concentration [*Lindsay and Zhang*, 2006] and sea surface temperature [*Schweiger et al.*, 2011].

[10] The seasonal forecast system is based on the assumption that the current climate is not fundamentally different from the recent past. This means that reanalysis data from the recent past may capture the current climate variability and therefore may be used to drive PIOMAS for ensemble seasonal forecasts. Here, the ensemble consists of seven members, each of which uses a unique set of NCEP/NCAR atmospheric forcing fields from recent years such that ensemble member 1 uses 2005 NCEP/NCAR forcing, member 2 uses 2006 forcing, and member 7 uses 2011 forcing. Each member starts with the same initial ice and ocean conditions on 1 June 2012. One limitation to using the reanalysis data is that there is no interaction between the atmosphere and the ice conditions. The advantage is that it is very simple to use past years and thereby quickly obtain an estimate of the range of possible outcomes given the current initial ice and ocean conditions. Only the previous seven summers are used because the near-surface atmospheric properties depend strongly on the ice conditions so using recent years with low ice extent is appropriate. More details about the ensemble prediction procedure can be found in *Zhang et al.* [2008].

3. Data

3.1. Operation IceBridge Quick Look Data

[11] Sea ice thickness data from Operation IceBridge (OIB) are taken from the quick look data product available via the National Snow and Ice Data Center (http://nsidc.org/data/docs/daac/icebridge/evaluation_products/sea-ice-freeboard-snowdepth-thickness-quicklook-index.html). The OIB quick look sea ice thickness data were obtained on 12 flights of the NASA P-3B Orion aircraft between 14 March and 2 April in the western Arctic Ocean basin and the Beaufort/Chukchi sea region. The quick look data were processed in an expedited manner to support the development of seasonal sea ice prediction capabilities such as this. Due to the expedited nature of the data production process, additional uncertainties may be present in the quick look data. The full assessment of the uncertainties in the quick look data is an ongoing research project, which will be undertaken after the release of the final OIB 2012 sea ice data products [*Kurtz et al.*, 2012].

[12] Sea ice thickness is inferred through measurements of the height of the sea ice and snow layers above sea level and an assumption of hydrostatic balance. The hydrostatic balance equation relating the measured sea ice freeboard (h_f, the height of the surface snow-plus-ice layer above the local sea surface elevation), and snow depth (h_s) properties to the sea ice thickness (h_i) is

$$h_i = \frac{\bar{\rho}_w}{\bar{\rho}_w - \bar{\rho}_i} h_f - \frac{\bar{\rho}_w - \bar{\rho}_s}{\bar{\rho}_w - \bar{\rho}_i} h_s,$$

Where the densities of snow, sea ice, and sea water are $\bar{\rho}_s$ = 320 kg m^3, $\bar{\rho}_i$ = 915 kg m^3, and $\bar{\rho}_w$ = 1024 kg m^3, respectively. Uncertainties in these densities are included in the estimates of the thickness uncertainties. The OIB sea ice thickness data are provided at a spatial resolution of 40 m along the aircraft track. The uncertainty in the retrieved sea ice thickness is provided at each along-track measurement location through propagation of the uncertainties of each component of the hydrostatic balance equation.

[13] Laser altimetry data from the Airborne Topographic Mapper (ATM) system [*Krabill*, 2009] were used to determine h_f. The sea surface elevation is determined at discrete locations through the measurement of surface elevation over open water and newly frozen leads. In the quick look data products, open water and newly frozen leads were identified using surface temperature results from a KT19 infrared pyrometer to retrieve the open water fraction within the viewing area. The sea surface height was then constructed along each flight line by subtracting out known sea surface height parameters (including the geoid, tidal, and atmospheric pressure induced fluctuations) and using an ordinary Kriging approach to interpolate between the discrete sea surface height observations and each measurement location. Uncertainties in the sea surface height are determined from the Kriging error in the interpolation scheme. Due to the irregular spacing of lead observations the freeboard uncertainty is highly variable along each flight track.

[14] Snow depth is determined from the University of Kansas' snow radar system [*Leuschen*, 2010; *Panzer et al.*, 2010] and is retrieved through the identification of the air–snow and snow–ice interfaces and determination of the distance between them. The air–snow and snow–ice interfaces are identified following the method described in *Kurtz and Farrell* [2011], with an update described in the OIB data products manual [*Kurtz et al.*, 2012] to account for the lack of radiometric calibration of the radar data. The snow depth is then calculated by differencing the air–snow and snow–ice interfaces in the time domain and multiplying this difference by the speed of light within the snow pack. Following the results described in *Farrell et al.* [2012], the uncertainty in the snow depth is here estimated to be 5.7 cm. Further refinement of the snow depth uncertainty is expected through the comparison with coincident in situ data collected in 2011 and 2012.

3.2. Airborne Electromagnetic Induction Snow and Ice Thickness From SIZONet

[15] Measurements of total ice-plus-snow thickness were made with an Airborne ElectroMagnetic (AEM) induction sounding system [*Eicken et al.*, 2007]. The surveys were part of the Seasonal Ice Zone Observation Network (SIZONet). Three helicopter flights were conducted from Barrow, Alaska, between 7 and 9 April. Each flight resulted in approximately 220 km of profile data. Data from similar flights exist from every spring since April 2007 and other flights have been conducted in many regions in the Arctic and Antarctic (see the Unified Sea Ice Thickness Climate Data Record; psc.apl.uw.edu/sea_ice_cdr [*Lindsay*, 2010]).

[16] Measurements were made with an EM sensor suspended 20 m below a helicopter and towed at an altitude of 10 to 15 m above the surface. The retrieval method is based on the contrast of electrical conductivity between sea ice and ocean. Electromagnetic fields are used to determine the range from the instrument to the ice–water interface and a laser altimeter is used to range to the snow surface, thus the

difference of the distances gives the ice-plus-snow thickness. This approach is based on a 1D representation of sea ice and a full description is given in *Haas et al.* [2009]. The instrument can be operated from helicopters or fixed-wing aircraft for long-range surveys [*Haas et al.*, 2010].

[17] When comparing AEM sea ice thickness with other products, two properties must be considered: AEM thicknesses always include snow depth and the footprint of the EM ranging is approximately 40–50 m. The consequence of the first point is that either snow depth has to be added to other sea ice thickness products or removed from AEM thickness estimates. The second point results in footprint smoothing of the ice thickness profile. Deformed sea ice features, such as ridges, are underestimated in maximum thickness and overestimated in width. It is assumed that the footprint effect has little impact on larger scale mean AEM thickness estimates, which is backed by inter-comparisons of thickness products from different methods [*Schweiger et al.*, 2011].

[18] The airborne EM sensor used in the SIZONet 2012 field campaign is designed to overcome the footprint limitation. MAiSIE, the Multi-Sensor Sea Ice Explorer, features an enhanced EM concept to allow a geophysical inversion for sub-footprint-scale sea ice thickness [*Pfaffhuber et al.*, 2012]. To meet the time constraints for a seasonal outlook in 2012, the AEM data for this study were processed with the traditional 1D processing and released shortly after the end of the field campaign. Mostly first-year sea ice was found with intermittent multi-year sea ice floes. The typical thickness of level first-year ice, represented by the maximum of the ice thickness distribution, was calculated to be 2.0 m.

[19] The AEM measurements were corrected to ice thickness by subtracting an estimate of the snow depth determined from the OIB snow depth measurements. All of the OIB mean ice thickness and snow depth measurements were used to determine a linear relationship between the ice-plus-snow depth h_{i+s} versus the snow depth alone, h_s:

$$h_s = -0.009 + 0.075 h_{i+s}, \quad N = 209, \quad R = 0.85,$$
$$RMSerr = 0.04 \text{ m}$$

This relationship was then used to determine the snow depth for each AEM point measurement before the clustering procedure.

3.3. Clustering

[20] The point data from each of the campaigns were grouped into 50-km clusters, independent of any grid, to determine the local ice thickness distribution. Each campaign was clustered independently, but all flights from each campaign were clustered together regardless of the date flown. All points within a 50-km circle were used to form the thickness distribution for the cluster using 10-cm bins. The centroid location of the observations was retained. The locations of the circles were chosen to minimize the number of clusters and maximize the number of points in each cluster.

[21] For the OIB measurements, only points that had an estimated uncertainty of $\varepsilon_h < 1 + 0.25\ h < 2.0$ m were included, where h is the mean thickness measurement and ε_h is the reported uncertainty. For unbiased errors the uncertainty of the mean ice thickness for the 50-km clusters is quite small because there were about 1000 point measurements in each cluster. However, a significant unknown bias may exist for the cluster means.

3.4. Model Comparisons

[22] The location of each cluster is plotted on a map of the mean ice thickness from the PIOMAS first guess field for 1 April 2012 in Figure 1a. We see that the model consistently underestimates the thickness of thick ice near the pole and overestimates the thickness of thinner ice in the Beaufort and Chukchi seas. This bias pattern in the PIOMAS model thickness has been observed previously when the model thickness was compared to submarine ice draft measurements [*Zhang and Rothrock*, 2005; *Lindsay and Zhang*, 2006; *Schweiger et al.*, 2011]. We have not yet established the ultimate source of this model bias.

4. Correcting the Model Ice Thickness

[23] A simple optimal interpolation (OI, or Kriging) procedure is used to merge the model estimates of the mean ice thickness and the collocated observed mean thicknesses and thickness distributions. First the difference between the observations and the first guess model estimates are determined for each observation location

$$\Delta_{obs}(x) = h_{mod}(x) - h_{obs}(x).$$

The difference at each location is shown in Figure 1b. The difference is then interpolated to the locations of all model grid points using three parameters: the uncertainty in the observations ε_{obs} = 0.5 m [*Kurtz et al.*, 2012], the uncertainty on the model estimates ε_{mod} = 1.0 m [*Schweiger et al.*, 2011], and a correlation length scale for the model errors, L_{err} = 500 km. The length scale for the model errors is not well known. The interpolated correction field was then added to the first guess model estimate of the mean ice thickness for 1 April 2012 to provide a revised estimate of the ice thickness. The interpolated difference field is also shown in Figure 1b.The revised model mean ice thickness has no bias with respect to the observations and a correlation of R = 0.88 (N = 214).

[24] The model, however, does not use the mean ice thickness as a state parameter, but instead uses a 12-bin thickness distribution to characterize the ice thickness. The model thickness distribution is modified in the same manner as the mean thickness. For each observation cluster the observed thickness distribution is divided into the same 12 bins that the model uses. The model minus observed area fraction difference is obtained for each bin independently at each observation location and the difference is then interpolated to the model grid locations using OI. The errors in the area fractions for the individual bins are not known, but we have again used an error for the model that is twice that of the observations, i.e., ε_{obs} = 0.05, ε_{mod} = 0.1. (It is the ratio of the errors that is important for the OI procedure). The interpolated difference in the area fraction of each bin is then added to the model first guess to obtain the new model initialization. Because the weighting of the model and the observations is the same for all bins at each location, the distribution remains normalized. In examining the correction fields for each of the bins it is apparent that area is removed from some bins and added to others in regions where the observations differ from the model distributions. For

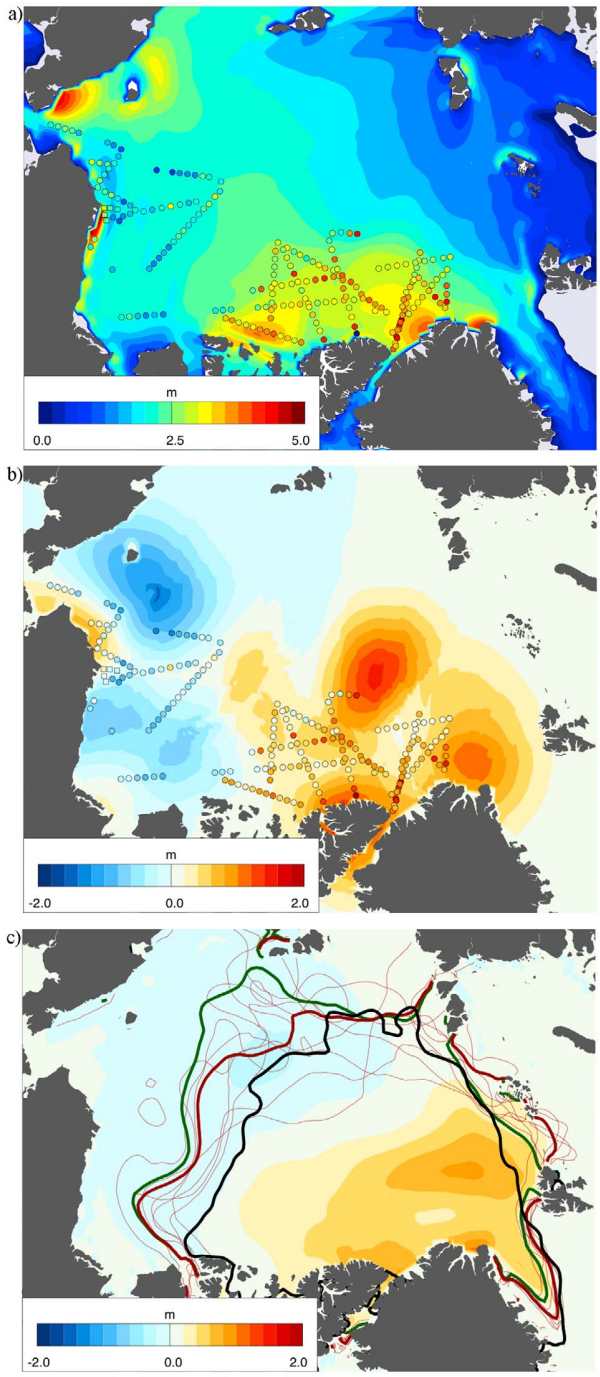

Figure 1. (a) PIOMAS first guess mean ice thickness for 1 April 2012 and estimates of the mean ice thickness from OIB (circles) and AEM estimates (squares, near Barrow). (b) The difference between the PIOMAS first guess mean ice thickness and the observations. The color field is the interpolated difference at all PIOMAS grid points. (c) The difference in mean ice thickness for September between the corrected and the control runs. The thin red lines are the ice extent (0.15 ice concentration) lines for each of the corrected ensemble members and the thick red line is the mean for the ensemble. The thick green line is the mean of the ensemble of control runs and the black line is the observed September mean ice extent.

example, where the model is too thick in the mean, area is removed from the thicker bins and added to thinner bins. The net result is a change in the mean thickness very similar to what we calculated above using the mean thickness field.

5. Ensemble Forecasts

[25] The forecasts in this exercise are made starting from the first of June to conform to the Sea Ice Outlook project guidelines. The NCEP reanalysis data for the months of April and May 2012 are used to force the model to obtain an estimate of the ice conditions for the first of June. This is a two-month hindcast starting with the revised initial conditions for the ice thickness distribution on 1 April. Control runs are also made with the original first guess ice conditions from 1 April. The forecast ice conditions are thus estimated for the months of June–September with two seven-member ensembles, one ensemble for the control and one for the corrected or initialized ice conditions.

[26] Figure 1c shows the mean thickness difference between the corrected and the control runs forecast for September and the ice extent lines for the seven corrected runs. The ensemble mean ice extent is significantly lower in the corrected runs in the region north of the East Siberian Sea. This reflects the reduced ice thickness in the Chukchi Sea in the corrected runs, which has migrated to the west. We also see a large amount of variability in the ensemble runs in this region so that our confidence in the ice extent forecast here is low. In the Beaufort Sea, where we had abundant ice thickness observations, there is only a very small reduction in the estimated ice extent in the corrected runs and a small reduction in the ice thickness. Near the Barents Sea and in Fram Strait the initialized forecast shows an extent greater than the control run. This reflects the increased ice thickness of the initialized run in the region near the pole; this anomaly migrated closer to Svalbard in September.

[27] The observed September 2012 mean ice extent is also shown in Figure 1c. The predicted extent from both the control run and the corrected run is generally lower than what actually occurred. The differences are greatest in the Pacific sector, though there is also a significant overestimation of the extent in both ensembles near the Barents Sea and an underestimation in Fram Strait. The largest difference between the initialized and the control runs is near the East Siberian Sea where the thinning for the initialized runs is largest and where the mean of initialized runs nearly matches the observed extent. Here the forcing from 2007 for the initialized runs produced an ice edge even farther north than what was observed. In the Pacific sector the mean ice edge of the initialized runs is closer to the observed edge than that of the control runs because of the thinning imposed by the observations.

[28] The net effect of the reduced extent on the Pacific side in the initialized run compared to the control run and increased extent on the European side is that the forecast of the total ice extent in the Arctic is similar in the initialized and control runs. Figure 2 shows the time evolution of the computed total ice extent for the entire Arctic and the differences for each pair of runs (control minus corrected). The observed total extent for September from the Sea Ice Index [*Fetterer et al.*, 2002] is also shown for the summer months. The ensemble median of the initialized forecasts is

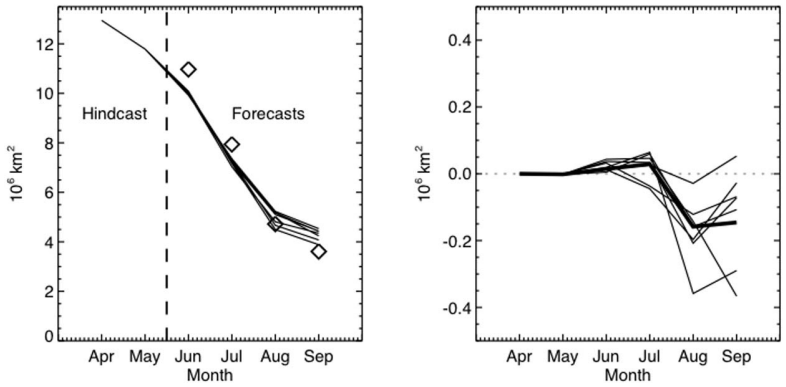

Figure 2. (a) Time evolution of the estimated monthly mean total ice extent from the seven ensemble members from the corrected initial conditions runs. Diamonds mark the observed monthly mean extent. (b) Differences for each pair of runs from the control and corrected runs; the thick line is the difference of the medians.

4.4 +/– 0.5 M km^2, i.e., 0.2 M km^2 less than the control forecast of 4.6 +/– 0.5 M km^2. Although the median of the initialized forecasts was less than that of the control forecast, it was still 0.8 ± 0.5 M km^2 higher than the actual observed September mean extent of 3.6 M km^2.

6. Discussion

[29] This first exercise in initialized sea ice seasonal prediction naturally raises as many questions as it answers. Many of the procedures are admittedly ad-hoc and point to where further improvements should be made.

[30] An extraordinary effort was made by the field teams to provide the near-real time quick look data products used in the forecasts. With repeated campaigns the effort will likely be smoother. The timing of the campaigns in late March and early April are not ideal for predicting the end-of-summer ice conditions from the first of June, but the ability of a model to use the information from early in the season makes the observations useful in correcting the model estimates of the initial ice thickness. The observations are also spatially limited, with no information about the model error on the Siberian side of the basin where there is significant variability in the ensemble members.

[31] The length scale used to interpolate the sparse observations to the model grid is another area of uncertainty. We used a length scale of 500 km because the correlation length scale of the model ice thickness is on the order of 500 km or more. However, there is a great deal of small-scale variability in the difference between the observations and the model. Because the model is used to project forward six months from the observations, we thought it best to smooth the differences and extend the observed differences beyond the immediate vicinity in which they were obtained. This smoothing and extrapolation is accomplished through the optimal interpolation procedure. If a 250-km length scale is used, the corrections to the initial ice thickness are more localized to the positions of the observations. The net effect on the predicted ice edge in this case compared to one using a 500-km length scale is very small in most areas, but in the area north of the Laptev Sea, where the uncertainty is large, the mean differences are large.

[32] An additional issue for initialized forecast is model bias. The model may have a bias in the ice extent, either regionally or for the Arctic as a whole. We saw above that there is a regional bias in the model ice thickness. An additional issue for forecasts is the time interval for which the model bias is developed. If the bias is developed quickly, the initialization may not be able to correct the forecast, while if the bias develops over a number of years the initialization will potentially improve the forecast. We currently have little information as to how quickly the model bias develops but the map in Figure 1c shows the anomaly introduced by the observation is significantly smoothed and reduced in magnitude in just six months.

[33] Why were the September forecast ice extents too high? Four-month forecasts depend heavily on the nature of the uncertain forcing fields. One consideration is that the ensemble of forcing years taken from the recent past is inherently conservative, given the upward trend in air temperatures and downward trend in ice extent. A second consideration is that the atmospheric forcing data is not interactive with the forecast ice cover so the thin or reduced ice is not allowed to influence atmospheric near-surface air temperatures. Finally, it may be that some aspects of the weather in the summer of 2012, such as the large storm that passed through the region in August, created conditions particularly conducive to a large melting event. The proximate and ultimate causes of the record-low ice extent observed in 2012 remain active research questions.

[34] Poor verification of this single forecast tells us little about eventual possible improvements in the accuracy of the forecast using observations because of the large uncertainty in the projected ice extent. In most locations the difference in the mean ice extent between the corrected and control runs is small compared to the variability seen in the ensembles. However, this first attempt to use ice thickness observations to improve forecasts shows that observations closer to the forecast time for forecasts made over shorter time intervals may have more of an impact. This forecast season also demonstrates that much of the uncertainty in long-range forecasts is likely not due to uncertain initial ice conditions but to uncertain summer weather.

[35] **Acknowledgments.** This study was conducted with support from the National Science Foundation Office of Polar Programs, the National Aeronautics and Space Administration Cryosphere Program and Operation IceBridge, the Office of Naval Research, and the Center for Remote Sensing of Ice Sheets.

[36] The Editor thanks two anonymous reviewers for their assistance in evaluating this paper.

References

Eicken, H., S. Hendricks, M. Kaufman, and A. Mahoney (2007), Barrow Airborne Sea Ice Thickness Surveys (SIZONET), doi:10.5065/D6CC0XMC, UCAR, Boulder, Colo.

Farrell, S. L., N. Kurtz, L. Connor, B. Elder, C. Leuschen, T. Markus, D. C. McAdoo, B. Panzer, J. Richter-Menge, and J. Sonntag (2012), A first assessment of IceBridge snow and ice thickness data over Arctic sea ice, *IEEE Trans. Geosci. Remote Sens.*, *50*, 2098–2111, doi:10.1109/TGRS.2011.2170843.

Fetterer, F., K. Knowles, W. Meier, and M. Savoie (2002), Sea Ice Index, digital media, Natl. Snow and Ice Data Cent., Boulder, Colo.

Haas, C., J. Lobach, S. Hendricks, L. Rabenstein, and A. Pfaffling (2009), Helicopter-borne measurements of sea ice thickness, using a small and lightweight, digital EM bird, *J. Appl. Geophys.*, *67*, 234–241, doi:10.1016/j.jappgeo.2008.05.005.

Haas, C., S. Hendricks, H. Eicken, and A. Herber (2010), Synoptic airborne thickness surveys reveal state of Arctic sea ice cover, *Geophys. Res. Lett.*, *37*, L09501, doi:10.1029/2010GL042652.

Krabill, W. B. (2009), IceBridge ATM L1B Qfit elevation and return strength, digital media, Natl. Snow and Ice Data Cent., Boulder, Colo.

Kurtz, N. T., and S. L. Farrell (2011), Large-scale surveys of snow depth on Arctic sea ice from Operation IceBridge, *Geophys. Res. Lett.*, *38*, L20505, doi:10.1029/2011GL049216.

Kurtz, N., M. Studinger, J. Harbeck, V. Onana, and S. Farrell (2012), IceBridge sea ice freeboard, snow depth, and thickness, digital media, Natl. Snow and Ice Data Cent., Boulder, Colo.

Leuschen, C. (2010), IceBridge Snow Radar L1B geolocated radar echo strength profiles, digital media, Natl. Snow and Ice Data Cent., Boulder, Colo.

Lindsay, R. W. (2010), A new sea ice thickness climate data record, *Eos Trans. AGU*, *91*(44), 405, doi:10.1029/2010EO440001.

Lindsay, R. W., and J. Zhang (2006), Assimilation of ice concentration in an ice-ocean model, *J. Atmos. Oceanic Technol.*, *23*, 742–749, doi:10.1175/JTECH1871.1.

Panzer, B., C. Leuschen, A. Patel, T. Markus, and P. Gogineni (2010), Ultra-wideband radar measurements of snow thickness over sea ice, in 2010, in *Proceedings of the IEEE International Geoscience and Remote Sensing Symposium*, pp. 3130–3133, Inst. of Electr. and Electron. Eng., New York, doi:10.1109/IGARSS.2010.5654342.

Pfaffhuber, A. A., S. Hendricks, and Y. Kvistedal (2012), Progressing from 1D to 2D and 3D near surface airborne electromagnetic mapping with a multi-sensor airborne sea ice explorer, *Geophysics*, *77*, WB109, doi:10.1190/geo2011-0375.1.

Schweiger, A., R. Lindsay, J. Zhang, M. Steele, and H. Stern (2011), Uncertainty in modeled arctic sea ice volume, *J. Geophys. Res.*, *116*, C00D06, doi:10.1029/2011JC007084.

Zhang, J., and D. A. Rothrock (2003), Modeling global sea ice with a thickness and enthalpy distribution model in generalized curvilinear coordinates, *Mon. Weather Rev.*, *131*(5), 845–861, doi:10.1175/1520-0493(2003)131<0845:MGSIWA>2.0.CO;2.

Zhang, J., and D. A. Rothrock (2005), Effect of sea ice rheology in numerical investigations of climate, *J. Geophys. Res.*, *110*, C08014, doi:10.1029/2004JC002599.

Zhang, J., M. Steele, R. Lindsay, A. Schweiger, and J. Morison (2008), Ensemble 1-Year predictions of Arctic sea ice for the spring and summer of 2008, *Geophys. Res. Lett.*, *35*, L08502, doi:10.1029/2008GL033244.

B

Co-Author Paper 2

This paper was reprinted from the Annals of Glaciology with permission of the International Glaciological Society.

I contributed with sea-ice field work and revision work to this paper. The German research station Neumayer III was approximately 10 km away from the sea ice, where the majority of data for this study were acquired. My contribution to the field work therefore already started with all the logistics, by packing of equipment and loading the snowmobiles. In the Atka Bay, I contributed to the regularly performed measurements of snow depth, freeboard, sea-ice and platelet-layer thicknesses along the main transect from the eastern to western end of the bay. I also contributed to validate the platelet-layer thickness measurements with the metal bar method and an under-ice camera.

Ice platelets below Weddell Sea landfast sea ice

Mario HOPPMANN,[1] Marcel NICOLAUS,[1] Stephan PAUL,[2] Priska A. HUNKELER,[1] Günther HEINEMANN,[2] Sascha WILLMES,[2] Ralph TIMMERMANN,[1] Olaf BOEBEL,[1] Thomas SCHMIDT,[1] Meike KÜHNEL,[1] Gert KÖNIG-LANGLO,[1] Rüdiger GERDES[1]

[1]*Alfred-Wegener-Institut Helmholtz-Zentrum für Polar- und Meeresforschung, Bremerhaven, Germany*
E-mail: Mario.Hoppmann@awi.de
[2]*Environmental Meteorology, University of Trier, Trier, Germany*

ABSTRACT. Basal melt of ice shelves may lead to an accumulation of disc-shaped ice platelets underneath nearby sea ice, to form a sub-ice platelet layer. Here we present the seasonal cycle of sea ice attached to the Ekström Ice Shelf, Antarctica, and the underlying platelet layer in 2012. Ice platelets emerged from the cavity and interacted with the fast-ice cover of Atka Bay as early as June. Episodic accumulations throughout winter and spring led to an average platelet-layer thickness of 4 m by December 2012, with local maxima of up to 10 m. The additional buoyancy partly prevented surface flooding and snow-ice formation, despite a thick snow cover. Subsequent thinning of the platelet layer from December onwards was associated with an inflow of warm surface water. The combination of model studies with observed fast-ice thickness revealed an average ice-volume fraction in the platelet layer of 0.25 ± 0.1. We found that nearly half of the combined solid sea-ice and ice-platelet volume in this area is generated by heat transfer to the ocean rather than to the atmosphere. The total ice-platelet volume underlying Atka Bay fast ice was equivalent to more than one-fifth of the annual basal melt volume under the Ekström Ice Shelf.

KEYWORDS: basal melt, ice/ocean interactions, sea ice, sea-ice growth and decay, sea-ice/ice-shelf interactions

INTRODUCTION

The expanse of Antarctic sea ice is currently one of the major puzzles in sea-ice research (Maksym and others, 2012). Recent observations of increasing Antarctic sea-ice extent (e.g. Parkinson and Cavalieri, 2012) are contradictory to an expected decline in a warming environment, as observed in the Arctic (Comiso and Hall, 2014). The failure of global climate models to reproduce this behavior is an indication that key processes are missing in the implementation of the models (Turner and others, 2013). One important piece of the puzzle might be the interactions and feedback processes between the sea-ice cover and the Antarctic ice shelves, which link the grounded ice sheet to the Southern Ocean (Bintanja and others, 2013). One aspect of these interactions is the accumulation of ice platelets, inclusion-free single crystals up to 0.2 m in diameter and <0.003 m in thickness, beneath a nearby sea-ice cover (Eicken and Lange, 1989). These form a dense layer of intertwined individual crystals, herein referred to as a sub-ice platelet layer, following the terminology of Gow and others (1998). The suspended crystals may attach to the sea-ice bottom and become incorporated into the sea-ice fabric through consequent freezing of interstitial water. This sea-ice type is then referred to as (consolidated) platelet ice, which has a distinct crystal structure and a *c*-axis distribution different from other sea ice (e.g. Jeffries and others, 1993; Tison and others, 1998). The ice platelets form and grow in supercooled water, which results from basal melting in the cavities below the floating ice shelves. Lewis and Perkin (1986) termed this process an 'ice pump'. This also means that ice-platelet formation and accumulation below a sea-ice cover may be an indirect indicator of basal melt.

However, continuous studies of ice platelets and associated processes are impossible in the mobile pack ice around the Antarctic continent, because they have only been observed up to 35 km from the coast (Eicken and Lange, 1989). In contrast to that, areas of immobile landfast sea ice (fast ice) are comparatively easy to access from nearby coastal stations, making them an ideal platform to study Antarctic sea-ice properties and associated processes (Heil and others, 2011). At the same time, fast ice may act as an early indicator of climate change affecting the polar system, through its link with atmospheric forcing (Heil, 2006).

Ice-platelet accumulations have been observed in several locations around Antarctica (e.g. Serikov, 1963; Moretskiy, 1965; Veazey and others, 1994). By far the most studies have been performed in the Ross Sea, benefiting from the presence of the US and New Zealand stations at McMurdo. Recent investigations of ice platelets near the McMurdo Ice Shelf, for example, focused on frazil deposition (Dempsey and others, 2010; Dempsey and Langhorne, 2012) and the links between supercooling of the ocean and platelet-ice formation (e.g. Mahoney and others, 2011; Gough and others, 2012).

In the eastern Weddell Sea, a number of smaller ice shelves fringe the coastline of Dronning Maud Land. This region is characterized by a narrow and steep continental shelf margin. Although deep or bottom water formation does not occur there (Fahrbach and others, 1994), this region is of critical importance to water-mass preconditioning and formation in the Weddell Sea (Thoma and others, 2006). At the same time, the geographic setting promotes the penetration of modified Warm Deep Water into the ice-shelf cavities (Nøst and others, 2011), which results in high basal melt rates and modifications of the coastal current (Hellmer,

2004). This also means that this region is particularly susceptible to changing climate conditions (Holland and others, 2008). According to previous studies by Lange and others (1989), a substantial fraction of the near-coastal sea-ice cover of Dronning Maud Land originates from incorporation of underlying ice platelets. However, most aspects of the mechanisms of platelet accumulation and their link to oceanographic conditions remain unclear, especially in this region. Wherever a sub-ice platelet layer is present, the solid sea ice grows thicker than can be accounted for by a conductive flux alone. This is due to the incorporation of ice mass formed by heat loss to the ocean, rather than to the atmosphere. It is therefore necessary to determine how much of the solid fast ice in this region results from ocean/ice-shelf interactions. To answer this question, an accurate estimate of the ice-volume fraction of the platelet layer is needed. As the platelet layer modifies the electrical conductivity below the solid sea ice (Hunkeler and others, 2015) and contributes to its freeboard, this parameter is also crucial to accurately determine near-coastal Antarctic sea-ice thickness based on electromagnetic induction sounding (Rack and others, 2013) or altimetry methods (Price and others, 2013). Finally, it is desirable to link the properties of the platelet layer to basal melt processes of nearby ice shelves, as these are particularly susceptible to future environmental changes (Hellmer and others, 2012).

In this paper, we aim to improve our understanding of how ice shelves influence nearby sea ice in Antarctic coastal waters. We present the seasonal cycle of sea ice attached to the Ekström Ice Shelf in the eastern Weddell Sea, a region that is currently under-represented in investigations of ice-shelf/sea-ice interactions. We continue the work of Kipfstuhl (1991) and Günther and Dieckmann (1999), who studied ice platelets underlying the solid fast ice of Atka Bay in the 1980s–90s. Through a combination of field observations and model studies, we derive the ice-volume fraction of the platelet layer at six sites on Atka Bay fast ice. Together with observations of platelet-layer thickness evolution, we estimate how much sea ice at Atka Bay is formed by heat transfer to the ocean rather than to the atmosphere. We relate this result to Ekström Ice Shelf basal melt and discuss several implications of the platelet layer for fast-ice properties in this region.

STUDY SITE AND METHODS

Study site

Atka Bay is a 440 km^2 large embayment in front of the Ekström Ice Shelf, which is part of a group of small ice shelves located on the coast of Dronning Maud Land, eastern Weddell Sea (Fig. 1). This relatively small ice shelf covers an area of 6800 km^2 (Bindschadler and others, 2011) and has been studied since the 1980s, when the first German year-round station was established there. Investigations of ice thickness, bedrock topography and basal melting in this region have been undertaken by, for example, Kipfstuhl (1991), Sandhäger and Blindow (2000) and Neckel and others (2012). Information about cavity geometry is available from Kobarg (1988).

Atka Bay is seasonally covered with fast ice attached to ice-shelf edges bordering to the west, south and east. Knowledge of the sea-ice conditions in this region is crucial to providing logistical support of the German and South African Antarctic stations. Information about general sea-ice conditions is obtained from satellite images, recorded by, for example, synthetic aperture radar on board Envisat, RADARSAT and TerraSAR-X, the Moderate Resolution Imaging Spectroradiometer on board Aqua and Terra, the Enhanced Thematic Mapper on board Landsat or the Advanced Very High Resolution Radiometer on board the Polar Orbiting Environmental Satellites. Satellite imagery is especially needed to fill the gap between late summer and early winter, when direct sea-ice observations are not available and dates of initial formation and break-up need to be determined.

Visual inspection of satellite imagery in previous years reveals that the seasonal fast-ice cover of Atka Bay usually starts to form during March–April. The extent mainly depends on the strength of winds and ocean currents offshore of Atka Bay, and also on the interaction with often passing icebergs. The fast ice does not melt in situ during summer, but breaks out once it is sufficiently destabilized. Although no studies exist to date which have investigated the responsible physical factors more closely, contributions from increased water and air temperatures, as well as from solar radiation, tidal motion, wind forcing and a combination thereof, are most likely. The interaction with stationary and passing icebergs also plays a role. The break-up usually happens after the retreat of the pack ice in front of the fast ice, and normally begins in the eastern part of the bay (generally in December or January). In the southwestern part, sea ice may persist until March, but in most years Atka Bay is completely ice-free at the end of March. Persistent strong easterly winds during initial formation lead to an increased dynamic growth towards the western ice-shelf edge. Once a solid sea-ice cover is established over the major part of Atka Bay (usually in April/May), further growth proceeds thermodynamically.

Meteorological data are readily available from the nearby Neumayer III station, where atmospheric conditions have been recorded since 1981 (König-Langlo and Loose, 2007). An overview for the period 1991–95 is given by König-Langlo and others (1998) and for the period 1982–2011 by Rimbu and others (2014). Generally, the region is characterized by low temperatures, extreme temperature fluctuations during winter and persistent easterly winds. The winds lead to frequent drifting and blowing snow.

Field measurements

We set up six study sites along a 25 km long west–east profile to monitor fast-ice thickness, snow depth, freeboard and platelet-layer thickness (Hoppmann and others, 2013a). These sites are referred to in this paper as ATKAxx, where xx represents their distance in kilometers to the western ice-shelf edge (Fig. 1; Table 2). Our measurements started in June 2012, as soon as enough snow had accumulated at the ice-shelf edge to access the sea ice several meters below with snowmobiles. We measured sea-ice thickness and freeboard through 0.05 m auger holes using regular (before August) and modified thickness tapes, while snow depth was measured using ruler sticks. Freeboard, the distance from the water surface to the sea-ice surface, is negative when the sea-ice surface is depressed below the water surface. Each time a study site was visited, up to five measurements were performed in an undisturbed area, one in the center and one at a distance of 5 m in each direction.

During the course of austral winter, the platelet accumulations started to complicate the measurements. In order to penetrate the platelet layer, it became necessary to weigh

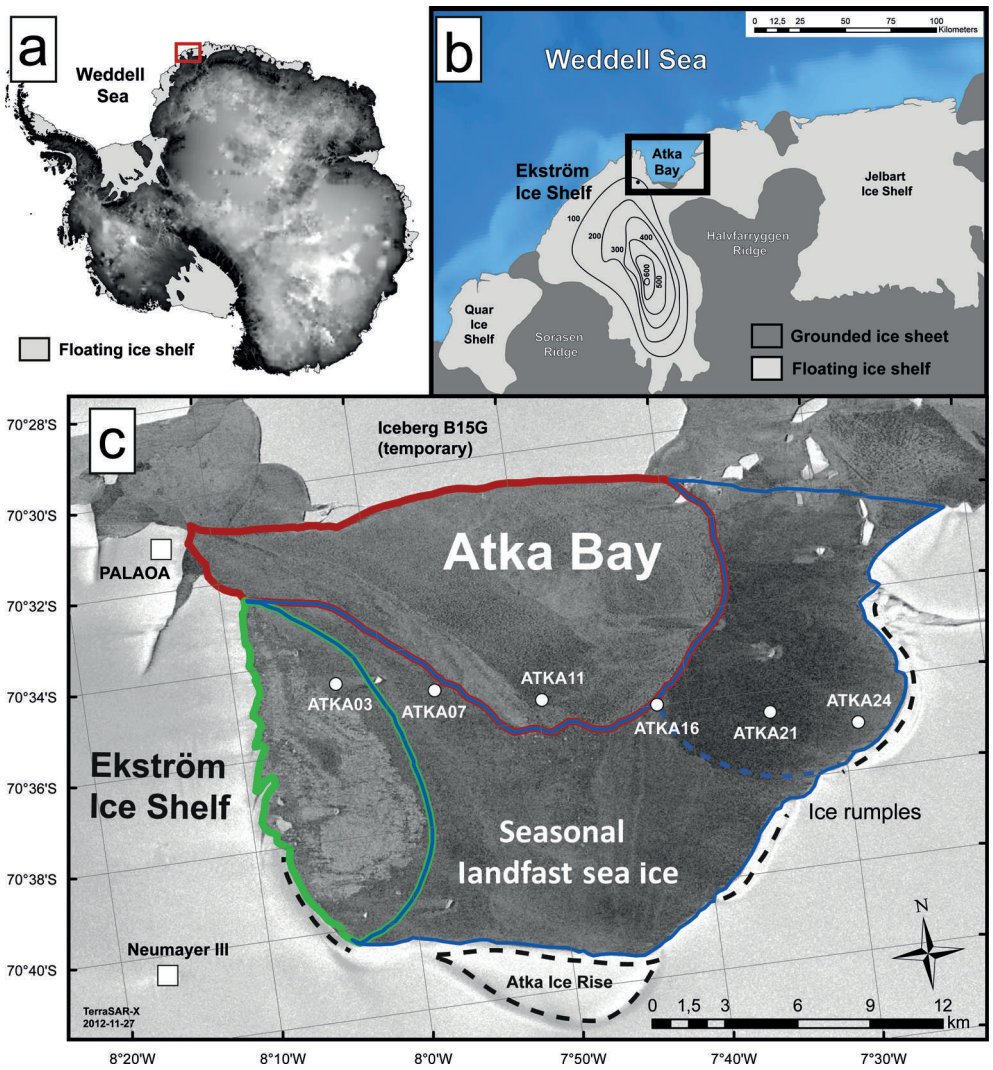

Fig. 1. Location of the study site. (a) The Ekström Ice Shelf is located in the eastern Weddell Sea (highlighted as red box). (b) Enlargement of (a). The contours show the depth of the water column below the ice shelf following Kobarg (1988). Bathymetry and coastline data were taken from Bedmap2 (Fretwell and others, 2013) and from SCAR (Scientific Committee on Antarctic Research) Antarctic Digital Database 6.0. (c) Enlargement of (b). Sampling sites are indicated by white circles. The TerraSAR-X image provided by the German Aerospace Center (DLR) reveals the different sea-ice regimes in 2012: second-year/first-year sea ice (green), first-year sea ice (blue) and new sea ice grown in October (red). The dotted black curves indicate the locations of ice rises and rumples.

down the tape using a metal bar (as described by Crocker, 1988; Gough and others, 2012). We located the bottom of this layer by gently pulling the tape upwards, trying to feel the first resistance to the metal bar. But during most of our measurements, the bottom of the platelet layer was not well defined: the interface was often mushy rather than consolidated. We also used an under-ice camera (CAM1) fitting through a regular borehole to obtain visual impressions of the platelet layer in real time. In doing so, it became apparent that using the 'metal-bar' method we frequently underestimated the 'true' platelet-layer thickness by up to 0.3 m. However, we then defined the thickness as the point where a first resistance was felt against a slight pressure, rather than the scratching of single crystals on the metal. The number of measurements at each study site varied, depending on the difficulties the platelet layer imposed on our sampling. The presence of consolidated parts within the otherwise mushy platelet layer sometimes prevented the metal bar from penetrating through the entire thickness. In addition, the bar got stuck several times and we were not able to retrieve it.

Several in situ observations of platelets suspended in the water column were made by colleagues, who installed an under-ice camera (CAM2) in a crack near the western ice-shelf edge (70°37.3′ S, 8°05.5′ W) between 22 and 30 November 2012, to observe the behavior of Weddell seals (personal communication from I. van Opzeeland, 2012).

In order to link our platelet-layer observations to the prevailing oceanographic conditions, we used conductivity–temperature–depth (CTD) data recorded by the Perennial Acoustic Observatory in the Antarctic Ocean (PALAOA; Boebel and others, 2006). PALAOA was constructed on the Ekström Ice Shelf in 2005/06, 1.53 km from the ice-shelf edge (70°31′ S, 8°13′ W). The instrument itself was lowered through a hot-water drillhole, and was installed in the water column at ~155 m depth, 70 m below the ice-shelf bottom and 90 m above the seafloor. Relevant oceanographic parameters were calculated using the Gibbs Seawater (GSW) Oceanographic Toolbox (McDougall and Barker, 2011).

We operated two automatic weather stations (AWS) on the fast ice in 2012, recording air temperature and relative humidity (shielded HMP155A, Vaisala; height ~2 m),

Table 1. Corrections applied to meteorological data measured at Neumayer III

Parameter	Correction
Air temperature (2 m)	+1.05°C
Relative humidity (2 m)	−3.6%
Barometric pressure (2 m)	+5.6 hPa
Upward longwave radiation	+8 W m^{-2}

barometric pressure (61302V, RM Young Company; height ~1 m), wind speed and direction (Marine Wind Monitor 05106-5, RM Young Company; height ~3 m), as well as downward and upward long- and shortwave radiation (CNR4, Kipp & Zonen; height ~2.4 m) at 1 min intervals (Hoppmann and others, 2013b,c). AWS1 was deployed at a site (70°35.135′ S, 7°54.802′ W) between ATKA07 and ATKA11 from 6 July to 17 August. AWS2 was deployed at ATKA03 from 2 October to 27 December 2012. We also deployed an eddy covariance (EC) station at ATKA03 between 21 November and 30 December 2012. The EC station was equipped with a three-dimensional sonic anemometer (CSAT3, Campbell Scientific Inc.; height 2.55 m) and a CO_2/H_2O analyzer (LI-7500, LI-COR Environmental; height 2.35 m). Turbulent fluxes of sensible and latent heat were calculated using a modified version of ECPACK (Van Dijk and others, 2004; Mauder and others, 2013).

Finally, we retrieved a set of full-length sea-ice cores (one at each study site) on 19 December 2012 to investigate the impact of ice platelets on the fast-ice crystal structure. All cores were drilled using a 0.09 m diameter titanium corer. The cores were transported to Bremerhaven, and a detailed texture analysis is currently in progress. In this study, we show one exemplary sea-ice core retrieved at ATKA24. We used a microtome to prepare horizontal and vertical thin sections ($\leq 5 \times 10^{-4}$ m) along the entire core length. All thin sections were photographed between crossed polarizing filters. Crystal *c*-axis orientation measurements were made on selected thin sections using a G50 Automated Fabric Analyzer (Wilson and others, 2003) and the Investigator software (Russell-Head Instruments). The data were plotted onto Schmidt equal-area nets, following Langway (1958), utilizing a uniform grid of 500 points covering the sample area.

Model simulations

We applied a one-dimensional thermodynamic model (Bitz and Lipscomb, 1999) to simulate sea-ice growth at Atka Bay with local atmospheric forcing. We used data recorded at the meteorological observatory of Neumayer III to generate a continuous time series of atmospheric conditions throughout the growth season (König-Langlo, 2013a,b). To account for the differences on the ice shelf and directly on the sea ice, we applied corrections to air temperature, barometric pressure, relative humidity and upward longwave radiation (Table 1). These corrections were based on comparison with the data recorded by the two weather stations (Hoppmann and others, 2013b,c). The corrected data are presented in Figure 2a–d.

We used these data to calculate sensible and latent heat fluxes by a bulk method (Andreas and others, 2010), and compared the results with the EC-based flux data. The two datasets are in good agreement (Fig. 2e and f). We used short- and longwave radiation, as well as sensible and latent heat fluxes, for model forcing. In addition, several other parameters were initialized in the model. We used a sea-ice density, ρ_{si}, of 925 kg m^{-3} (near the top of the range reviewed by Timco and Frederking, 1996), a snow density, ρ_s, of 330 kg m^{-3} (slightly higher than reviewed by Massom and others, 2001, for the Weddell Sea) and introduced a C-shaped salinity profile, typical of the southeastern Weddell Sea in winter (Eicken, 1992). Since the snow cover is a crucial factor in sea-ice growth, we included a step function based on the observed snow-depth evolution. Finally, we adjusted the bulk albedo to 0.9, which is in the upper range of our preliminary results of albedo measurements in November (0.8–0.9). This was necessary to avoid extensive surface melt in the model, which was not observed during summer. At sites where dynamic growth was not observed and the dates of initial sea-ice formation were accurately known from satellite imagery, the model was initialized with a minimal sea-ice thickness and the known date of initial formation. Otherwise we initialized the model with results from measurements of our first visit. Assuming that the platelet layer buffers the solid sea ice to potential positive oceanic heat fluxes throughout the growth season (May–December), we set the oceanic heat flux to 0 W m^{-2}. However, in our model runs an oceanic heat flux of +3 W m^{-2} starting in mid-December 2012 was necessary to prohibit further growth. Since the freezing interface grows into a water body with only a fraction of interstitial water available for freezing, we modified the sea-ice growth rate, GR, in the model by

$$\mathrm{GR}(\beta) = \frac{1}{1-\beta}\,\mathrm{GR}, \qquad (1)$$

where β is the ice-volume fraction in the platelet layer.

This is reasonable, since only the latent heat to freeze a water fraction of $1-\beta$ of a given volume is transported towards the colder atmosphere during sea-ice growth. If $\beta = 0$, ice crystals in the water near the freezing interface are absent, and growth progresses as usual. According to our field observations (see below), the platelet layer was not established before June in 2012, and we set $\beta = 0$ in the model accordingly. From the beginning of June 2012, ice platelets were present below the fast ice and the modified growth rate was used in the model. For the purposes of our simulations, the platelet layer is assumed to be infinite in extent and thickness with regard to the freezing interface.

RESULTS

Observed fast-ice thickness and snow cover

During our study in 2012, the recorded air temperatures ranged from –46.1°C (25 July) to +2.2°C (17 December). The average air temperature was –16.2°C, while the lowest and highest monthly averages of –29.5 and –3.4°C were measured in July and December, respectively. The average 2 m wind speed measured was 7.5 m s^{-1}, peaking at 34 m s^{-1} on 6 August. Easterlies dominated, with ~30% of the winds arriving in the range 80–100° from the north. Sea-ice thickness, snow depth and freeboard obtained at the various sites occupied during 2012/13 exhibited considerable spatial variability (Fig. 3, Table 2).

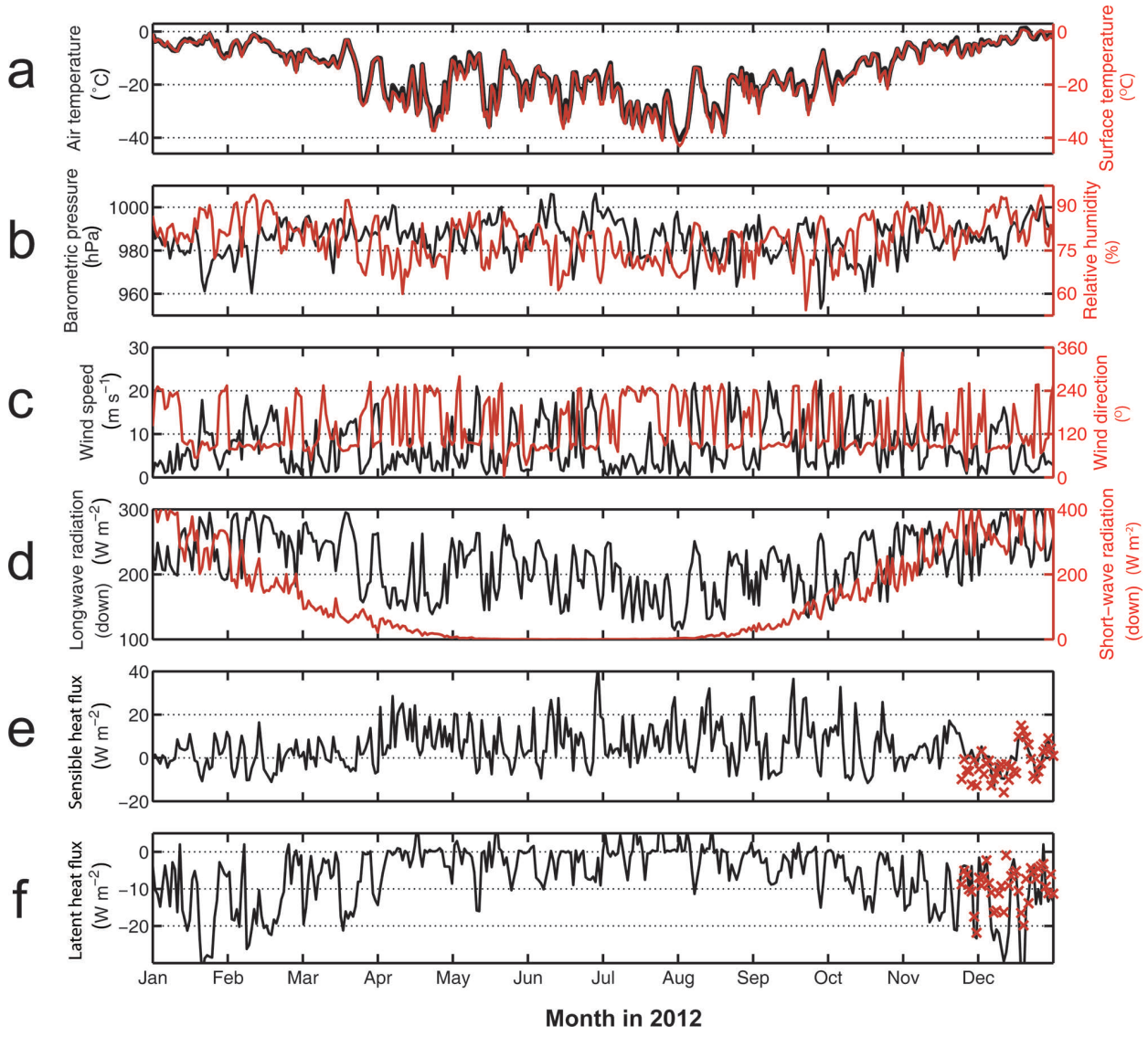

Fig. 2. Daily averages of modified atmospheric parameters recorded at the Neumayer III meteorological observatory in 2012. (a) Air (black) and surface (red) temperatures. (b) Barometric pressure (black) and relative humidity (red). (c) Wind speed (black) and wind direction (red). (d) Downward longwave (black) and shortwave (red) radiation. (e) Sensible heat flux calculated by the bulk method (black) and the eddy covariance method (red). (f) Latent heat flux determined by the bulk method (black) and the EC method (red). Fluxes are considered negative (positive) if directed towards the atmosphere (sea ice).

Sea-ice thickness and its spatial variability were generally higher at the westernmost sites, where persistent easterly winds (Fig. 2c) pushed the sea ice towards the ice-shelf edge. While sea-ice thicknesses greater than 2 m were measured at ATKA03 and ATKA07 as early as August/September 2012 (and later also at ATKA16), sea ice at the eastern sites was thinner. Sites with lower sea-ice thicknesses generally exhibited lower horizontal variability

Table 2. Study sites in 2012. Abbreviations: D: deformed ice; L: level ice; d_w: water depth determined by CTD casts in November and December 2012; T_{form}: formation of continuous sea-ice cover; max(z_{si}): maximum sea-ice thickness (December); $\overline{z_s}$: mean snow depth; $\overline{z_f}$: mean freeboard; β: ice-volume fraction in the platelet layer

Study site*	Latitude (S)	Longitude (W)	Ice type	d_w m	T_{form}	max(z_{si}) m	$\overline{z_s}$ m	$\overline{z_f}$ m	β
ATKA03	70°34.513′	8°02.961′	D	140	March	2.56	0.02	0.29	0.18
ATKA07	70°34.995′	7°56.732′	D	175	March	2.62	0.41	0.26	0.35
ATKA11	70°35.530′	7°49.485′	D/L	>250	March/October	0.73	0.17	–0.02	0.31
ATKA16	70°35.988′	7°42.095′	D	175	April	2.01	0.70	–0.06	0.3
ATKA21	70°36.471′	7°34.610′	L	135	May	1.71	0.27	0.1	0.28
ATKA24	70°36.955′	7°28.965′	L	135	May	1.83	0.08	0.14	0.22

*The number indicates the distance to the western ice-shelf edge.

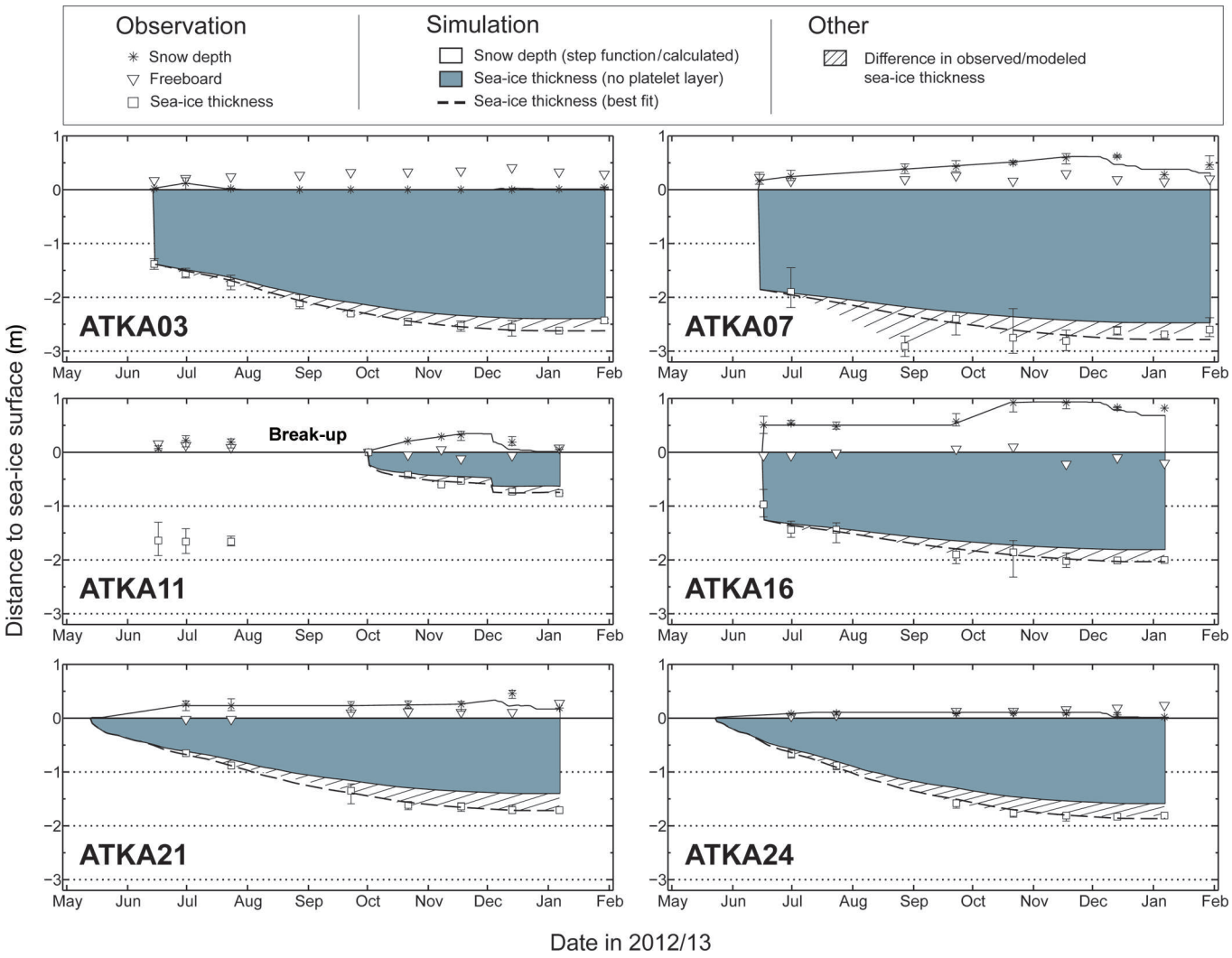

Fig. 3. Fast-ice and snow conditions at the six sampling sites on Atka Bay fast ice in 2012/13. Observed parameters and their variability ranges are indicated, along with results from simulated sea-ice growth.

(ATKA11 (late), ATKA21, ATKA24). Due to a partial break-up of fast ice in the central Atka Bay during a storm in late August 2012, sea ice at ATKA11 only grew to a maximum thickness of 0.73 m after its new formation. Although there had been early sea-ice break-up events in previous years, this is not generally representative.

The snow depth generally increased towards the center of Atka Bay, with highest snow depths (>0.5 m) at ATKA07 and ATKA16 in October 2012. Due to the fast-ice break-up, snow at ATKA11 was first exported with the sea ice and then blown into the ocean. As soon as a continuous sea-ice cover established again at ATKA11, in October 2012, snow accumulation followed the same pattern as at other sites. Low snow accumulations (<0.1 m) were observed at ATKA03, due to the influence of a nearby iceberg, and at ATKA24, due to the proximity of the ice-shelf edge. Intermediate accumulations were recorded at ATKA11 and ATKA21 (0.1–0.5 m). Wherever a snow cover was present, it was highly variable. Snow sastrugi up to 2 m long and 0.5 m wide were frequently observed, adding to local variability. The overall seasonal cycle of snow depth was generally characterized by an increase from initial sea-ice formation to November 2012, but no significant surface melt was observed until the end of our study in January 2013.

While freeboard was positive at most sites throughout the study, the snow load at ATKA11, and to a smaller extent at ATKA16, caused surface flooding in November. The subsequent snow-ice formation at ATKA11 led to a near-instant increase in sea-ice thickness of ~0.15 m. As the model does not account for snow-ice formation, this additional sea-ice growth was manually added in the simulation.

Simulated fast-ice growth

Due to substantial differences in initial formation dates, dynamic growth and snow cover among the study sites, we simulated local sea-ice growth for each site separately. Despite the high albedo of 0.9, the model results indicate that snow ablation would have taken place in summer when forced by the observed downwelling radiation. The control simulations without any ice platelets in the water column below the fast ice ($\beta = 0$) are depicted as gray areas in Figure 3, with the differences between them and the observed thickness hatched. In order to match the measured temporal evolution of the sea-ice thickness, the simulations were repeated, varying β between 0 and 0.5 in steps of 0.01. After each run, the difference from the measured sea-ice thickness was determined (Fig. 4). By minimizing this discrepancy, we were able to identify a best-fit β for each

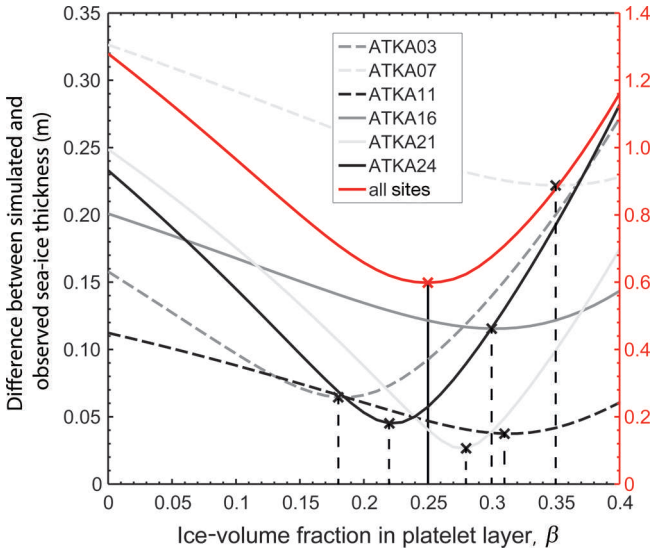

Fig. 4. The difference between simulated and observed sea-ice thicknesses with variable ice-volume fractions in the platelet layer.

site. The computed best-fit values of β ranged from 0.18 (ATKA03) to 0.35 (ATKA07), while intermediate values were 0.22 (ATKA24), 0.28 (ATKA21), 0.30 (ATKA16) and 0.31 (ATKA11). The simulated sea-ice thickness at each site with its best-fit β is also shown in Figure 3 (dashed curve). In order to calculate an average ice-volume fraction, we determined the combined difference between simulations and observations at all sites and samplings. By addition of all curves and subsequent determination of an overall minimum, we obtained an average β of 0.25 (Fig. 4, red curve). In contrast to a calculation of the arithmetic mean, in this approach the sampling sites with less-consistent measurements, resulting in a flatter curve (e.g. ATKA07), were weighted lower.

Sub-ice platelet-layer thickness

Figure 5 shows the evolution of the platelet-layer average thickness, z_p, at the six sites, along with a location map of the area and selected oceanographic data, as recorded by the CTD below the northern part of the ice shelf. The ice shelf is grounded in the south and east of Atka Bay (Fig. 5), resulting in ice rises (dark gray) and ice rumples (dashed curves), where no water exchange with the cavity is possible. The direction and magnitude of the Antarctic Coastal Current (ACoC) are mostly governed by wind patterns and tides, leading to small-scale fluctuations (even reversals) and high seasonal variability (Fahrbach and others, 1992).

The seasonal cycle of z_p (Fig. 5b) showed a nearly linear increase at all sites between June and December 2012. Due to equipment failure and the break-up in August 2012, the time series at ATKA16 only started in October 2012. z_p reached its maximum in December 2012 at five sites. The maximum at ATKA16 occurred in January 2013. This was most likely due to an underestimation of z_p in December 2012, which is an average of only two measurements. z_p was generally highest at the two westernmost sites ($z_p > 4$ m in December 2012), compared with the other sites ($z_p < 4$ m). The spatial distribution of z_p revealed a general increase towards the center of Atka Bay, with local maxima at ATKA07 and ATKA16. Of our sites, ATKA07 obtained the maximum observed platelet-layer thickness (5.65 m, December 2012), while ATKA11 recorded the lowest maximum platelet-layer thickness (1.32 m, December 2012). We attribute this to an export of platelets into the open ocean during the August 2012 break-up. The amount is unknown

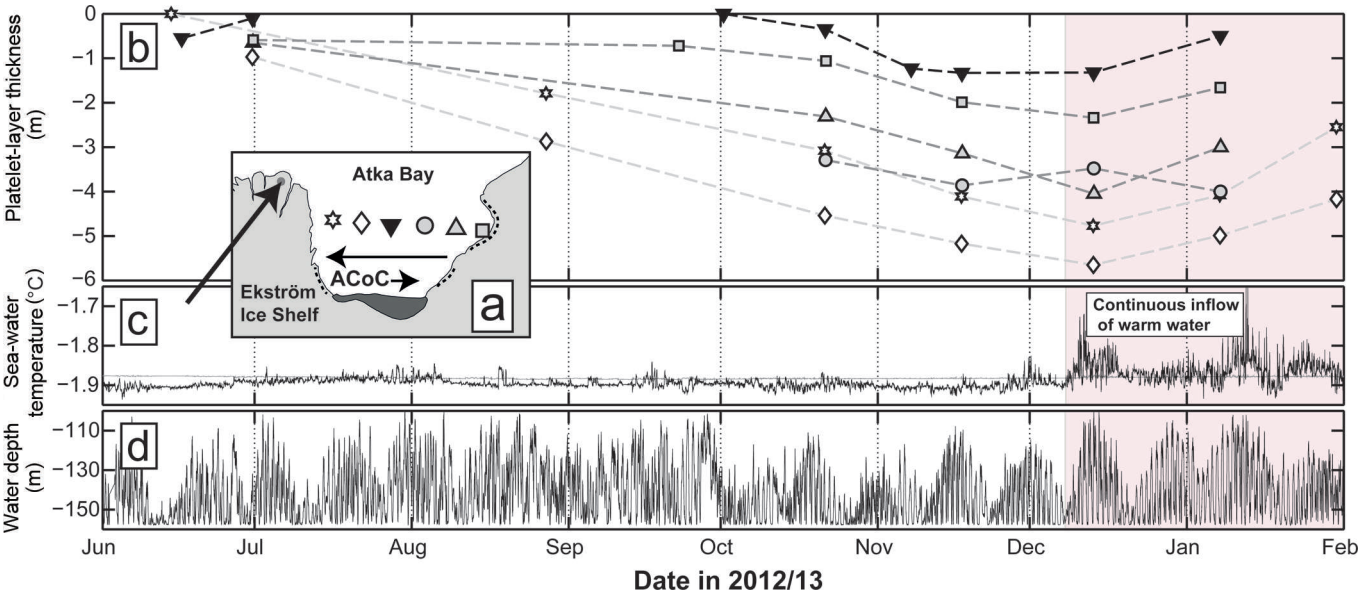

Fig. 5. Platelet-layer thickness at the six sampling sites on Atka Bay fast ice in 2012/13, along with oceanographic conditions recorded at a measurement site below the Ekström Ice Shelf. (a) Location map of the study area. Sampling sites are indicated by symbols (ATKA03: star; ATKA07: diamond; ATKA11: inverted black triangle; ATKA16: gray circle; ATKA21: gray triangle; ATKA24: gray square) and grouped into western, central and eastern sites. The location of the oceanographic measurements in (c) is indicated by the dot and the arrow. The two other arrows depict the two extremes of the strength and direction of the Antarctic Coastal Current in this area. (b) Sub-ice platelet-layer thickness evolution at the different sites, with symbols corresponding to their location according to (a). (c) In situ temperature (black) and corresponding surface freezing point (gray) of the water at a location below the northern Ekström Ice Shelf in 2012/13. When the temperature is below the surface freezing point, the water is potentially supercooled. The shaded area indicates the continuous inflow of warm water masses. (d) Water depth of the corresponding temperature record.

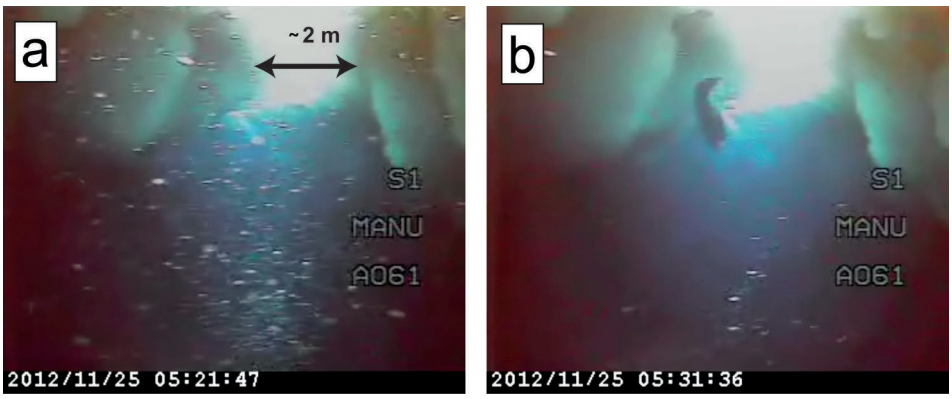

Fig. 6. Video still images from under-ice video recordings. (a) Masses of ice platelets float upwards during a high-flux event. (b) 'Normal' conditions at the end of November 2012.

and it cannot be assessed whether an absolute maximum in the center of Atka Bay would be observed under normal conditions. However, the small amount of platelets at the beginning of the measurements in June 2012 and the low accumulation rate after October 2012 suggest that a local minimum was to be expected in this area. Since sporadic measurements at other sites in southern central Atka Bay yielded thicknesses of up to 10 m, and assuming that z_p is generally lower in the northern part of Atka Bay, we estimate a bay-wide average of 4 m in December.

Figure 5c and d show the time series of sub-ice-shelf water temperature, the corresponding surface freezing point and the depth of the instrument during the temperature measurement. The depth variations revealed a 14 day cycle overlying the 12 hourly tidal cycle. The depth varied between 100 and 155 m, reflecting the strength and direction of the tidal- and wind-induced ACoC. The maximum depth of 155 m was limited by the length of the cable, while the ACoC was strong enough to lift the instrument to depths as shallow as 100 m. In this sense, the instrument became a vertical profiler of the water column between 100 and 155 m. The water temperatures ranged from –1.94 to –1.6°C. It is apparent that the in situ temperature of the water column was mostly below the surface freezing point between June and December 2012. At the beginning of December 2012, the water temperatures of nearly the entire water column rose above the surface freezing point. The high temperature variability indicated that the water column was also very inhomogeneous between December 2012 and February 2013. At the same time, the highest temperatures were measured at shallower water depths.

The video recordings of CAM2 indicated that platelet accumulation was not the result of a uniform flux of platelets. Instead, a small continuous upward flux was overlaid by periods of very high fluxes with a time span usually $\ll$1 hour (Fig. 6). Speed and direction of the ice platelets were highly variable, and most likely depended on their volume and the influence of tidal currents and local turbulences.

Upon arrival at the sea-ice/platelet-layer bottom, crystals of different sizes and shapes integrated into a porous layer in random orientations (Fig. 7). The individual platelets in the bottom part were not firmly fixed in the lattice, but were still prone to resuspension by turbulence and strong currents. Small filaments of phytoplankton growing at the platelet edges were frequently observed. These provide a rich food source for amphipods grazing the platelet layer, which were observed in great numbers on several occasions in November and December 2012 (Fig. 7d).

Sea-ice texture and growth history

As seen from the texture analysis of a 1.94 m long sea-ice core obtained at ATKA24 in mid-December 2012 (Fig. 8), the level sea ice in this area grew predominantly thermodynamically, with no indications of ridging or rafting. Satellite imagery revealed the establishment of a closed sea-ice cover at this site around 25 May 2012. This core is therefore representative of thermodynamically grown fast ice, but with a comparatively late formation date. Each core depth was assigned an approximate date of formation by comparison with the sea-ice thickness evolution at that site (Fig. 3).

Horizontal and vertical thin sections (Fig. 8) revealed a typical granular texture in the early period of formation (25 May to early June 2012). This is an indication of typical wind- and wave-induced growth, especially since snow ice did not contribute to sea-ice growth at this location. This granular ice contributed ~0.12 m (6%) of the total sea-ice thickness. The texture in the following 1.5 m (77%) mostly resembles that termed draped platelet ice by Jeffries and others (1993, their fig. 10b and c), Tison and others (1998, their fig. 1a) and Dempsey and others (2010, their figs 4 and 5). According to Jeffries and others (1993), those crystals are less angular, more equidimensional and have wavy, uneven edges. The lower 0.32 m (17%) of our core consisted of blade-like crystals, partially also with wavy edges. These resemble the bladed platelet ice shown by Jeffries and others (1993, their fig. 11), Eicken and Lange (1989, their fig. 5) and Dempsey and others (2010, their figs 4 and 5). The individual crystals in this part have various sizes, with crystal lengths of 0.01–0.1 m, even in the same thin section. As apparent from the Schmidt net plots (Fig. 8, right-hand side), the crystal *c*-axis orientations showed a random distribution for all the analyzed samples. This distribution is typical for platelet ice (Dempsey and Langhorne, 2012).

DISCUSSION

Seasonal cycle of fast-ice thickness and snow cover

We have performed regular year-round measurements of fast-ice properties at Atka Bay since 2010. Although differences in dynamic-growth contribution, dates of

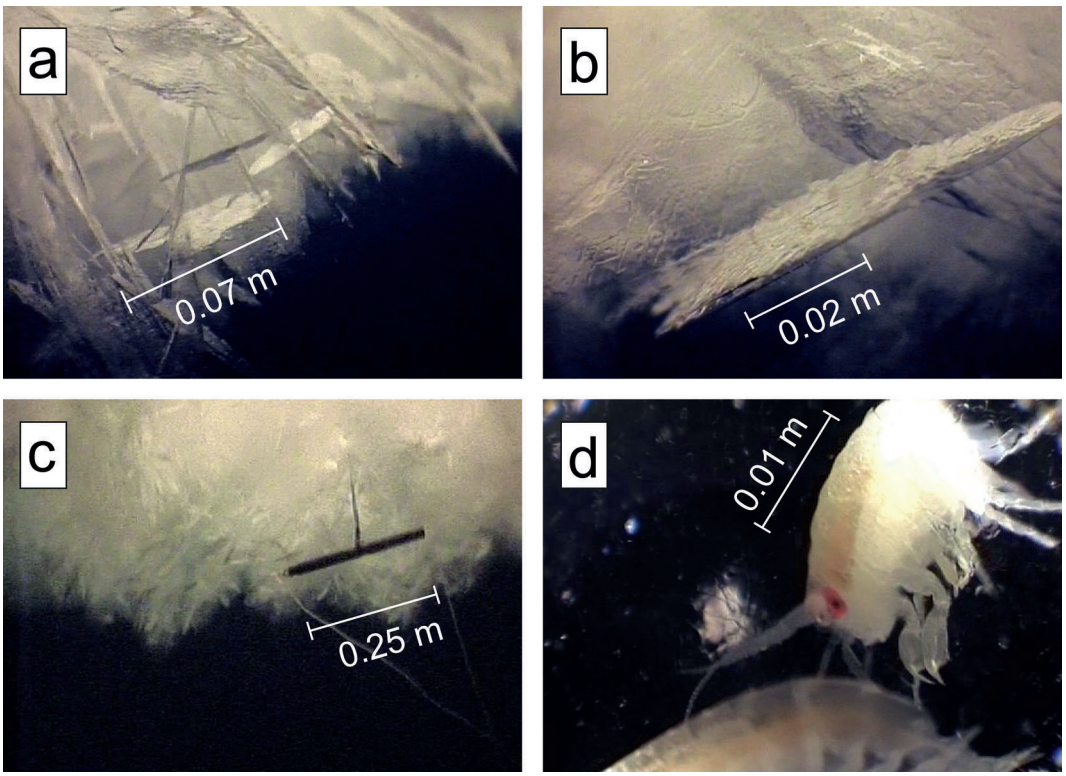

Fig. 7. Video still images of the platelet layer. (a) Single ice platelets several centimeters wide and <0.001 m thick stick together to form a porous layer. (b) Close-up of an ice platelet. (c) Measuring the platelet-layer thickness with a metal bar (0.25 m). (d) Amphipods (<0.02 m) grazing the platelets for phytoplankton growing at the platelet edges.

formation and snow cover determine the sea-ice evolution at Atka Bay each year, the results of our fast-ice observations in 2012 are generally in accordance with field measurements performed in previous years. The seasonal fast-ice cover of 2011 started to break up in late February 2012. Satellite observations revealed that several smaller sea-ice floes remained in the embayment, reattached to the ice-shelf edge in the southwestern part and became second-year sea ice. In the second half of March 2012, initial sea-ice growth started, while easterly winds constantly pushed the thin ice towards the ice-shelf edge. Visual observations confirmed a closed fast-ice sheet in the western part of Atka Bay at the end of April 2012, while the rough surface indicated the large contribution of dynamic processes to sea-ice growth. This area of mixed first/second-year sea ice is also characterized by a high radar backscatter (Fig. 1; bright color, marked in green). (A more detailed description of fast-ice surface properties at Atka Bay and their influence on TerraSAR-X radar backscatter is presented by Paul and others, 2015.) Strong winds constantly cleared away thin sea ice in the eastern part, where a closed fast-ice sheet was finally established 1 month later, at the end of May 2012. Dynamic growth again led to a greater thickness at ATKA16 than at the easternmost sites. A GPS buoy on one of the floes broken up in August 2012 revealed that it had drifted into the central Weddell Sea by the time data transmission finally stopped due to a power failure (69°43.8′ S, 45° 49.9′ W on 26 August 2013). New sea ice immediately started to grow in the break-up area, but was cleared out of the embayment by persistent winds. At the beginning of October 2012, a closed fast-ice cover was again formed in the break-up area (Fig. 1; marked in red) after the grounding of the large iceberg B15G in front of Atka Bay.

The great thicknesses and local variability (Fig. 3) confirm that dynamic growth contributed to sea-ice formation at ATKA03, ATKA07, ATKA11 (early) and ATKA16. No dynamic growth was observed at ATKA21 and ATKA24, where initial formation was delayed until May 2012. Kipfstuhl (1991) and Günther and Dieckmann (1999) found maximum sea-ice thicknesses of 2.19 and 2.17 m, and snow depths up to 0.62 m, at their study site ~3 km southwest of ATKA03 (70°35.05′ S, 8°8.41′ W) in 1982 and 1995, respectively. Our results showed a higher maximum thickness of 2.56 m at ATKA03, which may be attributed to higher growth rates due to increased upward conductive heat flux, owing to the lack of snow. While the small snow depths at ATKA24 were associated with topographic/local-wind patterns in close proximity to the ice shelf (~1 km away), the lack of snow at ATKA03 is explained by the presence of a small, grounded iceberg ~2 km to the east. In 2010 and 2011, we observed much higher snow depths (~0.8 m in December) in the western part of Atka Bay. While an east–west gradient in snow depth is expected, due to the prevailing wind conditions and consequent snow redistribution, local topographic features (e.g. icebergs and pressure ridges) alter snow accumulation locally (e.g. at ATKA03 and ATKA16). This gradient generally introduces additional variabilities in sea-ice growth rates, and at the same time opposes the gradient in dynamic growth. For example, the large contribution of dynamic thickening in the west of Atka Bay is partly compensated for by a lower thermodynamic growth, due to the greater snow depth.

Snow-ice formation is a major contributor to pack ice in the Southern Ocean (Eicken and others, 1995; Jeffries and others, 2001). Günther and Dieckmann (1999) observed no negative freeboard at Atka Bay during their study. Our

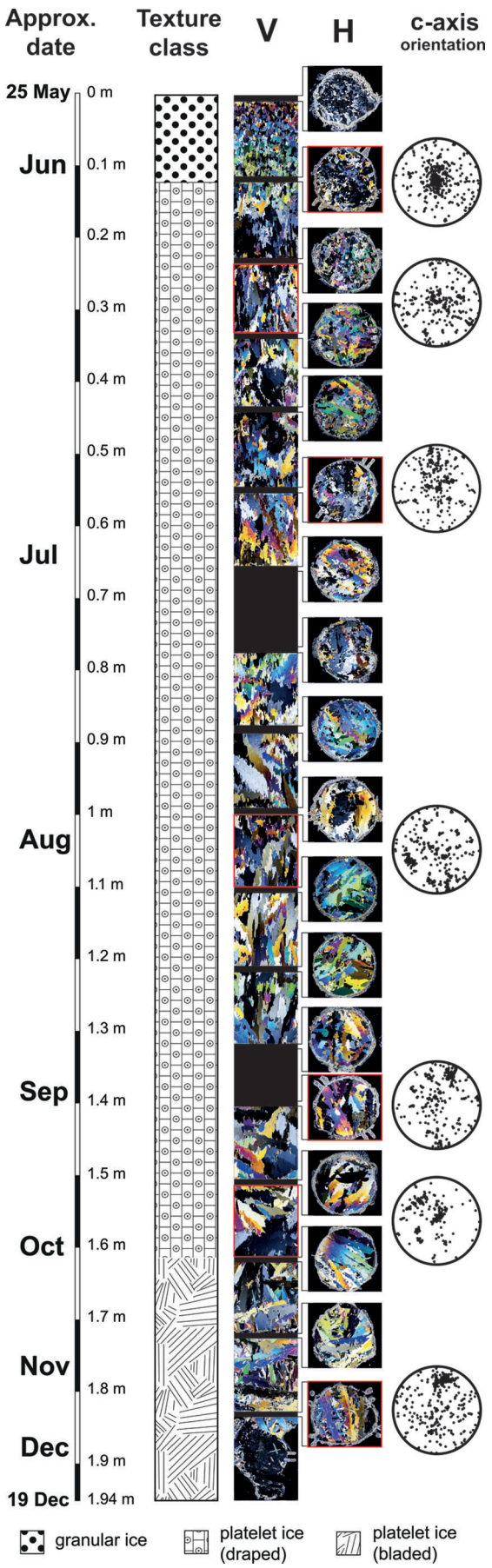

Fig. 8. Crystal structure of horizontal (H) and vertical (V) thin sections of a sea-ice core retrieved at ATKA24. The black areas represent segments where no data are available. The Schmidt equal-area net diagrams (right) depict the c-axis orientations of samples indicated by a red border.

results agree with the findings of Kipfstuhl (1991), who found flooding in areas with snow depths greater than 1 m. However, the relative number of negative freeboard observations was very low. An exception was the area of new ice with a negative freeboard in November 2012. The sea ice there became permeable at the beginning of December 2012, when subsequent surface flooding and refreezing of slush resulted in a 0.15 m thick, fine-grained layer of snow ice. But, since such a late formation and the resulting low thickness is usually not observed, we consider the contribution of snow-ice formation to total sea-ice mass at Atka Bay to be very low, despite the thick snow cover. This finding is directly linked to the presence of ice platelets below the fast ice. Through its buoyancy, the platelet layer effectively increases the freeboard and simultaneously reduces the occurrence of surface flooding and subsequent snow-ice formation, which would otherwise be more frequent. The strength of this effect depends on the thickness and ice-volume fraction of the platelet layer.

Seasonal cycle of the platelet layer

Günther and Dieckmann (1999) took advantage of the buoyancy effect and used Archimedes' law to calculate the platelet-layer thickness during their study. They obtained a platelet-layer thickness of ~1.2 m in December 1995. Kipfstuhl (1991) used a sinking weight of 1 kg to determine the depth at which it sank freely. By doing so, he was able to provide an estimate of a 4 m thick platelet layer in November 1982. Neither study provided an uncertainty estimate. While our results obtained with the 'metal-bar' method yield good agreement with the 'sinking-weight' method of Kipfstuhl (1991), the results of Günther and Dieckmann (1999) suggest that either the uncertainty in their method is very large or the platelet accumulations were profoundly different between the years. We consider the 'metal-bar' method as the most robust and exact of the three procedures. Finally, our result of platelet-layer thicknesses of several meters is also in accordance with Eicken and Lange (1989), who found platelet layers of >5 m below fast ice at Drescher Inlet.

We observed ice-platelet accumulations under the fast ice as early as June (Fig. 5). This is in accordance with Günther and Dieckmann (1999), while Kipfstuhl (1991) noticed ice platelets in boreholes as early as the end of April. The onset of ice-platelet accumulation below the fast ice of McMurdo Sound was also found to be variable. Gough and others (2012) recorded ice-platelet growth on suspended 'hot wires' in mid-July and a thin platelet layer of 0.02 m in early August, while Leonard and others (2006) identified a modified sea-ice texture in first-year sea-ice cores as early as April. Like similar structured studies involving the evolution of platelet-layer thickness, we observed a steady increase throughout the winter and spring. However, results obtained from CAM2 near the western ice-shelf edge in November 2012 suggest that the ice-platelet accumulation is mainly a result of episodic events of high flux overlying a very low continuous flux. This episodic flux was also observed in McMurdo Sound, where Leonard and others (2006) interpreted episodically present acoustic scatterers in the water column as a flux of buoyant platelet crystals.

Below McMurdo Sound fast ice, ice platelets have also been observed growing while already attached to the fast ice above, rather than being advected from depth (Smith and others, 2001). Smith and others (2012) found that single ice platelets attached to the fast-ice bottom grow in

discontinuous, episodic bursts, mainly depending on the influence of variable currents during periods of continuous supercooling directly below the fast ice. While the potential supercooling observed under the front of the Ekström Ice Shelf throughout the winter (Fig. 5c) is indicative of ice-platelet formation at depth, we currently have no indication of in situ supercooling directly below the fast ice. As the rising ice platelets observed in the videos were also already large in diameter, we hypothesize that the main mechanism for the establishment of the Atka Bay platelet layer is crystal growth at depth, while growth at the ice/water interface is of minor (if any) importance. This is in accordance with the conclusions of Eicken and Lange (1989), who suggested that the platelets in the southeastern Weddell Sea (pack ice) most likely form at greater depth.

Very little is known about the currents in the Ekström Ice Shelf cavity. Nicolaus and Grosfeld (2004) using model studies found that the circulation is dominated by a strong cyclonic gyre, taking half a year between eastern inflow and western outflow. Like Neckel and others (2012), they did not find any evidence for marine-ice accretion under the ice shelf itself. The presence of ice rises and rumples east of Atka Bay (Fig. 1) and the spatial distribution of ice platelets suggest that they are mainly advected from the area north of Neumayer III. As revealed by fluctuations of CTD recorded pressure (Fig. 5d), the magnitude of the ACoC is highly variable in the region (Fahrbach and others, 1992). Quantification of the current velocity derived from the pressure data is generally possible and currently under investigation. Tidal- and wind-induced currents may cause turbulence in the cavity when the predominantly westward ACoC weakens or even reverses in direction. The resulting turbulent flow is likely to provide transport for the platelet crystals (Fig. 5a). If this is true, a significant amount of supercooled water would be transported into the open ocean along the main current direction. Currently, we have no direct evidence for this hypothesis, but studies in the southwestern Weddell Sea (e.g. Eicken and Lange, 1989) found accumulations of ice platelets far from the coast, which agrees with our hypothesis.

As apparent from the evolution of water temperatures, the declining thickness of the platelet layer in December 2012 at nearly all study sites (Fig. 5b) is linked to the inflow of warm water masses and subsequent melt of ice platelets. Additional under-ice CTD casts in December 2012 revealed that warm surface water penetrates into Atka Bay from the east. At the same time, the buoyant ascent of ice platelets visible in the recordings ceased completely. Apart from the shrinking platelet layer, only a very slight bottom melt is apparent from the thickness data in Figure 3. Preliminary results (not shown) from high-resolution temperature profile data suggest that at ATKA03 no bottom melt occurred whatsoever. In addition, sea-ice cores taken in December 2012 showed a slight increase in sea-ice porosity from interior melt. Although we do not quantify the process here, the platelet layer acts as an efficient buffer between the fast ice and the incoming warm water in summer (Eicken and Lange, 1989). Usually the increased instability of the fast-ice cover through interior melt combined with tides and strong winds, as well as a pack-ice-free zone in front of the Ekström Ice Shelf, would lead to fast-ice break-up early in the following year. The flocking effect of iceberg B15G in front of Atka Bay (Fig. 1) held the 2012 fast ice in the bay, so 2013 saw second-year fast ice in the region. The iceberg itself detached and drifted westwards in August 2013. It is unclear whether the iceberg also modified the properties of the platelet layer in 2012 compared with other years.

Table 3. Selected estimates for the ice-volume fraction of the platelet layer, modified after Gough and others (2012)

Location	Ice fraction	Method	Source
Atka Bay	0.25	Modeled heat flux forced by atmosphere	This study
	0.29–0.43	Multi-frequency electromagnetic induction sounding	Hunkeler and others (2015)
	0.46	Archimedes' law	Günther and Dieckmann (1999)
	0.2	Modeled heat flux forced by atmosphere	Kipfstuhl (1991)
McMurdo Sound	0.16	Archimedes' law	Price and others (2014)
	0.25	Measured heat flux from sea-ice temperature profiles	Gough and others (2012)
	0.35	Measured heat flux from sea-ice temperature profiles	Purdie and others (2006)
	~0.33	Estimate from sea-ice temperature profiles	Trodahl and others (2000)
	>0.50	Estimate from horizontal thin sections	Jeffries and others (1993)
	0.50	Estimate from core holes	Crocker and Wadhams (1989)
	0.20	Estimate from core holes	Bunt and Lee (1970)
Model domain	0.06	Three-dimensional geometric model	Dempsey and others (2010)

Ice-volume fraction in the platelet layer

While ice platelets accumulate episodically below the fast ice during winter, the advancing freezing interface incorporates the upper portion of the underlying platelet layer into the sea-ice fabric by freezing of the interstitial water. As a result, part of the solid fast ice originates from heat loss to the ocean. This is in contrast to the usual process of heat conduction to the atmosphere, which gives rise to congelation growth. In this sense, the energy- and mass balance of the fast ice is altered and must be accounted for. To quantify this impact, it becomes necessary to determine the ice-volume fraction, β, in the platelet layer. The model results (Fig. 4) suggest a bay-wide average β of 0.25, with individual results 0.18–0.35.

Ice-volume fractions in the platelet layer have been estimated in a number of previous investigations (Table 3). Our average β of 0.25 agrees well with the findings of Kipfstuhl (1991), who derived a β of 0.2 from their comparison between a thermodynamic model and sea-ice thickness observations at their study site 3 km southwest of ATKA03. In addition, our result is in good agreement with a recent study at McMurdo Sound by Gough and others (2012), who calculated an ice-volume fraction of 0.25 from measured ice-temperature profiles and claim their 'result being the most precise to date'. This suggests that our growth model results are reasonably good. Three studies (Crocker and Wadhams, 1989; Jeffries and others, 1993; Günther and Dieckmann, 1999; Table 3) obtained significantly higher results (β >0.46), which we attribute either to profoundly different conditions or unsuitable methods. Dempsey and

others (2010) attribute their low result ($\beta = 0.06$) to in situ platelet growth and secondary platelet movement, which were not accounted for in their model.

Possible uncertainties in our calculation arise from the fact that some physical processes are not implemented in the model (e.g. gravity drainage) and from constant parameters (e.g. albedo, salinity profile and sea-ice and snow densities). However, the forcings of downward radiant heat fluxes are expected to be very reliable, as they were derived using data from a World Meteorological Organization standard meteorological observatory. Some uncertainty is introduced through the sensible and latent heat fluxes derived from the bulk method. Further potential uncertainties arise from the limited information about snow depths, individual dates of freeze onset, the uncertainty of sea-ice thickness measurements and the date of first platelet accumulation at each site. Furthermore, our approach of introducing a simple growth-rate modification does not reflect the true physics involved in this process. One example is the possible supercooling directly below the fast ice (Smith and others, 2012), though this might not be as important as it is below McMurdo Sound fast ice. At the same time, our metal-bar measurements revealed that the resistance of the platelet layer, and consequently the ice-volume fraction, is very variable, temporally as well as spatially (even during a single measurement). In addition, our method is, in principle, only suitable for determining the ice-volume fraction of the part which is already incorporated into the solid sea ice, not taking into account the lower platelet layer. This leads to additional uncertainties, particularly under the assumption that the upper part is likely compressed by the buoyancy pressure of the underlying ice platelets.

Since these uncertainties are so manifold, we performed sensitivity studies to identify the parameters and constants with the biggest impact on β. Simulations were set up to yield $\beta = 0.25$ as a control, then relevant input parameters and constants were varied by up to $\pm 5\%$, one at a time. In the following, the absolute minimum and maximum variations corresponding to the 5% are indicated in parentheses. The results show that the model is comparatively insensitive to changes in downward shortwave radiation (0–24 $\mathrm{W\,m^{-2}}$), wind speed (0.01–1.1 $\mathrm{m\,s^{-1}}$), relative humidity (2.6–4.6%) and constants such as sea-ice density (46 $\mathrm{kg\,m^{-3}}$), snow density (16 $\mathrm{kg\,m^{-3}}$) and surface albedo (0.05). In contrast, the outcomes for β vary strongly with varying sea-ice thickness (0.02–0.14 m), oceanic heat flux (+2 $\mathrm{W\,m^{-2}}$), air temperature (0.066–2°C), as well as downward longwave radiation (5.7–15.1 $\mathrm{W\,m^{-2}}$). The sea-ice thickness measurements are considered reliable, since the measurement itself has a very low uncertainty (± 0.01 m) and most data points are an average of up to five spot measurements. A positive oceanic heat flux is very unlikely to be present during sea-ice growth, due to the presence of the platelet layer. Air temperature and downward longwave radiation are measured directly at Neumayer III with high accuracy. By far the largest influence is exerted by the variation of the upward longwave radiation (7.9–16 $\mathrm{W\,m^{-2}}$), which is used to compute the surface temperature and to calculate the turbulent heat fluxes used as a model input. This significantly modifies the surface energy balance and heavily influences sea-ice thickness evolution and, consequently, β. Upward longwave radiation is, in principle, available from Neumayer III with the limitation that the surface temperature of the ice shelf naturally differs from that of the sea ice (as measured by the AWS). For this reason we applied a correction of +8 $\mathrm{W\,m^{-2}}$ to upward longwave radiation after careful analysis of both datasets, finally yielding the best match to the EC flux data. Our study also revealed that, with larger variations of upward longwave radiation, more surface melt occurs and a strong deviation from the sensible and latent heat fluxes measured by the EC method is evident. These effects become even more apparent when increasing the variation above 5%. We therefore consider a corresponding uncertainty of ± 0.05 as an upper limit. Since, according to our sensitivity study, the effect of a change in upward longwave radiation is as strong as that of all the other parameters combined, we estimate that their contributions sum to an additional uncertainty of ± 0.05. We therefore estimate the overall uncertainty at 0.1, yielding $\beta = 0.25 \pm 0.1$.

The impact of ice platelets on fast-ice crystal structure

The complete absence of columnar growth in a core representative of thermodynamical growth is atypical in most sea-ice covered areas. However, in our study region this seems to be the norm, due to the sustained contribution of ice platelets. Our texture analysis provides evidence that the ice platelets disrupted the potential columnar growth as early as June 2012, leading to a mix of incorporated ice platelets and interstitial congelation ice (Jeffries and others, 1993) in 94% of the core. However, the resulting texture is not always unambiguous. Sea-ice crystal structure is very variable and classification is not straightforward. Different analysts may describe the same texture entirely differently. This becomes especially evident when platelet ice is involved. Here *c*-axis measurements using the fabric analyzer provide independent confirmation, in agreement with our visually obtained texture classification. Although we currently have only a small number of analyzed samples, our data support the findings of earlier studies (Dempsey and others, 2010) that there is no apparent distinction in the *c*-axis distribution between draped and bladed platelet ice, which are both characterized by a Schmidt net with randomly distributed points.

Until now it has not been clear which processes govern the shapes and sizes of the crystals, of which there is a large spectrum visible in our core. Jeffries and others (1993) and Tison and others (1998) suggest that this fabric may be related to a variable amount of supercooling in the ice-shelf water from which the ice platelets form. In this study we were unable to address this question. The transition from draped to bladed platelet ice is striking in our vertical thin sections, and analysis of the other cores needs to be completed to gain additional insights.

It should be noted that our results based on one core may present a significant overestimation when compared with the entire Atka Bay. The governing factor is the present sea-ice thickness (and to a lesser degree the snow depth) at a sampling site when a platelet layer starts to form. The greater this thickness, the lower is the remaining growth of solid sea ice during winter and, at the same time, the relative contribution of platelet ice. For our sampling sites in 2012 (Fig. 3), we would expect the least contribution of platelet ice at ATKA07, as this site had a very high initial thickness (~2 m) and only grew ~1 m during winter. Estimating the fraction of platelet ice there as ~30%, an appropriate estimate of the average bay-wide platelet-ice fraction would be ~60%. Note

that these numbers do not represent the contribution of ice platelets to the total sea-ice mass (next subsection), but rather the fraction of platelet-influenced crystal structure.

Contribution of ice platelets to total fast-ice mass and freeboard

In order to assess the contribution of ice platelets to the total sea-ice mass and the influence on freeboard, it is necessary to separate the part of sea ice grown by heat conduction to the atmosphere on the one hand, and the ice-platelet formation by relieved supercooling in the water column on the other. Based on our field observations and model results, we assume $\beta = 0.25$, initial sea-ice formation in April and the accumulation of a moderate snow cover from June onwards. A sea-ice growth simulation with the model then yields a December maximum thickness of solid fast ice of 2 m. This is a reasonable estimate for the conditions of 2012, since the quick build-up of thickness in the west by wind stress is at least partly compensated by a delayed freeze onset in the east. Under these conditions, and taking into account that ice-platelet accumulation starts in June, our growth model suggests that the lower 1.2 m of solid sea ice contains incorporated ice platelets. This estimate is also supported by the sea-ice texture. Their total mass then amounts to an effective thickness of ~0.3 m, or 15% of the solid sea ice. This thickness gain is on the same order of magnitude as that found in the theoretical study of Hellmer (2004). He calculated that the ice-shelf/ocean interaction may contribute up to 0.2 m of the sea-ice thickness over significant areas of fast and pack ice in the Southern Ocean. However, his approach did not explicitly take into account the contribution of ice platelets. Subtracting this contribution of incorporated ice platelets, the remaining sea-ice thickness becomes 1.7 m, or 85%, as a result of growth by heat conduction from the ocean to the atmosphere. Multiplication of the average $z_p = 4$ m with $\beta = 0.25 \pm 0.1$, and addition of the contribution of incorporated ice platelets, yields an effective sea-ice thickness equivalent to $\sim 1.3 \pm 0.52$ m as a result of heat loss to the ocean during ice-platelet formation at depth. This corresponds to 43 ± 12% of solid and loose sea ice altogether.

Because the thickness of the platelet layer changes with time, its contribution to freeboard is also variable. Here we perform a sample calculation of how the additional buoyancy of the ice platelets influences freeboard under the assumption of hydrostatic equilibrium, using Archimedes' law:

$$z_f = \frac{z_p \cdot (\rho_p - \rho_w) + z_s \cdot \rho_s + z_{si} \cdot (\rho_{si} - \rho_w)}{\rho_w}, \qquad (2)$$

where the subscript 'f' refers to freeboard, 's' to snow, 'si' to sea-ice, 'p' to platelet layer and 'w' to water; z is the thickness and ρ is the density of the respective medium. Again considering the conditions in December, we assume an average sea-ice thickness of 2 m, a platelet-layer thickness of 4 m and $\beta = 0.25 \pm 0.1$. Using typical densities (ρ_w= 1032.3 kg m^{-3}, $\rho_{si} = 925$ kg m^{-3} and $\rho_s = 330$ kg m^{-3}), the resulting freeboard is $\sim 0.11 \pm 0.05$ m higher than the situation where underlying platelets are not present, independent of the snow cover.

Basalt melt of the Ekström Ice Shelf

Kipfstuhl (1991) calculated that the volume of ice platelets accumulated under Atka Bay landfast sea ice accounts for 12% of the basal melt volume observed under the Ekström Ice Shelf (for $\beta = 0.2$). Multiplication of the average effective thickness equivalent of ice platelets found in this study (1.3 m) by the fast-ice area (~440 km^2) yields a total annual platelet volume of $V_p = 0.57$ km^3 underlying the fast ice of Atka Bay. Table 4 shows average basal melt rates of the (main) western part of the Ekström Ice Shelf from selected studies, along with total basal melt volume calculated for an area of 6000 km^2. Based on our V_p and recent results of Neckel and others (2012) for basal melt from mass-flux divergence, we find that more than one-fifth of the basal melt volume of the Ekström Ice Shelf is refrozen as loose and incorporated platelets.

Table 4. Ekström Ice Shelf basal melt from previous studies and contribution of ice platelets to total melt volume. $\dot{a}_b$: mean basal melt rate; V_b: volume of basal melt for an area of 6000 km^2; $V_p\,V_b^{-1}$: fraction of ice-platelet volume from basal melt volume

Source	$\dot{a}_b$ m a^{-1}	Method	V_b km^3	$V_p\,V_b^{-1}$
Neckel and others (2012)	0.44	Mass balance	2.64	0.22
Nicolaus and Grosfeld (2004)	0.98	Ocean-circulation model	5.88	0.1
Sandhäger and Blindow (2000)	0.53	Ice-shelf flow model	3.18	0.18
Kipfstuhl (1991)	0.73	Mass balance	4.38	0.13

SUMMARY AND CONCLUSION

We have investigated the seasonal evolution of landfast sea ice and the underlying platelet layer at Atka Bay, eastern Weddell Sea, during 2012/13. Sea-ice formation started in March, and variable sea-ice conditions were observed across Atka Bay, with different dates of initial formation, contribution of dynamic growth processes and snow accumulation. Sea-ice thickness was ~2 m at the end of the growth season, while dynamic growth and snow depths of up to 1 m introduced large spatial variability. A thick platelet layer was observed underlying the entire solid fast-ice sheet, with first observations of platelets in boreholes and sea-ice cores in June. Potentially supercooled water was present under the ice shelf during the entire winter. Under-ice video recordings revealed episodic events of high upward fluxes of ice platelets, overlying a very low continuous flux. The platelet-layer thickness increased until December, with a bay-wide average of 4 m and a local maximum of 10 m. When warm surface water intruded into Atka Bay at the beginning of December, ice-platelet accumulation ceased and the platelet layer thinned, shielding the solid ice above from significant bottom melt. Through the additional buoyancy, surface flooding and snow-ice formation were rarely observed, despite the thick snow cover. Using a one-dimensional thermodynamic sea-ice model, we found a best-fit ice-volume fraction of $\beta = 0.25 \pm 0.1$ in the platelet layer. This corresponds to an effective sea-ice thickness equivalent of 1.3 m as a result of heat loss to the ocean, which is nearly half the combined mass of solid sea ice and the underlying platelet layer. In relation to Ekström Ice Shelf basal melt, we found that >20% of the basal melt volume is refrozen as ice platelets trapped

under Atka Bay fast ice. It is likely that the oceanographic conditions in this area promote the transport of potentially supercooled water out of the cavity, possibly leading to further ice-platelet formation away from the coast.

In conclusion, this study highlights the dependence of coastal sea-ice regimes on local ocean/ice-shelf interactions. Basal processes mostly dominate sea-ice properties, with platelet accumulations below the solid sea ice directly impacting sea-ice energy and mass balance. As a consequence, uncertainties are introduced into numerical models which do not account for heat loss to the ocean. Furthermore, the additional buoyancy complicates sea-ice thickness retrieval by altimetry techniques, an effect which adds to other difficulties of remote-sensing techniques in coastal areas (e.g. complex coastlines and snow cover). Since this study was limited to Atka Bay and the Ekström Ice Shelf, it is necessary to gain more insight into the temporal and spatial variability of ice-platelet accumulations over larger areas under Antarctic sea ice.

Although no obvious changes in sea-ice and oceanographic conditions were found in this study compared with investigations 30 years ago, this will not necessarily be the case in the future. Hellmer and others (2012), Pritchard and others (2012) and Depoorter and others (2013) have previously highlighted that the complex interactions between the Southern Ocean, the Antarctic ice shelves and the sea-ice cover have significant global implications, and they concluded that much more process understanding related to ice-shelf cavities is needed. But since sub-ice-shelf processes are particularly difficult to investigate in situ, alternative approaches are needed to detect eventual changes in this complex system. Studies of fast-ice properties are comparatively easy to conduct, and we emphasize that fast-ice characteristics, especially near ice shelves, may provide a very sensitive, and yet practical, indicator of the conditions and possible changes in the Antarctic. Hence there exists an urgent need to perform these studies on a more regular and circum-Antarctic basis, for example by extending and intensifying the work in the Antarctic Fast Ice Network (Heil and others, 2011).

ACKNOWLEDGEMENTS

We thank the Neumayer III overwintering teams 2010–13 for their dedicated fieldwork. We thank the German Aerospace Center (DLR) for the TerraSAR-X image, and Christine Wesche for post-processing and calibrating the satellite data. We are grateful to Holger Schmithüsen and Clemens Drüe for help with the meteorological and flux data. We also appreciate the helpful suggestions of Christof Lüpkes, Wolfgang Dierking and Martin Losch, and the technical support of Bernd Loose and Uwe Baltes. We thank Lars Kindermann for the CTD data and Ilse van Opzeeland for inspiring us with the platelet video recordings. We also thank Sepp Kipfstuhl and Ilka Weikusat for help with *c*-axis determination. Our research at Neumayer III would not have been possible without the support of the AWI logistics. This work was supported by the German Research Council (DFG) in the framework of the priority programme 'Antarctic Research with comparative investigations in Arctic ice areas' grants SPP1158, NI 1092/2 and HE2740/12, and the Alfred-Wegener-Institut Helmholtz Zentrum für Polar- und Meeresforschung. Supplementary data to this paper are available at http://dx.doi.org/10.1594/PANGAEA.824434. Finally, we thank two anonymous reviewers whose comments significantly improved the manuscript.

REFERENCES

Andreas EL and 6 others (2010) Parameterizing turbulent exchange over sea ice in winter. *J. Hydromet.*, **11**(1), 87–104 (doi: 10.1175/2009JHM1102.1)

Bindschadler R and 17 others (2011) Getting around Antarctica: new high-resolution mappings of the grounded and freely-floating boundaries of the Antarctic ice sheet created for the International Polar Year. *Cryosphere*, **5**(3), 569–588 (doi: 10.5194/tc-5-569-2011)

Bintanja R, Van Oldenborgh GJ, Drijfhout SS, Wouters B and Katsman CA (2013) Important role for ocean warming and increased ice-shelf melt in Antarctic sea-ice expansion. *Nature Geosci.*, **6**(5), 376–379 (doi: 10.1038/ngeo1767)

Bitz CM and Lipscomb WH (1999) An energy-conserving thermodynamic model of sea ice. *J. Geophys. Res.*, **104**(C7), 15 669–15 677 (doi: 10.1029/1999JC900100)

Boebel O and 7 others (2006) Real-time underwater sounds from the Southern Ocean. *Eos*, **87**(36), 361 (doi: 10.1029/2006EO360002)

Bunt JS and Lee CC (1970) Seasonal primary production in Antarctic sea ice at McMurdo Sound in 1967. *J. Mar. Res.*, **28**(3), 304–320

Comiso JC and Hall DK (2014) Climate trends in the Arctic as observed from space. *WIREs Climate Change*, **5**(3), 389–409 (doi: 10.1002/wcc.277)

Crocker GB (1988) Physical processes in Antarctic landfast sea ice. (PhD thesis, Cambridge University)

Crocker GB and Wadhams P (1989) Modelling Antarctic fast-ice growth. *J. Glaciol.*, **35**(119), 3–8 (doi: 10.3189/002214389793701590)

Dempsey DE and Langhorne PJ (2012) Geometric properties of platelet ice crystals. *Cold Reg. Sci. Technol.*, **78**, 1–13 (doi: 10.1016/j.coldregions.2012.03.002)

Dempsey DE, Langhorne PJ, Robinson NJ, Williams MJM, Haskell TG and Frew RD (2010) Observation and modeling of platelet ice fabric in McMurdo Sound, Antarctica. *J. Geophys. Res.*, **115**(C1), C01007 (doi: 10.1029/2008JC005264)

Depoorter MA and 6 others (2013) Calving fluxes and basal melt rates of Antarctic ice shelves. *Nature*, **502**(7469), 89–92 (doi: 10.1038/nature12567)

Eicken H (1992) Salinity profiles of Antarctic sea ice: field data and model results. *J. Geophys. Res.*, **97**(C10), 15 545–15 557 (doi: 10.1029/92JC01588)

Eicken H and Lange MA (1989) Development and properties of sea ice in the coastal regime of the southeastern Weddell Sea. *J. Geophys. Res.*, **94**(C6), 8193–8206 (doi: 10.1029/JC094iC06p08193)

Eicken H, Fischer H and Lemke P (1995) Effects of the snow cover on Antarctic sea ice and potential modulation of its response to climate change. *Ann. Glaciol.*, **21**, 369–376

Fahrbach E, Rohardt G and Krause G (1992) The Antarctic coastal current in the southeastern Weddell Sea. *Polar Biol.*, **12**(2), 171–182 (doi: 10.1007/BF00238257)

Fahrbach E, Peterson RG, Rohardt G, Schlosser P and Bayer R (1994) Suppression of bottom water formation in the southeastern Weddell sea. *Deep-Sea Res. I*, **41**(2), 389–411 (doi: 10.1016/0967-0637(94)90010-8)

Fretwell P and 59 others (2013) Bedmap2: improved ice bed, surface and thickness datasets for Antarctica. *Cryosphere*, **7**(1), 375–393 (doi: 10.5194/tc-7-375-2013)

Gough AJ, Mahoney AR, Langhorne PJ, Williams MJM, Robinson NJ and Haskell TG (2012) Signatures of supercooling: McMurdo Sound platelet ice. *J. Glaciol.*, **58**(207), 38–50 (doi: 10.3189/2012JoG10J218)

Gow AJ, Ackley SF, Govoni JW and Weeks WF (1998) Physical and structural properties of land-fast sea ice in McMurdo Sound,

Antarctica. In Jeffries MO ed. *Antarctic sea ice: physical processes, interactions and variability*. (Antarctic Research Series 74) American Geophysical Union, Washington, DC, 355–374

Günther S and Dieckmann G (1999) Seasonal development of high algal biomass in snow-covered fast ice and the underlying platelet layer in Atka Bay, Antarctica. *Antarct. Sci.*, **11**(3), 305–315 (doi: 10.1017/S0954102099000395)

Heil P (2006) Atmospheric conditions and fast ice at Davis, East Antarctica: a case study. *J. Geophys. Res.*, **111**(C5), C05009 (doi: 10.1029/2005JC002904)

Heil P, Gerland S and Granskog MA (2011) An Antarctic monitoring initiative for fast ice and comparison with the Arctic. *Cryos. Discuss.*, **5**(5), 2437–2463 (doi: 10.5194/tcd-5-2437-2011)

Hellmer HH (2004) Impact of Antarctic ice shelf basal melting on sea ice and deep ocean properties. *Geophys. Res. Lett.*, **31**(10), L10307 (doi: 10.1029/2004GL019506)

Hellmer H, Kauker F, Timmermann R, Determann J and Rae J (2012) Twenty-first-century warming of a large Antarctic ice-shelf cavity by a redirected coastal current. *Nature*, **485**(7397), 225–228 (doi: 10.1038/nature11064)

Holland PR, Jenkins A and Holland DM (2008) The response of ice shelf basal melting to variations in ocean temperature. *J. Climate*, **21**(11), 2558–2572 (doi: 10.1175/2007JCLI1909.1)

Hoppmann M, Nicolaus M, Paul S, Hunkeler PA, Schmidt T and Kühnel M (2013a) *Field measurements of sea-ice thickness, snow depth, freeboard and sub-ice platelet-layer thickness on the land-fast ice of Atka Bay in 2012* (doi: 10.1594/PANGAEA.824434)

Hoppmann M, Nicolaus M, Schmidt T and Kühnel M (2013b) *Meteorological observations by an automated weather station on Atka Bay land-fast sea ice, 2012-10-02 to 2012-12-27* (doi: 10.1594/PANGAEA.824527)

Hoppmann M, Nicolaus M, Schmidt T and Kühnel M (2013c) *Meteorological observations by an automated weather station on Atka Bay land-fast sea ice, 2012-07-06 to 2012-08-17* (doi: 10.1594/PANGAEA.824526)

Hunkeler P, Hendricks S, Hoppmann M, Paul S and Gerdes R (2015) Towards an estimation of sub-sea-ice platelet-layer volume with multi-frequency electromagnetic induction sounding. *Ann. Glaciol.*, **56**(69), (doi: 10.3189/2015AoG69A705) (see paper in this issue)

Jeffries MO, Weeks WF, Shaw R and Morris K (1993) Structural characteristics of congelation and platelet ice and their role in the development of Antarctic land-fast sea ice. *J. Glaciol.*, **39**(132), 223–238

Jeffries MO, Krouse HR, Hurst-Cushing B and Maksym T (2001) Snow-ice accretion and snow-cover depletion on Antarctic first-year sea-ice floes. *Ann. Glaciol.*, **33**, 51–60 (doi: 10.3189/172756401781818266)

Kipfstuhl J (1991) Zur Entstehung von Unterwassereis und das Wachstum und die Energiebilanz des Meereises in der Atka Bucht, Antarktis. *Ber. Polarforsch/Rep. Pol. Res.* 85

Kobarg W (1988) Die gezeitenbedingte Dynamik des Ekström-Schelfeises, Antarktis. *Ber. Polarforsch/Rep. Pol. Res.* 50

König-Langlo G (2013a) *Basic and other measurements of radiation at Neumayer Station in 2012, links to datasets.* Alfred Wegener Institute, Helmholtz Center for Polar and Marine Research, Bremerhaven (doi: 10.1594/PANGAEA.793020)

König-Langlo G (2013b) *Continuous meteorological observations at Neumayer station in 2012, links to datasets.* Alfred Wegener Institute, Helmholtz Center for Polar and Marine Research, Bremerhaven (doi: 10.1594/PANGAEA.792931)

König-Langlo G and Loose B (2007) The meteorological observatory at Neumayer Stations (GvN and NM-II) Antarctica. *Ber. Polar-Meeresforsch./Rep. Pol. Mar. Res.*, **76**(1–2), 25–38

König-Langlo G, King JC and Pettré P (1998) Climatology of the three coastal Antarctic stations Dumont d'Urville, Neumayer and Halley. *J. Geophys. Res.*, **103**(D9), 10 935–10 946 (doi: 10.1029/97JD00527)

Lange MA, Ackley SF, Wadhams P, Dieckmann GS and Eicken H (1989) Development of sea ice in the Weddell Sea. *Ann. Glaciol.*, **12**, 92–96

Langway CC Jr (1958) Ice fabrics and the universal stage. *SIPRE Tech. Rep.* 62

Leonard GH, Purdie CR, Langhorne PJ, Haskell TG, Williams MJM and Frew RD (2006) Observations of platelet ice growth and oceanographic conditions during the winter of 2003 in McMurdo Sound, Antarctica. *J. Geophys. Res.*, **111**(C4), C04012 (doi: 10.1029/2005JC002952)

Lewis EL and Perkin RG (1986) Ice pumps and their rates. *J. Geophys. Res.*, **91**(C10), 11 756–11 762 (doi: 10.1029/JC091iC10p11756)

Mahoney AR and 6 others (2011) The seasonal appearance of ice shelf water in coastal Antarctica and its effect on sea ice growth. *J. Geophys. Res.*, **116**(C11), C11032 (doi: 10.1029/2011JC007060)

Maksym T, Stammerjohn SE, Ackley S and Massom R (2012) Antarctic sea ice – a polar opposite? *Oceanography*, **25**(3), 140–151 (doi: 10.5670/oceanog.2012.88)

Massom RA and 12 others (2001) Snow on Antarctic sea ice. *Rev. Geophys.*, **39**(3), 413–445 (doi: 10.1029/2000RG000085)

Mauder M and 7 others (2013) A strategy for quality and uncertainty assessment of long-term eddy-covariance measurements. *Agric. Forest Meteorol.*, **169**, 122–135 (doi: 10.1016/j.agrformet.2012.09.006)

McDougall TJ and Barker PM (2011) Getting started with TEOS-10 and the Gibbs Seawater (GSW) Oceanographic Toolbox. (Tech. Rep.) SCOR/IAPSO, WG27 http://www.teos-10.org/software.htm

Moretskii VN (1965) Morskoy vnutrivodnyy led [Underwater sea ice]. *Probl. Arkt. Antarkt.,* **19**, 32–38 [in Russian] Translation by E.R. Hope, DRB Canada Report T-497-R, 1968

Neckel N, Drews R, Rack W and Steinhage D (2012) Basal melting at the Ekström Ice Shelf, Antarctica, estimated from mass flux divergence. *Ann. Glaciol.*, **53**(60 Pt 2), 294–302 (doi: 10.3189/2012AoG60A167)

Nicolaus M and Grosfeld K (2004) Ice–ocean interactions underneath the Antarctic Ice Shelf Ekströmisen. *Polarforschung*, **72**(1), 17–29

Nøst OA and 7 others (2011) Eddy overturning of the Antarctic Slope Front controls glacial melting in the Eastern Weddell Sea. *J. Geophys. Res.*, **116**(C11), C11014 (doi: 10.1029/2011JC006965)

Parkinson CL and Cavalieri DJ (2012) Antarctic sea ice variability and trends, 1979–2010. *Cryosphere*, **6**(4), 871–880 (doi: 10.5194/tc-6-871-2012)

Paul S and 6 others (2015) The impact of early-summer snow properties on landfast sea-ice x-band backscatter. *Ann. Glaciol.*, **56**(69) (doi: 10.3189/2015AoG69A715) (see paper in this issue)

Price D, Rack W, Haas C, Langhorne PJ and Marsh O (2013) Sea ice freeboard in McMurdo Sound, Antarctica, derived by surface-validated ICESat laser altimeter data. *J. Geophys. Res.*, **118**(7), 3634–3650 (doi: 10.1002/jgrc.20266)

Price D, Rack W, Langhorne PJ, Haas C, Leonard G and Barnsdale K (2014) The sub-ice platelet layer and its influence on freeboard to thickness conversion of Antarctic sea ice. *Cryosphere,* **8**(3), 1031–1039 (doi: 10.5194/tc-8-1031-2014)

Pritchard HD, Ligtenberg SRM, Fricker HA, Vaughan DG, Van den Broeke MR and Padman L (2012) Antarctic ice-sheet loss driven by basal melting of ice shelves. *Nature*, **484**(7395), 502–505 (doi: 10.1038/nature10968)

Purdie CR, Langhorne PJ, Leonard GH and Haskell TG (2006) Growth of first-year landfast Antarctic sea ice determined from winter temperature measurements. *Ann. Glaciol.*, **44**, 170–176 (doi: 10.3189/172756406781811853)

Rack W, Haas C and Langhorne PJ (2013) Airborne thickness and freeboard measurements over the McMurdo Ice Shelf, Antarctica, and implications for ice density. *J. Geophys. Res.*, **118**(C11), 5899–5907 (doi: 10.1002/2013JC009084)

Rimbu N, Lohmann G, König-Langlo G, Necula C and Ionita M (2014) Daily to intraseasonal oscillations at Antarctic research station Neumayer. *Antarct. Sci.*, **26**(2), 193–204 (doi: 10.1017/S0954102013000540)

Sandhäger H and Blindow N (2000) Surface elevation, ice thickness, and subglacial-bedrock topography of Ekström Ice Shelf (Antarctica) and its catchment area. *Ann. Glaciol.*, **30**, 61–68 (doi: 10.3189/172756400781820723)

Serikov MI (1963) Struktura morskogo antarkticheskogo l'da [Structure of Antarctic sea ice]. *Sov. Antarct. Exped. Inf. Bull.*, **39**, 13–14 [in Russian]

Smith IJ, Langhorne PJ, Haskell TG, Trodahl HJ, Frew R and Vennell MR (2001) Platelet ice and the land-fast sea ice of McMurdo Sound, Antarctica. *Ann. Glaciol.*, **33**, 21–27 (doi: 10.3189/172756401781818365)

Smith IJ, Langhorne PJ, Frew RD, Vennell R and Haskell TG (2012) Sea ice growth rates near ice shelves. *Cold Reg. Sci. Technol.*, **83–84**, 57–70 (doi: 10.1016/j.coldregions.2012.06.005)

Thoma M, Grosfeld K and Lange MA (2006) Impact of the Eastern Weddell Ice Shelves on water masses in the eastern Weddell Sea. *J. Geophys. Res.*, **111**(C12), C12010 (doi: 10.1029/2005JC003212)

Timco GW and Frederking RMW (1996) A review of sea ice density. *Cold Reg. Sci. Technol.*, **24**(1), 1–6 (doi: 10.1016/0165-232X(95)00007-X)

Tison J-L, Lorrain RD, Bouzette A, Dini M, Bondesan A and Stiévenard M (1998) Linking landfast sea ice variability to marine ice accretion at Hells Gate Ice Shelf, Ross Sea. In Jeffries MO ed. *Antarctic sea ice: physical processes, interactions and variability*. (Antarctic Research Series 74) American Geophysical Union, Washington, DC, 375–407 (doi: 10.1029/AR074p0375)

Trodahl HJ and 6 others (2000) Heat transport in McMurdo Sound first-year fast ice. *J. Geophys. Res.*, **105**(C5), 11 347–11 358 (doi: 10.1029/1999JC000003)

Turner J, Bracegirdle TJ, Phillips T, Marshall GJ and Hosking JS (2013) An initial assessment of Antarctic sea ice extent in the CMIP5 models. *J. Climate*, **26**(5), 1473–1484 (doi: 10.1175/JCLI-D-12-00068.1)

Van Dijk A, Moene AF and De Bruin HAR (2004) The principles of surface flux physics: theory, practice and description of the ECPACK library. (Internal Rep. 2004/1) Meteorology and Air Quality Group, Wageningen University, Wageningen

Veazey AL, Jeffries MO and Morris K (1994) Small-scale variability of physical properties and structural characteristics of Antarctic fast ice. *Ann. Glaciol.*, **20**, 61–66 (doi: 10.3189/172756494794586925)

Wilson CJL, Russell-Head DS and Sim HM (2003) The application of an automated fabric analyzer system to the textural evolution of folded ice layers in shear zones. *Ann. Glaciol.*, **37**, 7–17 (doi: 10.3189/172756403781815401)

C

Co-Author Paper 3

This paper was reprinted from Journal of Geophysical Research: Oceans with permission of John Wiley and Sons.

I contributed with sea-ice field work and revision work to this paper. Similar to the study of Appendix B, I was heavily involved in logistics and help to deploy the thermistor chain in the Atka Bay in November 2012. I also contributed to snow depth, freeboard, sea-ice and platelet-layer thickness measurements across Atka Bay, which was besides the study in Appendix B also relevant for this paper. I further contributed to this paper by discussing and comparing the obtained ice-volume fractions to the one I obtained with electromagnetic induction sounding (Chapters 2 and 4).

AGU PUBLICATIONS

JGR

Journal of Geophysical Research: Oceans

RESEARCH ARTICLE
10.1002/2014JC010327

Key Points:
- Ocean/ice-shelf interaction dominates coastal sea-ice mass balance
- Basal energy balance reveals platelet layer ice-volume fraction of a fifth
- Thermistor chain heating is a suitable tool to study platelet-layer evolution

Correspondence to:
M. Hoppmann,
Mario.Hoppmann@awi.de

Citation:
Hoppmann, M., M. Nicolaus, P. A. Hunkeler, P. Heil, L.-K. Behrens, G. König-Langlo, and R. Gerdes (2015), Seasonal evolution of an ice-shelf influenced fast-ice regime, derived from an autonomous thermistor chain, *J. Geophys. Res. Oceans*, *120*, doi:10.1002/2014JC010327.

Received 18 JUL 2014
Accepted 30 JAN 2015
Accepted article online 6 FEB 2015

Seasonal evolution of an ice-shelf influenced fast-ice regime, derived from an autonomous thermistor chain

M. Hoppmann[1], M. Nicolaus[1], P. A. Hunkeler[1], P. Heil[2,3], L.-K. Behrens[1], G. König-Langlo[1], and R. Gerdes[1]

[1]Alfred-Wegener-Institut Helmholtz-Zentrum für Polar-und Meeresforschung, Bremerhaven, Germany, [2]Australian Antarctic Division, Department of the Environment, Kingston, Tasmania, Australia, [3]Antarctic Climate and Ecosystems Cooperative Research Centre, University of Tasmania, Hobart, Tasmania, Australia

Abstract Ice shelves strongly interact with coastal Antarctic sea ice and the associated ecosystem by creating conditions favorable to the formation of a sub-ice platelet layer. The close investigation of this phenomenon and its seasonal evolution remains a challenge due to logistical constraints and a lack of suitable methodology. In this study, we characterize the seasonal cycle of Antarctic fast ice adjacent to the Ekström Ice Shelf in the eastern Weddell Sea. We used a thermistor chain with the additional ability to record the temperature response induced by cyclic heating of resistors embedded in the chain. Vertical sea-ice temperature and heating profiles obtained daily between November 2012 and February 2014 were analyzed to determine sea-ice and snow evolution, and to calculate the basal energy budget. The residual heat flux translated into an ice-volume fraction in the platelet layer of 0.18 ± 0.09, which we reproduced by a independent model simulation and agrees with earlier results. Manual drillings revealed an average annual platelet-layer thickness increase of at least 4 m, and an annual maximum thickness of 10 m beneath second-year sea ice. The oceanic contribution dominated the total sea-ice production during the study, effectively accounting for up to 70% of second-year sea-ice growth. In summer, an oceanic heat flux of 21 W m^{-2} led to a partial thinning of the platelet layer. Our results further show that the active heating method, in contrast to the acoustic sounding approach, is well suited to derive the fast-ice mass balance in regions influenced by ocean/ice-shelf interaction, as it allows subdiurnal monitoring of the platelet-layer thickness.

1. Introduction

Sea ice is a critical component in the global climate system, and an important marine habitat. Its influence ranges from the formation of polar deep water masses involved in the global thermohaline circulation [*Fahrbach et al.*, 2001], over the global radiation budget via albedo effects on the lower atmosphere [*Perovich et al.*, 2007] to the heat and light distribution in the water column [*Nicolaus et al.*, 2012]. In the Southern Ocean, sea ice spreads over millions of square kilometers at all times of the year. The Antarctic sea-ice cover has, on average, expanded since the late 1970s [*Parkinson and Cavalieri*, 2012], an evolution which is the sum of large regional differences whose drivers are currently only poorly understood. Proposed explanations include teleconnections of atmospheric circulation systems and changes in wind forcing [*Liu et al.*, 2004; *Lefebvre and Goosse*, 2008; *Simpkins et al.*, 2012; *Holland and Kwok*, 2012; *Li et al.*, 2014], increased precipitation [*Fichefet and Maqueda*, 1999; *Liu and Curry*, 2010], as well as atmosphere and ocean feedbacks [*Zhang*, 2007; *Stammerjohn et al.*, 2008]. Several other studies investigated the influence of an increased freshwater flux by enhanced melting of Antarctic ice shelves on sea-ice formation, but results remain inconclusive [*Swingedouw et al.*, 2008; *Bintanja et al.*, 2013, 2015; *Swart and Fyfe*, 2013]. In order to understand the complex interactions, much more insight into the relevant processes is needed.

The changing large-scale wind patterns almost exclusively affect the drifting pack ice, while sea ice attached to coastal features is often strongly influenced by nearby ice shelves [e.g., *Mahoney et al.*, 2011; *Smith et al.*, 2012]. This land-fast sea ice (fast ice) is an important interface between the Antarctic ice sheet and the pack ice or the ocean [*Massom et al.*, 2001] and constitutes between 5% and 35% of total sea-ice area during months of maximum and minimum total sea-ice area in East Antarctica [*Fraser et al.*, 2012], respectively. It is ideal to study in detail the processes which modify Antarctic sea-ice properties in general [*Heil et al.*, 2011].

Research on the physical properties of fast ice has largely been focusing on areas close to Antarctic bases, for example, at Lützow Holm Bay [*Kawamura et al*., 1997; *Ohshima et al*., 2000; *Uto et al*., 2006], Prydz Bay [*Heil*, 2006; *Tang et al*., 2007; *Lei et al*., 2010], and McMurdo Sound [*Jeffries et al*., 1993; *Purdie et al*., 2006; *Gough et al*., 2012].

Some of these locations exhibit characteristics that reflect a strong ocean/ice-shelf interaction, manifested through the presence of a sub-ice platelet layer. This special sea-ice type not only modifies the properties, mass and energy balance of an overlying solid sea-ice cover [*Hoppmann et al*., 2015], it also acts as a habitat for a substantial amount of algal biomass [*Arrigo et al*., 1993; *Günther and Dieckmann*, 1999, 2001], provides a protective environment for coastal fish species [*Vacchi et al*., 2000], and might also allow conclusions about processes in the ice-shelf cavity. While the formation mechanisms of ice crystals in supercooled waters are in principle understood [*Mager et al*., 2013], little is known about the spatiotemporal variability of sub-ice platelet layers in Antarctica. Despite their importance for the climate and ecosystem, a means to effectively monitor Antarctic platelet layers remains a challenge due to the lack of suitable methodology. A promising approach to determine its spatial variability is the application of (ground-based) multi-frequency EM induction sounding [*Hunkeler et al*., 2015]. However, no method is currently available to provide information about its temporal evolution without the need for extensive logistics.

Providing a relatively inexpensive alternative to field campaigns, autonomous Ice Mass Balance Buoys (IMBs) have been widely used in recent years to monitor the sea-ice mass balance at a fixed study site [*Perovich and Elder*, 2001]. Typical IMBs are equipped with a thermistor chain extending through the snow and sea-ice cover into the upper ocean, as well as with acoustic sensors monitoring the position of the ice/water and air/snow (air/ice) interfaces [*Richter-Menge et al*., 2006]. They usually also record GPS position, sea level pressure and 2 m air temperature. If combined, these data not only reveal changes in the sea-ice mass balance due to ice growth, surface melt, and bottom ablation, they also provide valuable information about the snow cover. In a next step, the observed changes can be correlated with variables associated with the external drivers, such as the beginning and duration of the summer melt season, the length of the growth season, and the oceanic heat flux. By doing so, one is not only able to obtain information about the state of the sea-ice cover, but also to gain important insight into the driving forces behind the ongoing changes. However, these instruments are usually expensive and take a substantial effort to deploy.

Recently, a promising new type of thermistor chain IMB has been developed [*Jackson et al*., 2013], which is significantly lower in cost than comparable instruments and very easy to deploy. A special feature of this design is the ability to actively heat embedded resistors near the temperature sensors, which is described in more detail below. Despite the growing demand and application of this buoy type, no consistent data set has been published to date and the instrument's full potential is still to be determined.

In this study, we analyzed data from such a thermistor chain, in order to determine the physical properties of an ice-shelf influenced sea-ice cover and its seasonal evolution. The instrument was operated on the fast ice of Atka Bay, eastern Weddell Sea, between November 2012 and February 2014. These measurements were combined with continuous meteorological and oceanographic data, as well as manual thickness measurements and model simulations, in order to quantify the processes governing sea-ice mass balance, and to characterize their seasonality. At the same time, we assessed the potential of this relatively new instrument design on the basis of this unique data set, highlighting its advantages and pointing out its caveats to assist the interpretation of such data sets in future studies.

2. Methods

2.1. Field Setting

This study was conducted on the generally first-year fast ice of Atka Bay, a sheltered embayment adjacent to the Ekström Ice Shelf (Figure 1). The geographic setting is described in more detail in *Hoppmann et al*. [2015] and references therein. A large iceberg (B15G) grounded in front of Atka Bay in September 2012 (Figure 1b, dashed red curve), which sheltered the fast ice and prevented a breakup in early 2013. The fast ice survived the summer and became thick second-year sea ice in 2013. The iceberg dislodged itself in August 2013 and drifted away westward with the coastal current. Between 9 and 16 February 2014, approximately two-thirds of the fast-ice area finally disintegrated into small floes, marking the end of our study (Figure 1c).

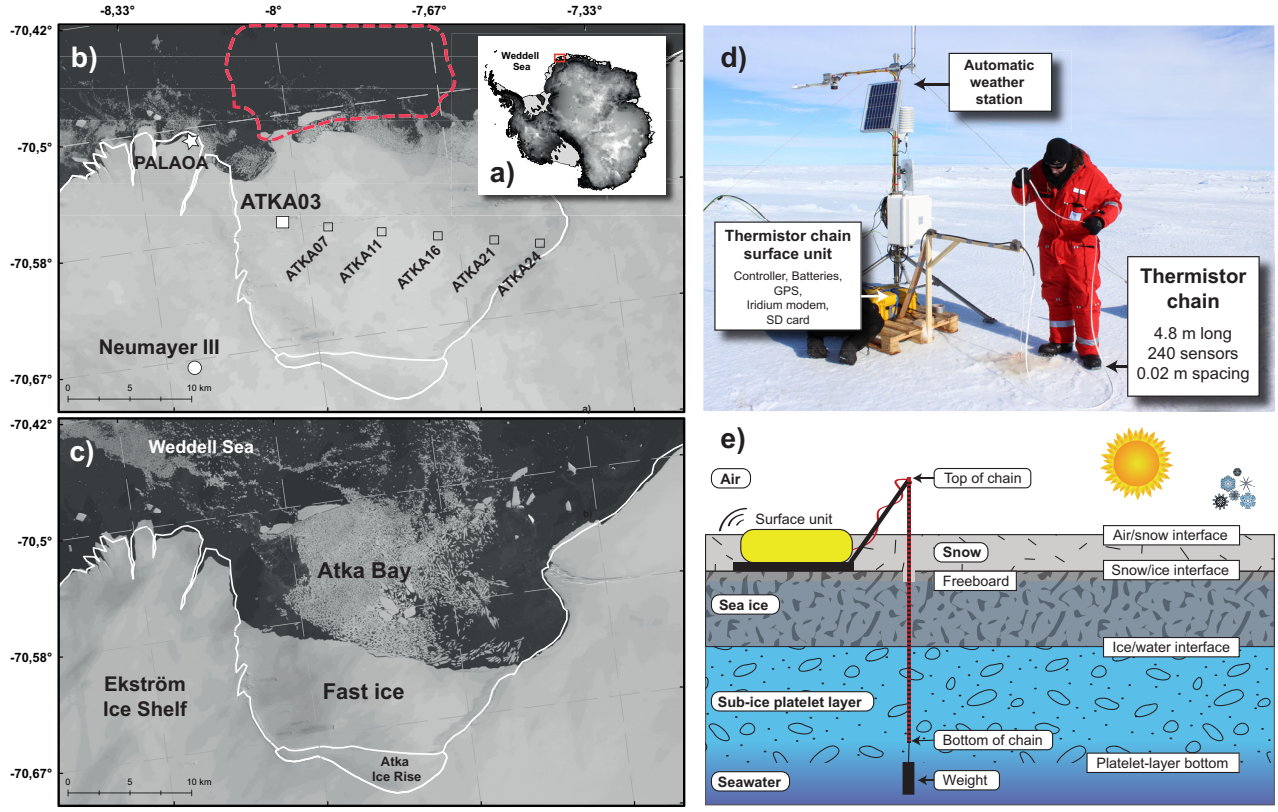

Figure 1. Study area and thermistor chain deployment. (a) Location of this study on a map of Antarctica. (b) Landsat image of Atka Bay at the beginning of the fast-ice breakup (9 February 2014). The main sampling site was located 3 km east of the western ice-shelf edge (ATKA03, white square). Auxiliary study sites are also indicated (squares), along with the former position of grounded iceberg B15G (dashed red curve). (c) Landsat image from 16 February 2014, when 2/3 of the sea ice has broken up. Landsat imagery courtesy of NASA Goddard Space Flight Center and U.S. Geological Survey, coastline data from Antarctic Digital Database 6.0. (d) Photo of thermistor chain deployment (21 November 2012). (e) Schematic diagram of thermistor chain extending through air, snow, sea ice, and the sub-ice platelet layer.

2.2. Thermistor Chains

On 21 November 2012, we deployed a thermistor chain (Scottish Association for Marine Science, Oban, Scotland) approximately 3 km from the Ekström Ice Shelf (Figure 1b). This location is a regular site of an ongoing sea-ice monitoring program, mainly chosen for logistical reasons. It was within an area of moderately deformed sea ice, which initially formed in March/April 2012. For consistency with other studies [*Hoppmann et al.*, 2015; *Paul et al.*, 2015; *Hunkeler et al.*, 2015], we refer to this site as ATKA03.

The vertical thermistor chain (TC) was installed on level sea ice, through a 0.05 m diameter borehole (Figure 1d). It consisted of 240 thermistors at a spacing of 0.02 m, with a total length of 4.8 m. To prevent the chain from floating upward in the platelet layer, we attached a weight of 3 kg to the end of the chain. The hole did not refreeze all the way up to the original snow/ice interface due to the large positive freeboard, so it was filled up with snow after deployment. For our analysis we neglect this effect, and define the original snow/ice interface as our reference snow/ice interface.

The surface unit was placed onto a wooden rack for stability, with a side arm to guide the chain (Figure 1e). The temperature sensors (Maxim DS28EA00) have a resolution of 0.0625°C, and a worst-case accuracy of ±2°C [*Jackson et al.*, 2013]. We did not calibrate the chain, as the temperature sensors are offset-corrected by the manufacturer in a precision temperature-controlled water bath at 1°C. Sensor drift is considered low. The unique feature of this design is the operation similar to a combination of constant-current hot-wire anemometer and needle-probe thermal conductivity mode: after each regular temperature reading, embedded resistors (1 kΩ) near the temperature sensors are heated to above ambient temperature with an excitation voltage of 8 V, generating 63 mW of thermal energy. Heat is conducted away from the thermistors at a rate dependent on the

temperature gradient, the thermal conductivity of the surrounding medium and its flow rate, if liquid. Needle-probe thermal conductivity measurements were previously in snow research [*Sturm and Johnson*, 1992; *Riche and Schneebeli*, 2013], while hot-wire anemometry is a standard technique of experimental fluid dynamics and has been described, for example, by *La Barbara and Vogel* [1976] and *Perry* [1982]. Generally, a greater temperature rise is expected in air and snow than in water and ice due to their lower thermal conductivities. Since ice and water thermal conductivities lie very close together, the additional cooling introduced by a nonzero flow velocity in water may counteract the seawater's slightly lower thermal conductivity, potentially leading to difficulties in the determination of an ice/water interface. A quantitative relationship between the temperature response of this instrument and the thermal conductivity or flow speed of a medium has not been found yet, mostly due to the complex geometry, and this is also beyond the scope of this study. However, we will investigate in detail how well the instrument is suited to accurately determine the location of the interfaces between air, snow, ice, and water under field conditions. A full description of the TC and the "heating mode" is available in *Jackson et al.* [2013].

In our study, the heating duration and duty cycle were 120 s and 100% (of 63 mW), respectively, while the temperature rise was recorded after 30 s and 120 s. This configuration represents the default setting, recommended by *Jackson et al.* [2013] to provide a clear separation between the different media without reaching saturation. The temperature difference after 30 s of heating is referred to as "30 s heating" or δT_{30} throughout this paper. The temperature difference after 120 s of heating is referred to as "120 s heating" or δT_{120}, accordingly.

Upon deployment, snow depth, freeboard, and sea-ice thickness at ATKA03 were 0.01 m, 0.40 $\pm$ 0.05 m, and 2.45 $\pm$ 0.05 m, respectively. Determination of freeboard was difficult due to ice platelets clogging the borehole. The high initial thickness was the result of early formation and additional thickening due to floe-rafting. Sub-ice platelet-layer thickness was 4 m, with several interfaces of varying mechanical resistance within the layer. Due to its deployment late in the growth season, the chain did not extend below the platelet layer. In the first 3 weeks, the TC was configured to record the data every 6 h. It was reconfigured to hourly measurements on 11 December 2012. During February 2013, the sea ice became nearly isothermal. To save energy, the measurement interval was set to twice a day from February 2013. The batteries were changed on 28 April 2013 and again on 5 January 2014, to prepare for a potential sea-ice breakup and subsequent drift into the central Weddell Sea. However, the instrument ceased operation during sea-ice disintegration on 9 February 2014 (Figure 1b).

Due to the variable measurement intervals, the data were interpolated to a daily grid. The thermistor numbers were converted to depth, with the original snow/ice interface as the zero reference. Data from one broken sensor were removed. Erroneous thermistor readings, appearing as spikes in the temperature profiles, occurred sporadically (about 200 instances), and were removed manually. Spikes in the heating data were removed automatically, and the missing data points were linearly interpolated. Air/snow/ice interfaces were extracted automatically from temperature and heating profiles. The algorithms are not supplied because they were specifically tuned to this data set. The ice/water interface was determined by visual inspection to ensure the highest possible quality.

The temperature profiles and the interfaces extracted from heating profiles were used to calculate the sea-ice basal energy balance. Sea-ice growth, which is essentially a phase change at the ice bottom (latent heat flux, F_l), is a function of the conductive heat transfer through the sea ice to the air (F_c), the specific heat flux due to internal warming or cooling (F_s), and the oceanic heat flux (F_w). Following the approach of *Gough et al.* [2012], we calculated the oceanic heat flux F_w by a residual method [*McPhee and Untersteiner*, 1982; *Purdie et al.*, 2006] as

$$F_w = F_c + F_l + F_s. \tag{1}$$

We calculated the conductive, latent, and sensible heat fluxes after *Semtner* [1976]:

$$F_c = k_{si} \cdot \frac{\partial T}{\partial z}, \tag{2}$$

$$F_l = \rho_{si} \cdot L_f \cdot \frac{\partial H}{\partial t}, \tag{3}$$

$$F_s = -\rho_{si} \cdot c_{si} \cdot \frac{\partial T}{\partial t} \cdot \Delta H, \quad (4)$$

where the thermal conductivity k_{si} (ρ, S, T) is given by *Pringle et al.* [2007], $\frac{\partial T}{\partial z}$ is the sea-ice temperature gradient, z is the vertical coordinate, ρ_{si} is sea-ice density, L_f (S, T) is the sea-ice latent heat of fusion given by *Yen* [1981] with a typographical error corrected as described by *Pringle et al.* [2007], $\frac{\partial H}{\partial t}$ is the sea-ice growth rate, c_{si} (S, T) is the specific heat capacity [*Yen*, 1981], $\frac{\partial T}{\partial t}$ is the temporal gradient in sea-ice temperature, and H is the position of the ice/water interface. The latent heat L_f (S, T) and the specific heat of sea ice c_{si} (S, T) are functions of its temperature and salinity according to *Untersteiner* [1961] and *Yen et al.* [1991]. Upward heat fluxes, warming and melting have positive sign, and z decreases from zero at the sea-ice surface. The energy balance has to be solved for a near-bottom reference level z_r, through which heat transport by brine convection is unlikely to contribute significantly [*Gough et al.*, 2012]. A stable bulk salinity may provide the necessary indication for this [*Petrich et al.*, 2006]. The selection of the reference level is critical for the calculation of F_c due to the nonlinearity of the vertical sea-ice temperature profile. A variety of reference levels have been used in the literature, most recently summarized by *Lei et al.* [2014]. *Gough et al.* [2012] defined the reference layer at 0.15 m above the ice/water interface, in a study comparable to ours. Based on the latter study and in agreement with our salinity measurements from the sea-ice core near ATKA03 (Figure 3), we used a reference level of 0.16 m from the ice/water interface for which we calculated the energy balance. The position of the ice/water interface H and also its change with time $\frac{\partial H}{\partial t}$ were derived from the heating profiles with an uncertainty of $\pm$0.02 m. The reference level always followed the ice/water interface by $z_r = H + 0.16$ m. The temperature gradient $\frac{dT}{dz}$ across the reference level is obtained by a linear fit to all thermistors within $\pm$0.14 m of z_r. $\frac{dT}{dt}$ is determined from the temperature T at the same level in neighboring time steps. Salinity is taken near z_r from the interpolated profile in Figure 3. We assumed ρ_{si} is 910 kg m^{-3} throughout, which is near the top of the range for multiyear sea ice reviewed by *Timco and Frederking* [1996]. This is slightly higher than the density measured from a sea-ice core in December 2012, where brine loss occurred during the measurement. The sea-ice growth rate was calculated as the temporal change in the evolution of the ice/water interface, derived from the δT_{120} data. The interface had previously been smoothed to remove the discrete steps originating from the thermistor spacing.

In order to assess the instrument's ability to detect the presence of a sub-ice platelet layer, we compared our main data set to a similar one obtained by a thermistor chain of the same type, deployed in the Weddell Sea during Polarstern cruise ANT-XXIX/9. This IMB was installed on a platelet-free floe at 74°23.340′S, 33°24.012′W on 5 February 2014.

2.3. Automatic Weather Station

We twice deployed an automatic weather station (AWS) at ATKA03. First, it was operated from 2 October to 27 December 2012, but only data since the deployment of the TC (21 November 2012) are shown here. The AWS was recovered to avoid instrument loss due to a weakening of the fast-ice cover in late summer. Second, we deployed the same setup again a few meters from the thermistor chain on 31 May 2013. Measurements comprised air temperature and relative humidity (shielded HMP155A, Vaisala), barometric pressure (61302V, RM Young Company), wind speed and direction (Marine Wind Monitor 05106-5, RM Young Company) as well as downward and upward longwave and shortwave radiation (CNR4, Kipp and Zonen) in 2 m height at 1 min intervals. We also recorded snow height using an acoustic sounder (SR50A, Campbell Scientific) as an independent measurement to compare to snow depth derived from TC temperature and heating profiles. Finally, the AWS data were combined with data obtained at the meteorological observatory of Neumayer III [*König-Langlo and Loose*, 2007] to generate a consistent forcing for a thermodynamic sea-ice growth model [*Bitz and Lipscomb*, 1999; *Hoppmann et al.*, 2015].

2.4. Oceanographic Data

We used oceanographic data from the Perennial Acoustic Observatory in the Antarctic Ocean (PALAOA) [*Boebel et al.*, 2006]. An unpumped Sea-Bird Electronics (SBE) 37 MicroCAT was installed in the water column at a depth of about 155 m, 70 m below the ice shelf bottom and 90 m above the sea floor, in 2006. Since then, PALAOA was gradually transported closer to the ice-shelf edge due to the flowing glacier, and an end of its operation is expected in 2015. The instrument continuously records conductivity, temperature, and pressure at 30 min intervals, with an accuracy of $\pm$0.0003 S m^{-1}, $\pm$0.002°C, and $\pm$0.5 m, respectively.

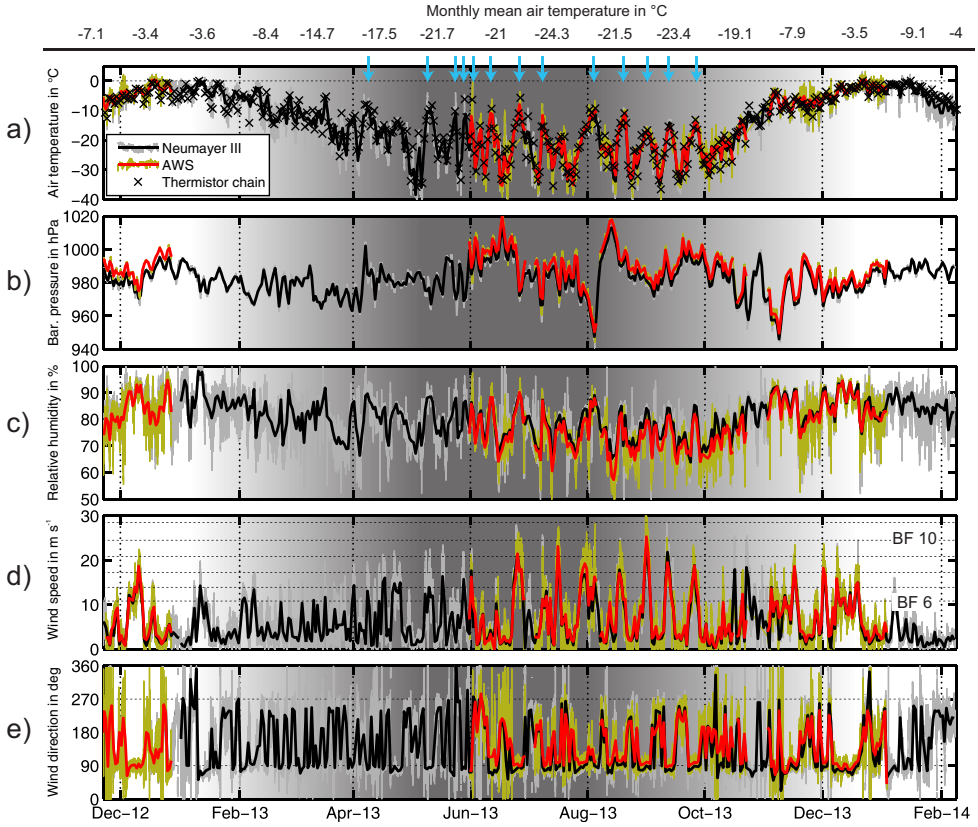

Figure 2. Meteorological conditions during the study period, as measured by the automatic weather station (red/green) and at Neumayer III (black/gray). Thin curves represent the measurements every minute, thick curves are daily averages. (a) Air temperature (2 m); (b) barometric pressure; (c) relative humidity; (d) wind speed (BF: Beaufort) and (e) wind direction. The blue arrows indicate the passage of synoptic systems in winter, associated with an advection of warm air, lower barometric pressure, high relative humidity, and strong easterly winds. The shaded area illustrates the annual cycle of polar day and night.

The distance to ATKA03 was ~10 km in 2012/2013 (Figure 1b). The data set was checked for consistency and it can safely be assumed that the recordings were not affected by ice accretion on the instrument due to the presence of supercooled water. From the measurements, we calculated absolute salinity, potential temperature, and the surface freezing point using the Gibbs Seawater (GSW) Oceanographic Toolbox [*McDougall and Barker*, 2011].

2.5. Sea-Ice Cores

Two full-thickness, 0.09 m diameter cores to determine sea-ice physical properties were retrieved at ATKA03 on 19 and 27 December 2013. We measured in situ temperatures in the core from 19 December in 0.1 m intervals, using a hand-held thermometer inserted into 2 mm holes drilled to the center of the core. The core was packed in a styrofoam box, temporarily stored at Neumayer III, and later transported to Bremerhaven at −20°C in order to perform a texture analysis. We drilled another core on 27 December, which was segmented into 0.1 m pieces on a bench immediately after being brought to the surface. The porosity of the segments was high and brine drainage could not be prevented. The segments were sealed in plastic boxes and transported to the laboratory. The density of each segment was calculated using a mass/volume approach [*Timco and Frederking*, 1996]. The segments were melted at a temperature of 4°C to minimize cell damage to algae present in the sea ice. Salinity was determined using a calibrated conductivity meter (WTW Cond3110). The samples were filtered and Chlorophyll-a was measured by a fluorometric method [*Welschmeyer*, 1994]. We used the sea-ice temperature, salinity, and density profiles to calculate brine and gas volume fractions according to *Leppäranta and Manninen* [1988]. Horizontal and vertical thin sections of the archived core were prepared and photographed between crossed polarizers.

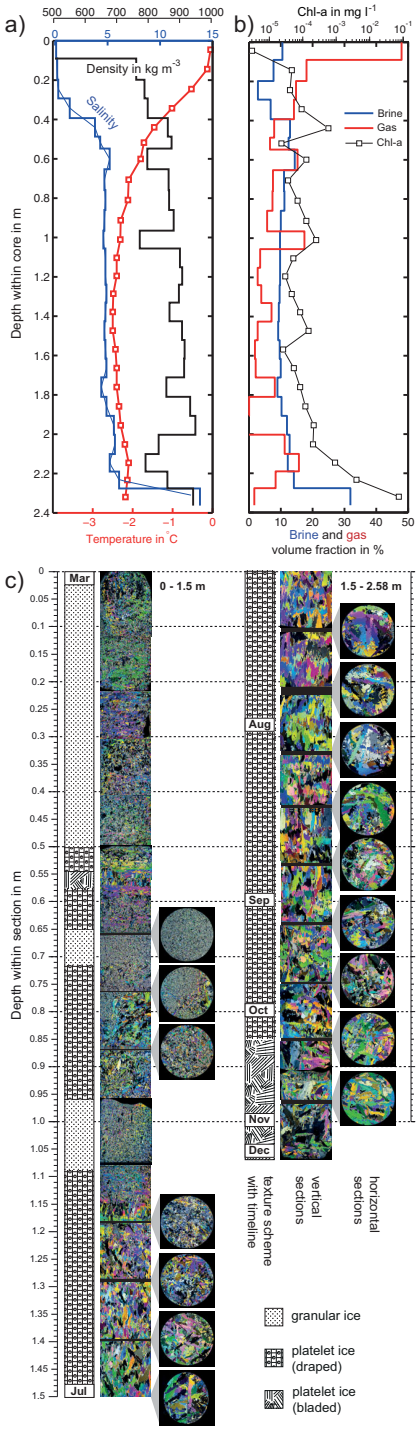

Figure 3. Sea-ice properties from cores retrieved at ATKA03 in December 2012. (a) Temperature (red), salinity (blue), and density profiles (black). The thin blue curve represents an interpolated salinity profile. (b) Brine (blue) and gas volume fractions (red), and Chlorophyll-a content (black). (c) Horizontal and vertical thin sections, photographed between crossed polarizers. The texture scheme to the left of the respective vertical thin sections was derived by visual inspection. The formation time in 2012 was determined by comparison to sea-ice thickness measurements (see text).

2.6. Drillings

Since the 4.8 m long thermistor chain did not extend through the entire platelet layer, the temperature and heating data shown here do not allow unambiguous conclusions about the evolution of its thickness. In order to reveal the platelet-layer's spatiotemporal evolution across the entire Atka Bay, we provide additional platelet-layer thickness data obtained by manual drillings at different sites throughout the study. One measurement was performed per site and visit. We thereby expand the study of *Hoppmann et al*. [2015], who described the platelet-layer evolution under first-year fast ice, to second-year fast ice.

2.7. Sea-Ice Growth Simulation

We simulated fast-ice growth by a one-dimensional, thermodynamic model [*Bitz and Lipscomb*, 1999] forced with local atmospheric data, and with snow depth derived from TC temperature profiles. We modified the original sea-ice growth rate $\frac{\partial H}{\partial t}$ in the model by

$$\frac{\partial H}{\partial t}(\beta) = \frac{1}{1-\beta} \cdot \frac{\partial H}{\partial t}, \tag{5}$$

where β is the fraction of solid ice mass in a defined volume in the platelet layer (ice-volume fraction).

The initial setup and preparation of the forcing data were performed as described by *Hoppmann et al*. [2015], with corrections applied to air temperature (+0.5°C), relative humidity (−2%), barometric pressure (+4.1 hPa), and upward longwave radiation (+6.5 W m^{-2}) to account for the different meteorological conditions on the sea ice compared to Neumayer III on the ice shelf (see Figure 2).

3. Results

This section is structured as follows: first, we highlight the environmental conditions during the study period, then we present results from our sea-ice core analysis. We investigate our main data set, thermistor chain temperature and heating profiles, and use these to calculate the basal energy balance. We then determine sea-ice growth from conductive heat flux alone and compare our observations to simulated fast-ice growth. Finally, we complement the results of our main data set with results of manual sub-ice platelet-layer thickness measurements and oceanographic conditions.

3.1. Environmental Conditions

Between TC deployment and mid-December 2012, the 2 m air temperature remained below the freezing point (Figure 2a). On 17 December, daily average temperatures rose above the freezing point for four consecutive days, before steadily decreasing until April 2013. During late autumn and winter, the air temperature fluctuated widely. Sudden changes in daily average air temperatures in excess of 20 K were recorded over 2 or 3 days. The overall minimum daily mean temperature of -38.5°C was measured on 3 May 2013. Temperatures stabilized in early spring, and increased again from October 2013.

Storm activities, accompanied by increased wind speed and warm air advection, occurred about twice a month during the entire study, and about once per week during winter (Figure 2d). Those events were always associated with easterly winds (Figure 2e). These observations are in accordance with the general climatology of Neumayer III [*König-Langlo et al.*, 1998].

3.2. Sea-Ice Cores

The sea-ice core recovered at ATKA03 on 19 December 2012 was 2.58 m long. There was no snow, freeboard was about 0.4 m, and the platelet-layer thickness was about 4 m. The core obtained on 27 December 2012 was 2.4 m long, without any snow on top. The platelet-layer thickness was 4.2 m, and freeboard was not recorded.

Temperatures were near-isothermal below 0.65 m, and above -2.5°C throughout the entire sea-ice core (Figure 3a). Salinity ranged from 0 at the surface to 13.8 in the skeletal layer at the bottom, with an overall average of 4.54. Sea-ice density was on average 850 kg m^{-3}, with a minimum of 490 kg m^{-3} near the top. This measurement underestimated the real density by up to 10% due to imprecise sawing, missing ice pieces, and especially brine loss at these high temperatures. For our calculation of air-volume fraction, we therefore used a sea-ice density of 910 kg m^{-3}. Air volume fraction was on average 9%, and highest at the top of the core (>40%), which is explained by surface melt and brine drainage. The brine volume fraction was on average 11%, with the usually observed maximum in the skeletal layer of 35%.

The crystal structure (Figure 3c) was classified by visual inspection of thin sections from the sea-ice core, acknowledging that this interpretation may be subjective. Fine-grained crystals and air inclusions were evident in the upper 0.5 m of the core. While crystal edges in the upper layer had largely eroded, these crystals mostly resembled typical granular new ice formed under turbulent conditions. In the next 0.15 m, the texture showed distinct, albeit randomly oriented frazil crystals. We refer to this texture as platelet ice [*Eicken and Lange*, 1989; *Jeffries et al.*, 1993; *Tison et al.*, 2013; *Dempsey et al.*, 2010], with a crystal structure unlike that of granular or columnar ice [*Dempsey et al.*, 2010]. Multiple rafting was indicated by fine-grained crystals, typical of snow ice (0.66–0.71 m), followed by platelet ice, and again by granular ice near 1 m. Below 1.15 m, larger crystals of draped platelet ice [*Tison et al.*, 2013; *Dempsey et al.*, 2010], also sometimes referred to as mixed columnar/platelet ice [*Mahoney et al.*, 2011] were apparent throughout a large part of the core length. Below 2.35 m, the shape of the platelets became blade-like [*Eicken and Lange*, 1989; *Tison et al.*, 2013; *Dempsey et al.*, 2010]. The growth history of the sea ice was determined by comparison to thickness measurements made at ATKA03 throughout 2012 [*Hoppmann et al.*, 2015]. These measurements started in mid-June, when the sea ice was already about 1.4 m thick. Rafting seemed to have occurred until May. Continuous thermodynamic growth set in afterward (at approximately 1.15 m), and was immediately disrupted by the presence of platelets. In summary, about 25% of the core consisted of granular ice (and eventually snow ice), the other 75% of platelet ice. A pure columnar texture was not observed.

3.3. Temperature and Heating Profiles

Figure 4 presents the main data set of this study, comprising (a) temperature, (b) δT_{30}, and (c) δT_{120} measurements obtained by the TC between 21 November 2012 and 9 February 2014, interpolated to daily profiles. The prominent vertical structures in Figures 4b and 4c were a result of a drop in voltage applied to the resistors during heating.

In the following, we will try to uncover the variety of information hidden in these data: the temporal evolution of (1) the snow cover, (2) the snow/ice interface (including surface melt); (3) the ice/water interface (sea-ice growth); (4) the presence of internal melt and refreezing; (5) sub-ice platelet-layer thickness; (6) conductive heat flux; and finally (7) the basal energy balance including the calculation of a residual (oceanic) heat flux. The effect of solar radiation penetrating into the snow and potentially leading to a warming of the upper thermistors is neglected throughout this paper.

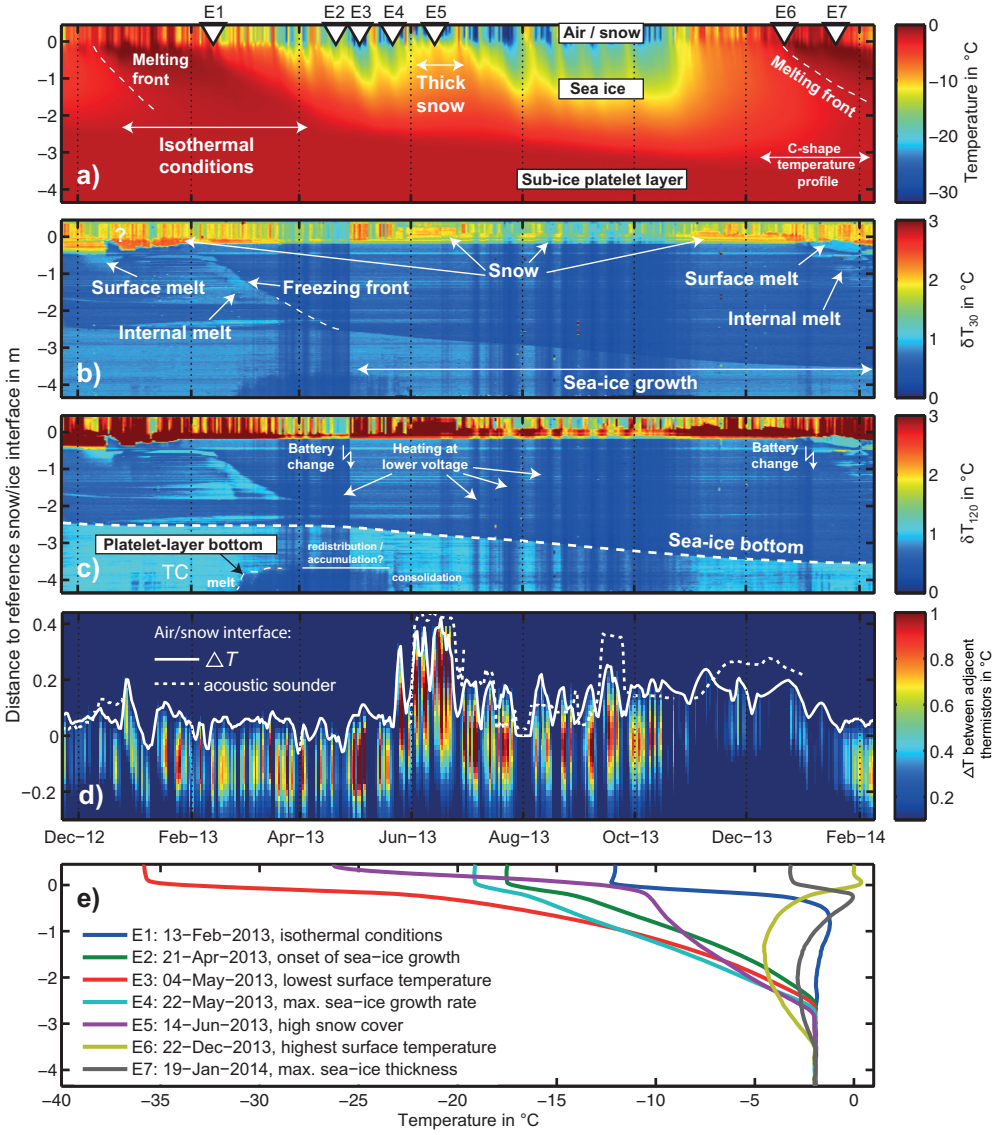

Figure 4. Data measured by the thermistor chain during the study period. (a) Daily temperature profiles; (b) temperature rise after 30 s heating (δT_{30}); (c) temperature rise after 120 s heating (δT_{120}); (d) snow surface retrieved from temperature difference between adjacent upper thermistors (ΔT, solid curve) and acoustic sounding (dashed curve); (e) selected temperature profiles under different environmental conditions at times indicated in (a).

3.4. Snow Depth

Comparison of snow depths derived from temperature differences between adjacent thermistors (ΔT) in the upper part of the chain with those determined from the AWS acoustic sounder revealed generally similar patterns and features, despite the high snow-depth variability (Figure 4d). The large temperature differences in the top 0.2–0.3 m of the sea ice originated from the lack of refreezing in the part of the deployment hole above the sea surface. Snow depth was on average 0.14 $\pm$ 0.09 m throughout the study. June exhibited by far the thickest snow cover, 0.31 $\pm$ 0.11 m, with a maximum of 0.42 m. Snow depth before June was 0.08 $\pm$ 0.05 m and 0.16 $\pm$ 0.06 m afterward.

3.5. Snow/Ice Interface

The evolution of the snow/ice interface was best identified from the δT_{30} and δT_{120} profiles (Figures 4b and 4c). It was characterized by a high temperature difference of up to 2°C between adjacent thermistors in the

Table 1. Monthly Average Residual Heat Flux (F_w) in W m^{-2} and Sea-Ice Thickness Increased (Δz_{si}) in mm During the Study

	2012		2013												2014		
Monthly average	Nov	Dec	Jan	Feb	Mar	Apr	May	Jun	Jul	Aug	Sep	Oct	Nov	Dec	Jan	Feb	Σ
Mean	−2.26	−0.74	0.63	−0.01	−0.40	−0.28	−2.31	−1.81	−1.61	−2.01	−1.02	−0.68	−1.13	−2.04	−0.60	0.97	
Std	0.44	1.45	0.30	0.13	0.07	0.32	1.11	0.64	0.45	0.68	0.57	0.84	0.83	0.48	0.81	0.09	
Δz_{si} in mm	20	46	5	1.2	4.4	49	147	113	101	140	132	123	95	74	32	0.01	1080
% due to F_w	36	21				7	21	20	21	19	10	7	15	36	24		18

δT_{120} data. This originated from the difference in thermal conductivity between snow and sea ice, which was about one order of magnitude. This interface was variable in height, differing by up to 0.3 m throughout the study. This was most likely again a consequence of the limited refreezing of the deployment hole, and does not reflect natural processes. However, the δT_{30} and δT_{120} profiles exhibited some interesting features near the snow/ice interface. During summer 2012/2013 and more pronounced in 2013/2014, areas with thermal characteristics that resemble the lower thermistors were apparent. It is likely that these were manifestations of meltwater formation and refreezing at the surface. Please note that the changing snow/ice interface described here is different from the reference snow/ice interface, which was assumed as constant for the calculation of snow depth and sea-ice thickness in this paper.

3.6. Ice/Water Interface

Isothermal conditions in the sea ice and the sub-ice platelet layer dominated the temperature profiles from January to May 2013, more than 1/3 of the year (Figure 4a). Under these circumstances, a determination of the ice/water interface from temperature measurements alone was impossible. However, the evolution of the ice/water interface was most pronounced in the δT_{120} profiles (Figure 4c, dashed white curve). For all further calculations in this study, we used an ice/water interface manually derived from the δT_{120} profiles. The resulting interface was additionally smoothed by a 10 day running mean to overcome the discrete distance between adjacent thermistors. During the study, the sea-ice thickness increased by 1.1 m, from 2.44 to 3.54 m. 0.1 m of this growth occurred between mid-November and mid-December 2012, when growth ceased for approximately 4 months. The remaining 1 m of growth occurred between mid-April 2013 and early January 2014. The average growth rate was 0.0024 ± 0.0017 m d^{-1} over the entire study, and 0.0033 ± 0.0011 m d^{-1} over the growth season only. The monthly sea-ice thickness increase is shown in Table 1.

3.7. Internal Melt and Refreezing

Several areas are present within the sea ice that exhibited a slightly higher δT_{30} and δT_{120} than the surrounding sea ice (Figures 4b and 4c, lighter blue). Due to the limited precision of the thermistors, these are difficult to identify. They are most likely indications of a phase transition from solid sea ice into the liquid phase, indicating internal melt. These structures were then altered by the advancing freezing front, which subsequently increased the solid fraction in the interior. This transition started approximately 0.5 m below the zero reference in February 2013. Shortly before April 2013, it was masked by the sea ice below, probably due to decreased melt in lower layers, leading to a reduction in the contrast. However, an artificial freezing front can be set to the bottom of the sea ice, marking the onset of active basal growth at the end of April 2013 (Figure 4b, dashed curve). Minor instances of different thermal characteristics inside the upper sea-ice layer were also apparent from January 2014, marking again the beginning of internal melt. Note that the freezing front (in contrast to the ice/water interface) may also be inferred from the temperature profiles (Figure 4a), by below-freezing temperatures which advanced through the sea-ice cover between February and April 2013.

3.8. Sub-ice Platelet Layer

TC-derived temperatures of the sub-ice platelet layer remained slightly below the freezing point throughout the study. Compared to simultaneous temperature measurements taken with a CTD75M (Sea and Sun Technology) in or near the platelet layer, thermistor temperatures were always lower. This is due to the thermistor's limited resolution causing a low signal-noise ratio given the very small temperature differences found in the seawater/platelet mixture. In order to interpret the heating data in the sub-ice platelet layer of Atka Bay (AB), it is useful to compare our results to measurements by an identical instrument in a sea-ice regime

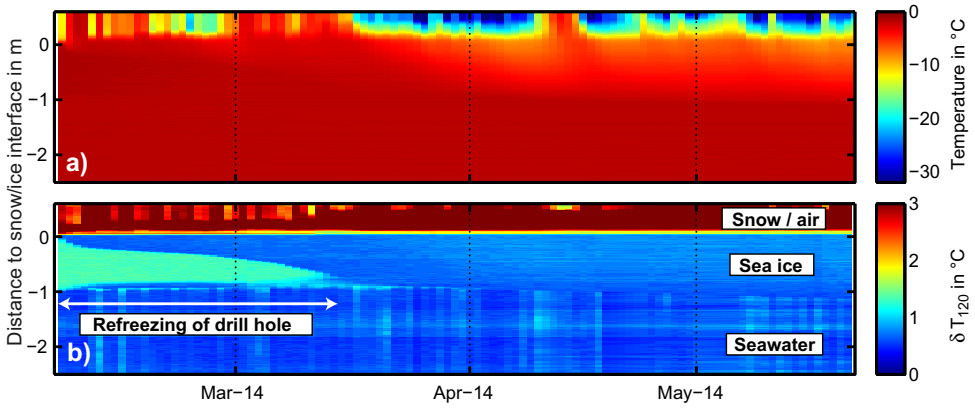

Figure 5. (a) Temperature and (b) δT_{120} profiles from a drifting thermistor chain in the central Weddell Sea.

without a platelet layer. Therefore, we chose to include a data set recorded in the central Weddell Sea (WS) in 2014 (Figure 5). It is immediately evident that the δT_{120} of sub-sea-ice thermistors at AB was ~0.5°C higher than in the WS, which is nearly 10 times the stated precision. Between February and May 2013, this difference partly vanished in the lowermost thermistors. This could be an indication of either the presence of flowing seawater, or sea ice temporarily attaching itself to the chain. We will discuss this in greater detail later.

When closely investigated, the WS data set exhibits another striking feature. When a thermistor chain is installed, it usually takes a while for the hole to refreeze entirely, especially under warmer conditions. Such a refreezing front is clearly visible in the heating data depicted in Figure 5b. At the same time, the thermistors located in the deployment hole obviously detected different thermal characteristics than those in the ocean below, again reflecting the sensitivity of this approach to the flow velocity of a medium.

3.9. Conductive Heat Flux

Bulk conductive heat flux F_c was estimated for layers of 0.2 m thickness through the entire sea-ice cover according to equation (2). For the calculation of k_{si} (ρ, S, T), we used a smoothed salinity profile based on Figure 3 and a sea-ice density of 910 kg m^{-3}. The average conductive heat flux was calculated between the actual snow/ice interface and the ice/water interface (Figure 6a).

The conductive heat flux near the snow/ice interface showed typical short-term fluctuations as a response to the rapid changes in the synoptic-scale atmospheric forcing, particularly air temperature. The absolute magnitude of F_c as well as the gradient generally decreased between upper and lower layers. The bottom layer lagged the induced variations in the upper sea-ice layer, which is most pronounced (up to 2 months) in autumn and spring. Apart from the expectedly low conductive heat flux in summer, several local minima also occurred during winter. These were especially apparent between August and October 2014, and are linked to relatively warm surface air advected to the site by passing synoptic systems (Figure 2). Another local minimum was observed during June 2013, lasting for more than 1 month. This was associated with a local maximum of snow cover (up to 0.4 m) described above. In contrast to the passage of the synoptic systems, this change of snow conditions also strongly affected the lower sea-ice layers.

Average F_c was low at the beginning of the study. Between December 2012 and February 2013, the temporal lag of warming in the sea-ice interior resulted in vertical temperature inversions and a subsequent negative F_c. This is a reflection of thermal energy transported into the sea-ice interior, downward at the top and upward at the base, leading to internal sea-ice warming and eventually also melt as described by *Lei et al.* [2014]. This condition was also observed between late December 2013 and February 2014. Typical vertical temperature inversion profiles are shown in Figure 4e (E1, E6, and E7). The average F_c increased gradually during atmospheric cooling in the transition from summer to winter (Figure 6b), reaching its absolute

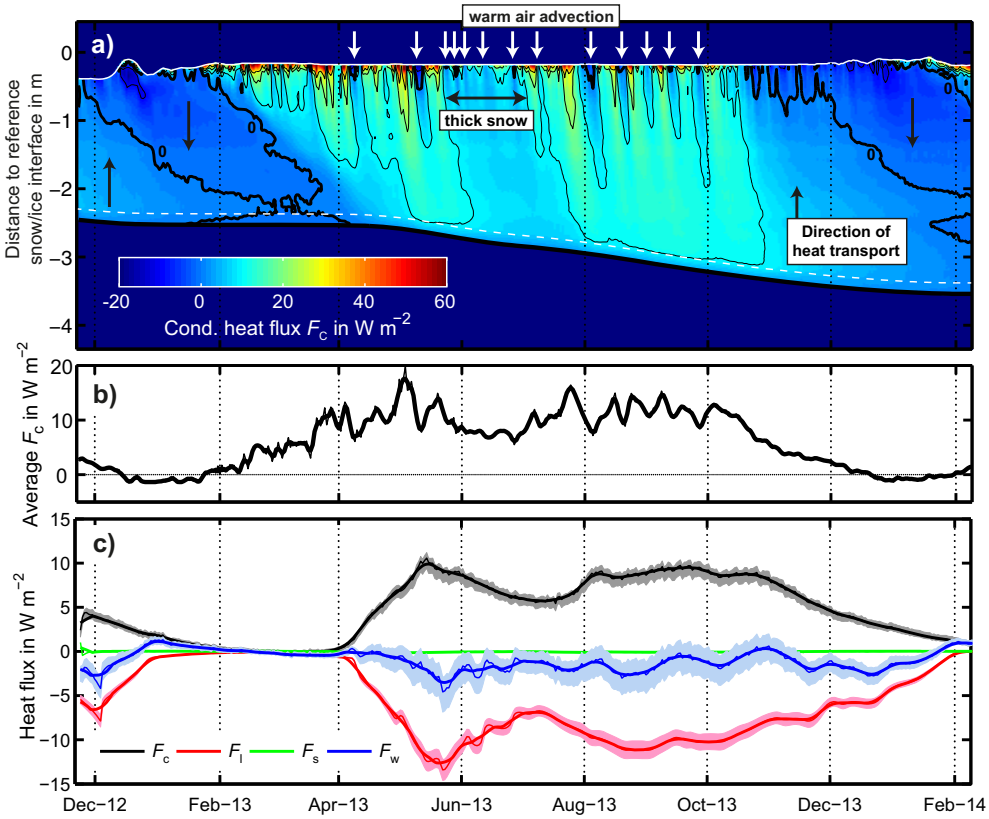

Figure 6. (a) Conductive heat flux through sea ice with contours at −20, −10, 0 (thick black curve), 10 and 20 W m^{-2}. Due to snow in the drill hole, the part between the reference snow/ice interface (zero) and the true snow/ice interface (solid white curve) was omitted. The white arrows correspond to the synoptic systems shown in Figure 2. (b) Average vertical conductive heat flux between the snow/ice interface and the ice/water interface. (c) Daily heat fluxes (thin curves) through a reference layer near the sea-ice base (dashed white curve in Figure 6a). The thick curves represent the 5 day running mean. F_c is the heat conducted upward through the reference layer, F_l is the latent heat required to form the thickness of sea ice added, F_s is the sensible heat flux which accounts for a temperature change in the reference layer, and F_w is the residual heat flux. The shaded areas represent the cumulative individual measurement uncertainties. Upward heat fluxes, warming and melting have a positive sign.

maximum of approximately 20 W m^{-2} in early May 2013. It then fluctuated around 10 W m^{-2}, until atmospheric warming from October 2013 as well as the increased sea-ice thickness again led to a gradual decrease.

3.10. Basal Energy Balance

In the basal energy balance (Figure 6c), upward heat fluxes, warming and melting have a positive sign, and shaded areas represent the overall uncertainties described below. The conductive heat flux through the reference layer (F_c, black) showed a similar pattern, although smoothed, to the vertically averaged conductive heat flux described above. The temperature change in the reference layer (F_s, green) was negligible. The (latent) heat removed to grow sea ice (F_l, red) roughly followed, but at the same time, exceeded the amount of heat conducted upward to the atmosphere and thus allowed for sea-ice thermodynamic growth. This resulted in a negative residual heat flux (F_w, blue) between −5 and 0 W m^{-2} throughout the growth periods (November 2012 to January 2013, April 2013 to January 2014). The monthly averages of F_w are given in Table 1. On average, 18% of the sea-ice thickness gain during the study period was not accounted for by upward heat conduction (thermodynamic growth).

The overall uncertainties were estimated by cumulative variation of individual uncertainties in the measurements. Those were ±1 for salinity, ±0.0625°C for thermistor readings and ±25 kg m^{-3} for the sea-ice density. Although the principal uncertainty in the retrieval of the ice/water interface is ±0.02 m, the uncertainty in the running mean, which is used for the growth-rate calculation, is considered to be very small. Note that

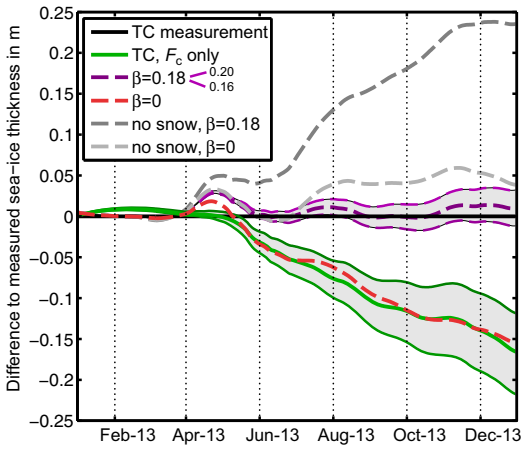

Figure 7. Comparison of sea-ice growth in 2013, derived from thermistor chain (TC) measurements and calculated from conductive heat flux alone (solid curves), along with results of different model simulations (dashed curves). The actual TC measurement (black line) is used as a zero reference. The upper half of the graph indicates thicker sea ice than this reference, the lower half indicates thinner sea ice. Filled areas represent a variation of ice-volume fraction β of ± 0.02 in the model (dashed violet curves), and the variation of the reference layer of ± 0.02 m for the calculation of the conductive heat flux (solid green curves).

these considerations do not account for a variation of the reference layer and the range of thermistors used for calculation of the temperature gradient, both of which move the curves upward and downward, and therefore have substantial influence on the residual flux.

3.11. Model Results and Ice-Volume Fraction

The results of different model runs (dashed curves) are shown in Figure 7, where the actual sea-ice thickness as determined from TC heating profiles is used as a zero reference. A positive sea-ice thickness difference (upper part of the graph) means thicker sea ice than observed, and vice versa.

Simulated sea-ice thickness with an unmodified growth rate and TC snow depth ($\beta = 0$, dashed red curve) differed from the observed sea-ice thickness by about 0.15 m at the end of growth. We performed additional model simulations with measured snow depth and modified growth rates according to equation (5), and show here only the results for $\beta = 0.16$, 0.18, and 0.20 (violet curves, bottom to top). The best fit between simulated and observed thickness was achieved for $\beta = 0.18$. Uncertainties of β were discussed in detail in *Hoppmann et al.* [2015], and are estimated as approximately 0.10 mainly due to uncertainties in upward longwave radiation. Further model experiments without a snow cover and $\beta = 0.18$ yielded a sea-ice thickness gain of 0.23 m (dashed, dark gray curve), while the combined absence of snow and platelets resulted in a net gain of 0.025 m (dashed, light gray curve).

Also shown is the adjusted growth rate $\left(\frac{\partial H}{\partial t}\right)_{adj}$, which was calculated from the basal energy balance only accounting for the conductive heat flux ($F_w = 0$, solid green curve):

$$\left(\frac{\partial H}{\partial t}\right)_{adj} = \frac{F_c + F_s}{\rho_{si} \cdot L_f}. \tag{6}$$

This generally represents a platelet-free scenario, and agrees well with the model result for $\beta = 0$. The uncertainties caused by a slight shift of the reference layer (± 0.02 m, shaded area between green curves) are also given for illustration.

3.12. Sub-ice Platelet Layer Thickness

Part of the platelet-layer thickness data (Figure 8; November 2012 to February 2013) were already described in detail in *Hoppmann et al.* [2015] and are included here due to the overlapping study interval. The initial platelet-layer thickness was on average about 4 m at the beginning of this study, decreasing to 3 m in January and toward 2 m in February. This thinning was associated with the inflow of warm water. Although not many data points are available between February and April 2013 due to safety concerns, it is likely that a platelet layer of 1–2 m thickness survived the summer. The first measurements at the end of April revealed an average thickness of about 4 m (with a high variability), steadily increasing at all sites between June and December 2013. The average platelet accumulation at all sites between April and December was approximately 4 m, leading to a mean overall thickness of about 8 m. The highest annual thickness gain of 6 m was observed at ATKA11 (Figure 8b, black triangle), the highest absolute thickness of 10 m was measured at ATKA07 (white diamond) in October 2013. The seawater temperature below the northern ice shelf (Figure 8c) was below the surface freezing point between April and November 2013, with a minimum in late May. With the continuous inflow of relatively warm water at the end of November 2013, as determined from CTD

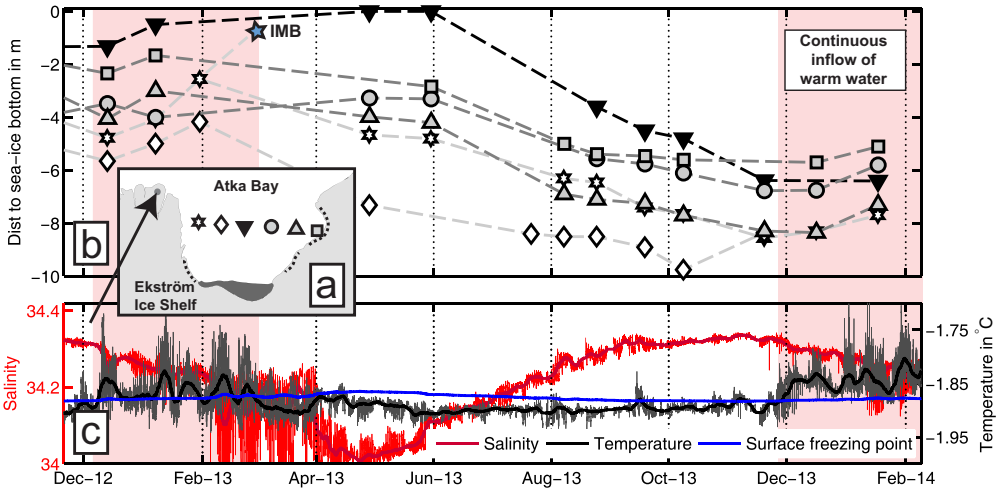

Figure 8. Platelet-layer thickness at the six sites between 2012 and 2014, along with oceanographic conditions recorded at a measurement site below the Ekström Ice Shelf. (a) Coarse map of the study area. The dark gray and dashed curves represent ice rises and rumples, respectively. (b) Sub-ice platelet-layer thickness evolution at different study sites, with symbols corresponding to their location according to Figure 8a. The blue star indicates the likely platelet-layer thickness determined by the IMB. (c) Seawater salinity (red) and temperature (black) measured by the MicroCAT at a depth of 155 m, at full resolution (thin curves) and 7 day running mean (thick curves). The corresponding surface freezing point is given in blue. The shaded area indicates the continuous inflow of relatively warm water.

measurements under the sea ice, the platelet-layer thickness again started to decrease. The time series stops shortly before the fast-ice breakup on 9 February 2014.

4. Discussion

In the first part of the discussion, we focus on the following factors that influenced the properties of the fast-ice cover and its basal energy balance in our study: (1) the general atmospheric conditions and the passage of synoptic systems, (2) the snow cover, (3) near-surface seawater temperatures, and (4) the properties of the sub-ice platelet layer. Combining all our results, we finally provide a schematic diagram depicting the seasonal evolution of fast ice in Atka Bay (2012–2014) near the Ekström Ice Shelf. In the second part, we discuss the potential of the instrument on the basis of this unique data set, and point out several limitations.

4.1. Seasonal Cycle of Fast Ice near an Ice Shelf

Since the sea-ice bottom was always near or at the freezing point (Figure 4a), near-surface air temperatures and snow depth governed the overall sea-ice temperature gradient, and with it the conductive heat flux. While the recurrent passage of relatively warm synoptic systems (Figure 2) strongly modified the temperature gradient in the upper part of the sea ice, these relatively rapid changes barely influenced the sea-ice bottom (Figure 6a). This is mainly due to the large thickness of the second-year sea ice and therefore these conditions did not influence the conductive heat flux through the near-bottom reference layer (Figure 6c). In contrast, the atmospheric conditions determined the presence of precipitation and snow drift, which play a crucial role in the evolution of a sea-ice cover through the low thermal conductivity of the snow. The strong insulating effect was particularly apparent in June and July 2013, when snow depth was at its maximum of up to 0.4 m (Figure 4e). With a delay of several weeks, this effect led to a drastic reduction of the temperature gradient, and consequently the sea-ice growth rate. As also shown in our model simulations, snow depth had a substantial influence on overall sea-ice growth. When comparing model runs with the measured snow depth throughout 2013 to a snow-free scenario, the sea-ice thickness at the end of the growth season was reduced by 23% (Figure 7). Unfortunately, ATKA03 was in the lee of an iceberg 2 km to the east (Figure 1), leading to a strong modification of snow deposition. The evolution of the snow cover shown here, with an average of 0.14 m, is therefore not representative for Atka Bay in general, which exhibited a significantly higher overall snow depth. A more realistic snow cover, derived from snow measurements on transects across Atka Bay at 1 km intervals, yielded bay-wide averages of 0.3 m in April, to 1.3 m in December 2013 (not shown). A corresponding model simulation with a linearly increasing snow cover revealed a sea-ice thickness increase of only 0.58 m (not shown), including a contribution from ice platelets. The observed

sea-ice growth of 1.1 m over this study (corresponding to 1 m in 2013) is therefore considered significantly above-average.

The presence of in situ supercooling in and in front of the ice-shelf cavity, also referred to as (supercooled) Ice Shelf Water plumes, [*Robinson et al*., 2014], determines the formation of ice platelets [*Lewis and Perkin*, 1986]. As we do not have near-surface ocean data available at depths where in situ supercooling is most likely to occur [*Smith et al*., 2001], we consider the presence of potentially supercooled water as an indicator for potential ice-platelet formation. Since the sub-ice shelf seawater temperature was consistently below the surface freezing point between late April and December 2013, and with higher variability even earlier (Figure 8b), platelet formation is possible throughout. *Hoppmann et al*. [2015] showed that in Atka Bay a sub-ice platelet layer starts to form during June. In contrast, results from our sea-ice texture analysis suggest that small platelets already modified the sea-ice texture up to two months earlier, although we cannot identify the exact timing from our measurements (Figure 3c). This is explained by the fact that the freezing interface in the early stage of formation may outgrow the comparably slow platelet accumulation [*Dempsey et al*., 2010]. This hypothesis is also confirmed by the pattern of platelet-layer thickness evolution in 2013, which showed already a net increase between February and May (Figure 8). It is unclear if this is the results of new accumulation or just redistribution from sites closer to the ice shelf with higher platelet-layer thickness. However, our results confirm the pattern of seasonal platelet-layer thickness evolution as found in *Hoppmann et al*. [2015], although a higher rate of thickness increase suggests the presence of strong platelet redistribution by currents directly under the sea ice. This has to be taken into account when interpreting platelet-layer thickness data in years where the fast ice did not break out completely during the previous summer. As soon as warm Antarctic Surface Water reaches the ice-shelf front in November/December [*Hattermann et al*., 2012], the platelet layer thinned at a rate of approximately 1 m month^{-1} (Figure 8b). Using an ice-volume fraction of 0.18, as found in the present study, this roughly corresponds to an oceanic heat flux of $+21$ W m^{-2}, in accordance with observations on fast ice in other regions [*Heil et al*., 1996; *Lei et al*., 2010]. At the same time, melting of the solid sea ice only occurred to a minor degree at the surface and in the ice interior (Figure 4). Despite the relatively high summer temperatures (Figure 2a), the increased radiative heating and the high oceanic heat flux, thermodynamic sea-ice growth even continued until the end of the study, albeit slowly (Figures 4b and 4c). This is due to the platelet layer shielding the sea ice from below and the slow temporal progression of the 0 W m^{-2} contour in the conductive heat flux (Figure 6a) due to the large sea-ice thickness.

According to the basal energy balance, about 18% (0.2 m) of the overall sea-ice growth (1.1 m) originated from a residual heat flux. The selection of the reference level and the number of thermistors for the linear fit of the temperature gradient may alter this result significantly. However, if the reference level is shifted, results for which this residual heat flux becomes positive, especially during the growth season, are implausible. It can therefore be safely assumed that the residual heat flux should be <0 W m^{-2} until at least mid-November. The negative residual heat flux can be interpreted as a representation of the ice crystals just below the advancing freezing interface [*Gough et al*., 2012]. These reduce the amount of heat that needs to be transported upward in order to grow a certain sea-ice thickness. In this interpretation, our results translate into an ice-volume fraction β, of 0.18. In order to provide an uncertainty estimate, β can also be calculated inserting equation (6) into equation (5) as a platelet-free growth rate:

$$\beta = 1 - \frac{F_c + F_s}{F_l}. \tag{7}$$

Averaging over the active sea-ice growth (May–January) results in $F_c = 7.06 \pm 2.08$ W m^{-2}, $F_l = -8.5 \pm 2.24$ W m^{-2}, and $F_s = -0.06 \pm 0.05$ W m^{-2}. According to equation (7), and using Gaussian error propagation, this corresponds to $\beta = 0.18 \pm 0.09$.

In an independent approach, our model simulations with local atmospheric forcing and a variable growth rate reproduced the observed sea-ice thickness evolution best with a $\beta = 0.18$ (Figure 7). In addition to the good agreement of this independent approach to our residual flux calculation, this result also agrees well with the findings of *Kipfstuhl* [1991] and especially *Hoppmann et al*. [2015], who simulated sea-ice growth at several study sites with the same model setup, but with forcing data and independent observations (drillings) for the year 2012. Their result for ATKA03, the site of the present study, agrees within error, giving further confidence in our results, the performance of the model and the quality of the forcing data. Using a similar approach, *Gough et al*. [2012] found in their study an ice-volume fraction of 0.25 ± 0.06. The

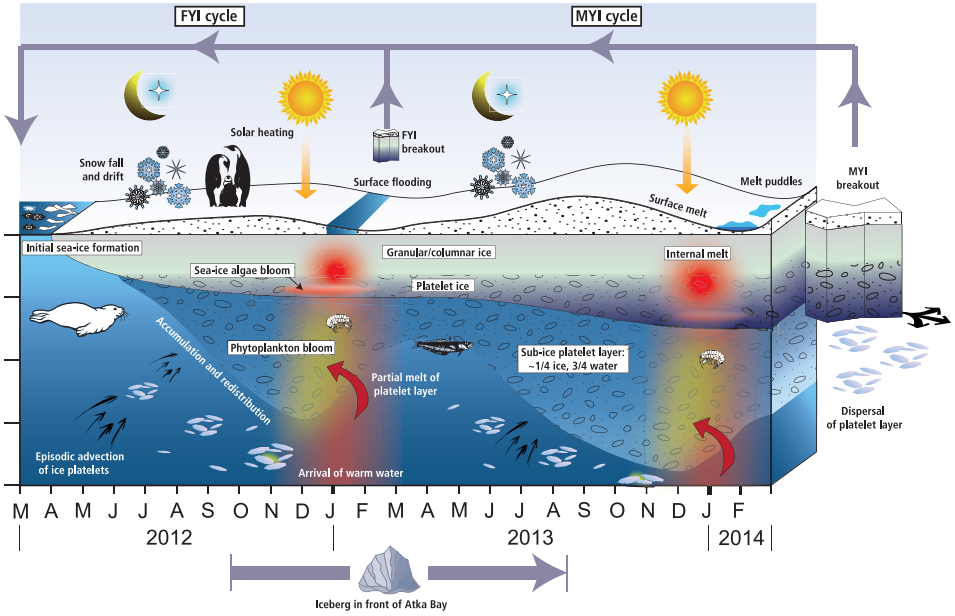

Figure 9. Schematic diagram of the seasonal cycle of Atka Bay fast ice and the sub-ice platelet layer, based on results of *Hoppmann et al.* [2015] for 2012 and this study for 2013/2014.

difference could be a reflection of the different TC setup, or more likely, the spatiotemporal variability in the platelet layer itself. It is for example currently unclear how the crystal-size distribution depends on the geographical setting and the time of the year, and how this potentially modifies the ice-volume fraction.

According to *Hoppmann et al.* [2015], accumulation and incorporation of platelets lead to an overall contribution to first-year sea-ice mass of about 50% in Atka Bay. Here we extend this result to multiyear sea ice: the platelet-layer thickness at ATKA03 increased by about 7 m, from approximately 1.5 m in February to 8.5 m in December. With $\beta = 0.18$, this corresponds to an effective sea-ice thickness of 1.26 m, or 60% of the combined solid and "loose" sea ice in 2013 (2.1 m). Including the amount that is already frozen into the sea ice (0.2 m), the overall oceanic contribution at the study site is 1.46 m, or 70% of the overall sea-ice thickness. This is considered an upper limit since it is unknown how much platelets were actually just redistributed from other locations.

It may also be useful to recalculate these results for the estimated bay-wide averages. The effective sea-ice thickness increase represented by the platelet layer is 4 m $\times$ 0.18 = 0.72 m. An estimation for the average sea-ice growth with incorporated platelets was already calculated earlier from a model simulation using bay-wide measurements of snow cover (0.58 m). Multiplication with β yields an effective sea-ice thickness from incorporated platelets of 0.10 m, with a thermodynamic growth of 0.48 m. Using these numbers, the contribution of ice platelets to the annual sea-ice thickness increase becomes 63%, or nearly 2/3. Taking into account a specific area and a defined sea-ice density, this result may be directly translated into sea-ice mass or volume. This result thereby shows that in areas where sea ice grows slowly, such as multiyear sea ice or where a thick snow cover is present, much of the sea-ice volume gained is a direct result of ocean/ice-shelf interaction in nearby cavities.

Finally, we present a schematic diagram (Figure 9) mainly incorporating findings from the present study and from *Hoppmann et al.* [2015], to summarize the seasonal evolution of the fast-ice regime of Atka Bay.

Although our study provided a further piece in the puzzle of how the physical environment of a fast-ice regime affected by platelet accumulations behaves and evolves over time, the major challenge is now to unravel its implications for the associated ecosystem and to identify the linkages between different trophic levels, such as micro algae [*Dieckmann et al.*, 1986; *Günther and Dieckmann*, 1999], invertebrates [*Günther et al.*, 1999], notothenioid fish [*La Mesa et al.*, 2004; *Vacchi et al.*, 2004], seals [*Davis et al.*, 1999], and penguins [*Zitterbart et al.*, 2014].

4.2. Assessment of the Instrument's Potential

Sea-ice mass balance buoys have been an important tool in sea-ice research in the recent past, and they remain crucial to monitor changes in the polar oceans. However, commonly used IMBs are too expensive to be deployed in large numbers, which would be needed to assess the large-scale changes and to identify responsible processes. The main difference between the TC used here and other, well established IMBs [*Richter-Menge et al.*, 2006], is the lack of acoustic sounders above the snow surface and below the sea-ice bottom. The simpler construction allows for easy deployment, taking one person about 30 min. At the same time, it is however difficult to infer the interfaces between air, snow, sea ice and seawater from temperature profiles alone. Based on our data, the main questions we try to address are: (1) How well is the heating mode able to compensate the loss of information due to the lack of acoustic sounders? (2) Which additional information about a sea-ice cover can be inferred from the heating data?

Due to the large air temperature fluctuations typically observed in polar regions, the temperature gradient near the upper snow surface is substantial. In contrast, thermistors in the air usually measure the same temperature (within their accuracy). Consequently, the air/snow interface, and hence the snow depth, may be inferred from temperature differences between adjacent thermistors. Although the heating profiles generally indicated a similar snow-depth evolution, the highest difference in temperature response between adjacent thermistors was generally located a few centimeters below the air/snow interface determined from temperature profiles. We explain this by the fact that the wind moves the upper part of the chain, creating an air gap around the upper few thermistors. Due to the lack of contact area, these thermistors then record the same characteristics as those in the air above. This effect did not influence the temperature measurements to a comparable degree. As a result, the temperature measurements provide a better indication of snow depth than the heating profiles, which reproduce the general pattern but underestimate snow depth by up to 0.1 m. In summer, the retrieval of the air/snow interface is additionally influenced by radiative warming of the chain, an effect which we have neglected here.

As stated earlier, the temperature response to a defined heat input is generally proportional to the thermal conductivity and specific heat capacity of a medium. The difference between δT_{120} and δT_{30} was close to zero for sea ice, around 0.1 K for the platelet/water mixture and some regions in the sea-ice interior, and up to 4 K for snow and air (not shown). For sea ice it was therefore not possible to derive a plausible thermal conductivity from these data, mainly because the measurements at 30 and 120 s were not in the linear part of the temperature rise curve. Although a calculation should in principal be possible for snow, the complex geometry of the sensors modifies the typical equations used for needle-probe measurements, and a detailed investigation was beyond of the scope of this paper.

Through the 10-fold difference in thermal conductivity of sea ice and snow, the snow/ice interface is sharply pronounced in the heating profiles and easily extracted. This is also true for the air/ice interface in the absence of snow. However, the evolution of the sea-ice surface is admittedly more interesting in the presence of surface melt, which is more pronounced in the Arctic compared to the Antarctic. To our knowledge, no study has yet been published using the heating mode of the TC to infer the evolution of surface melt and the formation of a melt pond. However, it has been shown above that determining a (nonflowing) ice/water interface is very promising with this method, provided only diffusive heat transfer is likely to take place. This should be the case for surface meltwater. Since it is expected that the location of an air/water interface is also easily determined, this approach is promising to monitor melt-pond depth evolution, and even refreezing (under the assumption that the instrument stays in place).

When calculating a sea-ice mass budget, internal melt processes are usually neglected due to the lack of a suitable methodology. As described above, several areas in the heating data sets can be interpreted as internal melt or even the formation of gap layers. These mainly occurred in summer, most prominently between February and April 2013. Although we do not study these in detail here, this potentially provides additional insight into melt processes.

In our case, the heating data effectively provided 3 months of additional information about the evolution the ice/water interface, mainly for isothermal conditions in summer 2013. However, such a clear identification was only possible due to a presence of a sub-ice platelet layer. Sea ice and flowing water exhibit a similar thermal response to an applied heating. Under flowing conditions, the ice/water interface may still be inferred from the variations of flow speed of the underlying water, which results in slightly variable

temperature differences. This behavior was also described in *Jackson et al*. [2013], and is indicated in the Weddell Sea data set as different shades of blue (Figure 5b). However, this effect significantly complicates the implementation of general algorithms to automatically retrieve the ice/water interface. In addition, a longer time series is needed to accurately interpret the subtle differences not visible from few measurements alone, noting a higher measurement frequency might also assist. Furthermore, Figure 5b demonstrates that the thermal characteristic of refreezing in the upper borehole differ from those of the surrounding medium. According to the scenario described above, this is most likely explained by a near-zero flow rate in the drill hole, in contrast to the ocean below.

This effect leads to an interesting application of this instrument in sea-ice regimes with a sub-ice platelet layer: dealing with supercooled seawater and associated processes, temperature differences in the order of several mK need to be resolved. This prerequisite is not met by the thermistors embedded in the chain. However, although the platelet layer is highly porous, it is safe to assume that the geometric properties of the platelet matrix impede the oceanic currents enough to significantly reduce the flow. Comparison of the Atka Bay (Figure 4c) and the Weddell Sea data sets (Figure 5b) suggest that it is therefore in principle possible to distinguish a sub-ice platelet layer from an unimpeded seawater flow. If this hypothesis holds, we are now able to interpret the darker blue areas below the sea-ice base from February to June 2013 (Figures 4b and 4c) as a temperature response associated with thinning and reconsolidation processes in the platelet layer. The thinning, or more specifically, the presence of ice-free, flowing seawater surrounding the lowermost thermistors in March is consistent with results from manual platelet-layer thickness measurements at ATKA03 (Figure 8b, star symbols), because further bottom melt is expected as long as relatively warm water is present until the beginning of March (Figure 8c). Between March and the beginning of May 2013, the data quality is too low due to artifacts caused by power issues. In mid-May, the lowermost thermistors exhibit a sudden increase in their temperature response, showing a signature similar to that before platelet-layer melt (especially visible in Figure 4c). This is again consistent with Figure 8b, in that our drillings showed the platelet-layer thickness had already increased to more than 4 m in April. This was seemingly not reproduced by the IMB data. However, a closer investigation of Figures 4b and 4c reveals that the temperature response of the lower thermistors in the first half of May was slightly different from that observed in March. We interpret this as a signature of the early phase of platelet-layer establishment, where the connectivity in the interstitial water is still high enough to allow for a detectable flow rate. The rapid transition in mid-May would then correspond to an enhanced consolidation, reduced connectivity and consequently, reduced flow rates. These results suggest that the heating mode is able to detect the platelet-layer bottom, although the possibility of the lower thermistors simply being encased in platelet ice cannot be ruled out entirely.

The most important constraint to this application, as also shown in our study, is the chain length. Although a typical thermistor chain length of 4.8 m seems long enough for a deployment in typical sea ice, it is too short to also monitor the evolution of a platelet layer over the course of winter, which can well reach up to 10 m. In our case, a length of about 10 m (with a wider thermistor spacing in the lower 5 m) would be needed to cover the entire seasonal cycle. But as the shear stresses on such a long chain increase dramatically due to the strong under-ice currents, the risk of a failure is high. Further testing is necessary to assess if such a long chain is practical. In addition, an IMB equipped with an acoustic sounder below the sea ice is generally not suited to be operated in areas where a sub-ice platelet layer is present or expected. Objects or instruments hanging below the sea ice serve as an ideal body for large amounts of ice crystals to grow on, a phenomenon for example photographed by *Mahoney et al*. [2011]. Even if the sensor would remain ice-free, a detection of the sea-ice/platelet layer interface would rely on temperature measurements alone, leading to higher uncertainties.

As usual, there are also several difficulties and problems associated with the operation of such an instrument. Here we identify some issues we experienced which the user needs to be aware of. The obvious is that predeployment calibration and testing is crucial to characterize the instrument.

The prominent vertical structures in Figures 4b and 4c are a result of a drop in voltage applied to the resistors during heating, which is usually 8 V. This effect leads to less pronounced contrasts between different media and occurred whenever the general battery voltage dropped below 10 V. It affected roughly 1/3 of the heating profiles. However, the other measurements were still sufficient for an accurate determination of interfaces between different media. The temperature profiles, and therefore all energy balance calculations,

are not impacted at all by this effect. For a calculation of thermal properties (not shown here), this effect has to be taken into account. The heating voltage is usually also recorded, and is included in the status message when operated via Iridium.

In order to obtain a continuous time series of snow depth throughout a certain study, a part of the thermistor chain has to remain above the snow surface (Figure 4b). The chosen length of this segment depends on the expected snow accumulation in a study region, and the construction of a suitable rack. In our study, 0.5 m above the snow surface was just enough to keep track of the snow-depth evolution. Under conditions of $>$0.5 m snow accumulation, continuous snow-depth retrieval is therefore difficult. In addition, the surface unit is quickly buried under the thick snow, and data transmission is potentially hampered when the snow becomes too thick or wet.

Our data processing, the development of algorithms and the setting of thresholds was tuned to fit the presented data set. Since the heating profiles strongly depend on a combination of the thermal characteristics of a medium and its flow speed, the presentation of a generally applicable procedure to infer the different interfaces for other sea-ice data sets is difficult and beyond the scope of this paper. However, with a quickly increasing number of such data sets, we identify the need for a set of generally applicable algorithms to facilitate speedy and unified data processing and interpretation.

5. Summary and Conclusion

Measurements of the atmosphere, sea ice, ocean, and sub-ice platelet layer have been made on Antarctic first/second-year fast ice over 15 month. The grounding of a large iceberg in front of Atka Bay, which prevented a usual sea-ice breakup in 2013, presented a unique opportunity to perform a continuous and detailed study of the sea-ice processes, and especially the sub-ice platelet-layer evolution, over such a long period. The main data set presented here is a consistent time series of air, snow, sea-ice, and ocean/platelet-layer temperature profiles recorded by a thermistor chain which is also able to actively heat resistor components mounted near the temperature sensors. This data set is one of the longest of its kind recorded to date, and highlights various features in the seasonal sea-ice evolution.

It is supplemented by simultaneous, consistent time series of sub-ice-shelf temperatures and salinities, and high quality meteorological data partly obtained directly next to the thermistor chain. The total solid sea-ice thickness gain during 2013 was about 1 m, due to the high initial thickness of 2.5 m and the snow cover that was thick for some of the time. In total, 18% of the ice grown between April and December 2013 was not accounted for by heat conduction to the atmosphere. The translation of this result to a platelet-layer ice-volume fraction of 0.18 ± 0.09 was also confirmed by independent sea-ice growth simulations, which yielded an ice-volume fraction of 0.18 ± 0.10. The platelet-layer thickness near ATKA03 increased by about 7 m (from 1.5 to 8.5 m) in 2013, with a bay-wide average of about 4 m. Overall, oceanic contribution to sea-ice thickness accounted for up to 70% of the total thickness. We showed that an approximate oceanic heat flux of 21 W m^{-2} during summer months is not sufficient to melt the entire platelet layer. Therefore, our study directly supplies evidence that in areas where sea ice grows slowly, such as thick multiyear sea ice or in the presence of a thick snow cover, most of the ice volume is contributed by ocean/ice-shelf interaction.

We also showed that, by the distinction of media through their thermal properties and flow speed, the heating mode is able to compensate the lack of acoustic sounders present on standard IMBs. This makes this buoy far easier to deploy and more reliable. By careful extraction of the interfaces from both measurement modes, it is possible to accurately determine the basal energy budget. In addition, the instrument is able to resolve internal structures such as gap layers and their refreezing. Although it is generally possible to derive the thermal conductivity and specific heat capacity of sea ice and snow with this approach, their quantification was beyond the scope of this work.

Finally, our study supplied evidence that a thermistor chain with active heating is capable of detecting the sub-ice platelet layer thickness through the lower current speed compared to the underlying ocean. Thereby it is currently the only automated method to continuously monitor the formation of a sub-ice platelet layer. This makes it the ideal tool to study sea-ice regimes influenced by ocean/ice-shelf interaction continuously over an extended time.

Acknowledgments
The authors are most grateful to the Neumayer III overwintering teams in 2012 and 2013 for their support in the field. We acknowledge Lars Kindermann and Olaf Boebel for the CTD data, and Sandra Schwegmann for the buoy deployment. Our research at Neumayer III and onboard RV Polarstern ANT-XXIX/9 would not have been possible without the help of the crew and the AWI logistics. This work was supported by the German Research Council (DFG) in the framework of the priority programme "Antarctic Research with comparative investigations in Arctic ice areas" by grants to SPP1158, NI 1092/2 and HE2740/12, and the Alfred-Wegener-Institut Helmholtz-Zentrum für Polar- und Meeresforschung. The data used here are publicly available at http://doi.org/10.1594/PANGAEA.833978. PH was supported under AAS grant #4301 and by the Australian Government's Cooperative Research Centre's Program through the Antarctic Climate and Ecosystems Cooperative Research Centre. Finally, the authors are grateful to two anonymous reviewers whose constructive comments significantly improved this manuscript.

References

Arrigo, K. R., D. H. Robinson, and C. W. Sullivan (1993), A high-resolution study of the platelet ice ecosystem in McMurdo Sound, Antarctica: Photosynthetic and bio-optical characteristics of a dense microalgal bloom, *Mar. Ecol. Prog. Ser.*, *98*(1–2), 173–185, doi:10.3354/meps098173.

Bintanja, R., G. J. van Oldenborgh, S. S. Drijfhout, B. Wouters, and C. A. Katsman (2013), Important role for ocean warming and increased ice-shelf melt in Antarctic sea-ice expansion, *Nat. Geosci.*, *6*, 376–379, doi:10.1038/ngeo1767.

Bintanja, R., G. J. van Oldenborgh, and C. A. Katsman (2015), The effect of increased fresh water from Antarctic ice shelves on future trends in Antarctic sea ice, *Ann. Glaciol.*, *56*(69), 120–126.

Bitz, C. M., and W. H. Lipscomb (1999), An energy-conserving thermodynamic model of sea ice, *J. Geophys. Res.*, *104*(C7), 15,669–15,677, doi:10.1029/1999JC900100.

Boebel, O., L. Kindermann, H. Klinck, H. Bornemann, J. Plötz, D. Steinhage, S. Riedel, and E. Burkhardt (2006), Real-time underwater sounds from the Southern Ocean, *Eos Trans. AGU*, *87*(36), 361, doi:10.1029/2006EO360002.

Davis, R. W., L. A. Fuiman, T. M. Williams, S. O. Collier, W. P. Hagey, S. B. Kanatous, S. Kohin, and M. Horning (1999), Hunting behavior of a marine mammal beneath the Antarctic fast ice, *Science*, *283*(5404), 993–996, doi:10.1126/science.283.5404.993.

Dempsey, D. E., P. J. Langhorne, N. J. Robinson, M. J. M. Williams, T. G. Haskell, and R. D. Frew (2010), Observation and modeling of platelet ice fabric in McMurdo Sound, Antarctica, *J. Geophys. Res.*, *115*, C01007, doi:10.1029/2008JC005264.

Dieckmann, G., G. Rohardt, H. Hellmer, and J. Kipfstuhl (1986), The occurrence of ice platelets at 250 m depths near the Filchner Ice Shelf and its significance for sea ice biology, *Deep Sea Res., Part A*, *33*(2), 141–148, doi:10.1016/0198-0149(86)90114-7.

Eicken, H., and M. A. Lange (1989), Development and properties of sea ice in the coastal regime of the southeastern Weddell Sea, *J. Geophys. Res.*, *94*(C6), 8193–8206, doi:10.1029/JC094iC06p08193.

Fahrbach, E., S. Harms, G. Rohardt, M. Schröder, and R. A. Woodgate (2001), Flow of bottom water in the northwestern Weddell Sea, *J. Geophys. Res.*, *106*(C2), 2761–2778, doi:10.1029/2000JC900142.

Fichefet, T., and M. A. M. Maqueda (1999), Modelling the influence of snow accumulation and snow-ice formation on the seasonal cycle of the Antarctic sea-ice cover, *Clim. Dyn.*, *15*(4), 251–268, doi:10.1007/s003820050280.

Fraser, A. D., R. A. Massom, K. J. Michael, B. K. Galton-Fenzi, and J. L. Lieser (2012), East Antarctic landfast sea ice distribution and variability, 2000–08, *J. Clim.*, *25*(4), 1137–1156, doi:10.1175/JCLI-D-10-05032.1.

Gough, A. J., A. R. Mahoney, P. J. Langhorne, M. J. M. Williams, N. J. Robinson, and T. G. Haskell (2012), Signatures of supercooling: McMurdo Sound platelet ice, *J. Glaciol.*, *58*(207), 38–50, doi:10.3189/2012JoG10J218.

Günther, S., and G. S. Dieckmann (1999), Seasonal development of algal biomass in snow-covered fast ice and the underlying platelet layer in the Weddell Sea, Antarctica, *Antarct. Sci.*, *11*(3), 305–315, doi:10.1017/S0954102099000395.

Günther, S., and G. S. Dieckmann (2001), Vertical zonation and community transition of sea-ice diatoms in fast ice and platelet layer, Weddell Sea, Antarctica, *Ann. Glaciol.*, *33*(1), 287–296, doi:10.3189/172756401781818590.

Günther, S., M. Gleitz, and G. S. Dieckmann (1999), Biogeochemistry of Antarctic sea ice: A case study on platelet ice layers at Drescher Inlet, Weddell Sea, *Mar. Ecol. Prog. Ser.*, *177*, 1–13.

Hattermann, T., O. A. Nøst, J. M. Lilly, and L. H. Smedsrud (2012), Two years of oceanic observations below the Fimbul Ice Shelf, Antarctica, *Geophys. Res. Lett.*, *39*, L12605, doi:10.1029/2012GL051012.

Heil, P. (2006), Atmospheric conditions and fast ice at Davis, East Antarctica: A case study, *J. Geophys. Res.*, *111*, C05009, doi:10.1029/2005JC002904.

Heil, P., I. Allison, and V. I. Lytle (1996), Seasonal and interannual variations of the oceanic heat flux under a landfast Antarctic sea ice cover, *J. Geophys. Res.*, *101*(C11), 25,741–25,752, doi:10.1029/96JC01921.

Heil, P., S. Gerland, and M. A. Granskog (2011), An Antarctic monitoring initiative for fast ice and comparison with the Arctic, *Cryosphere Discuss.*, *5*(5), 2437–2463, doi:10.5194/tcd-5-2437-2011.

Holland, P. R., and R. Kwok (2012), Wind-driven trends in Antarctic sea-ice drift, *Nat. Geosci.*, *5*, 872–875, doi:10.1038/ngeo1627.

Hoppmann, M., et al. (2015), Ice platelets below Weddell Sea land fast sea ice, *Ann. Glaciol.*, *56*(69), 175–190, doi:10.3189/2015AoG69A678, in press.

Hunkeler, P., S. Hendricks, M. Hoppmann, S. Paul, and R. Gerdes (2015), Towards an estimation of sub-sea-ice platelet-layer volume with multi-frequency electromagnetic induction sounding, *Ann. Glaciol.*, *56*(69), 137–146, doi:10.3189/2015AoG69A705.

Jackson, K., J. Wilkinson, T. Maksym, J. Beckers, C. Haas, D. Meldrum, and D. Mackenzie (2013), A novel and low cost sea ice mass balance buoy, *J. Atmos. Oceanic Technol.*, *30*, 2676–2688, doi:10.1175/JTECH-D-13-00058.1.

Jeffries, M. O., W. F. Weeks, R. Shaw, and K. Morris (1993), Structural characteristics of congelation and platelet ice and their role in the development of Antarctic land-fast sea-ice, *J. Glaciol.*, *39*(132), 223–238.

Kawamura, T., K. I. Ohshima, T. Takizawa, and S. Ushio (1997), Physical, structural and isotopic characteristics and growth processes of fast sea ice in Lützow-Holm Bay, Antarctica, *J. Geophys. Res.*, *102*(C2), 3345–3355, doi:10.1029/96JC03206.

Kipfstuhl, J. (1991), Zur Entstehung von Unterwassereis und das Wachstum und die Energiebilanz des Meereises in der Atka Bucht, Antarktis, *Ber. Polarforsch.*, *85*, 88 pp., doi:10013/epic.10085.d001.

König-Langlo, G., and B. Loose (2007), The meteorological observatory at Neumayer Station (GvN and NM-II) Antarctica, *Polarforschung*, *76*, 25–38.

König-Langlo, G., J. C. King, and P. Pettré (1998), Climatology of the three coastal Antarctic stations Dumont d'Urville, Neumayer, and Halley, *J. Geophys. Res.*, *103*(D9), 10,935–10,946, doi:10.1029/97JD00527.

La Barbara, M., and S. Vogel (1976), An inexpensive thermistor flowmeter for aquatic biology, *Limnol. Oceanogr.*, *21*, 750–756.

La Mesa, M., J. T. Eastman, and M. Vacchi (2004), The role of notothenioid fish in the food web of the ross sea shelf waters: A review, *Polar Biol.*, *27*(6), 321–338, doi:10.1007/s00300-004-0599-z.

Lefebvre, W., and H. Goosse (2008), An analysis of the atmospheric processes driving the large-scale winter sea ice variability in the Southern Ocean, *J. Geophys. Res.*, *113*, C02004, doi:10.1029/2006JC004032.

Lei, R., Z. Li, B. Cheng, Z. Zhang, and P. Heil (2010), Annual cycle of landfast sea ice in Prydz Bay, East Antarctica, *J. Geophys. Res.*, *115*, C02006, doi:10.1029/2008JC005223.

Lei, R., N. Li, P. Heil, B. Cheng, Z. Zhang, and B. Sun (2014), Multiyear sea ice thermal regimes and oceanic heat flux derived from an ice mass balance buoy in the Arctic Ocean, *J. Geophys. Res. Oceans*, *119*, 537–547, doi:10.1002/2012JC008731.

Leppäranta, M., and T. Manninen (1988), The brine and gas content of sea ice with attention to low salinities and high temperatures, technical report 1988-2, *Finn. Inst. of Mar. Res.*, Helsinki, Finland.

Lewis, E. L., and R. G. Perkin (1986), Ice pumps and their rates, *J. Geophys. Res.*, *91*(C10), 11,756–11,762, doi:10.1029/JC091iC10p11756.

Li, X., D. M. Holland, E. P. Gerber, and C. Yoo (2014), Impacts of the north and tropical Atlantic Ocean on the Antarctic Peninsula and sea ice, *Nature*, *505*(7484), 538–542, doi:10.1038/nature12945.
Liu, J. P., and J. A. Curry (2010), Accelerated warming of the Southern Ocean and its impacts on the hydrological cycle and sea ice, *Proc. Natl. Acad. Sci. U. S. A.*, *107*(34), 14,987–14,992, doi:10.1073/pnas.1003336107.
Liu, J. P., J. A. Curry, and D. G. Martinson (2004), Interpretation of recent Antarctic sea ice variability, *Geophys. Res. Lett.*, *31*, L02205, doi:10.1029/2003GL018732.
Mager, S. M., I. J. Smith, E. W. Kempema, B. J. Thomson, and G. H. Leonard (2013), Anchor ice in polar oceans, *Prog. Phys. Geogr.*, *37*(4), 468–483, doi:10.1177/0309133313479815.
Mahoney, A. R., A. J. Gough, P. J. Langhorne, N. J. Robinson, C. L. Stevens, M. M. J. Williams, and T. G. Haskell (2011), The seasonal appearance of ice shelf water in coastal Antarctica and its effect on sea ice growth, *J. Geophys. Res.*, *116*, C11032, doi:10.1029/2011JC007060.
Massom, R. A., K. L. Hill, V. I. Lytle, A. P. Worby, M. Paget, and I. Allison (2001), Effects of regional fast-ice and iceberg distributions on the behaviour of the Mertz Glacier polynya, East Antarctica, *Ann. Glaciol.*, *33*, 391–398, doi:10.3189/172756401781818518.
McDougall, T., and P. Barker (2011), Getting started with TEOS-10 and the Gibbs Seawater (GSW) Oceanographic Toolbox, 28 pp., SCOR/IAPSO WG127.
McPhee, M., and N. Untersteiner (1982), Using sea ice to measure vertical heat flux in the ocean, *J. Geophys. Res.*, *87*(C3), 2071–2074, doi:10.1029/JC087iC03p02071.
Nicolaus, M., C. Katlein, J. Maslanik, and S. Hendricks (2012), Changes in Arctic sea ice result in increasing light transmittance and absorption, *Geophys. Res. Lett.*, *39*, L24501, doi:10.1029/2012GL053738.
Ohshima, K. I., T. Kawamura, T. Takizawa, S. Ushio, and T. Miyakawa (2000), Current variability under landfast sea ice in Lützow-Holm Bay, Antarctica, *J. Geophys. Res*, *105*(C7), 17,121–17,132, doi:10.1029/2000JC900080.
Parkinson, C. L., and D. J. Cavalieri (2012), Antarctic sea ice variability and trends, 1979–2010, *Cryosphere*, *6*, 871–880, doi:10.5194/tc-6-871-2012.
Paul, S., S. Willmes, M. Hoppmann, P. A. Hunkeler, G. Heinemann, M. Nicolaus, and R. Timmermann (2015), The impact of early summer snow properties on land-fast sea-ice X-band backscatter, *Ann. Glaciol.*, *56*(69), 263–273, doi:10.3189/2015AoG69A715, in press.
Perovich, D. K., and B. C. Elder (2001), Temporal evolution of Arctic sea-ice temperature, *Ann. Glaciol.*, *33*(1), 207–211.
Perovich, D. K., S. V. Nghiem, T. Markus, and A. Schweiger (2007), Seasonal evolution and interannual variability of the local solar energy absorbed by the Arctic sea iceocean system, *J. Geophys. Res.*, *112*, C03005, doi:10.1029/2006JC003558.
Perry, A. (1982), *Hot-Wire Anemometry*, Clarendon, Oxford, U. K.
Petrich, C., P. Langhorne, and Z. Sun (2006), Modelling the interrelationships between permeability, effective porosity and total porosity in sea ice, *Cold Reg. Sci. Technol.*, *44*(2), 131–144, doi:10.1016/j.coldregions.2005.10.001.
Pringle, D. J., H. Eicken, H. J. Trodahl, and L. G. E. Backstrom (2007), Thermal conductivity of landfast Antarctic and Arctic sea ice, *J. Geophys. Res.*, *112*, C04017, doi:10.1029/2006JC003641.
Purdie, C., P. J. Langhorne, G. Leonard, and T. Haskell (2006), Growth of first-year landfast Antarctic sea ice determined from winter temperature measurements, *Ann. Glaciol.*, *44*(1), 170–176, doi:10.3189/172756406781811853.
Riche, F., and M. Schneebeli (2013), Thermal conductivity of snow measured by three independent methods and anisotropy considerations, *Cryosphere*, *7*(1), 217–227, doi:10.5194/tc-7-217-2013.
Richter-Menge, J., D. K. Perovich, B. C. Elder, K. Claffey, I. Rigor, and M. Ortmeyer (2006), Ice mass-balance buoys: A tool for measuring and attributing changes in the thickness of the Arctic sea-ice cover, *Ann. Glaciol.*, *44*, 205–210, doi:10.3189/172756406781811727.
Robinson, N. J., M. J. M. Williams, C. L. Stevens, P. J. Langhorne, and T. G. Haskell (2014), Evolution of a supercooled Ice Shelf Water plume with an actively growing sub-ice platelet matrix, *J. Geophys. Res. Oceans*, *119*, 3425–3446, doi:10.1002/2013JC009399.
Semtner, A. J. (1976), A model for the thermodynamic growth of sea ice in numerical investigations of climate, *J. Phys. Oceanogr.*, *6*(3), 379–389, doi:10.1175/1520-0485(1976)006<0379:AMFTTG>2.0.CO;2.
Simpkins, G. R., L. M. Ciasto, D. W. J. Thompson, and M. H. England (2012), Seasonal relationships between large-scale climate variability and Antarctic sea ice concentration, *J. Clim.*, *25*(16), 5451–5469, doi:10.1175/JCLI-D-11-00367.1.
Smith, I. J., P. J. Langhorne, T. G. Haskell, H. J. Trodahl, R. Frew, and M. R. Vennell (2001), Platelet ice and the land-fast sea ice of McMurdo Sound, Antarctica, *Ann. Glaciol.*, *33*(1), 21–27, doi:10.3189/172756401781818365.
Smith, I. J., P. J. Langhorne, R. D. Frew, R. Vennell, and T. G. Haskell (2012), Sea ice growth rates near ice shelves, *Cold Reg. Sci. Technol.*, *8384*, 57–70, doi:10.1016/j.coldregions.2012.06.005.
Stammerjohn, S. E., D. G. Martinson, R. C. Smith, X. Yuan, and D. Rind (2008), Trends in Antarctic annual sea ice retreat and advance and their relation to El Niño Southern Oscillation and Southern Annular Mode variability, *J. Geophys. Res.*, *113*, C03S90, doi:10.1029/2007JC004269.
Sturm, M., and J. B. Johnson (1992), Thermal-conductivity measurements of depth hoar, *J. Geophys. Res.*, *97*(B2), 2129–2139, doi:10.1029/91JB02685.
Swart, N. C., and J. C. Fyfe (2013), The influence of recent Antarctic ice sheet retreat on simulated sea ice area trends, *Geophys. Res. Lett.*, *40*, 4328–4332, doi:10.1002/grl.50820.
Swingedouw, D., T. Fichefet, P. Huybrechts, H. Goosse, E. Driesschaert, and M. F. Loutre (2008), Antarctic ice-sheet melting provides negative feedbacks on future climate warming, *Geophys. Res. Lett.*, *35*, L17705, doi:10.1029/2008GL034410.
Tang, S. L., D. H. Qin, J. W. Ren, J. C. Kang, and Z. J. Li (2007), Structure, salinity and isotopic composition of multi-year landfast sea ice in Nella Fjord, Antarctica, *Cold Reg. Sci. Technol.*, *49*(2), 170–177, doi:10.1016/j.coldregions.2007.03.005.
Timco, G. W., and R. M. W. Frederking (1996), A review of sea ice density, *Cold Reg. Sci. Technol.*, *24*(1), 1–6, doi:10.1016/0165-232X(95)00007-X.
Tison, J. L., R. D. Lorrain, A. Bouzette, M. Dini, A. Bondesan, and M. StiéVenard (2013), Linking landfast sea ice variability to marine ice accretion at Hells Gate Ice Shelf, Ross Sea, in *Antarctic Sea Ice: Physical Processes, Interactions and Variability*, edited by M. O. Jeffries, AGU, Washington, D. C., doi:10.1029/AR074p0375.
Untersteiner, N. (1961), On the mass and heat budget of Arctic sea ice, *Arch. Meteorol. Geophys. Bioklimatol., Ser. A*, *12*(2), 151–182, doi:10.1007/BF02247491.
Uto, S., H. Shimoda, and S. Ushio (2006), Characteristics of sea-ice thickness and snow-depth distributions of the summer landfast ice in Lützow-Holm Bay, East Antarctica, *Ann. Glaciol.*, *44*(1), 281–287, doi:10.3189/172756406781811240.
Vacchi, M., M. Mesa, and S. Greco (2000), The Coastal Fish Fauna of Terra Nova Bay, Ross Sea, Antarctica, in *Ross Sea Ecology*, edited by F. M. Faranda, L. Guglielmo, and A. Ianora, chap. 32, pp. 457–468, Springer, Berlin, doi:10.1007/978-3-642-59607-0_32.
Vacchi, M., M. La Mesa, M. Dalu, and J. Macdonald (2004), Early life stages in the life cycle of Antarctic silverfish, *Pleuragramma antarcticum* in Terra Nova Bay, Ross Sea, *Antarct. Sci.*, *16*(3), 299–305, doi:10.1017/S0954102004002135.

Welschmeyer, N. A. (1994), Fluorometric analysis of chlorophyll-a in the presence of chlorophyll-b and pheopigments, *Limnol. Oceanogr.*, *39*(8), 1985–1992, doi:10.4319/lo.1994.39.8.1985.

Yen, Y.-C. (1981), Review of thermal properties of snow, ice and sea ice, technical report, U.S. Army Cold Reg. Res. and Eng. Lab., *81*(10), CRREL Report, 35 pp., Hanover, N. H.

Yen, Y.-C., K. C. Chen, and S. Fukusako (1991), Review of intrinsic thermophysical properties of snow, ice, sea ice, and frost, in *Proceedings of 3rd International Symposium on Cold Regions Heat Transfer, Fairbanks, AK.*, June 11–14, edited by J. P. Zarling and S. L. Fausett, pp. 187–218, Univ. of Alaska, Fairbanks.

Zhang, J. (2007), Increasing Antarctic sea ice under warming atmospheric and oceanic conditions, *J. Clim.*, *20*(11), 2515–2529, doi:10.1175/JCLI4136.1.

Zitterbart, D. P., et al. (2014), Are environmental factors responsible for changed breeding behaviour in emperor penguins?, *Antarct. Sci., FirstView*, *26*(5), 563–564, doi:10.1017/S0954102014000285.

D

Co-Author Paper 4

This paper was reprinted from the Annals of Glaciology with permission of the International Glaciological Society.

I contributed to this paper mainly with revision work, but also logistics in Atka Bay, similar to studies in Appendices B and C.

The impact of early-summer snow properties on Antarctic landfast sea-ice X-band backscatter

Stephan PAUL,[1] Sascha WILLMES,[1] Mario HOPPMANN,[2] Priska A. HUNKELER,[2] Christine WESCHE,[2] Marcel NICOLAUS,[2] Günther HEINEMANN,[1] Ralph TIMMERMANN[2]

[1]*Environmental Meteorology, University of Trier, Trier, Germany*
[2]*Alfred-Wegener-Institut Hemlholtz-Zentrum für Polar- und Meeresforschung, Bremerhaven, Germany*
Correspondence: Stephan Paul <paul@uni-trier.de>

ABSTRACT. Up to now, snow cover on Antarctic sea ice and its impact on radar backscatter, particularly after the onset of freeze/thaw processes, are not well understood. Here we present a combined analysis of in situ observations of snow properties from the landfast sea ice in Atka Bay, Antarctica, and high-resolution TerraSAR-X backscatter data, for the transition from austral spring (November 2012) to summer (January 2013). The physical changes in the seasonal snow cover during that time are reflected in the evolution of TerraSAR-X backscatter. We are able to explain 76–93% of the spatio-temporal variability of the TerraSAR-X backscatter signal with up to four snowpack parameters with a root-mean-squared error of 0.87–1.62 dB, using a simple multiple linear model. Over the complete study, and especially after the onset of early-melt processes and freeze/thaw cycles, the majority of variability in the backscatter is influenced by changes in snow/ice interface temperature, snow depth and top-layer grain size. This suggests it may be possible to retrieve snow physical properties over Antarctic sea ice from X-band SAR backscatter.

KEYWORDS: remote sensing, sea ice, snow, snow metamorphosis, snow physics

INTRODUCTION

Snow on sea ice is an important factor for the sea-ice mass and energy balance, due to its high albedo and low thermal conductivity (Yackel and Barber, 2007). Together with sea ice, snow plays a major role in modifying and influencing high-latitude atmospheric, oceanic and biogeophysical processes. Snow on sea ice accumulates and redistributes at different rates and shows a high spatio-temporal variability. However, the number of direct observations and measurements of snow is very limited for both polar regions (e.g. Barber and Thomas, 1998; Massom and others, 2001; Yackel and Barber, 2007). Understanding the relationship between snow properties (limited point measurements) and high-resolution spaceborne monitoring systems is desirable (Yackel and Barber, 2007).

As noted by Barber and Thomas (1998), interactions between the sea-ice snow cover and microwave radiation hold the potential for developing algorithms to estimate snow depth/snow-water equivalent, as well as snow physical properties over sea ice from satellite synthetic aperture radar (SAR) data. Snow affects the microwave interaction with sea ice through direct scattering based on the snow's physical properties (e.g. density, salinity, grain size and shape) and through thermodynamically controlled effects on the dielectric properties of the snow (e.g. its brine volume and wetness). Even a very shallow dry snow layer increases the backscatter from sea ice. However, additional dry snow does not further alter the received backscatter signal significantly (e.g. Kim and others, 1984; Barber and Thomas, 1998). This effect is linked to a higher ice-surface roughness and an increase in the dielectric contrast, which again is caused by brine wicking into the snow layer from the sea-ice surface (Kim and others, 1984).

The backscatter signal of sea ice in general is affected by two-way loss through the snow cover. If liquid water is present in the snowpack, both the real and the imaginary part of the dielectric constant increase, resulting in a higher signal loss. This makes the measured backscatter signal less sensitive to the underlying sea ice and boosts the surface- and volume-scattering contribution of the snowpack to the total signal (Kim and others, 1984; Barber and Thomas, 1998; Yackel and others, 2007).

Recent spaceborne SAR systems operate in different bands, at swath widths 30–500 km and at different spatial resolutions of 1–1000 m (Dierking, 2013). These systems are widely used for sea-ice monitoring and ice-type classification (e.g. Dierking, 2010, 2013; Eriksson and others, 2010), where the snow cover can generally be neglected in cold and dry conditions (e.g. Drinkwater and others, 1995; Dierking, 2013).

In the Arctic, several studies have investigated the relationship between snow physical properties and C-band SAR backscatter. Barber and Thomas (1998) investigated the general role of first-year sea-ice snow cover on microwave emission and scattering under laboratory conditions. Modelled and measured results suggest that, at 5 GHz, the volume-scattering contribution surpasses the surface-scattering contribution to the signal. This is reversed at 10 GHz, increasing the contribution of surface-scattering to the overall signal. The same study also found a strong influence of both snow-grain size and thermal effects on the microwave backscatter. Barber and Nghiem (1999) continued this work by further looking into the role of snow on the thermal dependence of sea-ice microwave backscatter. They highlighted the importance of the snow basal layer on the microwave backscatter and its controlling factors (e.g. snow/

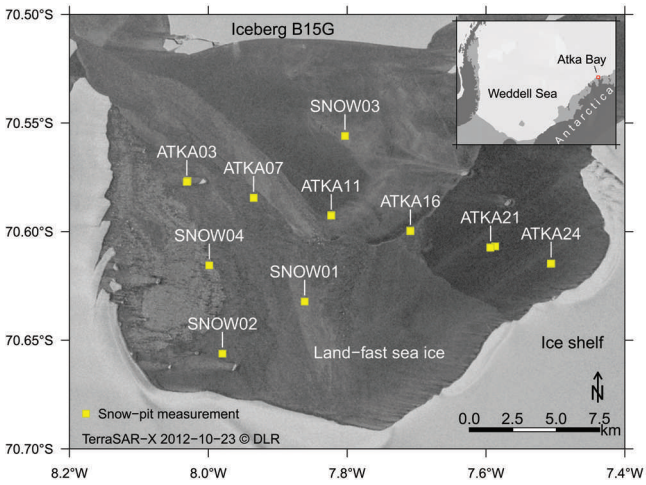

Fig. 1. Locations of all snow-pit measurements shown on a TerraSAR-X ScanSAR image of Atka Bay, Antarctica, 23 October 2012. Yellow squares mark the positions of all recorded snow pits. Both the main study sites (ATKA03–ATKA24) and additional snow pits (SNOW01–SNOW04) are shown. The inset shows the location of Atka Bay in the Weddell Sea region.

ice interface temperature, basal-layer grain size, ice-surface roughness and brine pockets within the sea-ice frazil layer).

The temporal evolution of European Remote-sensing Satellite (ERS) and RADARSAT C-band SAR backscatter time series was analysed by Barber (2005), in the context of sea-ice and snowpack evolution from freeze-up to melt. Yackel and others (2007) used RADARSAT data to detect changes in the snow water equivalent of the snow cover of first-year landfast ice. Yackel and Barber (2007) investigated the capabilities of C-band SAR to detect the onset of Arctic sea-ice melt in backscatter time series and the relationship between measured backscatter and snow albedo.

In the Antarctic, multiple studies have investigated the influence of snow cover on SAR backscatter, with a view to potentially retrieving snow properties over ice sheets (e.g. Kendra and others, 1998; Zahnen and others, 2003; Nagler and Rott, 2004; Dierking and others, 2012). However, few investigations concerned with the microwave signature of snow on sea ice have been conducted in the Antarctic, compared with the Arctic. Drinkwater and others (1995) investigated C-band backscatter of winter sea ice in the central Weddell Sea, where the dry snow cover can normally be neglected. Recent studies (e.g. Willmes and others, 2011) have examined the relation between Ku-band QuikSCAT scatterometer data and snow properties in high-backscatter pack-ice regions. Other studies investigated C-band SAR data and Ku-band scatterometer data for different regions in Antarctica (e.g. Worby and others, 2008; Kern and others, 2011; Ozsoy-Cicek and others, 2011). Nevertheless, further spatio-temporal high-resolution information about the snow on sea ice is required to validate satellite-derived data.

In this study, we present a combined analysis of in situ snow observations (physical/stratigraphic properties) and high-resolution TerraSAR-X (TSX) calibrated backscatter data (σ^0 (dB)), and their spatio-temporal evolution. Measurements originate from a field campaign on the landfast sea ice (fast ice) of Atka Bay, Antarctica, between November 2012 and January 2013. Atka Bay is a ~440 km^2 large embayment at the front of the Ekström Ice Shelf, Dronning Maud Land (Fig. 1) featuring a seasonal fast-ice cover. A more detailed description of the study area is given by Hoppmann and others (2015).

Compared to C-band SAR, X-band SAR is considered to be more sensitive to the snow cover, the upper subsurface ice layer and the onset of melt and freeze/thaw processes, due to its shorter wavelength (higher frequency) (e.g. Eriksson and others, 2010). We further present and discuss the interrelationship between TSX σ^0 data and coincident snow properties and evaluate the potential of X-band SAR backscatter to gather wider-scale information on physical and stratigraphic snow properties.

DATA AND METHODS

Field measurements

The meteorological data used here (Fig. 2) combine measurements recorded at the meteorological observatory of the German research station Neumayer III (50 m a.s.l.) and synoptic weather observations (König-Langlo, 2013a,b, c,d,e,f). While there are deficiencies due to local topography and elevation differences, the meteorological conditions at Atka Bay and Neumayer III are assumed to be comparable due to the general weather situation there. For example, Hoppmann and others (2015) found a general offset in 2 m air temperature of −1.05 K between the measurements at Neumayer III and Atka Bay.

In 2012, air temperatures increased to above the freezing point for the first time on 16 December (Fig. 2a). The onset of early melt is particularly important for our study because the existence of liquid water in the snowpack is expected to have a significant influence on the received radar signal (e.g. Yackel and Barber, 2007). The subsequent onset of freeze/thaw cycles leads to the formation of ice lenses and icy layers in the snowpack, as well as to the formation of superimposed (freshwater) ice, which is especially rich in air bubbles. These layers, in combination with the air bubbles, act as internal scatterers (Fierz and others, 2009; Willmes and others, 2011; Dierking, 2013).

Another important feature of our study is the occurrence of an 8 day storm event from 5 to 12 December 2012 (Fig. 2b). Sustained snowfall and redistribution occurred during this time, so no fieldwork was possible to monitor the snowpack changes. Other than the storm, we only recorded two single snowfall events during the entire study from 23 November 2012 to 7 January 2013. In general, easterly winds predominated (bringing higher wind speeds), which is in line with the long-term climatology for this region.

During the field campaign, we obtained snow physical property data from a total of 41 snow pits. Each comprised measurements of snowpack temperature and density gradients, 2 m air temperature and snow stratigraphy (i.e. grain-size distribution, snowpack layering and, mainly qualitative, estimates of snow liquid-water content, hardness and crystal type), following Fierz and others (2009). Our measurements focused on regular sampling sites along a ~25 km long west–east transect (ATKA03–ATKA24; Fig. 1), while additional snow-pit data were recorded sporadically at different locations on the Atka Bay fast ice (SNOW01–SNOW04; Fig. 1). The snow-pit locations were chosen to be representative of the surrounding area. Quantitative measurements of liquid-water content in the snowpack were possible only at the very end of our field campaign, due to the late arrival of the instrument.

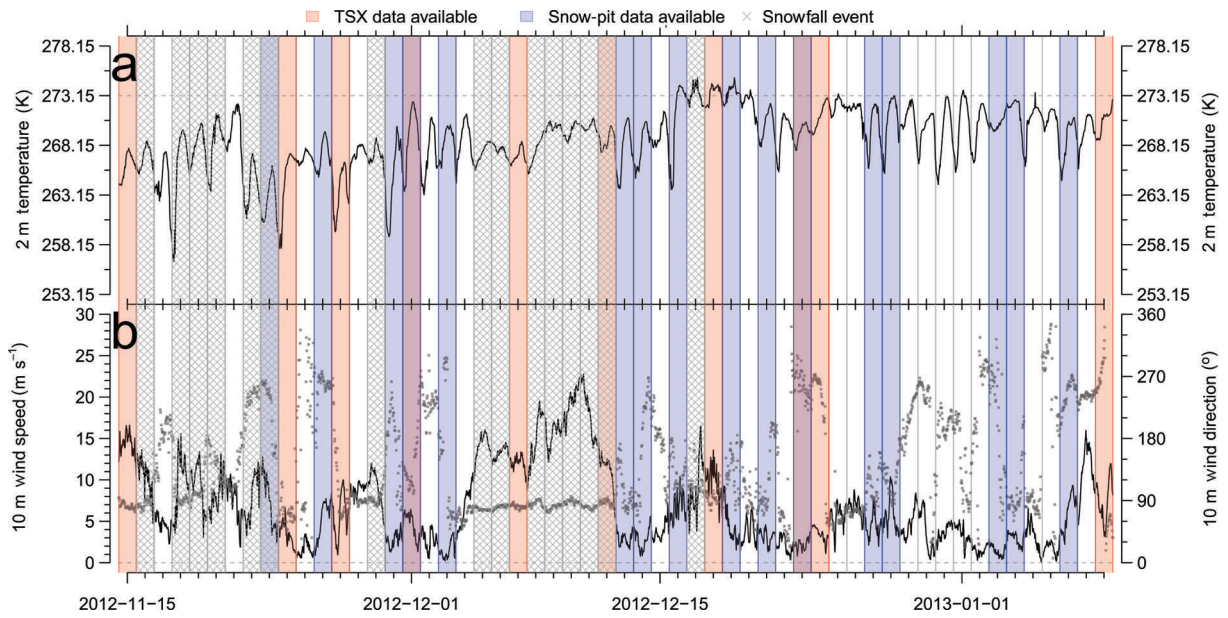

Fig. 2. Meteorological measurements of (a) 2 m air temperature and (b) 10 m wind speed (solid curve) and wind direction (dots). These datasets were recorded at Neumayer III station, ~8 km southwest of Atka Bay and are presented here as 30 min averages. Additionally, the red and blue bars indicate available TerraSAR-X swaths and snow-pit measurements acquired. Hatched areas mark days with snowfall events. Date format is yyyy-mm-dd.

We recorded snowpack temperature profiles using a penetration thermometer at a regular spacing. We also determined snow density of each layer by forcing a metal tube of known volume and weight into the snowpack, extracting it and measuring its weight in the field with a spring scale. Layers were distinguished by differences in grain size, crystal type, hardness and liquid-water content. Grain size and snow crystal type were determined visually using a magnifying glass, following Fierz and others (2009). Snow hardness was estimated by resistance to penetration (Fierz and others, 2009). Liquid-water content was categorized into 'dry' and 'not dry' by visual observation and manual probing, following Fierz and others (2009). Quantitative estimates of snow liquid-water content were recorded using a snow fork (Sihvola and Tiuri, 1986), but this was only possible at the very end of our field campaign, due to the late arrival of the instrument.

Snow conditions at Atka Bay in 2012 are briefly summarized here (they are discussed in more detail by Hoppmann and others, 2015). ATKA03 featured no consistent snow cover, due to its location ~2 km to the east of a grounded iceberg. The snow pits near ATKA03 therefore largely represent records from snow banks and larger snow patches. While icebergs shelter their leeward area from snow accumulation, ridges and icebergs increase the snow accumulation in their close windward proximity, leading to locally thicker snow and a more heterogeneous snowpack stratigraphy. This influenced the snow-pit records of ATKA07 and ATKA16. Additionally, ATKA16 was influenced by surface flooding by sea water. In a similar fashion to icebergs, the ice-shelf edge prevents large snow accumulations on its leeward side. This is considered to be the primary reason for the small snow depths but relative homogeneity in the snow cover at ATKA24. Due to the earlier breakout of sea ice at ATKA11 (Hoppmann and others, 2015), the ice as well as the snow cover was rather thin and influenced by flooding and refreezing over the course of the field campaign. ATKA21 exhibited a consistent but thicker snowpack than ATKA24.

The ice surface roughness is also a major factor influencing radar backscatter, depending on the horizontal roughness scale compared to the SAR wavelength. On sea ice with a surface roughness of comparable scale to the SAR wavelength, specular reflection leads to relatively low backscatter (Dierking, 2013). This circumstance was characteristic for the ice surface underlying the snow pits at ATKA11, ATKA16, ATKA21, ATKA24 and SNOW02. In the other pits, the ice surface was found to be rough compared to the X-band SAR wavelength.

The number of records in each snow pit varies with snow depth (i.e. more data points in deeper pits), existence of ice lenses/layers (e.g. it is difficult to measure the density in a layer of pure ice), number of layers, etc. Moreover, the snow-pit measurements comprise numerical (e.g. grain size, temperature profiles, snow depth, liquid-water content) and more qualitative values (e.g. hardness, liquid-water content, crystal type) of different nature. Consequently, difficulties arise when comparing measurements between snow pits and also when comparing them to the satellite observations. Hence, we derived several numerical snowpack parameters from our measurements (Fig. 3) in order to explain the variations in TSX σ^0. These parameters include the snow thickness, z_{snow} (m), the quantitative measurements of bulk liquid-water content in the snowpack from snow fork measurements, LWC (vol.%), the snowpack temperature gradient, $\partial T/\partial z$, not shown (K m^{-1}), 2 m air temperature, T_a, snow-surface temperature, T_s, and snow/ice interface temperature, T_i (K), the number of different layers, n_{lay}, the number of ice layers, n_{ice}, the number of layers containing liquid water, n_{lwc}, the grain size of the top/bottom layers, E_{top}/E_{bot} (m), the average snowpack grain size, $\overline{E}$, and the weighted-average snowpack grain size, $\overline{E}_w$ (m). The latter takes the different layer thicknesses into account. Due to the

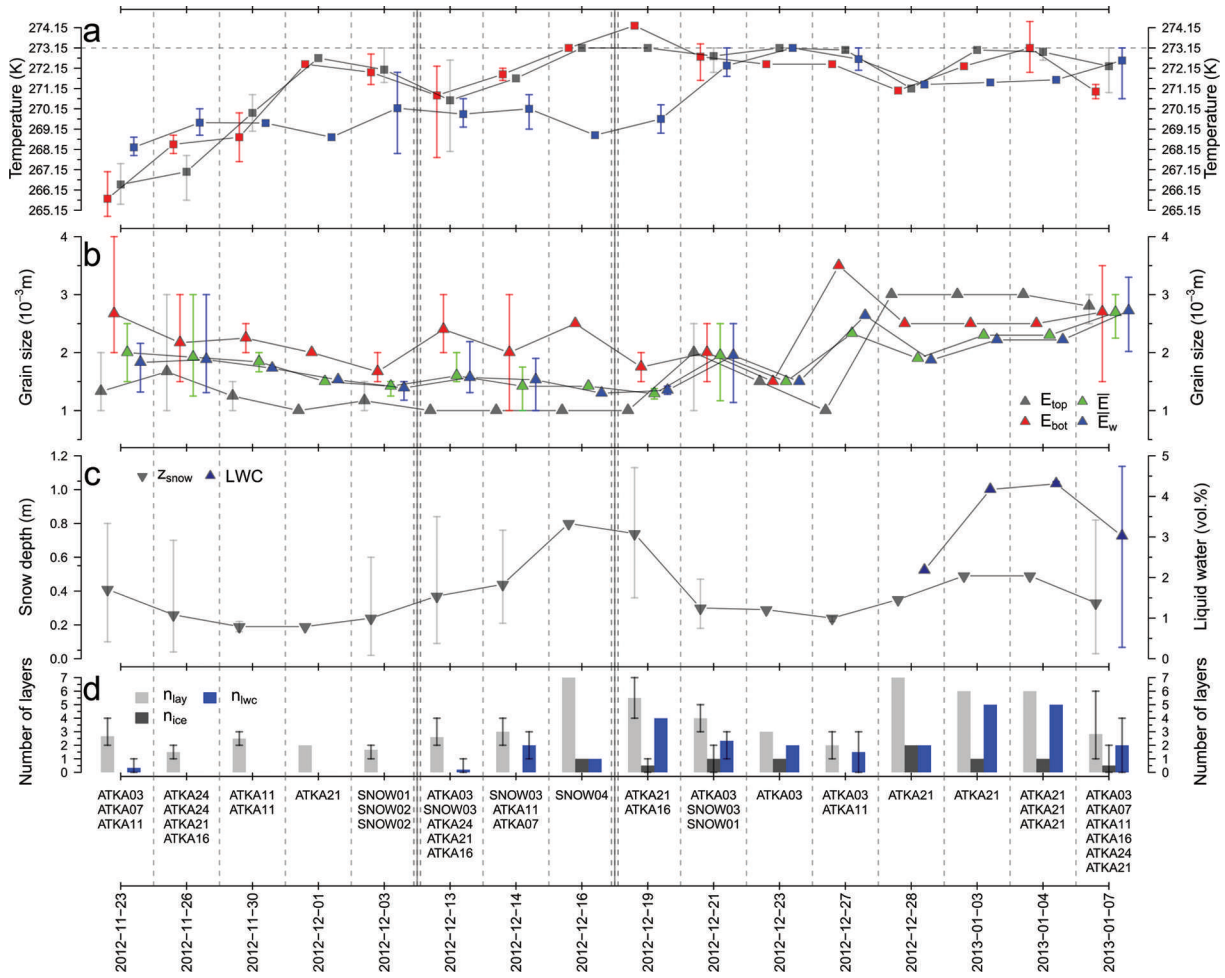

Fig. 3. Time series of daily averaged snowpack parameters. (a) 2 m air temperature measured at the snow-pit location (T_a, red squares), the snow-surface temperature (T_s, grey squares) and the snow/ice interface temperature (T_i, blue squares). (b) Top-/bottom-layer grain size (E_{top} and E_{bot}, grey/red triangles) and average/weighted-average snowpack grain size ($\overline{E}$ and $\overline{E}_w$, green/blue triangles). (c) Snow depth (z_{snow}, grey triangles) and the liquid-water content (LWC, blue triangles). (d) The numbers of layers in the snowpack (n_{lay}, light grey), ice layers (n_{ice}, dark grey) and layers containing liquid water (n_{lwc}, blue). Error bars indicate minimum/maximum values on days with several measurements. The corresponding measurement sites are shown under the bars (Fig. 1). The highlighted vertical double-dashed lines indicate large snowfall events between measurements. The *x*-axis spacing is not to scale, but distorted. Date format is yyyy-mm-dd.

frequent large wind-slab layers in the snowpacks, we felt the need to account for their very small grain sizes in an average snow grain-size parameter. However, the effects on σ^0 are small, as shown below.

For clarification, E_{bot} gives the grain size of the lowest layer in the snowpack that is still snow, i.e. E_{bot} potentially states values several cm above the snow/ice interface. This was necessary due to the frequent presence of ice layers in the bottommost part of the snowpack, which do not yield any grain-size information. This happened especially during the later stages of the field campaign. The density measurements (not shown) were used to calculate the bulk snow-water equivalent (SWE, not shown) for each snow pit, but were otherwise omitted from all calculations, due to the limited number of measurements per pit and their low vertical resolution. The course of SWE is naturally very similar to that of z_{snow} and is therefore not shown.

Due to logistical constraints, we were not able to collect snow samples to estimate snowpack salinity for all snow-pit measurements. Salinity is, however, a crucial parameter in determining σ^0, due to its influence on the dielectric properties of snow and sea ice and its impact on the penetration depth. This shortcoming represents an obstacle for the interpretation of temporal backscatter changes. Dierking (2013) states a typical penetration depth of 0.03–0.15 m for X-band SAR on first-year sea ice under dry snow conditions. Barber and others (1995) showed that the snow/ice interface temperature influences the brine volume fraction. This rise in brine volume fraction leads to an increase in the dielectric constant in the sea-ice surface, which again increases σ^0. However, the snow basal layer is also likely to have high salinity values (Massom and others, 2001), which might mask out underlying changes in the sea ice, especially after the onset of freeze/thaw cycles and in the presence of liquid water (Yackel and others, 2007).

Similar to the records of 2 m air temperature (Fig. 2a), the averaged snowpack temperature values (Fig. 3a) of all snow-pit measurements acquired on a given day increased towards the freezing point, and T_a as well as T_s reached this as early as 16 December 2012. Because of this, we considered all measurements after 16 December 2012 as being after the onset of early freeze/thaw processes.

Satellite measurements

TerraSAR-X is a spaceborne side-looking X-band SAR instrument run by the German Aerospace Center (DLR).

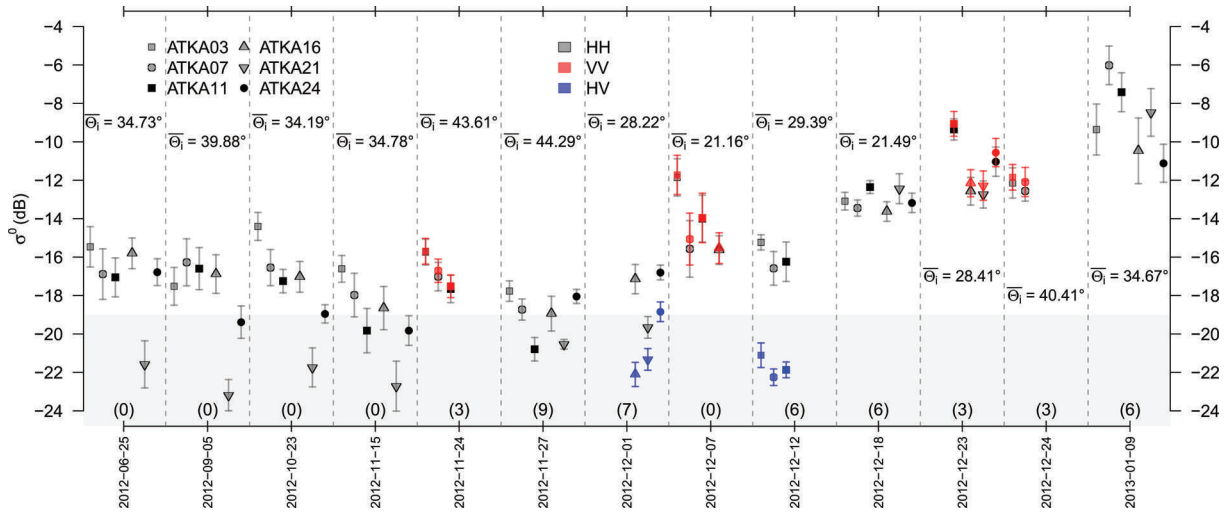

Fig. 4. Temporal evolution of the TSX backscatter (σ^0) for all available TSX swaths and polarizations (HH = black, VV = red, HV = blue). Shown is the average σ^0 for a 5 pixel × 5 pixel raster of each main study site (different symbols). Error bars indicate two standard deviations. Due to the smaller spatial coverage of the TSX StripMap mode, not all ATKA03–ATKA24 sites are covered by each swath. Additionally, the mean local incidence angle, $\overline{\Theta_i}$, is shown and the number of matched snow-pit measurements is given in parentheses (including match-ups with system-noise-influenced σ^0 values). Values influenced by the system noise, i.e. the noise-equivalent sigma zero (NESZ), are highlighted by the grey area at the bottom. Date format is yyyy-mm-dd.

The satellite has been operational since June 2007 in a polar orbit at 514 km altitude and can operate in four different imaging modes. Relevant to this study are the ScanSAR mode (SC) in single polarization and StripMap mode (SM) in single and dual polarization, due to their capability to sufficiently cover Atka Bay. The swath width changes with mode and polarization. In ScanSAR mode, a swath covers a ground area of $150 \times 100\,\mathrm{km}^2$. In StripMap mode, the coverage changes to $50 \times 30\,\mathrm{km}^2$ ($50 \times 15\,\mathrm{km}^2$) in single (dual) polarization mode (Fritz and Eineder, 2008).

A total of 13 TerraSAR-X swaths were obtained before and during the field campaign (Table 1). Five scenes were recorded in single HH-polarization SC mode, while four scenes were acquired in dual-polarization SM mode in HH/VV configuration and two in HH/HV. Additionally, two scenes were acquired in single HH-polarization SM mode. All TSX scenes were radiometrically calibrated using a commercial software package (SARscape) and georeferenced on a common pixel size of 25 m. Due to increasing pixel size by multi-looking, the effect of speckle was reduced. The equivalent number of looks (ENL) increased by the grade of multi-looking, which depends on the initial pixel size (e.g. SC: 18.5 m; SM dual: 6.6 m; and SM single: 3.3 m (Table 1)). It is important to note that the noise-equivalent sigma zero (NESZ) level is −19 dB. All pixel values below the NESZ are influenced by system noise and were excluded from further investigation as a precaution (Fig. 4).

Due to logistical constraints, the number of snow-pit measurements directly matching a coincident TSX swath is very low (Fig. 2). Unfortunately, the two temporal matches between snow-pit measurements and TSX acquisitions could not be incorporated into our analysis. The respective

Table 1. Overview of TSX data, including initial acquisition resolution, swath coverage and minimum/maximum local incidence angles (LIA). SC/SM indicate the TerraSAR-X acquisition mode of ScanSAR/StripMap. HH/VV/HV indicate the polarization as a combination of transmitted and received signal. Start and end time give the time of acquisition in UTC of each TSX swath. Also shown are the number of snow-pit measurements assigned to each TSX swath

Date	Mode	Polarization	Initial resolution	Coverage	Minimum LIA	Maximum LIA	Start time	End time	Snow pits
dd/mm/yy			m	km²	°	°			
25/06/2012	SC	HH	18.5	150 × 100	33.18	36.55	04:23:44	04:24:06	0
05/09/2012	SC	HH	18.5	150 × 100	38.47	41.56	04:15:10	04:15:32	0
23/10/2012	SC	HH	18.5	150 × 100	31.84	35.60	20:38:12	20:38:34	0
15/11/2012	SC	HH	18.5	150 × 100	33.23	36.60	04:23:46	04:23:58	0
24/11/2012	SC	HH	18.5	150 × 100	33.20	36.26	04:23:41	04:24:00	3
27/11/2012	SM	HH/VV	6.6	50 × 15	42.63	45.03	20:55:20	20:55:28	9
01/12/2012	SM	HH	3.3	50 × 30	43.42	45.94	04:06:47	04:06:55	7
07/12/2012	SM	HH/HV	6.6	50 × 15	27.42	29.51	04:32:20	04:32:28	0
12/12/2012	SM	HH/VV	6.6	50 × 15	19.85	21.95	20:21:14	20:21:22	6
18/12/2012	SM	HH/HV	6.6	50 × 15	28.43	30.85	04:32:19	04:32:27	6
23/12/2012	SM	HH	3.3	50 × 30	19.84	23.13	20:21:13	20:21:21	3
24/12/2012	SM	HH/VV	6.6	50 × 15	27.43	29.55	04:32:18	04:32:26	3
09/01/2013	SM	HH/VV	6.6	50 × 15	39.62	41.58	04:15:17	04:15:25	6

TSX σ^0 value of the first coincident match was influenced by system noise, while the second snow pit fell outside the TSX StripMap image. We chose to extract the average TSX backscatter values, σ^0, of a 5 pixel $\times$ 5 pixel raster (i.e. $125 \times 125\,m^2$), along with its standard deviation at the position of each snow-pit measurement. To link as many snow-pit measurements as possible to the TSX backscatter extracts, we used the TSX data from all available swaths in a $\pm$5 day range of each snow-pit measurement. By doing so, we were able to match at least one TSX σ^0 record with one of our snow-pit measurements, despite differences in spatial coverage of each TSX swath.

While this approach is not ideal given the synoptic-scale atmospheric changes that can influence the snowpack during a 5 day window, we tried to reduce the influence of known meteorological events. Following the lack of observational snow data during the storm, we excluded the TSX swath of 7 December 2012 from our analysis. Also we did not match snow-pit measurements recorded before the second snowfall event on 17 December 2012 with TSX swaths acquired after that snowfall event (Figs 2 and 3). This left us with 35 match-ups, excluding those with system-noise-influenced σ^0 values. The majority of these data pairs (22) show a maximum temporal difference of 2 days. Five cases each have a time lag of 3 or 4 days, and three cases a time lag of 5 days.

In the following, we explore information regarding resolution, coverage, acquisition time and local incidence angle of the TSX data (Table 1). In order to account for the wide range of local incidence angles (LIAs) covered by the TSX swaths (Table 1), we divided our dataset into three different LIA classes (LIA1: LIA > 36°; LIA2: 36° $\geq$ LIA > 27°; and LIA3: LIA < 27°), so as to review similar TSX swaths together. We chose this approach in order to examine the potential influences on the TSX σ^0 signal of different snowpack parameters on different LIAs. Due to the bipolar temporal distribution of the TSX swaths by means of acquisition time (early morning/late evening), no further steps were taken to account for diurnal variations in the signal.

Correlation coefficients were calculated to analyse relationships between individual snowpack parameters and corresponding TSX σ^0 values. In addition, simple linear regression models were fitted to the σ^0 values and snowpack parameter groups to investigate the power and significance of the correlation, as well as the significance of the explained σ^0 variance. Finally, we fitted a simple multiple linear regression model to our different datasets, to investigate its potential for maximizing the explained σ^0 variance with a minimum of snowpack parameters per LIA class. Due to the limited number of matched snow-pit and TSX-swath measurements, the focus lies on the extracted HH-like polarization TSX backscatter data, hereafter named σ^0_{HH}.

RESULTS AND DISCUSSION

Spatio-temporal snowpack changes

Because of the irregular temporal coverage of measurements at the different study sites and the different initial snowpack situation at each study site, further investigation of the various datasets (Fig. 3) is required. The observations taken on 23 and 26 November 2012 represent the late-winter setting of a still relatively cold environment (Figs 2a and 3a). At this stage, at all main study sites (ATKA03–ATKA24) measurements were taken once, with ATKA07/16 at the upper end of the spectrum with regard to snow depth, number of layers and bottom-layer grain sizes and ATKA11/24 at the lower end.

Proceeding in time, a general increase in surface temperature, T_s, and air temperature, T_a, was noticeable. However, the snow/ice interface temperature, T_i, remained fairly constant, only varying with snow depth (Fig. 3a and c). On 16 December 2012, temperature measurements of T_a above the freezing point and T_s at the freezing point were recorded, followed by an increase in T_i. This led to near-isothermal snow conditions.

Between the initial conditions on 23/26 November 2012 and the end conditions on 7 January 2013, when coincident sampling at all main study sites took place again, an average increase and vertical equalization of the grain-size parameters occurred (Fig. 3b). This was driven by the equi-temperature metamorphism processes in the snowpack (Fierz and others, 2009). Furthermore, our few direct measurements of liquid-water content covered the whole spectrum between 1 and 5 vol.% on 7 January 2013. Such a range is expected to significantly affect the received backscatter signal (e.g. Yackel and Barber, 2007). In general, liquid water was found throughout the snow column (Fig. 3d), with the exceptions of 23 November 2012 and 13 December 2012, when flooded slush layers occurred at the snowpack base (ATKA11 and ATKA16).

Following the onset of freeze/thaw cycles and early melt, the degree of snowpack stratification increased, with an increase in the number of layers in general and in ice layers (Fig. 3d). Note that average values are shown, which might lead to the false impression that the degree of stratification falls off again at the end of the field campaign.

Spatio-temporal backscatter variations

Analysing the spatio-temporal variations of the TSX backscatter (σ^0; Fig. 4), one needs to consider that not all study sites were covered in each swath (Table 1). We consider the HH-polarization data (Fig. 4, black) in SC and SM modes as well as the VV-polarization data (red) and the HV cross-polarization data (blue) in SM mode. Observed differences between the measurements at both HH and VV polarization are fairly small, while cross-polarization yields generally lower backscatter values. However, variations between the study sites can be large.

In the extracted TSX backscatter values of the first four swaths, there was an increasing spread in σ^0 between the different study sites, in addition to a steady overall decrease in σ^0. In particular, ATKA21 peaks compared with the other study sites, despite differences in σ^0 due to different average LIA, $\overline{\Theta_i}$. It should be added that the very low values of σ^0 for the first few swaths are very close to or below the noise floor of TSX, which starts influencing the received signal below a threshold of -19 dB (worst case)/-22 dB (normal) as stated by Fritz and Eineder (2008). However, the TSX data used in the later analyses were generally well above this noise floor and are unlikely to have been affected by it.

The X-band SAR microwave radiation did not significantly interact with the present dry snowpack in the early TSX swaths; this is consistent with the observations of Dierking (2013) and Drinkwater and others (1995). The spatial differences (Fig. 4) for the first four swaths are primarily linked to localized growth conditions during sea-ice formation and differing sea-ice compositions (salinity, proportion

of incorporated frazil ice, columnar ice and platelet ice) which each affect the X-band SAR microwave radiation in a different way (e.g. Dierking, 2013). The small decrease in σ^0 over time (on average ~2 dB) is probably due to a decrease in brine volume fraction in the snow-basal layer, as well as the ice-surface layer, due to low winter temperatures and still increasing ice thickness, which decreases the dielectric constant. This was noted for C-band SAR time series (e.g. Yackel and Barber, 2007) and also seems applicable for X-band SAR data. However, our data are not sufficient to assess this quantitatively. The comparably high σ^0 values on 24 November 2012, despite the large local incidence angle, might be correlated to the increase in temperature around 20/21 November 2012 and the subsequent drop in temperature by ~10 K (Fig. 2a). Unfortunately, there are no in situ temperature observations to verify this.

Hoppmann and others (2015) discuss the different types of sea ice at Atka Bay and their structures. Their description of the primary ice-formation processes can be linked to the σ^0 signals (Figs 1 and 4) before the onset of melt and freeze/thaw cycles. In areas where dynamical-growth processes dominated, σ^0 is generally higher (e.g. the area around ATKA03/07). This results from the presence of pressure ridges that increase the surface scattering of the X-band radiation (Eriksson and others, 2010). The highest signal is returned from the area of second-year sea ice close to the western ice-shelf edge. Here volume scattering is increased by air bubble inclusions, as well as surface scattering by the overall deformed structure of the ice. This adds up to a higher overall signal. An area of thermodynamic growth (ATKA21/24) generally has level ice with lower backscatter values (e.g. Dierking, 2013).

Across all incidence angles, there is an increase in σ^0 over the field study. For LIA of 34–35°, there is an average increase of 10–12 dB in σ^0 for all ATKA stations between 15 November 2012 and 9 January 2013. A similar, but smaller, increase was found for swaths with an average LIA of ~29°. However, considerable spatial variability was evident, with ATKA11 exhibiting the highest variability.

The high σ^0 values in the 9 January 2013 swath very likely originate from several freeze/thaw cycles, especially between 31 December 2012 and 5 January 2013 (Fig. 2a). These potentially increased the amount of volume scattering, through the formation of ice layers and an increase in grain sizes (Willmes and others, 2011). A steady increase in snow surface and snow/ice interface temperature and grain enlargement is seen in our measurements (Fig. 3a and b). Also, more stratification and an increased number of ice layers occur after the onset of freeze/thaw processes. All this potentially raises the returned backscatter. Nothing can be said about LIA3, due to the limited number of swaths and measurements taken in this LIA class.

The general increase in σ^0 can be attributed to significant volume scattering by the snow basal-layer grains at ~1–3 vol.% of liquid water. With increasing liquid-water content, surface scattering further contributes to the overall signal (Barber and others, 1994; Barber, 2005).

Relationship between backscatter and snowpack characteristics

Here we correlate σ^0_{HH} and the previously discussed snowpack parameters (Table 2; only significant correlations are shown). The statistical parameters include the correlation coefficient, R, the stability index, R^2, stating the explained variance, the p-value of the calculated f-test, p, stating the level of significance of the regression, and the sample size, n, as well as the statistical power. Power gives the probability that the H_0 hypothesis is rejected (i.e. there is no correlation), where H_0 is truly false (Cohen, 1988).

Table 2. Summary of statistical parameters explaining the relationship between TSX backscatter σ^0_{HH} and snowpack parameters (only parameters with significant correlations are shown, $\alpha = 0.95$). Presented are the correlation coefficient, R, the stability index, R^2, the p-value of the calculated f-test, p, the sample size, n, and the statistical power. The results are shown per LIA class and data subset, where ALL equals all measurements per LIA class, SDS indicates a snow data subset of sites with $z_{snow} < 0.6$ m and EMO corresponds to measurements after the onset of early melt

		Subset	R	R^2	p	n	Power
LIA1							
σ^0_{HH}	T_a	ALL	0.843	0.711	0.002	10	0.906
σ^0_{HH}	T_s	ALL	0.895	0.801	<0.001	10	0.971
σ^0_{HH}	T_i	ALL	0.859	0.738	0.001	10	0.930
σ^0_{HH}	T_a	SDS	0.831	0.691	0.011	8	0.763
σ^0_{HH}	T_s	SDS	0.890	0.792	0.003	8	0.892
σ^0_{HH}	T_i	SDS	0.845	0.714	0.008	8	0.794
σ^0_{HH}	SWE	SDS	0.716	0.513	0.046	8	0.517
σ^0_{HH}	n_{lay}	SDS	0.889	0.790	0.003	8	0.890
LIA2							
σ^0_{HH}	T_s	ALL	0.506	0.256	0.023	20	0.632
σ^0_{HH}	T_i	ALL	0.771	0.594	<0.001	20	0.989
σ^0_{HH}	E_{top}	ALL	0.677	0.458	0.001	20	0.927
σ^0_{HH}	$\overline{E}$	ALL	0.504	0.254	0.023	20	0.628
σ^0_{HH}	$\overline{E}_w$	ALL	0.493	0.243	0.027	20	0.605
σ^0_{HH}	T_i	EMO	0.760	0.577	0.011	10	0.753
σ^0_{HH}	E_{top}	EMO	0.847	0.717	0.002	10	0.913
σ^0_{HH}	$\overline{E}$	EMO	0.772	0.596	0.009	10	0.777
σ^0_{HH}	T_s	SDS	0.620	0.385	0.014	15	0.711
σ^0_{HH}	T_i	SDS	0.881	0.776	<0.001	15	0.998
σ^0_{HH}	E_{top}	SDS	0.665	0.442	0.007	15	0.796

The results of Table 2 indicate a rather moderate dependency of observed σ^0_{HH} on the chosen snowpack parameters. However, there is a recurring set of snowpack parameters showing significant correlations to different degrees for all LIA classes and most data subsets. However, the rather low-to-moderate correlation coefficients and stability indices, as well as the low power values, have to be considered and are constrained by the small sample size. For LIA3, there were not enough samples to conduct meaningful calculations.

After visual screening and simple linear model iterations to find the best fit, we found that subsetting the dataset to measurements taken on snowpacks with a maximum depth of 0.60 m reveals a significantly higher correlation between z_{snow} and σ^0_{HH} for all LIA classes (Fig. 5). While 0.60 m of snow is rather thick for Antarctic sea ice, 8 out of 35 of our snow-pit measurements featured a snow depth exceeding this threshold, while still being representative for their general area. However, these correlations are not necessarily significant (Table 2), given a level of significance (α) of 0.95, but exclusion of our very deep snow-pit measurements is likely to influence the correlations of other snowpack parameters to σ^0_{HH} (e.g. the snow/ice-surface temperature due to the X-band signal penetration depth (Table 2)).

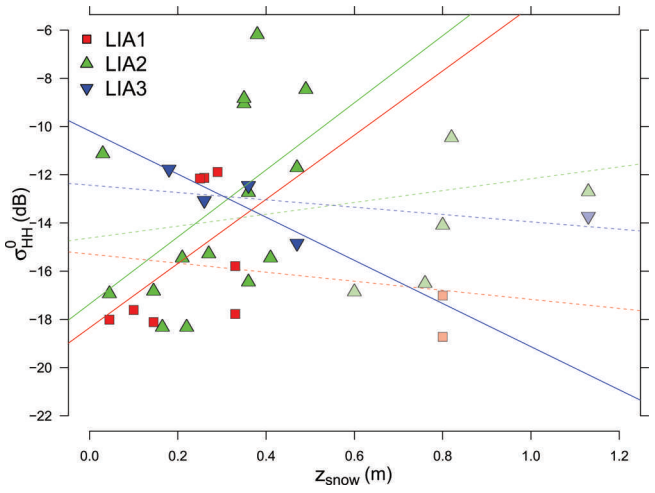

Fig. 5. Scatter plot of snow depth (z_{snow}) against TSX HH backscatter (σ^0_{HH}). Shown are the snow depths and their corresponding local incidence angle (LIA) class-based σ^0_{HH} values. Value pairs above/below the 0.6 m threshold are plotted transparent/solid. The corresponding regression lines are shown, where solid lines correspond to the value pairs with $z_{snow} < 0.6$ m and dashed lines are for the complete dataset.

Neglecting the scatter loss, we calculated the theoretical penetration depths from the bulk dielectric constant for a range of bulk snow liquid-water content and bulk snow densities from our measurements, by solely considering the absorption loss. This was done using the governing equations for wet snow provided by Hallikainen and Winebrenner (1992). A liquid-water content of 0.35–0.5 vol.%, for example, led to a penetration depth at TSX X-band of 0.4–0.75 m. This might explain the increase in correlation between σ^0_{HH} and, especially, T_i. At a snow liquid-water content of 1–3 vol.%, the theoretical penetration depth decreases to 0.05–0.20 m. However, given the temperature records (Fig. 2a), the high values of liquid water within the snow are likely to be snapshots of a constantly changing snowpack, due to thaw/refreeze cycling.

The overall most reliable results were found for the LIA2 class (Table 2), i.e. LIA 36–27°, where sufficient sample size corresponds to the high statistical power of the significant correlations. Snow/ice interface temperature, T_i, and top-layer grain size, E_{top}, showed significant correlation coefficients ($p < 0.01$) with high power values close to 1. This implies (with high confidence) that the results are not based on random noise. These numbers change slightly, depending on the subset used. Limiting ourselves to measurements with snow depths of <0.6 m (SDS), the correlation coefficient and stability index for the snow/ice interface temperature, T_i, increase, probably due to their capturing the penetration depth of X-band radar. For greater snow depths, the ice/snow interface becomes invisible, due to the limited penetration depth of X-band radar (Yackel and Barber, 2007).

We chose an approach to evaluate the amount of variance in our TSX σ^0_{HH} that can be explained by the snowpack parameters, by using a simple multiple linear model. Each model estimate started with all the snowpack parameters as input. Using stepwise regression modelling, the parameter with the highest p-value (i.e. the least significant contribution to the overall explained variance, R^2, was removed from the model at each iteration. After several iterations, a significant model fit was achieved in most cases. The iteration stopped when, in a subsequent step, the overall explained variance dropped significantly and the model significance decreased. However, no significant model fits could be found for some LIA classes and data subsets, due to the limited sample size (especially for the LIA3 class).

Table 3. Different model fits to the TSX backscatter σ^0_{HH} data. Presented are the sample size, n, the p-value of the calculated f-test, p, the adjusted stability index, R^2_{adj}, that shows the explained variance adjusted for the different amount of predictors, and the predictors of σ^0. Also shown is the root-mean-squared error of the cross validation (dB; RMSE). Model fits are identified by tags based on the LIA and data limitations, where SDS stands for snow-depth subset and EMO means early-melt onset

Model fit	n	p	R^2_{adj}	Predictors	RMSE
LIA1	10	0.002	0.7595	z_{snow}, SWE	1.50
LIA2	20	<0.001	0.8421	z_{snow}, T_i, E_{top}	1.56
LIA3	5			no model fit found	
LIA1SDS	8	0.007	0.9158	T_i, SWE	1.00
LIA2SDS	15	<0.001	0.8584	z_{snow}, T_i, E_{top}	1.62
LIA3SDS	4			no model fit found	
LIA1EMO	3			no model fit found	
LIA2EMO	10	<0.001	0.9323	T_s, T_i, E_{top}, $\overline{E}$	0.87
LIA3EMO	5			no model fit found	

The model name tags (Table 3) correspond to the underlying data subsets (e.g. limited to measurement sites with $z_{snow} < 0.6$ m (SDS) or after the onset of early-melt processes on 16 December 2012 (EMO)). Table 3 also shows the sample size, n, the p-value of the calculated f-test, p, and the stability index, R^2_{adj}. The latter is corrected (adjusted) for the different amount of predictors which can lead to an increased general stability index, R^2. All model fits are significant and explain 76–93% (R^2_{adj}) of their representative observed σ^0_{HH} variance.

To evaluate the quality of our model fits we chose a cross-validation approach, due to the limited sample size. Here the model was set up with the significant predictors calculated from the complete sample size, n, but based on a sample size of $n - 1$. Iteratively, each member of the initial sample was excluded from the set-up, and was instead calculated by the model. The root-mean-squared error (RMSE) between the modelled and observed σ^0_{HH} values was then calculated. The results (Table 3) vary between 0.87 and 1.62 dB (LIA2EMO and LIA2SDS, respectively). These compare favourably with the absolute/relative radiometric accuracy of the TSX sensor (0.6/0.3 dB; Fritz and Eineder, 2008). However, the quite high stability indices of >90% were achieved on very small datasets with a comparably large number of predictors.

During the cross validation, it became clear that the σ^0_{HH} signatures of certain snow-pit measurements are more difficult to derive from the various model fits using different predictor set-ups, i.e. excluding those snow-pit measurements drastically decreased the RMSE, compared with the RMSE changes of the remaining iterations. An example is ATKA11. We attribute this to the recurrent surface flooding and refreezing that occurred during the course of our field campaign, which cannot be explained sufficiently with the snowpack parameters used here.

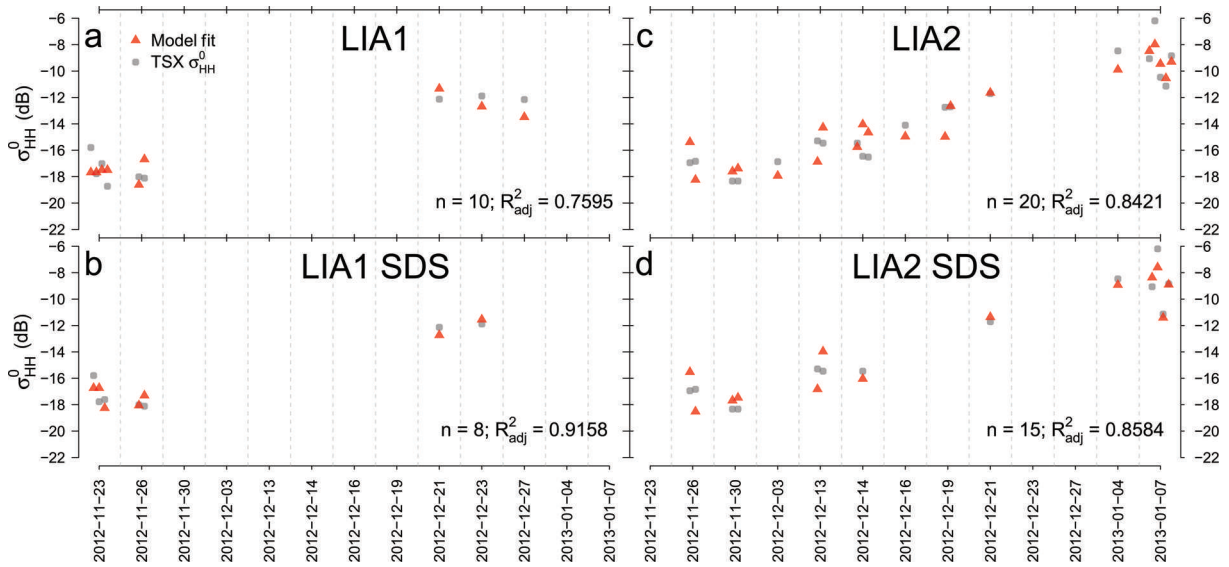

Fig. 6. Four different multiple linear model fits (a–d) (red triangles) to the extracted σ^0_{HH} values from all available snow-pit measurements in a ±5 day range (grey dots). (a) Based on all available snow-pit measurements for LIA1. (b) Limited to snow-pit measurements with $z_{snow} < 0.6$ m for LIA1. (c, d) the same set-ups as (a, b) for LIA2. All model fits are significant ($\alpha < 0.001$) and explain 76–91% (R^2_{adj}) of the total variance of σ^0_{HH}. Date format is yyyy-mm-dd.

The significant snow parameters (Table 2) also appear as model predictors in Table 3. Furthermore, the snow depth and snow water equivalent are significant contributors to the overall variance, despite showing non-significant correlations with σ^0_{HH} by themselves. While there are definitive internal correlations (e.g. between z_{snow} and SWE, or the temperature parameters), they are not interchangeable without a large drop in the stability indices.

Four representative model fits are discussed here (Fig. 6; grey dots indicate the measured TSX σ^0_{HH} values; red triangles correspond to the modelled backscatter). Model fit LIA1 (Fig. 6a) explains 76% (R^2_{adj}) of the σ^0_{HH} variance, spans a sample size of ten value pairs and is based on the predictors z_{snow} and SWE (Table 3). Model fit LIA2 (Fig. 6c) explains 84% (R^2_{adj}) of the σ^0_{HH} variance, spans a larger sample size of 20 value pairs and is based on the predictors z_{snow}, T_i and E_{top}. Furthermore, the overall temporal coverage of pre-melt-onset conditions as well as post-melt-onset conditions is better represented in the LIA2 than the LIA1 data. In combination with the larger sample size, this gives higher confidence in the general quality of the model fit to the LIA2 data. However, the dataset is too limited to further investigate differences between the different LIA classes.

The corresponding equations for the four model fits are:

$$\sigma^0_{LIA1} = -18.52 - 64.40 z_{snow} + 0.19\mathrm{SWE} \quad (1)$$

$$\sigma^0_{LIA2} = -524.11 + 6.42 z_{snow} + 1.87 T_i + 1007.44 E_{top} \quad (2)$$

$$\sigma^0_{LIA1SDS} = -261.32 + 0.90 T_i + 0.03\mathrm{SWE} \quad (3)$$

$$\sigma^0_{LIA2SDS} = -474.02 + 9.50 z_{snow} + 1.68 T_i + 1310.29 E_{top} \quad (4)$$

where σ^0 represents the modelled backscatter values, z_{snow} is the snow depth (m), SWE is the snow water equivalent (kg m^{-2}), T_i is the snow/ice interface temperature (K) and E_{top} is top-layer grain size (m).

All model fits are more sensitive to changes in grain size or temperature parameters (large slopes) than to snow depth or snow water equivalent (small slopes), based on Eqns (1–4). Even small changes in grain size and temperature predictors have a higher impact on the modelled backscatter. However, the snow depth shows a much higher spread in our dataset (Fig. 5) compared with the small spectrum of different top-layer grain sizes (Fig. 3b).

As stated by, for example, Yackel and Barber (2007) and Barber (2005), the snow/ice interface temperature as it affects the dielectric properties of the basal-snow layer (liquid-water content and brine volume fraction) is crucial for explaining the received radar backscatter. Although we did not measure snow salinity, the importance of snow/ice interface temperature is apparent in our results. Related as they are to the liquid-water content, snow grain size and volume are important determinants of volume scattering in the snowpack. Both are also reflected in our results, especially for the LIA2 class.

Because of the limited sample size, the additional potential of VV like-polarization and HV cross-polarization acquisitions could not be taken into account. It is expected that this capability will improve the retrieval of the physical properties of snow on Antarctic sea ice from X-band SAR backscatter data, but additional measurements and further investigation are necessary. This potential is underlined by the spatial and temporal differences between the like/like and like/cross-polarization TSX StripMap images (Fig. 4) for the different study sites. We were able to show that both the snow cover and the snow/ice interface have a strong influence on the TSX σ^0_{HH} signal. However, there are sources of error and uncertainties, due in large part to the lack of simultaneous daily measurements of snow physical properties and TSX swath coverage. Nonetheless, the onset of melt processes and freeze/thaw cycles is clearly recognizable in the X-band SAR backscatter time series.

SUMMARY AND CONCLUSION

In our study, we compared the spatio-temporal evolution of TerraSAR-X backscatter to in situ physical properties of snow on sea ice for a 2 month field campaign in Atka Bay from austral winter to early summer. Multiple linear models based

on different subsets of our data with respect to different local-incidence angles, were able to explain 76–93% of the observed TerraSAR-X HH-polarized backscatter, given a RMSE of 0.87–1.62 dB. The different quality of the model fits, i.e. their potential to explain a maximum percentage of the observed TerraSAR-X HH-polarized backscatter variance, results from the different subsets and limitations to the dataset, such as the exclusion of dry snow measurements. The correlation between the TerraSAR-X HH-polarized backscatter and the snow depth increases when the dataset is reduced to measurements in areas with a snow depth <0.6 m, which is still a rather large amount of snow for Antarctic sea ice. The potential to explain the variations in single-polarization HH X-band SAR backscatter with a few snow physical properties has not yet been presented in comparable detail under non-laboratory conditions. The possibility of fitting a simple multiple linear model to the measured TerraSAR-X HH-polarized backscatter based on up to four snowpack parameters also yields the potential to derive snow physical properties from X-band backscatter using an inverse approach. However, the data presented here cannot directly be used to retrieve snow physical parameters, particularly due to the limited sample size. Additional measurements are necessary (e.g. snow salinity and (quantitative) snow liquid-water content, which were very limited in our study). The addition of backscatter models, as well as snow/sea-ice models, might be informative in future studies and will further increase the potential of this dataset. Future snow-pit measurements and simultaneous TerraSAR-X acquisitions, especially in StripMap dual-polarization mode, are expected to further improve the potential for an inverse approach. Based on the relationships and links shown in this study, future work will necessarily focus on the development of an inverse approach to derive snow physical properties from X-band SAR backscatter.

ACKNOWLEDGEMENTS

This study was funded by the Deutsche Forschungsgemeinschaft in the framework of the priority programme SPP1158 'Antarctic Research with comparative investigations in Arctic ice areas' by grants HE2740/12 and NI1092/2. We thank the Neumayer III overwintering teams for their field support and also the Alfred Wegener Institute (AWI) logistics team for providing the infrastructure. We also thank the German Space Agency for the acquisition and provision of the TerraSAR-X data within the OCE1592 project and Gert König-Langlo for provision of the meteorological data. The help of Oliver Gutjahr with the statistical modelling is very much appreciated. We are also grateful to two anonymous reviewers, chief editor, Petra Heil, and scientific editor, Rob Massom, who helped to improve this study with their positive and constructive feedback.

REFERENCES

Barber DG (2005) Microwave remote sensing, sea ice and Arctic climate. *Phys. Can.*, **61**, 105–111

Barber DG and Nghiem SV (1999) The role of snow on the thermal dependence of microwave backscatter over sea ice. *J. Geophys. Res.*, **104**(C11), 25 789–25 803 (doi: 10.1029/1999JC900181)

Barber DG and Thomas A (1998) The influence of cloud cover on the radiation budget, physical properties, and microwave scattering coefficient (σ^0). *IEEE Trans. Geosci. Remote Sens.*, **36**(1), 38–50 (doi: 10.1109/36.655316)

Barber DG, Papakyriakou TN and LeDrew EF (1994) On the relationship between energy fluxes, dielectric properties, and microwave scattering over snow covered first-year sea ice during the spring transition period. *J. Geophys. Res.*, **99**(C11), 22 401–22 411 (doi: 10.1029/94JC02201)

Barber DG, Reddan SP and LeDrew EF (1995) Statistical characterization of the geophysical and electrical properties of snow on landfast first-year sea ice. *J. Geophys. Res.*, **100**(C2), 2673–2686 (doi: 10.1029/94JC02200)

Cohen J (1988) *Statistical power analysis for the behavioral sciences*, 2nd edn. Lawrence Erlbaum Associates, Hillsdale, NJ

Dierking W (2010) Mapping of different sea ice regimes using images from Sentinel-1 and ALOS synthetic aperture radar. *IEEE Trans. Geosci. Remote Sens.*, **48**(3), 1045–1058 (doi: 10.1109/TGRS.2009.2031806)

Dierking W (2013) Sea ice monitoring by synthetic aperture radar. *Oceanography*, **26**(2), 100–111 (doi: 10.5670/oceanog.2013.33)

Dierking W, Linow S and Rack W (2012) Toward a robust retrieval of snow accumulation over the Antarctic ice sheet using satellite radar. *J. Geophys. Res.*, **117**(D9), D09110 (doi: 10.1029/2011JD017227)

Drinkwater MR, Hosseinmostafa R and Gogineni P (1995) C-band backscatter measurements of winter sea-ice in the Weddell Sea, Antarctica. *Int. J. Remote Sens.*, **16**(17), 3365–3389 (doi: 10.1080/01431169508954635)

Eriksson LEB and 7 others (2010) Evaluation of new space-borne SAR sensors for sea-ice monitoring in the Baltic Sea. *Can. J. Remote Sens.*, **36**(S1), S56–S73 (doi: 10.5589/m10-020)

Fierz C and 8 others (2009) *The international classification for seasonal snow on the ground*. (IHP Technical Documents in Hydrology 83) UNESCO–International Hydrological Programme, Paris

Fritz T and Eineder M (2008) TerraSAR-X Ground Segment. *Basic Product Specification Document* TX-GS-DD-3302 Deutsches Zentrum für Luft- und Raumfahrt (DLR), Cologne

Hallikainen M and Winebrenner D (1992) The physical basis for sea ice remote sensing. In Carsey FD and 7 others eds. *Microwave remote sensing of sea ice*. American Geophysical Union, Washington, DC, 29–46

Hoppmann M and 11 others (2015) The role of ice platelets for Weddell Sea landfast sea ice. *Ann. Glaciol.*, **56**(69) (doi: 10.3189/2015AoG69A678) (see paper in this issue)

Kendra JR, Sarabandi K and Ulaby FT (1998) Radar measurements of snow: experiment and analysis. *IEEE Trans. Geosci. Remote Sens.*, **36**(3), 864–879 (doi: 10.1109/36.673679)

Kern S, Ozsoy-Cicek B, Willmes S, Nicolaus M, Haas C and Ackley S (2011) An intercomparison between AMSR-E snow-depth and satellite C- and Ku-band radar backscatter data for Antarctic sea ice. *Ann. Glaciol.*, **52**(57 Pt 2), 279–290 (doi: 10.3189/172756411795931750)

Kim YS, Onstott RG and Moore RK (1984) Effect of a snow cover on microwave backscatter from sea ice. *IEEE J. Ocean. Eng.*, **9**(5), 383–388 (doi: 10.1109/JOE.1984.1145649)

König-Langlo G (2013a) Continuous meteorological observations at Neumayer station (2012-11). *PANGAEA* (doi: 10.1594/PANGAEA.812150)

König-Langlo G (2013b) Continuous meteorological observations at Neumayer station (2012-12). *PANGAEA* (doi: 10.1594/PANGAEA.812151)

König-Langlo G (2013c) Continuous meteorological observations at Neumayer station (2013-01). *PANGAEA* (doi: 10.1594/PANGAEA.812152)

König-Langlo G (2013d) Meteorological synoptical observations at Neumayer station (2012-11). *PANGAEA* (doi: 10.1594/PANGAEA.811884)

König-Langlo G (2013e) Meteorological synoptical observations at Neumayer station (2012-12). *PANGAEA* (doi: 10.1594/PANGAEA.811889)

König-Langlo G (2013f) Meteorological synoptical observations at Neumayer station (2013-01). *PANGAEA* (doi: 10.1594/PANGAEA.811894)

Massom RA and 12 others (2001) Snow on Antarctic sea ice. *Rev. Geophys.*, **39**(3), 413–445 (doi: 10.1029/2000RG000085)

Nagler T and Rott H (2004) Snow classification algorithm for Envisat ASAR. In Lacoste H and Ouwehand L eds. *Proceedings of the 2004 Envisat and ERS Symposium, 6–10 September 2004, Salzburg, Austria*. (ESA SP-572) European Space Agency, Noordwijk

Ozsoy-Cicek B, Kern S, Ackley SF, Xie H and Tekeli AE (2011) Intercomparisons of Antarctic sea ice types from visual ship, RADARSAT-1SAR, Envisat ASAR, QuikSCAT, and AMSR-E satellite observations in the Bellingshausen Sea. *Deep-Sea Res. II*, **58**(9–10), 1092–1111 (doi: 10.1016/j.dsr2.2010.10.031)

Sihvola A and Tiuri M (1986) Snow fork for field determination of the density and wetness profiles of a snow pack. *IEEE Trans. Geosci. Remote Sens.*, **24**(5), 717–721 (doi: 10.1109/TGRS.1986.289619)

Willmes S, Haas C and Nicolaus M (2011) High radar-backscatter regions on Antarctic sea ice and their relation to sea-ice and snow properties and meteorological conditions. *Int. J. Remote Sens.*, **32**(14), 3967–3984 (doi: 10.1080/01431161003801344)

Worby AP, Markus T, Steel AD, Lytle VI and Massom RA (2008) Evaluation of AMSR-E snow depth product over East Antarctic sea ice using in situ measurements and aerial photography. *J. Geophys. Res.*, **113**(C5), C05S94 (doi: 10.1029/2007JC004181)

Yackel JJ and Barber DG (2007) Observations of snow water equivalent change on landfast first-year sea ice in winter using synthetic aperture radar data. *IEEE Trans. Geosci. Remote Sens.*, **45**(4), 1005–1015 (doi: 10.1109/TGRS.2006.890418)

Yackel JJ, Barber DG, Papakyriakou TN and Breneman C (2007) First-year sea ice spring melt transitions in the Canadian Arctic Archipelago from time-series synthetic aperture radar data, 1992–2002. *Hydrol. Process.*, **21**(2), 253–265 (doi: 10.1002/hyp.6240)

Zahnen N, Jung-Rothenhäusler F, Oerter H, Wilhelms F and Miller H (2003) Correlation between Antarctic dry snow properties and backscattering characteristics in RADARSAT SAR imagery. *EARSeL Proc.*, **2**(1) http://www.eproceedings.org/static/vol02_1/contents.html

E

Field campaigns

Date	Campaigns and relevant measurements
April 2012	**SIZONet 2012, Barrow, Alaska** ▷ Sea-ice thickness from airbone electromagnetic induction sounding in the Western Beaufort Sea
Nov-Dec 2012	**ANT-LAND 2012/2013, Neumayer III, Antarctica** ▷ EM calibration experiments at different height above ground ▷ Multi-frequency EM data from transects across Atka Bay ▷ Validation data (freeboard, snow thickness, sea-ice and platelet-layer thickness, temperature and salinity from sea-ice cores)
April 2013	**SIZONet 2013, Barrow, Alaska** ▷ Sea-ice thickness from airbone electromagnetic induction sounding in the Western Beaufort Sea
June-Aug 2013	**ANT-XXIX/6, Polarsten campaign, Antarctica** ▷ EM calibration experiments (at different height above ground, free-air recordings) ▷ Multi-frequency EM data from transects across deformed sea ice ▷ Validation data (freeboard, snow thickness, sea-ice thickness, voids in sea ice, temperature and salinity from sea-ice cores)

F

Conferences

Date	Conferences and personal contribution
4-7 June 2012	**PhD Days, Sylt, Germany** Poster: "Airborne Electromagnetics for Enhanced Sea-Ice Thickness Retrieval"
6-8 January 2013	**SEG/AGU joint workshop: Cryosphere Geophysics: Understanding a Changing Climate with Subsurface Imaging, Boise, USA** Talk: "Enhanced Sea-Ice Thickness Retrieval with Multi-Frequency Electromagnetic Devices"
23-27 September 2013	**25th Schmucker-Weidelt-Colloquium on deep electromagnetic sounding, Kirchhundem Rahrbach, Germany** Poster: "Multi-Frequency Electromagnetics for Sea-Ice Thickness Retrieval"
10-14 March 2014	**International Symposium on Sea Ice in a Changing Environment, Hobart, Tasmania, Australia** Talk: "Platelet-Layer Volume with Electromagnetic Induction Sounding"
05-08 May 2014	**PhD Days, Helgoland, Germany** Talk: "Platelet-Layer Volume Estimation using Electromagnetic Induction Sounding "

Statutory Declaration

(on Authorship of a Dissertation)

I, Priska A. Hunkeler, hereby declare that I have written this PhD thesis independently, unless where clearly stated otherwise. I have used only the sources, the data and the support that I have clearly mentioned. This PhD thesis has not been submitted for conferral of degree elsewhere.

I confirm that no rights of third parties will be infringed by the publication of this thesis.

Lucerne, January 18, 2016

Signature